

INFORMATION TO USERS

This manuscript has been reproduced from the microfilm master. UMI films the text directly from the original or copy submitted. Thus, some thesis and dissertation copies are in typewriter face, while others may be from any type of computer printer.

The quality of this reproduction is dependent upon the quality of the copy submitted. Broken or indistinct print, colored or poor quality illustrations and photographs, print bleedthrough, substandard margins, and improper alignment can adversely affect reproduction.

In the unlikely event that the author did not send UMI a complete manuscript and there are missing pages, these will be noted. Also, if unauthorized copyright material had to be removed, a note will indicate the deletion.

Oversize materials (e.g., maps, drawings, charts) are reproduced by sectioning the original, beginning at the upper left-hand corner and continuing from left to right in equal sections with small overlaps.

**ProQuest Information and Learning
300 North Zeeb Road, Ann Arbor, MI 48106-1346 USA
800-521-0600**

UMI[®]

**ROLE OF DYNAMICS IN INTERACTING FERMION SYSTEMS: THE STRUTINSKY
METHOD AND GROUND STATE PROPERTIES OF QUANTUM DOTS**

By

TATSURO NAGANO

**A dissertation submitted in partial fulfillment of
the requirements for the degree of**

DOCTOR OF PHILOSOPHY

**WASHINGTON STATE UNIVERSITY
Department of Physics**

DECEMBER 2002

UMI Number: 3086309

UMI[®]

UMI Microform 3086309

Copyright 2003 by ProQuest Information and Learning Company.


**All rights reserved. This microform edition is protected against
unauthorized copying under Title 17, United States Code.**

**ProQuest Information and Learning Company
300 North Zeeb Road
P.O. Box 1346
Ann Arbor, MI 48106-1346**

To the Faculty of Washington State University:

The members of the Committee appointed to examine the dissertation of TATSURO NAGANO find it satisfactory and recommend that it be accepted.


Chair


Matthew D. McChesney


David Miller

ACKNOWLEDGMENTS

I would like to thank the people for their support in helping to make this research possible throughout my years of graduate study. In particular, I would like to acknowledge my research advisor Steven Tomsovic for his patience and intellectual advise under rigorous discipline. His high standard is extremely valuable and necessary to complete my Ph.D research project. I also would like to acknowledge my collaborator Denis Ullmo who was a constant source of perspective and ideas originated from his broad theoretical background. None of the work would have been possible without his patient support and enthusiasm to this project. Regardless of the physical distance between his institution LPTMS (Orsay, France) and here in Washington state, we have been able to work together on this project with more than four years of e-mail communications and my visit to Orsay twice in 2001.

All of the members of the group during my graduate study, Nicholas Cerruti, Katherine Hegewisch, and Brian Watkins and visitors Michael Wolfson, Arul Lakshminarayan, Srihari Keshavamurthy, and Jian Huang have contributed to this dissertation with helpful ideas and valuable discussions. I would particularly like to acknowledge Nicholas Cerruti for his contribution. His extremely patient support, beneficial discussions, and the computer network system administration have my appreciation.

I would like to thank my parents for their constant encouragement and support for my challenge to study abroad.

Finally, I would like to acknowledge the funding support from the National Science Foundation and the Office of Naval Research.

ROLE OF DYNAMICS IN INTERACTING FERMION SYSTEMS: THE STRUTINSKY METHOD AND GROUND STATE PROPERTIES OF QUANTUM DOTS

Abstract

by Tatsuro Nagano, Ph.D.
Washington State University
December 2002

Chair: Steven Tomsovic

We investigate nano-structure quantum dots which show conductance peak oscillations in the Coulomb blockade regime. Although a random matrix theoretical approach (RMT) has made successful predictions, the statistical behaviors of the peak spacings remain mysterious, indicating the necessity of a more subtle treatment of the residual interaction. We pursue a many-body framework, which explicitly includes electron-electron interaction in the context of density functional theory. Based on the idea of the Strutinsky shell correction method, the ground state energy is expressed by an approximate series expansion in the fluctuation part of the density functional, and the physical interpretation of each successive term is analyzed. We identify the energy contribution of the residual interaction due to the screened Coulomb potential. Given that irregularly shaped quantum dots consist of quasiparticles interacting through a screened Coulomb interaction, we employ the two-dimensional coupled quartic oscillator as an effective confinement. The advantage of employing the quartic oscillator is that the degree of chaos can be tuned continuously from integrability to pure chaos, allowing us to study how the nature of the dynamics influences the single-particle orbital occupancies

when spin is taken into account. In the analysis of the ground state configuration and spin polarization, the conductance peak spacings are reproduced and the electron orbital occupations are observed to depend upon the nature of the dynamics. The greater the chaos, the less effective the residual interaction in altering the occupations.

Table of Contents

Acknowledgments	iii
Abstract	iv
List of Tables	xi
List of Figures	xii
1 Introduction	1
1.1 Introduction and Motivation	1
1.2 Organization of This Thesis	6
2 Quantum Dots and Coulomb Blockade	7
2.1 Structure of Quantum Dots	7
2.2 Quantum Point Contacts	10
2.3 Coulomb Blockade	12
2.3.1 Coulomb Blockade in Classical Regime	12

2.3.2	Coulomb Blockade in the Quantum Regime	14
2.4	Constant Interaction Model and Conductance Peak Spacings	18
2.5	Theoretical Approaches to Many-Body Systems	22
2.5.1	Approximations to Many-Body Hamiltonian	23
3	Random Matrix Theory	29
3.1	Introduction	29
3.2	Gaussian Ensemble	30
3.3	Chaotic Systems and Random Matrix Theory	32
4	Semiclassical Density Functional Theory:	
	Strutinsky Energy Corrections in Quantum Dots	38
4.1	Introduction	38
5	Density Functional Theory	44
5.1	Generalized Thomas-Fermi Approximation	
	([Semi]Classical Level)	44
5.2	Kohn-Sham Equations	
	(Quantum Mechanical Level)	47
6	Approximate Ground State Energy:	
	The Strutinsky Energy-Correction Method	49
6.1	Expansion of the Density Functional Theory Ground State Energy	49
6.2	Interpretation of the First-Order Corrections	55

6.3	Interpretation of the Second-Order Corrections	56
7	Contribution of the Residual Interaction to Peak Spacing Distributions	59
8	The Quartic Oscillator: A Case Study	61
8.1	Thomas-Fermi Numerical Calculations	62
8.2	Quantum Numerical Calculations	64
8.3	Strutinsky Energy Corrections	67
8.4	Peak Spacings	77
8.5	Deformation of the Effective Potential	79
9	Role of Dynamics in Interacting Fermion Systems:	
	Ground State Properties of Quantum Dots	82
9.1	Introduction	82
10	Dynamical Systems - Coupled Quartic Oscillator	89
10.1	Semiclassical Effective Potential	89
10.2	Two-Dimensional Coupled Quartic Oscillator	90
10.2.1	Classical Mechanical Level	90
10.2.2	Quantum Mechanical Level	93
10.3	Eigenstates of the System	96
10.3.1	Matrix Representation of Hamiltonian	96
10.3.2	Spectra	99
10.4	Residual Interaction: Study of M_{ij}	102

10.4.1	Local Approximation to the Screened Potential	102
10.4.2	Numerical Approach to M_{ij}	105
11	Breaking anti-unitary symmetry	116
11.1	Anti-Unitary Symmetries	116
11.2	Hamiltonian of System	117
11.3	Numerical Calculations: Energy Spectra	119
11.3.1	Radial harmonic oscillator basis	120
11.3.2	Basis rotation and parity	121
11.3.3	Operator recurrence formulas	122
11.3.4	Matrix representation of Hamiltonian	123
11.3.5	Spectra	129
11.4	Residual Interaction and M_{ij}	136
12	Random Superposition of Plane Waves	152
12.1	Construction of Wave Functions	153
12.2	Validity of the Plane Wave Superposition Approximations	156
12.3	Distribution of Diagonal Elements M_{ii}	157
12.4	Fluctuations of M_{ii}	167
13	Peak Spacing distribution and Ground State Spin Polarization	169
13.1	Ground State Energy	169
13.2	Conductance Peak Spacings	172

13.3 Ground State Spin Polarization	177
13.3.1 Orbital Occupation Scenario	185
13.3.2 Conditional Probability	189
14 Conclusion	193
A Functional Differentiation	204
B Perturbation on the Single-Particle Energy	205
C Optimization of Radial Basis: Choice of Angular Frequency	207
D Number Variance Statistics	215
E Moments of a Distribution	221
F Fluctuations of M_{ij}	223
G Finite Temperature Effects on M_{ij}	230

List of Tables

10.1 Moments of scaled M_{ii} distribution for the quartic oscillator system (TRI) .	111
11.1 Moments of scaled M_{ii} distribution for the quartic oscillator system (TRNI)	151
12.1 Moments of scaled M_{ii} distribution for PWSA system (TRI)	161
12.2 Moments of scaled M_{ii} distribution for PWSA system (TRNI)	164
13.1 Moments of peak spacing distribution	177
13.2 Widths and skewness of even/odd spacing distributions	180

List of Figures

2.1	GaAs/AlGaAs heterostructure	8
2.2	Quantum dot configuration	9
2.3	Coulomb blockade in classical regime	15
2.4	Coulomb blockade in quantum regime	17
2.5	Prediction of CI model	21
3.1	Spectral fluctuation: degree of chaos	36
3.2	Spectral fluctuation: time-reversal symmetry	37
8.1	Electron densities and effective potentials	65
8.2	Convergence of approximations to the quantum ground state energy for electron charge $e = 0.5$	70
8.3	Convergence of approximations to the quantum ground state energy for electron charge $e = 1.0$	71
8.4	Convergence of approximations to the quantum ground state energy for electron charge $e = 1.5$	72
8.5	The electron density and effective potential for $N=20$ particles and $e=1.5$	74

8.6	Comparison between the exact $\delta n \equiv n_{\text{DFT}} - n_{\text{GTF}}$ and its approximation for $e = 1.5$ and $N = 19$	75
8.7	Comparison between the exact $\delta n \equiv n_{\text{DFT}} - n_{\text{GTF}}$ and its approximation for $e = 1.5$ and $N = 20$	76
8.8	The discrete inverse compressibility as a function of electron number N . . .	78
8.9	The fluctuating part of the discrete inverse compressibility scaled by the mean level spacing	81
10.1	Number variance Σ^2 for coupled quartic oscillator	101
10.2	M_{ij} matrix elements for the TRI system with $\lambda = -0.05$	107
10.3	M_{ij} matrix elements for the TRI system with $\lambda = -0.35$	108
10.4	M_{ij} matrix elements for the TRI system with $\lambda = -0.55$	109
10.5	Diagonal elements M_{ii}	110
10.6	Distribution of diagonal elements M_{ii}	112
10.7	Distribution of off-diagonal elements M_{ij} ($i \neq j$)	113
10.8	Eigenstates of two-dimensional coupled quartic oscillator	115
11.1	Poincaré surface of section for $\lambda = 0.20$ and $\epsilon = -1.0$	131
11.2	Poincaré surface of section for $\lambda = -0.20$ and $\epsilon = -1.0$	132
11.3	Poincaré surface of section for $\lambda = -0.80$ and $\epsilon = -1.0$	133
11.4	Spectra convergence for TRNI system	135
11.5	Number variance Σ^2 for TRNI system	137
11.6	M_{ij} for TRNI system with $\lambda = 0.20$	145

11.7 M_{ij} for TRNI system with $\lambda = -0.20$	146
11.8 M_{ij} for TRNI system with $\lambda = -0.80$	147
11.9 Diagonal elements M_{ii} for TRNI system	148
11.10 Distribution of diagonal elements M_{ii} for TRNI system	149
11.11 Distribution of off-diagonal elements M_{ij} ($i \neq j$) for TRNI system	150
12.1 Node counts of wave functions	158
12.2 Random superpositions of plane waves	160
12.3 Diagonal elements M_{ii} for the real random superposition of plane waves . . .	162
12.4 Distribution of diagonal elements M_{ii} for the real random superposition of plane waves	163
12.5 Diagonal elements M_{ii} for the complex random superposition of plane waves	165
12.6 Distribution of diagonal elements M_{ii} for the complex random superposition of plane waves	166
13.1 Fluctuation of peak spacings	174
13.2 Peak spacing distributions	178
13.3 Peak spacing distributions - even/odd structure	179
13.4 Ground state spin polarization	181
13.5 Ground state orbital occupation for the even electron case	183
13.6 Ground state orbital occupation for the odd electron case	184
13.7 Orbital occupation scenario for near integrable system	187
13.8 Orbital occupation scenario for mixed system	188

13.9 Slice of M matrix at i th row	191
13.10 Conditional probability of M_{ij}	192
G.1 Temperature effect on M_{ij}	235

Chapter 1

Introduction

1.1 Introduction and Motivation

It is difficult to imagine people's daily life without electricity. From a light bulb to high-end computers, a battery to power plant, the use of electricity can be found anywhere around us.

The interaction law between charged objects was discovered by Coulomb in the late 1700's. Later, Millikan observed single electron effects in his experiment of falling rate of oil droplets in 1911. Ampere, Ohm, Faraday, Gauss, Maxwell, Lorentz, and many others contributed to the development of the field of electrodynamics in the 19th century.

With the discovery of the Planck theory of radiation employing Planck's constant h in 1900, microscopic phenomena began to receive significant attention. Einstein proposed light quanta in the illustration of the photoelectric effect, and de Broglie, Heisenberg, Schrödinger, and Dirac devoted themselves to the establishment of quantum mechanics in early 1900s. They investigated the microscopic - atomic scale - phenomena.

In the last 20 years, nanostructure technology has undergone dramatic progress due to breakthroughs in sample fabrication techniques. These technologies enable us to investigate the electronic properties of devices within sub-micron scales. At these dimensions and at low temperatures, quantum mechanical interference effects play an important role, but at

the same time, such systems are large enough to consider averaging behaviors. The scale, intermediate between the microscopic and the macroscopic levels, is called mesoscopic. Mesoscopic physics, a word created by Van Kampen in 1981 [1], deals with phase coherent transport phenomena and also thermodynamical properties of disordered electronic systems. The remarkable growth of the field is also due to the fact that the researchers working in different areas have found important underlying commonalities in apparently distinct phenomena. For example, random matrix theory (RMT) [2,3,10,62] gave insight into the physics of conductance fluctuations, and transport properties of disordered systems are well understood within the framework of diagrammatic perturbation theory [4]. These two are interrelated and deeply connected as well to the semiclassical mechanics of chaotic systems [5–7]. One of the significant phenomena in mesoscopic physics [50], especially concerning quantum transport, is the universal conductance fluctuations (UCF) [8–10]. Fluctuations of measured physical quantities are random but reproducible with respect to some external parameter. Although detailed information of each individual measurement is essentially impossible to predict, the statistical behavior of ensemble measurements shows universal features for fully chaotic systems.

In this dissertation, semiconductor quantum dots are studied in the Coulomb blockade (isolated) regime. The “dot” represents an extremely small region, and it contains from one to a few thousand free electrons. The size of the dot ($\sim 100nm - 1\mu m$) is comparable to the electron wavelength ($\sim 40nm$), and the energy of the dot is discretized. Quantum dots are sometimes referred as artificial atoms [11] because of the following characteristics. The

discretized energy levels are analogous to the orbitals of atoms, and the charging energy, the energy required to add/remove an electron to/from the dot has similarity to the atom's ionization energy. While the study of atoms usually involves interaction with light, the measurements of concern to us involve the conductance, which is determined by electron transport properties. It should be emphasized that the advantage of "artificial" atoms is the precise controllability of the system. The number of electrons in the dot, the size and shape, the connection to the environment are all adjusted by externally applied electric fields. In addition, the symmetries of the dot can be controlled by shape and/or by an external magnetic field. Thus, the quantum dot is powerful probe with which to investigate the role of quantum mechanics in mesoscopic physics.

In transport measurements, the dot region is attached to three terminals. Two of the terminals allow electron exchange, called source and drain, while the third terminal is used as a gate electrode. The quantum dot is considered isolated or closed when the electron transport through the region can only be achieved by tunneling through the terminal junctions (source-dot and dot-drain) which act as "quantum point contacts" [12–16], and the charge inside the dot becomes quantized. This situation leads to the Coulomb blockade (CB) oscillation of conductance observed in many experiments [30]. An additional important consideration is that the conductance behavior is greatly influenced by temperature [17, 56]. The Coulomb blockade itself is a classical phenomenon [51], and current flow through the system is suppressed due to its charging.

Quantum dots and point contacts can be created, for instance, in a two-dimensional elec-

tron gas (2DEG) which exists at the interface of a GaAs-AlGaAs heterostructure [55, 56, 58, 93]. The size of the dots is typically $100\text{nm} - 1\mu\text{m}$, which is larger than the Fermi wavelength of electrons ($\sim 40\text{nm}$) but smaller than the mean free path of electrons ($\sim 10\mu\text{m}$), and so the measurements are performed in the ballistic regime. There are from a hundred to a thousand electrons contained in the dot depending on design and doping. At low temperature (few hundred milli-Kelvin), the mean energy level separation of electrons exceeds the thermal energy, and transport through the quantum dot occurs by resonant tunneling. By adjusting the gate voltage, this resonant tunneling produces conductance oscillations. When the charging energy of the dot and the electron level spacings are comparable, both the Coulomb blockade and the resonant tunneling have significant roles.

The Coulomb blockade conductance oscillations have been studied within the simple theoretical framework referred to as the constant interaction (CI) model [52, 54, 55, 63]. This model represents the system's energy in terms of the classical charging cost, the energy required to add an electron to an isolated metal region, and electron occupation energies (the quantum mechanical energy due to the discretized levels of the dots). The CB peak period and peak shapes are successfully predicted by this theory. RMT was originally developed by Wigner [31–34] to investigate neutron resonances of compound nucleus. Energy spectra are obtained in term of eigenvalues of a large sized random matrix which approximates the Hamiltonian of complex systems. Based on the Bohigas-Giannoni-Schmit conjecture [64], the validity of RMT has been broadened to the study of single-particle chaotic systems. Based on the fact that many of the dots come in irregular shapes, RMT provides a theoretical de-

scription of the dot's single-particle energy levels, and the statistical behavior of peak height distributions are well understood in this context [55]. On the other hand, this “constant interaction plus random matrix theory” (CI+RMT) approach failed to predict the statistics of the peak spacing distributions. Taking into account the electron spin degree of freedom, the theory yields a δ -function distribution (when adding the odd number electron) and the Wigner surmise (when adding the even number electron) for the spacing distribution. Thus, the resulting probability density gives a strong bimodal structure due to the spin. However, the experimental measurements give Gaussian distributions with broad non-Gaussian tails on both sides, and there is no such even/odd structure observed [57, 57–59] (or at most weakly).

Although some of the statistical properties of quantum dots have been successfully described by RMT, the assumption that the ballistic quantum dots are generally chaotic must be reconsidered for its validity. In fact, most of the irregular shaped dots produce smooth effective potentials which represents both stable and unstable dynamical motions, and experiments are proceeded with systems in the non-chaotic regime; see Ref. [93], for example. Motivated by the discrepancies between the theoretical predictions and experimental observations concerning the conductance peak spacing distribution, we incorporate many-body effects which explicitly account for the electron-electron interaction in the framework of density functional theory. As opposed to the RMT approach, in which by definition the Hamiltonian is represented as a random matrix, we employ a two-dimensional quartic oscillator confinement, which has an ability of tuning the degree of chaos from near-integrability

to fully chaos, to study the role of dynamics within the peak spacing distribution and the ground state properties of quantum dots.

1.2 Organization of This Thesis

This chapter has introduced basic ideas of nanostructure quantum dots and our motivation for the study of ground state properties of the quantum system in the Coulomb blockade regime. The next two chapters give a more detailed introduction to quantum dots in the Coulomb blockade regime and some basic foundation of RMT. Chapter 4 provides an introduction to density functional theory and its application to quantum dots. Chapter 5 gives a formulation of density functional theory to describe ground state energies. Chapter 6 presents the development of the Strutinsky energy correction method. Chapter 7 discusses the contribution of the residual interaction to conductance peak spacings. Chapter 8 demonstrates the validity of the Strutinsky scheme employing a one-dimensional “toy” model. Chapter 9 discusses the applicability of the Strutinsky method to realistic two-dimensional confined systems. Chapter 10 gives the study of coupled quartic oscillators and behavior of the residual interactions. Chapter 11 deals with the system which breaks all anti-unitary symmetries and discusses the residual interaction effects. Chapter 12 provides the system constructed by the random superposition of plane waves and discusses the relations to the quartic oscillator systems. Chapter 13 discusses conductance peak spacings and ground state properties of quantum dots. Finally, Chapter 14 summarizes the results. Some of the computational concepts and detailed derivations of certain relations are provided in the Appendices.

Chapter 2

Quantum Dots and Coulomb Blockade

2.1 Structure of Quantum Dots

There exist many kinds of quantum dots. Each dot differs in shape, size, material, and fabrication process, depending on the purpose of experiments. Here, we introduce the semiconductor quantum dot generated in a two-dimensional electron gas (2DEG) which forms at the interface of a GaAs/ $\text{Al}_x\text{Ga}_{1-x}\text{As}$ heterostructure [18–20].

The heterostructure layering consists of a GaAs substrate, a AlGaAs layer with an n-type dopant, which provides electrons to form a 2DEG, and thin GaAs cap to prevent the AlGaAs layer from oxidation. Typical layer thicknesses are 50-200nm of AlGaAs within a 10nm GaAs cap. This places the 2DEG 60-210nm below the surface. The band structure provides a potential well at the interface of GaAs-AlGaAs layers, and electrons only occupy the conduction band (the subband of the potential well) below the Fermi energy. At low temperature, there is only one subband available below the Fermi energy; the second subband is 150meV above. Since the typical Fermi energy is 10meV and the device temperature is set below 1K (86 μeV), the second subband is essentially completely unoccupied, and the electron gas can be treated as two-dimensional. Due to the fact that GaAs and AlGaAs have only a slight lattice mismatch, the 2DEG layer is essentially defect free. As a consequence, the electron mean free path in the 2DEG layer can be 10 μm or more. Other significant

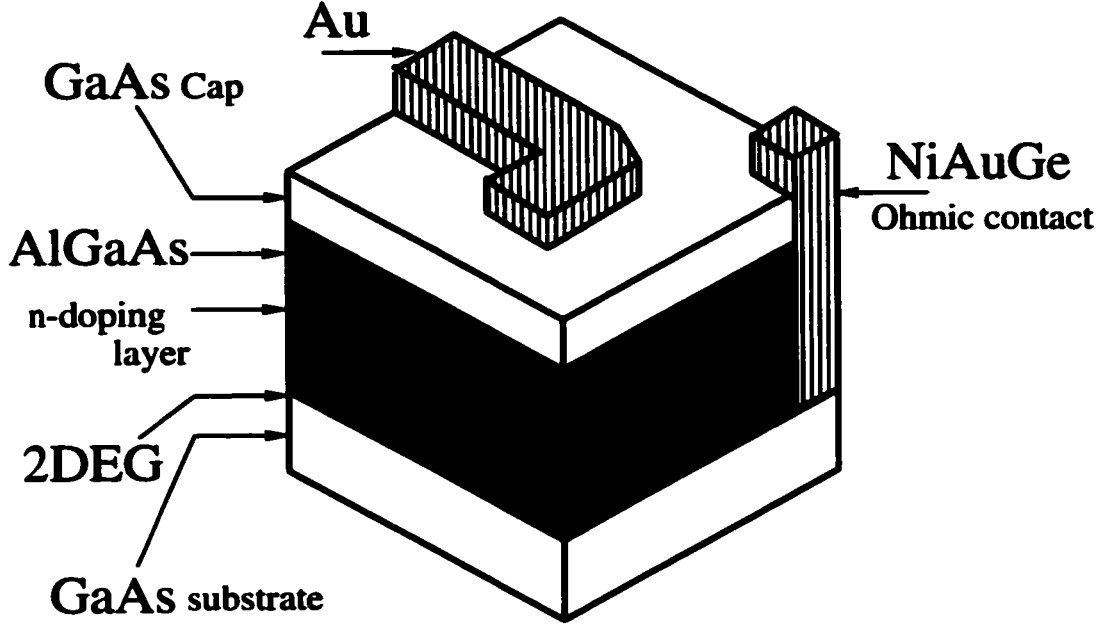


Figure 2.1: Schematic diagram of a GaAs/AlGaAs heterostructure. A Au gate is deposited on the surface, and the 2DEG region can be accessed through a NiAuGe ohmic contact. The 2DEG layer is located at the interface of the GaAs/AlGaAs heterostructure. For more detail, see Ref. [20].

parameters in the 2DEG are [19,21]: effective mass $m^* = 0.067m_e$ where m_e is the electron mass, density of states $\rho(E) = 2m^*/2\pi\hbar^2 = 2.8 \times 10^{10} \text{ (cm}^{-2}\text{meV}^{-1}\text{)}$, level spacing $\Delta(E) = 1/\rho(E) = 3.57 \text{ (}\mu\text{eV}\mu\text{m}^2\text{)}$, Fermi wave vector $k_F = 1.58 \times 10^6 \text{ (cm}^{-1}\text{)}$, Fermi wavelength $\lambda_F = 2\pi/k_F = 40 \text{ (nm)}$, Fermi energy $E_F = (\hbar k_F)^2/2m^* = 14.0 \text{ (meV)}$, Fermi velocity $v_F = \hbar k_F/m^* = 2.7 \times 10^7 \text{ (cm/s)}$, scattering time $\tau = 0.38 - 38 \text{ (ps)}$, and mean free path $l = v_F\tau = 10^2 - 10^4 \text{ (nm)}$.

In addition to the vertical confinement of the 2DEG layer, one must restrict the electrons to a small region to create a “dot”. With electron lithography, the thin film of metal (Au) is patterned on top of the GaAs cap layer to provide the gates. Applied negative gate voltages

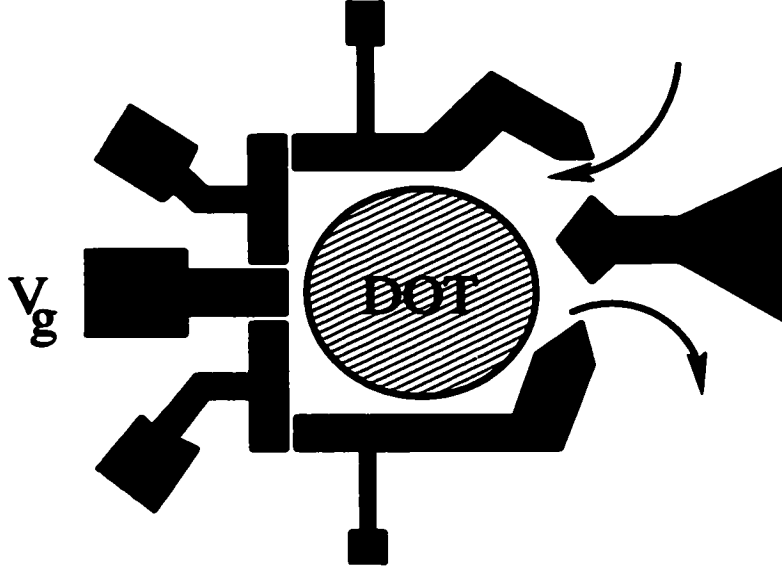


Figure 2.2: Schematic diagram of quantum dot from the top. Grey colored regions are gates, and the circle represents the confined dot region. Applied negative voltages effectively confine electrons in the 2DEG layer. The shape of the dot can be distorted by changing the strength of the gate voltage. Arrows indicate the direction of current flow. For actual STM images; see Ref. [20] for example.

generate confining potential barriers at the 2DEG surface and depletes the electrons. In many cases, there are several gates patterned on the wafer. The dot shape is controlled by tuning some of the gates, and other gates are used to control the connection to outside electron reservoirs, source and drain. The quantum point contact is accomplished by the control of these gates. The statistical ensemble of data is obtained by altering the shape of the dot without changing the capacitance of the system. The resulting effective dot size is typically a few microns or less, the dot contains from one to a thousand electrons, and the temperature is kept below a few hundred milli-Kelvin.

The direct electrical connection to the 2DEG is achieved by ohmic contacts, and a small

source to drain bias voltage V_{sd} is applied. The current flow across the system can be detected by measuring the voltage change in V_{sd} . Thus, it is important to retain the voltage small such that $eV_{sd} < k_B T$.

2.2 Quantum Point Contacts

As the simplest mesoscopic device, we introduce quantum point contacts. They are also used in the coupling to quantum dots. Quantum point contacts (QPCs) are short one-dimensional channels connecting electron source and drain. As we just explained in the fabrication of quantum dots, the point contacts are created at the 2DEG layer with negatively applied gates to produce potential barriers. By adjusting the gate voltage, one can make the size of the opening comparable to the Fermi wavelength, and the conductance through the junction becomes quantized [13, 14, 19, 22–24].

Let us consider the conductance through QPCs following the description given in Ref. [19, 24]. Suppose two gates are arranged in line with a small gap in between, the x-y coordinate is conveniently defined such that the direction of the current is taken as y-direction and the gates are aligned in x-direction. This way, the Hamiltonian is given as

$$\hat{H} = \frac{\hat{p}_x^2}{2m^*} + eV(x) + \frac{\hat{p}_y^2}{2m^*} \quad (2.1)$$

where m^* is the effective mass of electron, $V(x)$ is the potential due to the negatively applied gate voltages, and electrons propagate as free particles in the y-direction. This assumption is

valid when the 2DEG layer is reasonably defect free [25]. Assuming the harmonic oscillator confinement in x-direction [12], $V(x) = m^* \omega^2 x^2 / 2$, the energy eigenvalues are

$$E_n = \left(n - \frac{1}{2}\right) \hbar \omega + \frac{\hbar^2 k_y^2}{2m^*} \quad (2.2)$$

where $n = 1, 2, \dots$ (note n starts with 1). When a small bias voltage V_{sd} is applied between source and drain, the chemical potential of both sides becomes $eV_{sd} = \mu_s - \mu_d$, and this defines the upper bound of the electron energy $\mu_d < E_F < \mu_s$. Electrons travel through the junction only via the energy levels $E_n < E_F$ at $k_y = 0$ occupying the lowest N orbitals. Thus, the net current is given by

$$I = e \sum_{n=1}^N \int_{\mu_d}^{\mu_s} dE (1/2) \rho_n(E) v_n(E) T_n(E), \quad (2.3)$$

where the sum is taken over all occupied subbands, the one-dimensional density of states is $\rho_n(E) = \sqrt{2m^*/E}/\pi\hbar$, the velocity of electrons is $v_n(E) = \sqrt{2E/m^*}$, and $T_n(E)$ is the transmission probability of the n th subband. $T_n(E)$ are the eigenvalues of the product of transmission matrix and its Hermitian conjugate, and its values range from 0 to 1. For small V_{sd} bias, $T_n(E) \simeq T_n(E_F)$, and one obtains the conductance

$$G = \frac{I}{V_{sd}} = \frac{2e^2}{h} \sum_{n=1}^N T_n(E_F) \simeq \frac{2e^2}{h} N \quad (2.4)$$

where in the last step, $T_n(E_F)$ is approximated to 1, provided that the quantum point

contact is ideal; that is, no backscattering. Each occupied subband equally contributes to the conductance by $2e^2/h$. Thus, by sweeping the gate voltage V_g , a conductance staircase with step height of $2e^2/h$ can be observed. This is the case of zero temperature and no magnetic field, and the factor of 2 represents the spin degree of freedom. For finite temperature, the stairs are smeared, and for non-zero magnetic field, the spin degeneracies are split and the conductance shows a staircase with step of e^2/h giving the quantum unit of conductance.

Therefore, to close a quantum dot, the conductance through a QPCs is set to $g < e^2/h$ making the number of modes at each point contact less than one.

2.3 Coulomb Blockade

2.3.1 Coulomb Blockade in Classical Regime

When an isolated region is weakly coupled to two leads by the quantum point contacts ($g < e^2/h$) and controlled with the gate electrode to adjust the energy of the region, the current through this region is suppressed. Considering the device as two initially neutral regions consisting of the isolated “island” and its environment, it requires the system to pay an energy cost to transfer an electron from one region to the other. This energy cost is the capacitive charging energy, and at low temperature, the suppression of the conductance is known as the Coulomb blockade [53].

The theory of the Coulomb blockade was developed earlier by Kulik and Shekhter [91,92] in the classical regime where $\Delta \ll k_B T \ll e^2/C$, k_B is the Boltzman’s constant, and Δ is the

mean level separation of island's energy levels. In this regime, the island's energy is treated as a continuum, and this is considered as a good approximation for metals. The total energy of classical electrostatic energy of the system is

$$U(n) = -(ne)V_g + \frac{(ne)^2}{2C} \quad (2.5)$$

where n is the number of electrons in the island and V_g is the externally applied gate voltage. Because of the point contacts, electron charge is discretized, and so the relation $Q = C_g V_g$ does not hold. For the range $(N - 1/2)e/C_g < V_g < (N + 1/2)e/C_g$ or equivalently $V_g = (N + x)e/C_g$ with $|x| < 1/2$, where C_g is capacitance between the island and the gate, the total energy is minimized when $n = N$, and the charge of the island changes linearly in V_g from $-e/2$ to $e/2$. However, when $V_g = (N + 1/2)e/C_g$ or $x = 1/2$ the total energy becomes minimum both at $n = N$ and $N + 1$ giving $U(N) = U(N + 1)$, and the charge becomes either $\pm e/2$. Only at this charge degeneracy point, electrons are allowed to move from the source to the island and back to the drain, allowing the number of electrons inside the island to fluctuate from $N \rightarrow N + 1 \rightarrow N$. As a consequence, current flows across the dot. By sweeping the gate voltage, the oscillation of conductance emerges. The period of this oscillation is $\Delta V_g = e/C_g$, and it is related to the energy cost of removing the Coulomb blockade $\Delta E = e^2/C_g$. Since there exist source-dot and dot-drain capacitances, the total capacitance is, in fact, $C_{\text{tot}} = C_g + C_s + C_d$, and this gives the period

$$\Delta V_g = \frac{e}{C_g} = \frac{1}{\alpha} \frac{E_c}{e} \quad (2.6)$$

where $E_c = e^2/C_{\text{tot}}$ is the charging energy and $\alpha = C_g/C_{\text{tot}}$.

2.3.2 Coulomb Blockade in the Quantum Regime

In semiconductor quantum dots, the situation is different from a metal. Due to the small system size, the energy of the isolated region “dot” becomes discrete, and at low enough temperature, one has to take the effects of the discreteness of the energy levels into account. In this regime, the charging energy, the single-particle energy spacing, and the thermal energy are related as $e^2/C \sim \Delta \gg k_B T$. To isolate the dot, the leads must be attached via a point contact by $g < e^2/h$. The total energy of the system containing N electrons is

$$U(N) = E_{\text{dot}}(N) - (Ne)\alpha V_g \quad (2.7)$$

where the energy of the dot region is

$$E_{\text{dot}}(N) = \frac{(Ne)^2}{2C_{\text{tot}}} + \sum_i \epsilon_i \quad (2.8)$$

where ϵ_i is the single-particle energy levels of the dot. It should be mentioned that the dot energy now consists of the single-particle energies of all occupied levels in addition to the charging energy.

Whereas in the classical regime, the current flow occurs at the degeneracy point, there is an additional condition for quantum systems in order to have current flow. In the limit of zero-temperature and small, applied source-drain bias V_{sd} , the gate voltage must be tuned

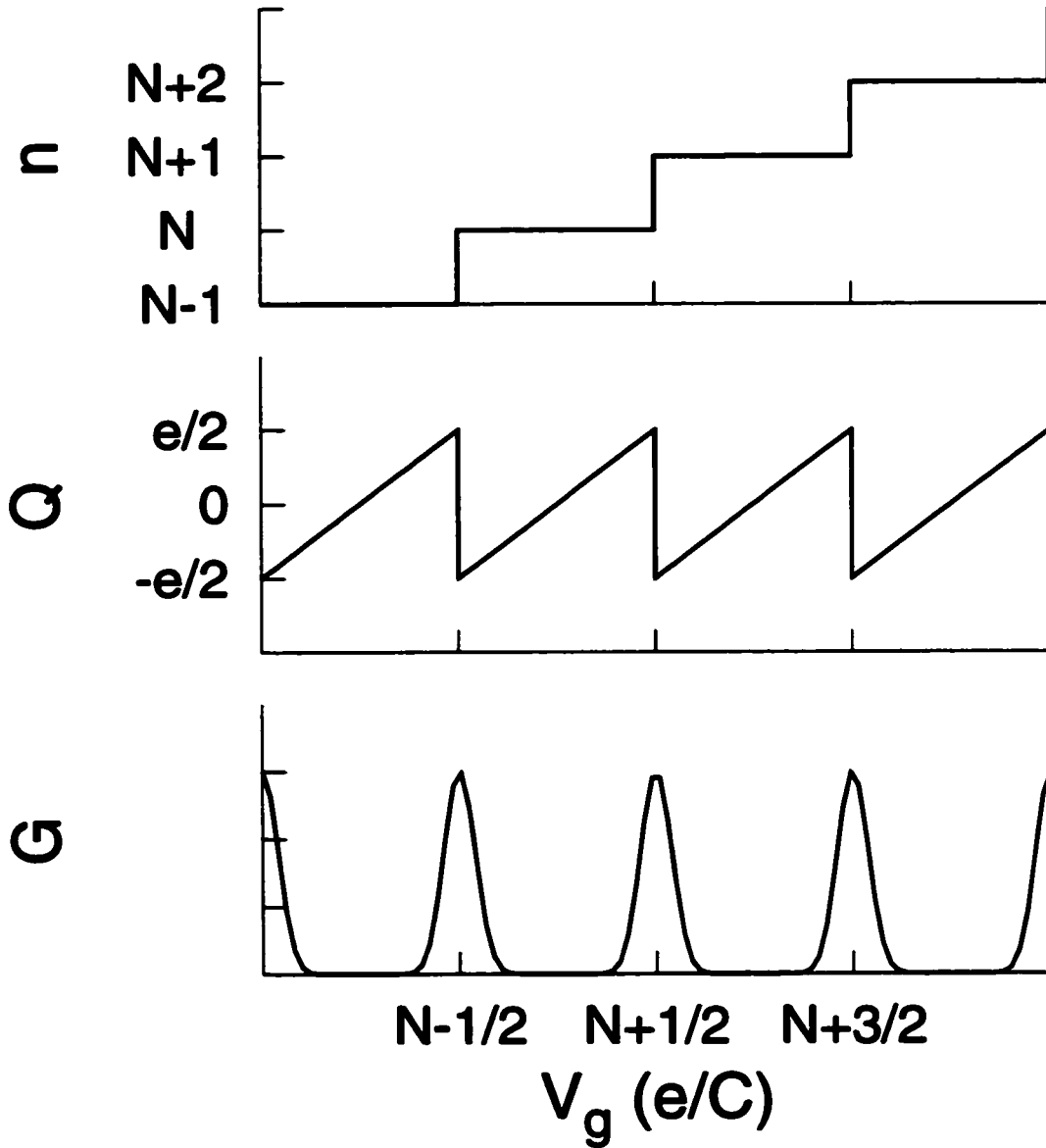


Figure 2.3: Schematic view of Coulomb blockade in the classical regime. Number of electrons in an isolated island, n , charge of island, Q , and conductance through island, G (in arbitrary units), are plotted as functions of gate voltage respectively from top to bottom. Voltage is in the unit of e/C . Current flow is suppressed between conductance peaks due to the Coulomb blockade.

such that the first unoccupied energy level of the dot matches the Fermi energy of the electron reservoirs (source and drain). As a consequence, an electron can move into the dot and out to the drain by resonant tunneling, and current will flow in response to the bias voltage.

When the gate voltage is tuned such that $e\alpha V_g = E_{\text{dot}}(N+1) - E_{\text{dot}}(N)$, the total energy is degenerate, $U(N) = U(N+1)$, and current flows through the dot. The period of oscillation or the conductance peak spacing ΔV_g is expressed as

$$e\alpha\Delta V_g = E_{\text{dot}}(N+1) - 2E_{\text{dot}}(N) + E_{\text{dot}}(N-1) \equiv \Delta^2 E_{\text{dot}}(N), \quad (2.9)$$

where $\Delta^2 E_{\text{dot}}$ represents the second difference in the ground state energies of the dot. Assuming that N electrons fill the lowest N states, the peak spacing becomes

$$\Delta^2 E_{\text{dot}}(N) = \frac{e^2}{C} + \epsilon_{N+1} - \epsilon_N. \quad (2.10)$$

Furthermore, if one takes the electron spin degeneracy into account, the spacings are

$$\Delta^2 E_{\text{dot}}(N) = \begin{cases} e^2/C + \epsilon_{N+1} - \epsilon_N & N \text{ even} \\ e^2/C & N \text{ odd.} \end{cases} \quad (2.11)$$

This is called the constant interaction (CI) model since the electron interaction is always taken as constant through the charging energy e^2/C .

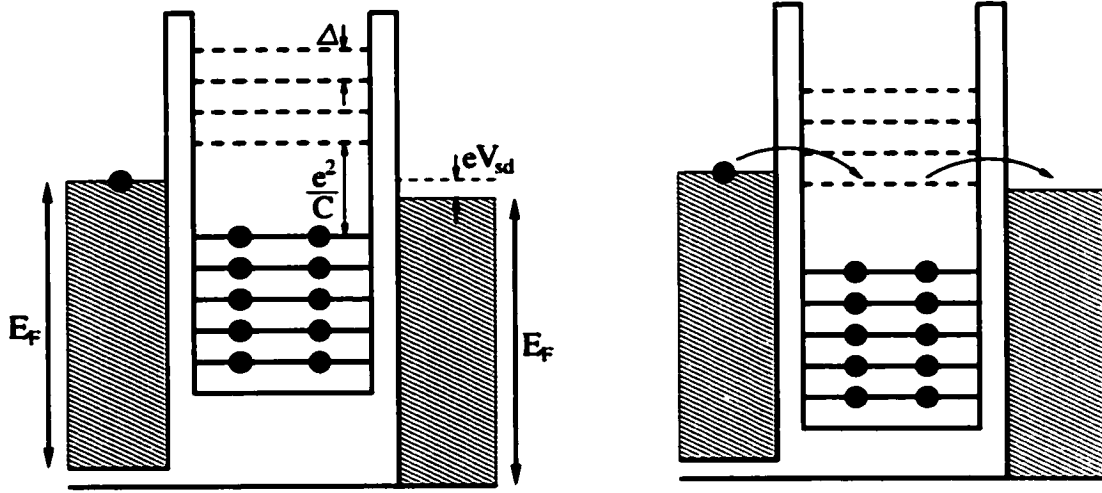


Figure 2.4: Schematic illustration of Coulomb blockade in quantum dots. Fermi energy of source and drain is E_F with negligibly small bias V_{sd} , and the discrete energy levels are shown (Δ is the associated mean level spacing). Left figure: the charging energy creates an effective gap e^2/C between the highest filled level and the lowest unoccupied level. Since the chemical potential of the dot does not match the Fermi levels of the source and drain, the electron tunneling process is prohibited. The number of electrons inside the dot is fixed. Right figure: the gate voltage is tuned such that the lowest unoccupied energy level matches the Fermi energy of reservoirs. This situation lifts the Coulomb blockade and allows an electron to tunnel through the barrier one at a time. As a consequence, the conductance shows a peak.

2.4 Constant Interaction Model and Conductance Peak Spacings

Within the constant interaction model, the conductance peak spacings are given as a sum of the charging energy and the single-particle energy level spacing. In practice, since the charging energy is a smoothly varying function of gate voltage, the spacing variations come from quantum fluctuations.

Random matrix theory (RMT) was originally developed for the study of strongly interacting many-body systems such as compound nuclei. Based on the Bohigas-Giannoni-Schmit conjecture, the single-particle quantum system, whose classical counterpart represents chaotic dynamics, can be investigated in terms of RMT; see next chapter for more detailed explanation of RMT. Because many of the dots come with disordered or irregular shape, the energy spectrum of the dot can be approximated by the eigenvalues of a random matrix. In addition, quantum dot experiments normally proceed by collecting an ensemble of measured data. This indicates that the important physical quantities are not system specific information, such as shape for example, but more generic properties such as symmetry classes. This, in fact, supports the applicability of RMT to the study of irregular systems. Time-reversal symmetry within a dot is controlled by applying a magnetic field. The presence (absence) of magnetic field breaks (preserves) the time-reversal symmetry.

Based on the Gaussian ensemble, the Wigner-Dyson statistics give the distribution of nearest neighbor energy level separations $\epsilon_{N+1} - \epsilon_N$ (NNS) for chaotic systems. For time-

reversal invariant systems and for time-reversal non-invariant systems, the NNS distributions are approximately given as

$$P_{WD}(s) = \frac{\pi}{2} s e^{-(\pi/4)s^2} \quad (\text{GOE}) \quad (2.12)$$

$$P_{WD}(s) = \frac{32}{\pi^2} s^2 e^{-(4/\pi)s^2} \quad (\text{GUE}) \quad (2.13)$$

where $s = (\epsilon_{i+1} - \epsilon_i)/\Delta$ and Δ is orbital mean level spacing. GOE and GUE represent Gaussian orthogonal ensemble and Gaussian unitary ensemble respectively (they will be discussed in the next chapter). Using these distributions, the distributions of the CB peak spacings are found to be

$$P(s) = \frac{1}{2} \left[\delta(s) + \frac{\pi}{2} s e^{-(\pi/4)s^2} \right] \quad (B = 0) \quad (2.14)$$

$$P(s) = \frac{1}{2} \left[\delta(s) + \frac{32}{\pi^2} s^2 e^{-(4/\pi)s^2} \right] \quad (B \neq 0). \quad (2.15)$$

where the δ -function comes from the charging energy e^2/C . This approach is often called the constant interaction plus random matrix theory (CI+RMT) or CI+SDRMT where SD represents “spin degenerate”. In Fig. (2.5), the distribution curves are plotted for both the presence and absence of magnetic fields. For each case, the bimodal structure is clearly observed representing the electron spin effect. The width of the distribution (standard deviation in the unit of the orbital mean level spacing $\Delta = 2\pi\hbar/m^*A$) are $\sigma_{B=0} = 0.62$ and $\sigma_{B \neq 0} = 0.58$. For integrable systems, statistics of energy spectra can be described by the Poisson distribution [110]. Within the CI model, the CB peak spacing distributions are

given as

$$P(s) = \frac{1}{2} \left[\delta(s) + ae^{-as} \right]. \quad (2.16)$$

The width of the distribution is $\sigma = 0.87$.

The peak spacings are experimentally measured in irregular shaped quantum dots in the Coulomb blockade regime [56,57,59,60,93]. The statistics obtained are significantly different from the CI+RMT predictions. The distributions are symmetric and well described by a Gaussian fit except for the long tails on both sides. The width (fluctuation) of distributions are larger than predicted, and the fluctuations are of order 0.1 - 0.15 measured in units of the classical charging energy E_c [57, 59, 60]. Most importantly, no bimodal structure has been observed as if the statistics are independent of the electron spin. The gas parameter of the experimental dot setup [56, 57, 59, 60] ranges from $0.93 \leq r_s \leq 1.35$ with the exception of $r_s = 2.1$ in Ref. [60]. The gas parameter, r_s , is often used to characterize an electron gas in metal; see next section.

Spacing distributions are expected to be bimodal in the absence of electron interactions. The experimentally observed unimodal behavior is due to the strong electron interaction effect as explained in Ref. [27]. Of the recent experimental study [93], the spin-pairing effects in the peak spacings are observed in the measurements of dots with higher electron densities. The gas parameter of their dots is $r_s = 0.72$ and the electron interactions are weaker than previous experiments. However, the spacing distributions are still far from the CI model predictions.

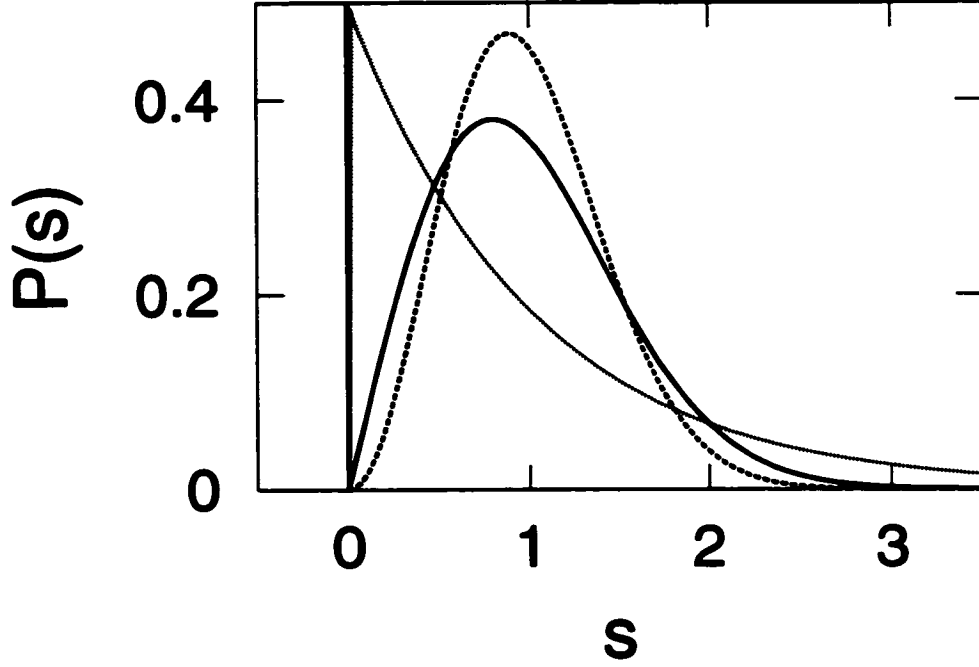


Figure 2.5: CB conductance peak spacing distributions predicted by CI+SDRMT. Solid line represents the spacing distribution in the absence of magnetic field ($B = 0$), and the dashed line represents the distribution in the presence of a magnetic field ($B \neq 0$). The charging energy is subtracted off from each point to shift the distributions by e^2/C . Delta functions are shown for both at $s = 0$ (on top of each other). Distributions are based on the Wigner surmise, and energy level separations are measured in the unit of the orbital mean level spacing. For the sake of comparison, the dotted line represents the spacing distribution for integrable case. The Wigner surmise for chaotic case are replaced by the Poisson statistics.

2.5 Theoretical Approaches to Many-Body Systems

The failure of the constant interaction model in predicting the statistical behavior of the conductance peak spacing, indicates that the non-interacting single-particle treatment of the system has to be replaced by more involved many-body, explicitly interacting electron systems.

To characterize the interacting electron systems, the gas parameter r_s is often used [30]. r_s represents the electron interaction strength at an average spacing among electrons relative to the kinetic energy. Let us consider an electron gas in two-dimensional space. Since the electron is a fermion, each particle can stay at the same position \mathbf{r} only by having different momentum values based on the semiclassical point of view. In momentum space, this situation can be considered as the states occupying the circle of radius p_F where p_F is the Fermi momentum. Knowing that each state occupies a volume of h in phase space, the number of states in unit coordinate space, or equivalently density of electrons, is given by $n = (2/h^2)\pi p_F^2$, where 2 represents the electron spin degree of freedom. The gas parameter and electron density are related as $\pi(r_s a_0)^2 n = 1$ because r_s is the radius of the circle which encloses the unit electron charge in units of Bohr radius $a_0 = \hbar^2/m e^2$. Therefore, the typical electron interaction energy and the averaged kinetic energy are given as $\bar{E}_p = e^2/(2r_s a_0)$ and $\bar{E}_k = E_F/2$, and the ratio becomes

$$\frac{\bar{E}_p}{\bar{E}_k} = \frac{e^2/(2r_s a_0)}{(p_F^2/2m)/2} = r_s. \quad (2.17)$$

where the Fermi energy is $E_F = (\hbar^2/2m)(2/r_s^2 a_0^2)$. If the interaction is weak and the system is dominated by kinetic motion, the ratio r_s becomes small and it describes a high density system. In this limit $r_s \ll 1$, the interaction can be treated as a perturbation to the free propagating particle motion. On the other hand, when the interaction exceeds the kinetic energy, r_s has a large value representing low density electron systems. For $r_s \gg 1$, electrons tend to form a lattice to minimize the interaction. In the intermediate range, neither of the effects can be treated perturbatively, and many of the metal electron systems fall into this range $1 < r_s < 6$ [26], requiring the most difficult theoretical treatment. For the 2DEG system of our interest, the ratio is $r_s \sim 1$.

2.5.1 Approximations to Many-Body Hamiltonian

In principle, a single-particle system governed by the time-independent Schrödinger equation $[\hat{\mathbf{p}}^2/2m + V(\mathbf{r})]\psi(\mathbf{r}) = E\psi(\mathbf{r})$ can be solved exactly for any potential confinement. Whereas, for many-body systems, the Schrödinger equation becomes

$$\left(\sum_i^N \left[-\frac{\hbar^2}{2m} \nabla_i^2 + V(\mathbf{r}_i) \right] + \frac{e^2}{2} \sum_{i \neq j}^N \frac{1}{|\mathbf{r}_i - \mathbf{r}_j|} \right) \Psi(\mathbf{r}_1, \dots, \mathbf{r}_N) = E\Psi(\mathbf{r}_1, \dots, \mathbf{r}_N) \quad (2.18)$$

where the Coulomb interaction is employed as mutual particle interaction. Because of the coupling of the interaction term, it is prohibited to decompose the Hamiltonian into N -independent equations for each electron. To solve this, one has to rely on approximation techniques. We introduce three commonly used approaches in the study of CB peak spacing: an exact diagonalization method [27, 57], the Hartree-Fock method [71–73], and density

functional theory [28, 29, 77, 100].

The exact diagonalization is suitable for a system containing a small number of particles. Although, in principle, the matrix representation of the Hamiltonian requires a complete set of some infinite basis; with a suitable choice of basis, there are cases in which the eigenstates of the system can be approximated well by a finite basis set which spans the sub-space in Hilbert space. The Hamiltonian matrix is constructed by evaluating the exact many-body Hamiltonian in terms of this truncated basis set. Matrix diagonalization proceeds numerically to obtain energy eigenvalues and corresponding eigenstates. The choice of a suitable basis or matrix truncation technique will be discussed in chapter 11. Due to finite computer resources, the particle number is limited ($N \sim 15$) in this scheme. Although this number is rather small, it has an advantage of accounting for all of the interaction effects including correlation of wavefunctions.

In the Hartree-Fock method, many-body wavefunctions are approximated as the Slater determinant of N spin-orbit functions,

$$\Psi(\mathbf{r}_1, \dots, \mathbf{r}_N) = \frac{1}{\sqrt{N!}} \det \begin{bmatrix} \phi_1(\mathbf{r}_1) & \phi_1(\mathbf{r}_2) & \dots & \phi_1(\mathbf{r}_N) \\ \phi_2(\mathbf{r}_1) & \phi_2(\mathbf{r}_2) & \dots & \phi_2(\mathbf{r}_N) \\ \vdots & \vdots & & \vdots \\ \phi_N(\mathbf{r}_1) & \phi_N(\mathbf{r}_2) & \dots & \phi_N(\mathbf{r}_N) \end{bmatrix} \quad (2.19)$$

where \mathbf{r} represents the spatial coordinate and spin. It should be noted that the Pauli exclusion

principle is satisfied by the antisymmetry under the position exchange of any two particles,

$$\Psi(\mathbf{r}_1, \dots, \mathbf{r}_i, \dots, \mathbf{r}_j, \dots, \mathbf{r}_N) = -\Psi(\mathbf{r}_1, \dots, \mathbf{r}_j, \dots, \mathbf{r}_i, \dots, \mathbf{r}_N). \quad (2.20)$$

Now the task is to find a set of ϕ which minimizes the total energy of the system under the constraint that the each ϕ is normalized. This can be done by using the Lagrange multiplier method,

$$\frac{\delta}{\delta \phi} \left(\langle \hat{H} \rangle - \sum_i \lambda_i \int d\mathbf{r} |\phi_i|^2 \right) = 0 \quad (2.21)$$

where λ_i are the Lagrange multipliers. It reduces the many-body Hamiltonian into the one-electron Schrödinger equation of the form,

$$\left[-\frac{1}{2} \nabla^2 + V_{\text{ext}}(\mathbf{r}) \right] \phi_i(\mathbf{r}) + \sum_j \int d\mathbf{r}' \frac{|\phi_j(\mathbf{r}')|^2}{|\mathbf{r} - \mathbf{r}'|} \phi_i(\mathbf{r}) - \sum_{j;\sigma=\sigma'} \int d\mathbf{r}' \frac{\phi_j^*(\mathbf{r}') \phi_i(\mathbf{r}')}{|\mathbf{r} - \mathbf{r}'|} \phi_j(\mathbf{r}) = \epsilon_i \phi_i(\mathbf{r}). \quad (2.22)$$

The first and second terms are single-particle kinetic energy and potential energy due to an external confinement. The third term, called the direct or the Hartree term, is the electrostatic potential due to the charge distribution of all electrons. The infinite self-interaction energy at $j = i$ is canceled by the fourth term. The fourth term, denoted as the exchange or the Fock term, stems from the inclusion of the Pauli exclusion principle. The exchange term only sums over states with spins which are parallel, and it represents the effect of the spatial avoidance of particles having the same spin. This ends up reducing the energy cost, and so the sign of exchange energy is negative. The calculation of the Hartree-Fock equa-

tion proceeds by determining the direct and exchange interaction terms in a self-consistent manner. The largest source of error comes from the absence of the correlation effect between electrons.

Density functional theory is also a widely known technique to deal with many-body systems. We introduce this method following Ref. [26]. The approach starts with two theorems proved by Hohenberg and Kohn [78]: (1) the electron density in the ground state energy is a functional of a given potential, and (2) the potential is a unique functional of the electron density. This leads to the statement that the ground state energy is given by a minimum of the total energy functional with respect to electron density variations. The ground state functional consists of five terms: kinetic energy, potential energy due to the external confinement $V_{\text{ext}}(\mathbf{r})$, Hartree energy, exchange energy, and correlation energy. The explicit functional forms of the kinetic, exchange, and correlation energies are not known. However, the kinetic energy is simply expressed by the quantum mechanical operator,

$$T = \frac{\hbar^2}{2m} \int d\mathbf{r} \sum_i |\nabla^2 \phi_i|^2. \quad (2.23)$$

When one requires an explicit functional for T , the Thomas-Fermi approach gives an approximate form

$$T[n] = \frac{3}{5} (3\pi^2)^{2/3} \int d\mathbf{r} n^{5/3}(\mathbf{r}), \quad (2.24)$$

where the square bracket represents that the quantity is a functional of its argument function, and $n(\mathbf{r}) = \sum_i |\phi_i|^2$ is the electron density. Since the Thomas-Fermi approach is semiclassical,

it only captures an averaging behavior and misses some quantum mechanical fluctuations; see later chapters. The confining energy and the Hartree energy are given respectively by

$$E_{\text{ext}}[n] = \int d\mathbf{r} n(\mathbf{r}) V_{\text{ext}}(\mathbf{r}) \quad (2.25)$$

$$E_{\text{H}}[n] = \frac{e^2}{2} \int d\mathbf{r} d\mathbf{r}' \frac{n(\mathbf{r})n(\mathbf{r}')}{|\mathbf{r} - \mathbf{r}'|}. \quad (2.26)$$

The difficult part is to include the exchange and correlation energy functionals. Kohn and Sham [79] developed the method called the local density approximation (LDA) which describes the ground state functional with the approximate exchange and correlation energies. In LDA, exchange and correlation energy contributions are combined as $E_{\text{xc}}[n]$, and the approximation is carried out as follows. First, they make the assumption that the exchange and correlation energy in the ground state is represented by $\epsilon_{\text{xc}}(n_0)$ for each electron, where n_0 is the uniform electron gas density. Then, the exchange-correlation energy for N electrons becomes

$$E_{\text{xc}}[n] = \int d\mathbf{r} n_0 \epsilon_{\text{xc}}(n_0). \quad (2.27)$$

The crucial point is that they replaced this uniform electron gas density with an inhomogeneous density $n(\mathbf{r})$,

$$E_{\text{xc}}[n] = \int d\mathbf{r} n(\mathbf{r}) \epsilon_{\text{xc}}(n(\mathbf{r})). \quad (2.28)$$

This approximation is good as long as the density $n(\mathbf{r})$ is slowly varying function of position. In fact, it was found that this approach approximates well even in atoms and solids where the density changes significantly. Therefore, the total energy functional is given by the sum

of all the contributions

$$E_{\text{tot}}[n] = T[n] + E_{\text{ext}}[n] + E_{\text{H}}[n] + E_{\text{xc}}[n]. \quad (2.29)$$

The ground state energy is obtained by minimizing this functional under the constraint $N = \int d\mathbf{r} n(\mathbf{r})$. Using the Lagrange multiplier λ ,

$$\frac{\delta}{\delta \phi_i^\dagger} \left[E_{\text{tot}} - \lambda \int d\mathbf{r} n(\mathbf{r}) \right] = 0, \quad (2.30)$$

the Kohn-Sham equation is derived,

$$\left[-\frac{\hbar^2}{2m} \nabla_i^2 + V_{\text{eff}}[n](\mathbf{r}) \right] \phi_i(\mathbf{r}) = \lambda_i \phi_i(\mathbf{r}) \quad (2.31)$$

where V_{eff} is the functional derivative of $E_{\text{ext}} + E_{\text{H}} + E_{\text{xc}}$. One solves this equation by a self-consistent technique. The advantage of the density functional approach is that the correlation effect, which is missed in the Hartree-Fock method, is included. In addition, the scheme allows one to compute a system containing few hundred particles. Since typical quantum dots contain on the order of 100-500 electrons, this is considered to be the best suited approach. A more detailed application and numerical procedures are described in later chapters in the context of developing the Strutinsky energy correction method.

Chapter 3

Random Matrix Theory

3.1 Introduction

In the study of the compound nucleus, Wigner [31–34] introduced in 1951 a theory for the statistical fluctuations of neutron resonances. The approach is called random matrix theory (RMT) since it describes Hamiltonians of complex system by matrices with randomly selected elements. RMT was further developed by Porter [35], Mehta [36,37], Dyson [38], and many others. Instead of trying to calculate explicit individual eigenvalues and eigenfunctions, the theory provides the means to study statistical behaviors of systems. Since it is practically impossible to obtain exact Hamiltonians of strongly interacting, highly excited many-body systems, such as an excited nucleus, RMT assumes no information except for the symmetries that the system carries. The statistics are obtained with ensembles of Hamiltonians which belong to the same symmetry class, and it was found by Dyson [38] that random matrix ensembles can be grouped into three fundamental classes.

Use of RMT is not restricted to the analysis of compound nuclei. The quantum mechanical behavior of small metals, the sequence of zeros on the critical line of the Riemann zeta function, and the statistical aspects of chaotic dynamical systems, are among others studied in the context of RMT. The application of RMT to other fields is greatly dependent on two major breakthroughs. One is the Bohigas-Giannoni-Schmit conjecture [64] connecting

RMT to the statistical behavior of quantum mechanical systems whose classical counterpart is chaotic, and the other is the supersymmetry method developed by Efetov [39]. The application of RMT to chaotic systems will be discussed in section 3.3. Reviews of RMT can be found in Ref. [109, 112]. Use of RMT in nuclear physics is discussed in Ref. [65], and applications to quantum dots are given in Ref. [62, 136].

3.2 Gaussian Ensemble

The study of the RMT is based on the assumption that the Hamiltonian of some complex quantum system is represented by a large $N \times N$ matrix which consists of random elements, and ensembles of such matrices give a description of statistical fluctuations of the system. According to Dyson [38], the matrix ensembles are always classified into three different types, depending on the underlying symmetries. They are denoted as orthogonal, unitary, and symplectic ensembles. For systems having both time-reversal and rotational symmetries, the Hamiltonian matrix is real symmetric and belongs to the orthogonal group. For systems breaking time-reversal symmetry, the Hamiltonian matrix is complex Hermitian and belongs to the unitary group. For systems which preserve time-reversal symmetry but break rotational symmetry and have half-odd integer angular momentum, the Hamiltonian matrix is real quaternion and belongs to the symplectic group. The real quaternion matrix is $2N \times 2N$ matrix, and if it is considered as $N \times N$ blocks of 2×2 matrices, each block

matrix \mathbf{q} is constructed by

$$\mathbf{q} = a_0 \mathbf{I} + i(a_1 \sigma_1 + a_2 \sigma_2 + a_3 \sigma_3) \quad (3.1)$$

where the coefficients a_i are real and σ_i are the Pauli matrices,

$$\sigma_1 = \begin{pmatrix} 0 & 1 \\ 1 & 0 \end{pmatrix}, \quad \sigma_2 = \begin{pmatrix} 0 & -i \\ i & 0 \end{pmatrix}, \quad \sigma_3 = \begin{pmatrix} 1 & 0 \\ 0 & -1 \end{pmatrix}. \quad (3.2)$$

In all three ensemble classes, each matrix element of Hamiltonian has different number of real parameters. These number of components are $\beta = 1, 2, 4$ for orthogonal, unitary, and symplectic respectively. For example, the Hamiltonian matrices for $N = 2$ are

$$\mathbf{H} = \begin{pmatrix} a & c \\ c & b \end{pmatrix} \quad (\beta = 1) \quad (3.3)$$

$$\mathbf{H} = \begin{pmatrix} a & z \\ z^* & b \end{pmatrix} \quad (\beta = 2) \quad (3.4)$$

$$\mathbf{H} = \begin{pmatrix} a & 0 & z_1 & z_2 \\ 0 & a & -z_2^* & z_1^* \\ z_1^* & -z_2 & b & 0 \\ z_2^* & z_1 & 0 & b \end{pmatrix} \quad (\beta = 4) \quad (3.5)$$

where a, b, c are real and z, z_1, z_2 are complex numbers.

Consider the similarity transformation $\mathbf{H}' = \mathbf{W}^{-1}\mathbf{H}\mathbf{W}$. The definition of a Gaussian ensemble requires that the transformed matrix \mathbf{H}' must belong to the same ensemble as \mathbf{H} does. If \mathbf{W} is any real orthogonal matrix ($\mathbf{W}^{-1} = \mathbf{W}^T$) for $\beta = 1$, the ensemble is called the Gaussian orthogonal ensemble (GOE), if \mathbf{W} is unitary ($\mathbf{W}^{-1} = \mathbf{W}^\dagger$) for $\beta = 2$, the ensemble is called the Gaussian unitary ensemble (GUE), and if \mathbf{W} is symplectic (see below) for $\beta = 4$, the ensemble is called the Gaussian symplectic ensemble (GSE). In addition, for the GOE, the matrix elements $H_{mn}, m \leq n$ must be statistically independent and for GUE and GSE, linearly independent components must be statistically independent. By components we mean a, b in $H_{mn} = a + ib$ for GUE, and a_0, \dots, a_3 in $\mathbf{q} = a_0 I + i \sum_j a_j \sigma_j$ for GSE. For each ensemble, the components are randomly selected real numbers with a Gaussian distribution. The symplectic matrix is defined as follows: a matrix \mathbf{A} is symplectic if $\mathbf{A}^\dagger \mathbf{K} \mathbf{A} = \mathbf{K}$ where \mathbf{K} is the antisymmetric orthogonal matrix.

3.3 Chaotic Systems and Random Matrix Theory

The meanings of “complex system” and “large number of interacting particles” were not clearly defined by Wigner or Dyson for the validity of RMT. Based on the conjecture made by Bohigas, Giannoni, and Schmit [64], applicability of RMT has been broadened to study “single-particle chaotic systems”, and a large number of numerical studies has supported the validity of RMT in such dynamical systems [112].

Although there is no explicit manner to characterize the irregularity within quantum systems, their classical analog is used to determine the irregularity or the degree of chaos

of the system. Classical dynamical systems range from integrable (the most regular) to hard chaos (the most irregular). For integrable systems, such as circular billiards (a billiard represents a system confined by infinite potential boundary; inside of the wall, the motion of particle is free propagation), with d degrees of freedom, there are d constants (or integrals) of motion including energy conservation. For fully chaotic systems, stadium billiards for instance (a stadium billiard consists of two parallel straight lines with semi-circular end caps), the constants of motion do not exist except for the energy. Consider two neighboring trajectories with slightly different initial conditions. While in the integrable system, the two trajectories linearly separate from each other, in the fully chaotic system, they exponentially diverge in time. In between, the extreme dynamical limits, there exists an intermediate regime called mixed systems. In such systems, as the word indicates, the behavior is mixed between integrable and chaotic motions depending on the initial conditions. The three-body interacting system, or simple planetary systems, falls into this category.

According to Bohigas [64], the statistical study of spectral fluctuations of quantum systems exhibit a signature of the corresponding classical dynamics. More importantly, the fluctuation statistics of irregular quantum systems can be investigated within the context of RMT, depending on the system's symmetry. Although RMT does not reproduce the system dependent energy spectrum or eigenstates, it describes the local fluctuations of the spectrum. Suppose a confining potential of a quantum system has no rotational symmetry, for simplicity, the system having time-reversal symmetry is described by the GOE statistics, and if time-reversal symmetry is broken, the GUE statistics represents the spectral fluctu-

ations. To illustrate this, let us consider two-dimensional rectangular billiard and coupled quartic oscillator confining systems $V = a(x^4/b + by^4 + 2\lambda x^2y^2)$ in time-reversal regime. Although there are several statistical measures available, the nearest-neighbor spacing and the number variance statistics are suffice for this purpose; see Appendix D. The rectangular billiard system has conserved momenta in the x and in the y direction (or energy and one of the two momenta) as integrals of motion, and it is known as integrable system (since there are two constants of motion for a two-dimensional system). The coupled quartic oscillator system has the flexibility of adjusting the degree of chaos from near integrability to pure chaos by tuning the coupling of two modes. The coupling strength is set to $\lambda = -0.35$ and -0.55 to represent mixed and chaotic dynamics respectively. In Fig. (3.1), the statistics of spectral fluctuations are plotted. The nearest-neighbor spacing statistics for the rectangular billiard follows the Poisson statistics precisely. For the time-reversal invariant (TRI) quartic oscillator, the systems in chaotic regime captures the GOE statistics in small spacing domain, where the probability $P(s)$ is linear in spacing s , but the distinction from the mixed regime is not obvious in other spacing domain. On the other hand, the number variance statistics clearly show the difference between two statistics: while the chaotic case follows the GOE curve, the mixed case is located in between the Poisson and the GOE statistics as expected from the behavior of “mixed” system. With the time-reversal symmetry breaking term added to the quartic oscillator, the spectral fluctuation statistics are compared to the previous TRI case in Fig. (3.2). The number variance statistics captures well the behavior of spectral fluctuations of the time-reversal non-invariant (TRNI) quartic oscillator system

with GUE statistics. The study of the quartic oscillator systems will be discussed more in later chapters.

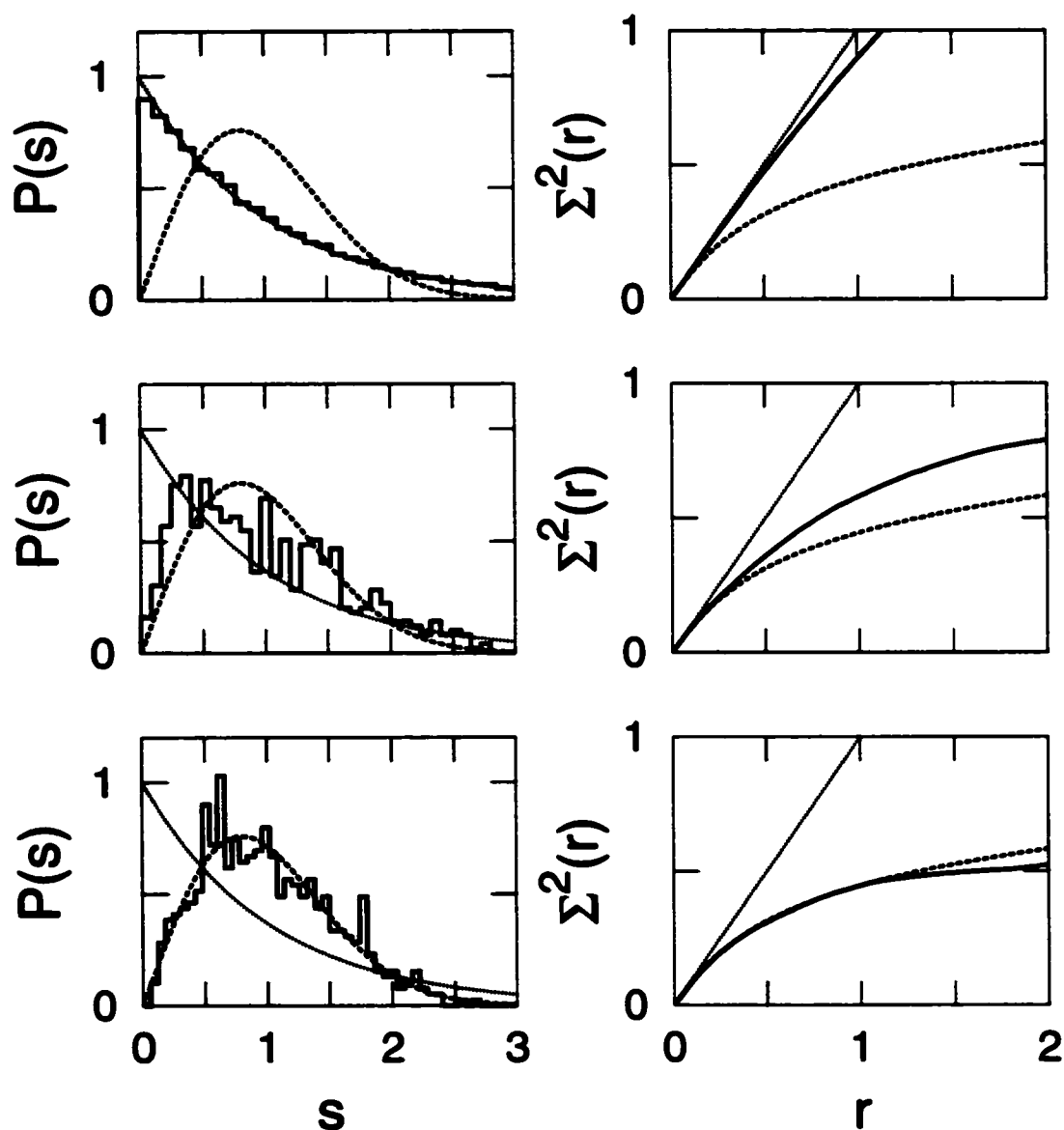


Figure 3.1: Statistics of spectral fluctuations. Figures in left column represent the nearest-neighbor spacing distributions, and figures in right column are the number variance statistics. Top: Rectangular billiard. Middle: two-dimensional coupled quartic oscillator (time-reversal invariant) with coupling constant $\lambda = -0.35$ (mixed). Bottom: same quartic oscillator with $\lambda = -0.55$ (chaotic). Histogram (or solid line) is obtained from numerical data, dashed line is reference the GOE statistics, and dotted line is the Poisson statistics. For more detailed statistical studies of the quartic oscillator, see Ref. [114].

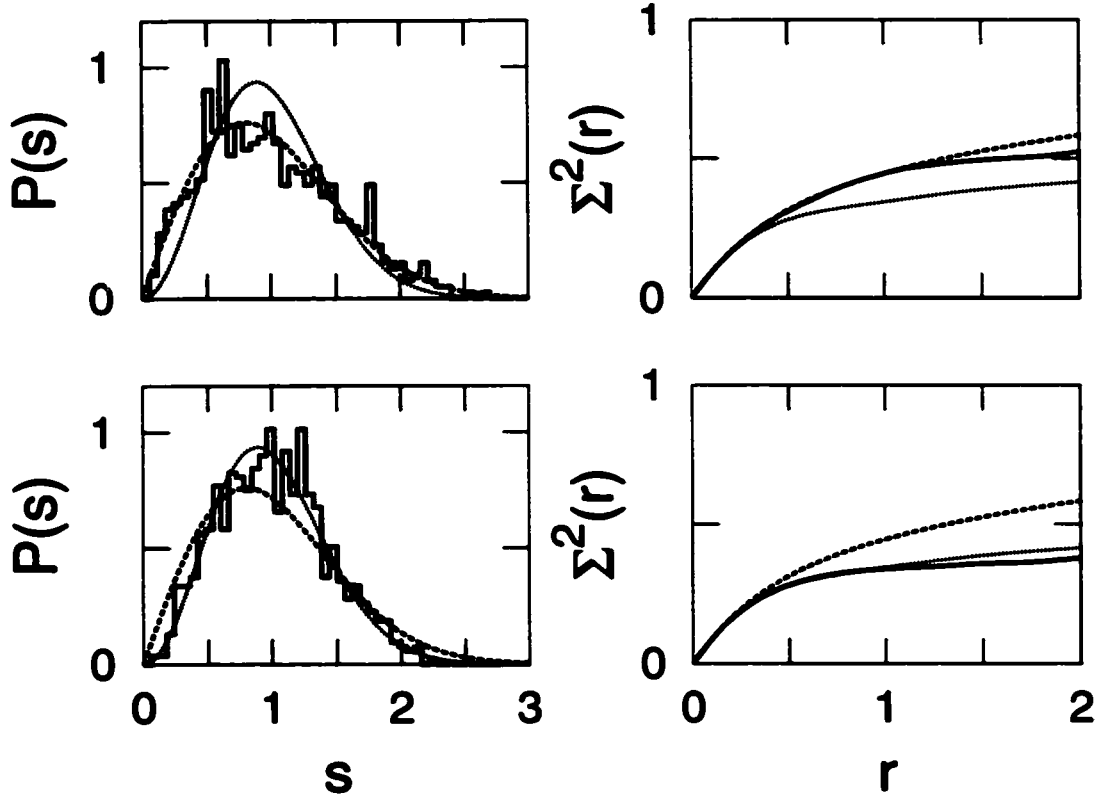


Figure 3.2: Statistics of spectral fluctuations. Figures in left column represent the nearest-neighbor spacing distributions, and figures in right column are the number variance statistics. Top: time-reversal invariant two-dimensional coupled quartic oscillator with coupling $\lambda = -0.55$. Bottom: Time-reversal non-invariant coupled quartic oscillator with $\lambda = -0.80$ and symmetry breaking strength $\epsilon = -1.0$. Histogram (or solid line) is obtained from numerical data, dashed line is reference the GOE statistics, and dotted line is the GUE statistics.

Chapter 4

Semiclassical Density Functional Theory: Strutinsky Energy Corrections in Quantum Dots

By Denis Ullmo, ¹ Tatsuhiro Nagano, Steven Tomsovic,
and Harold U. Baranger ²

Department of Physics, Washington State University,
Pullman, Washington 99164

Physical Review B **63**, 125339 (2001)

Copyright 2001 by the American Physical Society.

4.1 Introduction

A recurring problem in modern physics is how to add quantization effects to a basically successful macroscopic theory. This question arises particularly in the semiclassical regime—large quantum number—where the quantum effects are often corrections to the essentially classical macroscopic physics. Perhaps the best known example starts with the Thomas-Fermi theory of the atom [40], which is macroscopic in essence, and then evaluates the

¹Laboratoire de Physique Théorique et Modèles Statistiques (LPTMS), 91405 Orsay Cedex, France

²Department of Physics, Duke University, Box 90305, Durham, NC 27708-0305, USA

contribution of electronic shell structure to the ground state energy [40–42]. The very natural result that the shell contribution is given by the quantized levels of the self-consistent Thomas-Fermi potential has been used extensively [43–45]. However, it has only been in recent decades, starting with the work of V. M. Strutinsky [46–49], that a systematic way of answering the recurring general problem has been developed.

Our own immediate interest is in quantum dots—small electrically conducting regions in which the quantum properties of the confined electrons are important [50]—and our aim here is to treat quantum corrections to the ground state energy of these dots by further developing the Strutinsky method.

Quantum dots can be formed, for instance, by gate depletion of a two-dimensional electron gas (2DEG) in a GaAs-AlGaAs heterostructure. Because of the high quality of this material and interface, the mean free path of the electrons far exceeds the size of the quantum dot. One can view an electron as propagating ballistically within a confining potential created by electrostatic gates patterned on the surface of the heterostructure. For transport measurements, dots can be coupled weakly to leads; when the conductance of each lead falls below $2e^2/h$, electron transport through the dot occurs only by tunneling, and the number of particles within the dot becomes quantized. In this regime, the conductance is suppressed due to the electrostatic energy associated with a localized charge [50], an effect known as the Coulomb blockade (reported in 1951 by Gorter [51]). When the dot potential is tuned by a gate voltage so that adding one electron costs no energy, a large conductance peak appears [50]—though the electrons must still tunnel from the leads, there is no additional

electrostatic barrier to conduction. Sweeping such a gate voltage produces periodic Coulomb blockade oscillations of the conductance through dots [50, 52, 53].

The Coulomb blockade is a classical effect observable in a broad temperature range, $k_B T < e^2/C$, where C is the total dot capacitance. Over most of this range, both the spacing and height of the peaks is constant—the spacing is e^2/C and the height is given by the resistance of the two tunneling barriers acting in series. However, there is a low temperature regime below a few hundred millikelvin for which $k_B T < \Delta$, where Δ is the mean single-particle level spacing of the isolated dot. There, quantum interference and coherence become important [50]. The Coulomb blockade peaks grow as the temperature decreases, and novel fluctuation properties emerge involving both the peak heights [54–56] and spacings [57–61]. The spacings give information about the ground state energies while the heights involve the magnitude of the wavefunction near the levels.

With some success, random-matrix-theory (RMT) based approaches [62] have been used in order first to predict [63] and then to explain the statistical properties found. In the simplest approximation [57], known as the constant interaction model, the ground state energy of the dot is expressed as

$$E(N) = \frac{e^2 N^2}{2C} + \sum_{i=1}^N \epsilon_i \quad (4.1)$$

where N is the number of electrons in the dot and ϵ_i are single-particle energies. The first term is the classical charging energy; the second is the total energy of a system of non-interacting quasi-particles. Supposing that the single-particle classical dynamics within the

dot is chaotic, the Bohigas-Giannoni-Schmit conjecture applies [64] and implies that the single-particle quantum properties follow RMT. It is well-established that RMT predicts repulsion amongst the ϵ_i and Gaussian random behavior in the eigenfunctions [65]. Within this model, the conductance peak height statistics are in good agreement with experimental results [54, 55] after also incorporating non-zero temperature effects and interference modulations due to periodic paths coupled to the leads [63, 66, 67]. On the other hand, it is found [57–61] that the fluctuations in the peak spacings are considerably larger than the predictions [57, 68, 69], and there is little evidence for the level repulsion or electron spin degeneracy expected from a single-particle-like approach [61, 70]. These discrepancies between the predictions of the constant interaction model and the observations point to the need for a quantum treatment of the electron-electron interactions, and, in particular, have triggered a number of studies based on Hartree-Fock calculations [71–73], or density functional theory in the local density approximation (LDA) [74–77].

In nuclear physics, it has long been known that the dependence of many-body ground state quantities on particle number can be decomposed into an average and a fluctuating part. While the average part varies smoothly with particle number, the fluctuating part reflects the shell structure of the system. A similar decomposition is possible for any finite-size interacting fermion system. The smooth part comes basically from the bulk energy per unit volume integrated over the finite-size system, and the oscillating contributions come from quantum interference effects explicitly caused by the confinement. By supposing that the smooth part is known while the unknown oscillatory contribution is a correction,

Strutinsky introduced in the late 60's a physically motivated systematic approach to obtain the shell corrections [46,47]. Introductions to the Strutinsky shell correction method and its application through LDA to metal clusters can be found in Ref. [48,49].

Strutinsky's shell correction method is essentially a *semiclassical* approximation. It rests on the fact that the number of particles in the system considered is large, rather than on the interaction between the particles being weak. (One must, of course, work in a regime where the smooth starting point is basically valid.) Since the quantum dots in which we are interested contain on the order of 100 electrons, they are a perfect place to apply the Strutinsky method. However, before doing so for a particular, realistic, two-dimensional geometry, we shall in this paper limit ourselves to a formal discussion of this method in conjunction with a one-dimensional illustrative example. In spite of the literature existing on this subject [49], we find it useful for two main purposes. First, the discussion and resulting expressions are noticeably simpler for quantum dots than for nuclei. This occurs because the existence of a smooth confining potential in the dot means that gradient corrections to the smooth density are not needed to confine the system at the zeroth-order (classical-like) approximation. The effect of these gradient terms can therefore be included in the first-order "shell" corrections, simplifying both the zeroth-order calculations (no gradient terms) and the first-order terms (no corrections to the Weyl part).

Our main purpose, however, is to take advantage of the fact that we use density functional theory (DFT) rather than Hartree-Fock as a starting point, the former being presumably better suited to deal with the long-range Coulomb interaction present in quantum dots than

the latter. While first-order Strutinsky corrections to a DFT description of nanoparticles has been considered in Ref. [48], our focus is to use this approach to derive and discuss in detail the second-order “residual interaction” terms of the Strutinsky method. By residual interaction we mean the weak interaction between Landau quasi-particles that comes from dressing the bare electron added to the quantum dot. In particular we will show, and illustrate, how these terms are related to the screened Coulomb interaction.

The remainder of the paper is organized as follows. The Thomas-Fermi and density functional theories are summarized in the next section, establishing our notation. Section 6 contains the Strutinsky method applied to density functional theory. This is the core of the paper; in particular, the relation of the second order terms to the screened Coulomb potential is derived. Section 7 recalls how the residual interaction terms contribute to conductance peak spacing distribution. Section 8 compares the whole approximation scheme to numerical calculations of a simplified model: interacting electrons in a one-dimensional quartic oscillator. Finally, we comment on the relationship between the Strutinsky development and the constant interaction model, and possible applications of the method.

Chapter 5

Density Functional Theory

The Hohenberg-Kohn theorem [78] states that for a system of interacting electrons in an external potential, $V_{\text{ext}}(\mathbf{r})$, there exists a functional, $\mathcal{F}_{\text{HKS}}[n]$, of the density of electrons, $n(\mathbf{r})$, such that: i) the density, $n_g(\mathbf{r})$, corresponding to the ground state of N particles is an extremum of $\mathcal{F}_{\text{HKS}}[n]$ under the constraint that the total number of particles,

$$N[n_g] \equiv \int d\mathbf{r} n_g(\mathbf{r}) , \quad (5.1)$$

is fixed, and ii) $\mathcal{F}_{\text{HKS}}[n_g]$ is the total energy of the system. The explicit form of the Hohenberg-Kohn-Sham functional is not known [78, 79]. In practice, one must be satisfied with approximations. We describe here first a generalized Thomas-Fermi approach and, second, the case when an explicit form of the density functional is assumed.

5.1 Generalized Thomas-Fermi Approximation

([Semi]Classical Level)

It is convenient to view the density functional as the sum of three parts: a classical charge contribution, the kinetic energy, and the unknown exchange-correlation functional which accounts for the balance [79, 80]. The first part is simple: the energy of a system of classical

charges confined by an external potential, V_{ext} , is

$$\mathcal{E}[n] = \mathcal{E}_{\text{ext}}[n] + \mathcal{E}_{\text{coul}}[n] \quad (5.2)$$

where

$$\begin{aligned} \mathcal{E}_{\text{ext}}[n] &= \int n(\mathbf{r}) V_{\text{ext}}(\mathbf{r}) d\mathbf{r} \\ \mathcal{E}_{\text{coul}}[n] &= \frac{e^2}{2} \int \int \frac{n(\mathbf{r})n(\mathbf{r}')}{|\mathbf{r} - \mathbf{r}'|} d\mathbf{r} d\mathbf{r}' . \end{aligned} \quad (5.3)$$

For the kinetic energy, in the Thomas-Fermi approach the Pauli exclusion principle is introduced semiclassically by employing the idea that one quantum state occupies a volume $(2\pi\hbar)^d$ in phase space. This implies that if many electrons want to be at the same place, they can do so only by increasing their kinetic energy. This gives the Thomas-Fermi approximation to the kinetic energy part of the density functional, $\mathcal{T}_{\text{TF}}[n]$, expressed as

$$\begin{aligned} \nu(\epsilon) &= \frac{1}{(2\pi\hbar)^d} \int \Theta\left(\epsilon - \frac{\mathbf{p}^2}{2m}\right) d\mathbf{p} \\ t_{\text{TF}}(n) &= \int_0^n \epsilon(\nu) d\nu \\ \mathcal{T}_{\text{TF}}[n] &= \int t_{\text{TF}}(n(\mathbf{r})) d\mathbf{r} \end{aligned} \quad (5.4)$$

where d is the dimensionality of the system, Θ is the Heaviside step function, t_{TF} is the kinetic energy density, and $\nu(\epsilon)$ is the number of states per unit volume with energy less than ϵ . An additional factor of 2 in $\nu(\epsilon)$ is required if the electron spin degeneracy is taken

into account.

Finally, the effect of exchange and correlation is included through a term $\mathcal{E}_{\text{xc}}[n]$. In practice, an explicit form for this functional must be taken. For example, if the electron density is a sufficiently slowly varying function of position, one can approximate $\mathcal{E}_{\text{xc}}[n]$ by taking the exact results for the uniform electron gas at the local density integrated over space, the well-known local density approximation (LDA).

Within this approximation, then, the density functional is

$$\mathcal{F}_{\text{GTF}}[n] = \mathcal{T}_{\text{TF}}[n] + \mathcal{E}_{\text{tot}}[n] \quad (5.5)$$

where

$$\mathcal{E}_{\text{tot}}[n] \equiv \mathcal{E}_{\text{ext}}[n] + \mathcal{E}_{\text{coul}}[n] + \mathcal{E}_{\text{xc}}[n] . \quad (5.6)$$

The ground state energy and its electron distribution are obtained by minimizing \mathcal{F}_{GTF} under the constraint (5.1), yielding the self-consistency equation

$$\frac{\delta \mathcal{T}_{\text{TF}}}{\delta n}[n_{\text{GTF}}](\mathbf{r}) + V_{\text{eff}}[n_{\text{GTF}}](\mathbf{r}) = \mu_{\text{GTF}} \quad (5.7)$$

with the effective potential

$$V_{\text{eff}}[n](\mathbf{r}) \equiv \frac{\delta \mathcal{E}_{\text{tot}}}{\delta n}[n](\mathbf{r}) . \quad (5.8)$$

Notice that to make use of Eq. (5.7), one must have an explicit form for \mathcal{E}_{xc} in order to take the functional derivative in Eq. (5.8).

We call this approach “generalized-Thomas-Fermi” (GTF) because it uses the Thomas-Fermi approximation for the kinetic energy but retains macroscopic aspects of exchange and correlation. In particular, the short-range effects of exchange-correlation in a uniform system can be included.

5.2 Kohn-Sham Equations

(Quantum Mechanical Level)

In standard implementations of density functional theory (DFT), the kinetic energy is treated quantum mechanically rather than (semi)classically as in GTF. To accomplish this, in the Kohn-Sham scheme [80–82] one considers the problem of N noninteracting electrons which has exactly the same density as the original interacting problem. The quantum mechanical kinetic energy for this auxiliary problem is then used to develop an approximation to the true kinetic energy.

The auxiliary noninteracting problem defines N orthogonal functions $\{\phi_1(\mathbf{r}), \dots, \phi_N(\mathbf{r})\}$ which are solutions of a Schrödinger equation

$$\left(-\frac{\hbar^2}{2m} \nabla^2 + V_{\text{eff}}[n](\mathbf{r}) \right) \phi_i(\mathbf{r}) = \epsilon_i \phi_i(\mathbf{r}) , \quad i = 1, \dots, N \quad (5.9)$$

where the effective potential is again defined by Eq. (5.8). These are the Kohn-Sham equa-

tions [79]. In terms of these orbitals, the electron density is

$$n(\mathbf{r}) \equiv \sum_{i=1}^N |\phi_i(\mathbf{r})|^2, \quad (5.10)$$

and the kinetic energy of the noninteracting problem is

$$\begin{aligned} \mathcal{T}_{\text{DFT}}[n] &= \sum_{i=1}^N \langle \phi_i | \hat{T} | \phi_i \rangle \\ &= \frac{\hbar^2}{2m} \int \sum_{i=1}^N |\nabla \phi_i(\mathbf{r})|^2 d\mathbf{r}. \end{aligned} \quad (5.11)$$

Thus, the density functional becomes

$$\mathcal{F}_{\text{DFT}}[n] = \mathcal{T}_{\text{DFT}}[n] + \mathcal{E}_{\text{tot}}[n] \quad (5.12)$$

where $\mathcal{E}_{\text{tot}}[n]$ includes interaction corrections to the kinetic energy [Eq. (5.6)]. Equations (5.8)-(5.10) are the set of self-consistent equations for finding the electron density, $n_{\text{DFT}}(\mathbf{r})$, and then the ground state energy $E_{\text{DFT}} = \mathcal{F}_{\text{DFT}}[n_{\text{DFT}}]$.

As in the discussion of the GTF above, in order to actually solve the Kohn-Sham equations, an explicit form for the exchange-correlation functional is required. The simplest case is when \mathcal{E}_{xc} is an integral over space of a function (*not* functional) of the local density; this is the well-known local-density approximation (LDA) [80–82]. But other more complicated explicit forms are possible, for example the generalized gradient corrections to LDA [80, 82].

Chapter 6

Approximate Ground State Energy: The Strutinsky Energy-Correction Method

6.1 Expansion of the Density Functional Theory Ground State Energy

In this section we develop an approximation to $E_{\text{DFT}}[n_{\text{DFT}}]$ starting from the solution of the generalized-Thomas-Fermi equation, n_{GTF} . The main motivation is to develop a physical interpretation of the difference between these two approaches in finding the ground state energy. In addition, the approximation is of interest numerically for large problems since it involves a self-consistent solution of only the GTF equation rather than the more involved Kohn-Sham equations. We use the method introduced by V. M. Strutinsky [46, 47] originally in the context of a Hartree-Fock rather than density-functional approach. His method describes the interacting system self consistently, first with the quantum interference effects turned off, and then by introducing them perturbatively. As discussed in the introduction, the idea is to add the “oscillatory” effects caused by interference in the confined system to a “smooth” essentially macroscopic description—these effects are essentially the Friedel oscillations [83] familiar in the context of impurities or surfaces.

To study the role of quantum interference effects in the DFT ground state energy, we will

first show that the generalized-Thomas-Fermi result is a [semi]classical approximation to the DFT energy. The GTF approximation does, of course, contain some quantum mechanics—notably the Pauli exclusion principle which gives rise to the Fermi surface—and so is not truly classical. But only the simplest local quantum effects are present in GTF rather than the effects of interfering paths that one expects in a true semiclassical theory, hence our characterization of GTF as “[semi]classical”.

To see this clearly, we introduce a convenient notation adapted from the semiclassical treatment of single-particle problems: it is customary there to express the density of states as a sum of a smooth term slowly varying in energy, called the Weyl part, and a term which varies rapidly in energy (on the scale of the mean level separation), called the oscillatory part [84]. For a system governed by the Hamiltonian $H[V] \equiv \mathbf{p}^2/2m + V(\mathbf{r})$, where the potential is as yet unspecified, one can define the probability density of N independent particles

$$n[V](\mathbf{r}) = \sum_{i=1}^N |\phi_i(\mathbf{r})|^2 \quad (6.1)$$

in terms of the eigenstates $\{\phi_i\}$ of H . We also define the Weyl part of $n[V]$ by

$$n^W[V](\mathbf{r}) \equiv \frac{1}{(2\pi\hbar)^d} \int \Theta[\mu^W - \mathbf{p}^2/2m - V(\mathbf{r})] d\mathbf{p} \quad (6.2)$$

where μ^W must be chosen so that $N = \int n^W(\mathbf{r}) d\mathbf{r}$. Note that $n^W[V](\mathbf{r})$ is smooth in that it neglects quantum fluctuations in much the same way that the GTF approximation does.

With this notation, one can derive the useful relation

$$\frac{\delta \mathcal{T}_{\text{TF}}}{\delta n} [n^W[V]](\mathbf{r}) + V(\mathbf{r}) = \mu^W . \quad (6.3)$$

Indeed, using

$$\frac{\delta \mathcal{T}_{\text{TF}}}{\delta n} [n](\mathbf{r}) = \epsilon(n(\mathbf{r})) , \quad (6.4)$$

Eq. (6.3) reads $\epsilon(n^W[V](\mathbf{r})) = \mu^W - V(\mathbf{r})$. Applying the function ν introduced in Eq. (5.4) to both sides of the equality gives the definition of $n^W[V](\mathbf{r})$, Eq. (6.2).

Recalling that $V_{\text{eff}}[n]$ is defined as the variational derivative of \mathcal{E}_{tot} (to be completely clear, it is not the inverse of $n[V_{\text{eff}}]$), we see that the self-consistency equation (5.10) which defines n_{DFT} is

$$n_{\text{DFT}}(\mathbf{r}) = n[V_{\text{eff}}[n_{\text{DFT}}]](\mathbf{r}) . \quad (6.5)$$

Similarly, Eq. (5.7) which defines n_{GTF} can, in applying the above prescription, be put in the form

$$n_{\text{GTF}}(\mathbf{r}) = n^W[V_{\text{eff}}[n_{\text{GTF}}]](\mathbf{r}) . \quad (6.6)$$

These equations do not signify that n_{GTF} is the Weyl part of n_{DFT} ; however, they do indicate that if one neglects the quantum interference terms (i.e. the difference between the exact particle density and its Weyl part), then the definitions of n_{GTF} and n_{DFT} become equivalent. It is in this sense that n_{GTF} is the [semi]classical approximation of n_{DFT} .

Supposing $n_{\text{GTF}}(\mathbf{r})$ and $E_{\text{GTF}} = \mathcal{F}_{\text{GTF}}[n_{\text{GTF}}]$ known, we now seek to evaluate the correc-

tions to the Thomas-Fermi energy,

$$\Delta E \equiv E_{\text{DFT}} - E_{\text{GTF}} , \quad (6.7)$$

up to second order in

$$\delta n \equiv n_{\text{DFT}} - n_{\text{GTF}} . \quad (6.8)$$

For this purpose, we first introduce the quantities

$$\begin{aligned} \tilde{n}(\mathbf{r}) &\equiv n[V_{\text{eff}}[n_{\text{GTF}}]](\mathbf{r}) \\ \tilde{n}^W(\mathbf{r}) &\equiv n^W[V_{\text{eff}}[n_{\text{GTF}}]](\mathbf{r}) = n_{\text{GTF}}(\mathbf{r}) \\ \tilde{n}^{\text{osc}}(\mathbf{r}) &= \tilde{n}(\mathbf{r}) - \tilde{n}^W(\mathbf{r}) . \end{aligned} \quad (6.9)$$

Note that once $V_{\text{eff}}[n_{\text{GTF}}]$ is known, all of these can be computed through the diagonalization of the known single particle GTF Hamiltonian. As is well-known, the sum of the eigenvalues of the Kohn-Sham equations, $\mathcal{E}_{\text{ip}}[V] \equiv \sum_i^N \epsilon_i$, does not give the total energy of the N particles because of double counting of the interaction energy, but rather [85]

$$E_{\text{DFT}} = \mathcal{E}_{\text{ip}}[V_{\text{eff}}[n_{\text{DFT}}]] - \int d\mathbf{r} V_{\text{eff}}[n_{\text{DFT}}](\mathbf{r}) n_{\text{DFT}}(\mathbf{r}) + \mathcal{E}_{\text{tot}}[n_{\text{DFT}}] . \quad (6.10)$$

To proceed further, we use the relation proved in the Appendix B

$$\mathcal{E}_{\text{ip}}[V + \delta V] - \mathcal{E}_{\text{ip}}[V] \simeq \frac{1}{2} \int \delta V(\mathbf{r}) (n(\mathbf{r}) + n'(\mathbf{r})) d\mathbf{r} \quad (6.11)$$

where $n(\mathbf{r}) \equiv n[V](\mathbf{r})$ and $n'(\mathbf{r}) \equiv n[V + \delta V](\mathbf{r})$ and which is correct through second order in the changes. Upon inserting $V = V_{\text{eff}}[n_{\text{GTF}}]$ and $V + \delta V = V_{\text{eff}}[n_{\text{DFT}}]$, and thus $n = \bar{n}$ and $n' = n_{\text{DFT}}$, the first term on the right-hand-side of Eq. (6.10) becomes

$$\mathcal{E}_{\text{lp}}[V_{\text{eff}}[n_{\text{DFT}}]] = \mathcal{E}_{\text{lp}}[V_{\text{eff}}[n_{\text{GTF}}]] + \frac{1}{2} \int d\mathbf{r} \delta V_{\text{eff}}(\mathbf{r}) (n_{\text{DFT}}(\mathbf{r}) + \bar{n}(\mathbf{r})) \quad (6.12)$$

where $\delta V_{\text{eff}} \equiv V_{\text{eff}}[n_{\text{DFT}}] - V_{\text{eff}}[n_{\text{GTF}}]$. Similarly, the second term in $E_{\text{DFT}}[n_{\text{DFT}}]$ is

$$\begin{aligned} \int V_{\text{eff}}[n_{\text{DFT}}](\mathbf{r}) n_{\text{DFT}}(\mathbf{r}) d\mathbf{r} &= \int V_{\text{eff}}[n_{\text{GTF}}](\mathbf{r}) n_{\text{GTF}}(\mathbf{r}) d\mathbf{r} \\ &+ \int V_{\text{eff}}[n_{\text{GTF}}](\mathbf{r}) \delta n(\mathbf{r}) d\mathbf{r} \\ &+ \int \delta V_{\text{eff}}(\mathbf{r}) n_{\text{DFT}}(\mathbf{r}) d\mathbf{r} . \end{aligned} \quad (6.13)$$

Finally, the third term is

$$\mathcal{E}_{\text{tot}}[n_{\text{DFT}}] = \mathcal{E}_{\text{tot}}[n_{\text{GTF}}] + \int (V_{\text{eff}}[n_{\text{GTF}}](\mathbf{r}) + \delta V_{\text{eff}}(\mathbf{r})/2) \delta n(\mathbf{r}) d\mathbf{r} \quad (6.14)$$

with corrections which are third order in δn .

Combining all the terms together, we obtain

$$\begin{aligned} E_{\text{DFT}} &\simeq \mathcal{E}_{\text{lp}}[V_{\text{eff}}[n_{\text{GTF}}]] - \int n_{\text{GTF}}(\mathbf{r}) V_{\text{eff}}[n_{\text{GTF}}](\mathbf{r}) d\mathbf{r} + \mathcal{E}_{\text{tot}}[n_{\text{GTF}}] \\ &+ \frac{1}{2} \int \delta V_{\text{eff}}(\mathbf{r}) \bar{n}^{\text{osc}}(\mathbf{r}) d\mathbf{r} . \end{aligned} \quad (6.15)$$

In order to express directly the difference between the DFT and GTF ground states, it is convenient to use

$$E_{\text{GTF}}[n_{\text{GTF}}] = \mathcal{T}_{\text{TF}}[n_{\text{GTF}}] + \mathcal{E}_{\text{tot}}[n_{\text{GTF}}] \quad (6.16)$$

for \mathcal{E}_{tot} . In order to simplify the last term in Eq. (6.15), note that \tilde{n}^{osc} is of order δn , and that therefore one only needs the first order variation of the effective potential, $\delta V_{\text{eff}}(\mathbf{r}) = \int (\delta V_{\text{eff}}/\delta n)[n_{\text{GTF}}](\mathbf{r}, \mathbf{r}') \delta n(\mathbf{r}') d\mathbf{r}'$, to obtain E_{DFT} correct through second order. Thus the final expression for the Strutinsky energy correction is

$$E_{\text{DFT}} \simeq E_{\text{GTF}} + \Delta E^{(1)} + \Delta E^{(2)} \quad (6.17)$$

where the first and second order correction terms are

$$\Delta E^{(1)} = \mathcal{E}_{\text{lp}}[V_{\text{eff}}[n_{\text{GTF}}]] - \int n_{\text{GTF}}(\mathbf{r}) V_{\text{eff}}[n_{\text{GTF}}](\mathbf{r}) d\mathbf{r} - \mathcal{T}_{\text{TF}}[n_{\text{GTF}}] \quad (6.18)$$

$$\Delta E^{(2)} = \frac{1}{2} \int \int \tilde{n}^{\text{osc}}(\mathbf{r}) \frac{\delta V_{\text{eff}}}{\delta n}[n_{\text{GTF}}](\mathbf{r}, \mathbf{r}') \delta n(\mathbf{r}') d\mathbf{r} d\mathbf{r}' . \quad (6.19)$$

In this approach, the DFT ground state energy is, then, the sum of a classical contribution—the generalized-Thomas-Fermi result E_{GTF} —and two quantum contributions— $\Delta E^{(1)}$ and $\Delta E^{(2)}$. We now discuss and interpret these two correction terms.

6.2 Interpretation of the First-Order Corrections

The first-order correction is simply the oscillatory part of the single particle energy for a system of N electrons evolving in the potential $V_{\text{eff}}[n_{\text{GTF}}]$. Indeed, the Weyl part of $\mathcal{E}_{\text{lp}}[V]$ is

$$\mathcal{E}_{\text{lp}}^W[V] \equiv \frac{1}{(2\pi\hbar)^d} \int \left(\frac{\mathbf{p}^2}{2m} + V(\mathbf{r}) \right) \Theta\left(\mu^W - \frac{\mathbf{p}^2}{2m} - V(\mathbf{r})\right) d\mathbf{p} d\mathbf{r} \quad (6.20)$$

where μ^W is fixed by $N = \int n^W[V](\mathbf{r}) d\mathbf{r}$. Separately integrating the kinetic and potential energy terms for $V = V_{\text{eff}}[n_{\text{GTF}}]$, one obtains

$$\mathcal{E}_{\text{lp}}^W[V_{\text{eff}}[n_{\text{GTF}}]] = \int d\mathbf{r} \int_0^{\mu^W - V_{\text{eff}}[n_{\text{GTF}}](\mathbf{r})} \epsilon \frac{d\nu}{d\epsilon} d\epsilon + \int n^W[V_{\text{eff}}[n_{\text{GTF}}]](\mathbf{r}) V_{\text{eff}}[n_{\text{GTF}}](\mathbf{r}) d\mathbf{r} . \quad (6.21)$$

In the first term one recognizes the Thomas-Fermi kinetic energy, $\mathcal{T}_{\text{TF}}[n_{\text{GTF}}]$, while in the second term $n^W[V_{\text{eff}}[n_{\text{GTF}}]] = n_{\text{GTF}}$. Thus the first-order Strutinsky correction is

$$\Delta E^{(1)} = \mathcal{E}_{\text{lp}}[V_{\text{eff}}[n_{\text{GTF}}]] - \mathcal{E}_{\text{lp}}^W[V_{\text{eff}}[n_{\text{GTF}}]] \equiv \mathcal{E}_{\text{lp}}^{\text{osc}}[V_{\text{eff}}[n_{\text{GTF}}]] . \quad (6.22)$$

The leading quantum corrections to GTF are found, then, by quantizing the single-particle levels in the GTF self-consistent potential: this is a very natural result which, in fact, was used extensively in atomic and nuclear physics [42–45] before it was first justified by Strutinsky [46, 47].

6.3 Interpretation of the Second-Order Corrections

The second-order correction, Eq. (6.19), requires further work: this form is not useful because it expresses $\Delta E^{(2)}$ as a function of the unknown δn . A second equation is necessary for us to determine δn . Note that this is not the case for $\Delta E^{(1)}$ which is written completely in terms of n_{GTF} .

The required second equation is obtained by relating δn to the oscillatory part of $\tilde{n} \equiv n[V_{\text{eff}}[n_{\text{GTF}}]]$ which, of course, is known since it depends only on n_{GTF} . We start with the two equations

$$\frac{\delta \mathcal{T}_{\text{TF}}}{\delta n}[n_{\text{GTF}}] + V_{\text{eff}}[n_{\text{GTF}}] = \mu_{\text{GTF}} \quad (6.23)$$

$$\frac{\delta \mathcal{T}_{\text{TF}}}{\delta n}[n_{\text{DFT}}^W] + V_{\text{eff}}[n_{\text{DFT}}] = \mu_{\text{DFT}}^W. \quad (6.24)$$

The first equation here is the definition of n_{GTF} , and the second one follows directly from the general relation (6.3). Now expand n_{DFT} about n_{GTF} in the second equation and subtract the first one from it. In the term involving V_{eff} , δn appears. However, in the kinetic energy term, the density difference is $n_{\text{DFT}}^W - n_{\text{GTF}} = (n_{\text{DFT}} - n_{\text{GTF}}) - (n_{\text{DFT}} - n_{\text{DFT}}^W) = \delta n - n_{\text{DFT}}^{\text{osc}}$. To close the equation we must relate $n_{\text{DFT}}^{\text{osc}}$ to n_{GTF} . This is possible because in an equation for δn , which is by definition first order in corrections, only the first order part of the other quantities need be kept. Thus, we can approximate $n_{\text{DFT}}^{\text{osc}}$ by similarly expanding n_{DFT} about n_{GTF} , yielding

$$n_{\text{DFT}}^{\text{osc}} = (n_{\text{DFT}} - n_{\text{DFT}}^W) \simeq (\tilde{n} - n_{\text{GTF}}) = \tilde{n}^{\text{osc}}. \quad (6.25)$$

The combination of these results gives the closure equation

$$\int d\mathbf{r}' \frac{\delta V_{\text{eff}}}{\delta n}(\mathbf{r}, \mathbf{r}') \delta n(\mathbf{r}') + \int d\mathbf{r}' \frac{\delta^2 \mathcal{T}_{\text{TF}}}{\delta n^2}(\mathbf{r}, \mathbf{r}') (\delta n(\mathbf{r}') - \tilde{n}^{\text{osc}}(\mathbf{r}')) = \Delta\mu \quad (6.26)$$

where $\Delta\mu \equiv \mu_{\text{DFT}}^W - \mu_{\text{GTF}}$ is fixed by the condition $\int \delta n(\mathbf{r}) d\mathbf{r} = 0$. This is an integral equation for δn in terms of GTF quantities. If a numerical calculation of $\Delta E^{(2)}$ is needed, the computational cost is relatively modest, largely the inversion of an operator.

One obtains a very natural interpretation of the second-order correction (6.19) by using this closure equation. Consider the generalized-Thomas-Fermi problem, Eq. (6.23), and suppose the external potential is slightly modified by the quantity $\delta V_{\text{ext}}(\mathbf{r})$. One thus obtains a new solution of the GTF equation $n'_{\text{GTF}} = n_{\text{GTF}} + \delta n_{\text{GTF}}$ which would verify

$$\frac{\delta \mathcal{T}_{\text{TF}}}{\delta n}[n'_{\text{GTF}}] + V_{\text{eff}}[n'_{\text{GTF}}] + \delta V_{\text{ext}} = \mu'_{\text{GTF}} . \quad (6.27)$$

Subtracting Eq. (6.23) as before yields

$$\int d\mathbf{r}' \frac{\delta^2 \mathcal{T}_{\text{TF}}}{\delta n^2}(\mathbf{r}, \mathbf{r}') \delta n_{\text{GTF}}(\mathbf{r}') + \int d\mathbf{r}' \frac{\delta V_{\text{eff}}}{\delta n}(\mathbf{r}, \mathbf{r}') \delta n_{\text{GTF}}(\mathbf{r}') + \delta V_{\text{ext}} = \Delta\mu . \quad (6.28)$$

If we now choose the variation of the potential to be

$$\delta V_{\text{ext}}(\mathbf{r}) = \int d\mathbf{r}' (\delta^2 \mathcal{E}_{\text{tot}} / \delta n^2)[n_{\text{GTF}}](\mathbf{r}, \mathbf{r}') \tilde{n}^{\text{osc}}(\mathbf{r}') , \quad (6.29)$$

$\delta n_{\text{GTF}} + \tilde{n}^{\text{osc}}$ satisfies the same Eq. (6.26) as δn . This means that, at this level of approx-

imation, δn is the sum of \tilde{n}^{osc} and the displacement of charges δn_{GTF} screening \tilde{n}^{osc} in the GTF approximation. Indeed, the definition of a screened interaction V_{sc} implies

$$\int d\mathbf{r}' \frac{\delta V_{\text{eff}}}{\delta n}(\mathbf{r}, \mathbf{r}') \delta n(\mathbf{r}') = \int d\mathbf{r}' V_{\text{sc}}(\mathbf{r}, \mathbf{r}') \tilde{n}^{\text{osc}}(\mathbf{r}') , \quad (6.30)$$

and therefore that the second-order correction, Eq. (6.19), can be written

$$\Delta E^{(2)} = \frac{1}{2} \int d\mathbf{r} d\mathbf{r}' \tilde{n}^{\text{osc}}(\mathbf{r}) V_{\text{sc}}(\mathbf{r}, \mathbf{r}') \tilde{n}^{\text{osc}}(\mathbf{r}') . \quad (6.31)$$

Thus the second-order correction is simply the energy of interaction between the additional charge oscillations caused by the quantization, where the interaction is screened because, after all, the “other” electrons treated in GTF are around. Note that V_{sc} is the screened interaction within the finite sized system, not in the bulk, and so includes boundary effects [68]; under certain conditions, the bulk screened potential may be used [86]. More importantly, while the screened interaction here does include exchange-correlation at the GTF (macroscopic) level, the result (6.31) is a “direct-like” contribution while an “exchange-like” term is missed. This is related to the deficiencies of the LDA-like treatment of DFT here; presumably it could be fixed through a more sophisticated density functional approach.

Chapter 7

Contribution of the Residual Interaction to Peak Spacing Distributions

As an example of the utility of the Strutinsky method for adding quantization effects to a macroscopic result, we turn to considering the spacing between peaks in the conductance through a quantum dot in the Coulomb blockade regime. The contribution of residual interactions have been estimated for chaotic systems within a random matrix theory framework [68,87–89]. There it was found to be small, but not too far from the scale necessary to explain the failure of the constant interaction model. Here our ultimate aim is to evaluate the effect of the residual interaction in specific model systems which often are not in a regime where their quantum properties have fully converged to the purely statistical behavior found in random matrix theory. Systems tend not to be purely chaotic, and even when chaotic, still exhibit manifestations of short time dynamics in their eigenproperties. This can often lead to important deviations from statistical limiting behaviors. We therefore briefly sketch the relationship between the residual interaction and the Coulomb blockade peak spacings.

The position of a conductance peak as a function of gate voltage is proportional to the change in the total energy of the system when an electron is added [52],

$$\mu_N = E(N) - E(N - 1) , \tag{7.1}$$

and the conductance peak spacing is proportional to the discrete inverse compressibility

$$\chi_N = \mu_{N+1} - \mu_N \quad (7.2)$$

$$= E(N+1) + E(N-1) - 2E(N) . \quad (7.3)$$

For each of the ground state energies here we will insert the second-order Strutinsky approximation to the DFT energy. The first term, E_{GTF} , is the ground state energy in the generalized-Thomas-Fermi approximation, and is essentially the charging energy of the dot. The first-order correction contains the single-particle quantization effects. In some sense these two terms together constitute the same level of approximation as the much used constant interaction model. In fact, more physics is included here since changes in the self-consistent confining potential [69] are explicitly contained in the Strutinsky approach [89], whereas due to the ad hoc nature of the constant interaction model, therein exists no information at all on the self-consistent potential. The second-order correction term, $\Delta E^{(2)}$, contains, then, the effects of the residual interaction.

Chapter 8

The Quartic Oscillator: A Case Study

Let us now illustrate the above approach with a particular example. For the sake of simplicity, we choose a one-dimensional model system consisting of N electrons in the confining potential $V_{\text{ext}}(x) = x^4/2$ with the interactions governed by the one-dimensional Poisson equation $d^2V_{\text{int}}[n](x)/dx^2 = -4\pi e^2 n(x)$. This is a simple limit of a three-dimensional problem: the system is assumed to be invariant in the transverse directions y and z so that the interactions are between planes of charge, but the medium is extremely inhomogeneous with the transverse mass taken to infinity so that only one-dimensional quantum mechanics is needed. Exchange and correlation effects are turned off; thus the interaction functional is

$$V_{\text{int}}[n](x) = -2\pi e^2 \int_{-\infty}^{\infty} n(x') |x - x'| dx' . \quad (8.1)$$

Note that use of the 1D Poisson equation causes an interaction which grows with distance. Use of the subscript “int” in this section, rather than “coul” above, is meant to distinguish this case from the three-dimensional Coulomb interaction. We emphasize that our interest in this simple model system is only as an illustration for better understanding of the Strutinsky method.

We vary the electron charge e to see how well the Strutinsky scheme works for different strengths of the interaction, $e = 0.5, 1.0$ and 1.5 in units where $\hbar = m = 1$. The electron

spin degeneracy is not considered here. First, we perform generalized-Thomas-Fermi and density-functional-theory calculations directly. Next, using the GTF results, we apply the Strutinsky techniques to find approximate DFT results. Finally, these approximate results are compared to the actual DFT values. Because of the neglect of exchange-correlation here, the GTF approach reduces to true Thomas-Fermi and the DFT approach is simply the coupled Schrödinger-Poisson equations.

8.1 Thomas-Fermi Numerical Calculations

For one-dimensional systems

$$\nu(\epsilon) = \frac{1}{2\pi\hbar} \int_{-\infty}^{\infty} \Theta(\epsilon - p^2/2m) dp = \frac{\sqrt{2m\epsilon}}{\pi\hbar} \quad (8.2)$$

and, thus, the kinetic energy term, Eq. (5.4), can be written explicitly as

$$\mathcal{T}_{\text{TF}}[n] = \frac{\pi^2\hbar^2}{6m} \int_{-\infty}^{\infty} n(x)^3 dx . \quad (8.3)$$

The ground state density is obtained by solving the Thomas-Fermi equation [cf. Eq. (5.7)]

$$\frac{\pi^2\hbar^2}{2m} n_{\text{GTF}}^2(x) + \frac{1}{2}x^4 + V_{\text{int}}[n_{\text{GTF}}](x) = \mu_{\text{GTF}} \quad (8.4)$$

where we have used $(\delta T_{\text{TF}}/\delta n)[n] = \epsilon(n) = (\pi^2 \hbar^2/2m)n(x)^2$. By differentiating twice and using the Poisson equation, one obtains the second order differential equation

$$\frac{\pi^2 \hbar^2}{2m} \frac{d^2 n_{\text{GTF}}^2(x)}{dx^2} + 6x^2 - 4\pi e^2 n_{\text{GTF}}(x) = 0. \quad (8.5)$$

This can then be transformed into coupled first-order equations

$$\begin{aligned} y_1(x) &= n_{\text{GTF}}^2(x) \\ \frac{dy_1(x)}{dx} &= y_2(x) \\ \frac{dy_2(x)}{dx} &= \frac{2m}{\pi^2 \hbar^2} \left(4\pi e^2 \sqrt{y_1(x)} - 6x^2 \right) \end{aligned} \quad (8.6)$$

which can be conveniently solved. Because of the symmetry of the system, $dn/dx = 0$ at the origin and one needs only specify the density at the origin as an initial condition. One repeats solving Eq. (8.3) adjusting $n_{\text{GTF}}(x=0)$ on each iteration until the normalization condition $N = \int n_{\text{GTF}}(x)dx$ is satisfied. Once the electron density $n_{\text{GTF}}(x)$ is found, the ground state energy is obtained from

$$E_{\text{GTF}} = \mathcal{T}_{\text{TF}}[n_{\text{GTF}}] + \mathcal{E}_{\text{ext}}[n_{\text{GTF}}] + \mathcal{E}_{\text{int}}[n_{\text{GTF}}], \quad (8.7)$$

where \mathcal{T}_{TF} is given in Eq (8.3) and

$$\mathcal{E}_{\text{ext}}[n_{\text{GTF}}] = 2 \int_0^\infty n_{\text{GTF}}(x) \frac{1}{2} x^4 dx$$

$$\mathcal{E}_{\text{int}}[n_{\text{GTF}}] = 2 \cdot \frac{1}{2} \int_0^\infty n_{\text{GTF}}(x) V_{\text{int}}[n_{\text{GTF}}](x) dx . \quad (8.8)$$

The electron densities n_{GTF} for $N = 5, 10$ and 20 with $e = 1.0$ are plotted in Fig. 8.1(a) and the effective potential, $V_{\text{eff}}[n_{\text{GTF}}]$ given by Eq. (5.8), in Fig. 8.1(b). All three cases show the same basic structure which can be simply understood as follows. Without the interaction ($e = 0$), the density would have one maximum at the origin since the external potential has a minimum at the center. Once the interaction is turned on, electrons repel each other and avoid the center, making two maxima in the density. Though not pictured, the larger the value of the electron charge e , the lower the central valley in the density, and the more the density maxima move away from the origin. As intuitively expected, the minimum points in the effective potential correspond to the maximum points of electron density, and increasing e increases rapidly the bimodal nature of the density.

8.2 Quantum Numerical Calculations

The numerical calculation of the DFT energy requires self-consistently solving

$$\begin{aligned} \left(-\frac{\hbar^2}{2m} \frac{d^2}{dx^2} + V_{\text{eff}}[n](x) \right) \phi_i(x) &= \epsilon_i \phi_i(x) \\ n(x) &= \sum_{i=1}^N |\phi_i(x)|^2 \\ V_{\text{eff}}[n](x) &= \frac{1}{2} x^4 - 2\pi e^2 \int_{-\infty}^{\infty} n(x') |x - x'| dx' \end{aligned} \quad (8.9)$$

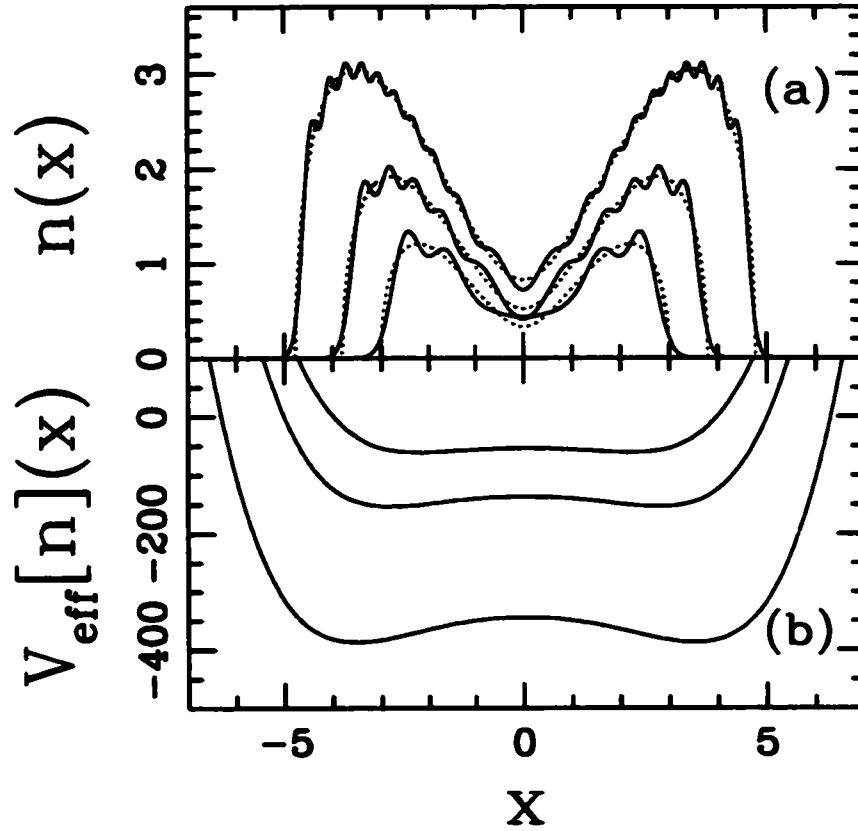


Figure 8.1: The electron densities (upper panel) and effective potentials (lower panel) for interacting particles in a quartic potential. The results for both the Thomas-Fermi (dashed) and coupled Schrödinger-Poisson (solid) approximations are given. The electron charge is $e = 1.0$, and the electron number is $N = 5, 10$, and 20 from bottom to top in upper panel, top to bottom in lower panel. $V_{\text{eff}}[n_{\text{GTF}}]$ and $V_{\text{eff}}[n_{\text{DFT}}]$ coincide so well that one cannot distinguish the differences here.

which are the coupled Schrödinger-Poisson equations. We start the self-consistent iterations with the Thomas-Fermi potential $V_{\text{eff}}[n_{\text{GTF}}]$. At each iteration, we first diagonalize the Hamiltonian $\hat{H} = \hat{\mathbf{p}}^2/2m + V_{\text{eff}}(\mathbf{r})$ expressed in the basis of $\hat{H}_0 = \hat{\mathbf{p}}^2/2 + x^4/2$. From the eigenvalues and eigenvectors of $\hat{H}[V_{\text{eff}}[n]]$, we can construct the electron density and the corresponding effective potential. Self-consistency is evaluated by comparing the effective potentials $V_{\text{eff}}^{\text{Old}}$ and $V_{\text{eff}}^{\text{New}}$ before and after each iteration (or equivalently the densities n^{Old} and n^{New}).

Because of the well-known instability of the Poisson equation, one cannot simply use the output from one iteration, $V_{\text{eff}}^{\text{New}}$, as the input to the next [90]. Instead, we feedback only part of the output

$$V_{\text{eff}}^{\text{Old, Next Iteration}} = V_{\text{eff}}^{\text{Old}} + \alpha(V_{\text{eff}}^{\text{New}} - V_{\text{eff}}^{\text{Old}}), \quad 0 < \alpha < 1 \quad (8.10)$$

where α is initially set as 0.5. If the self-consistency is not improved, α is reduced by half and the iteration redone so that improvement is guaranteed for every iteration. We repeat this until the density reaches self-consistency,

$$\max_{|x| \leq x_{\text{max}}} |n^{\text{New}}(x) - n^{\text{Old}}(x)| \leq 10^{-9}. \quad (8.11)$$

We require self-consistency in the density rather than the potential because the overall magnitude of the density does not change significantly as N increases.

Once the self-consistent density and effective potential are obtained, the Weyl part of the

density, n_{DFT}^W , as well as the chemical potential μ_{DFT}^W can be calculated from Eq. (6.2); the oscillating part of the density follows from $n_{\text{DFT}}^{\text{osc}} = n_{\text{DFT}} - n_{\text{DFT}}^W$. Finally, the self-consistent ground state energy is obtained using

$$\mathcal{T}_{\text{DFT}}[n_{\text{DFT}}] = \mathcal{E}_{\text{lp}}[V_{\text{eff}}[n_{\text{DFT}}]] - 2 \int_0^\infty n_{\text{DFT}}(x) V_{\text{eff}}[n_{\text{DFT}}](x) dx \quad (8.12)$$

and the same expressions for \mathcal{E}_{ext} and \mathcal{E}_{int} as in the Thomas-Fermi calculation, Eq. (8.8). We have used the above relation for the kinetic energy instead of the definition since the eigenvalues are more stable than the eigenvectors in the numerical calculations.

The quantum electron densities for $N = 5, 10$, and 20 are superposed in Fig. 8.1(a) for electron charge $e = 1.0$. One can see the quantum mechanical oscillations whose number of peaks corresponds to the electron number N . Note the decreasing oscillation amplitudes with increasing particle number, as well as the tunneling outside of the potential wall at the classical turning points. The effective potentials, superposed in Fig. 8.1(b), are indistinguishable from the corresponding Thomas-Fermi potentials.

8.3 Strutinsky Energy Corrections

In order to find the approximate ground state energy using the Strutinsky method, we start with the Thomas-Fermi density and potential, calculated above, and quantize in this potential by solving the Schrödinger equation $\left(-\frac{\hbar^2}{2m} \frac{d^2}{dx^2} + V_{\text{eff}}[n_{\text{GTF}}]\right) \phi_i = \epsilon_i \phi_i$ for the eigenvalues and eigenvectors.

The first-order energy correction is given by Eq. (6.22); in our example, the expression for the Weyl part reduces to

$$\mathcal{E}_{\text{lp}}^W[V_{\text{eff}}[n_{\text{GTF}}]] = 2 \frac{\sqrt{2m}}{3\pi\hbar} \int_0^\infty (\mu^W + 2V_{\text{eff}}[n_{\text{GTF}}](x)) \sqrt{\mu^W - V_{\text{eff}}[n_{\text{GTF}}](x)} dx . \quad (8.13)$$

The second-order energy correction, from Eq. (6.19), is

$$\begin{aligned} \Delta E^{(2)} &= -\pi e^2 \int_{-\infty}^\infty \int_{-\infty}^\infty \tilde{n}^{\text{osc}}(x) |x - x'| \delta n(x') dx dx' \\ &= 4\pi e^2 \int_0^\infty \tilde{n}^{\text{osc}}(x) \left\{ \int_x^\infty (x - x') \delta n(x') dx' \right\} dx . \end{aligned} \quad (8.14)$$

The required input δn follows from Eq. (6.26). This equation can be simplified by noting, first, for the kinetic energy term

$$\frac{\delta^2 \mathcal{T}_{\text{TF}}}{\delta n^2}[n_{\text{GTF}}](x, x') = \frac{\delta \epsilon(\nu)}{\delta \nu}[n_{\text{GTF}}] \delta(x - x') . \quad (8.15)$$

Second, for the term depending on V_{eff} note that

$$\int_{-\infty}^\infty \frac{\delta V_{\text{eff}}}{\delta n}[n_{\text{GTF}}](x, x') \delta n(x') dx' = -2\pi e^2 \int_{-\infty}^\infty \delta n(x') |x - x'| dx' = V_{\text{int}}[\delta n](x) \quad (8.16)$$

implies

$$\frac{d^2 V_{\text{int}}[\delta n](x)}{dx^2} = -4\pi e^2 \delta n(x) . \quad (8.17)$$

Thus, by taking the second derivative with respect to x of Eq. (6.26), one obtains

$$\frac{\pi^2 \hbar^2}{m} \frac{d^2}{dx^2} \{n_{\text{GTF}}(x) \cdot (\delta n(x) - \tilde{n}^{\text{osc}}(x))\} - 4\pi e^2 \delta n(x) = 0. \quad (8.18)$$

This equation can be converted into the coupled first-order equations

$$\begin{aligned} y_1(x) &= n_{\text{GTF}}(x) \cdot (\delta n(x) - \tilde{n}^{\text{osc}}(x)) \\ \frac{dy_1(x)}{dx} &= y_2(x) \\ \frac{dy_2(x)}{dx} &= \frac{4me^2}{\pi \hbar^2} \left(\frac{y_1(x)}{n_{\text{GTF}}(x)} + \tilde{n}^{\text{osc}}(x) \right) \end{aligned} \quad (8.19)$$

which can be conveniently solved.

With the energy correction terms calculated, the Strutinsky scheme allows us to approximate the quantum ground state energy using essentially classical Thomas-Fermi quantities. We plot $\Delta E \equiv E_{\text{DFT}} - E_{\text{GTF}}$, $\Delta E - \Delta E^{(1)}$, and $\Delta E - \Delta E^{(1)} - \Delta E^{(2)}$ as functions of N to see the series convergence of the Strutinsky scheme in Figs. 8.2, 8.3 and 8.4 for $e = 0.5, 1.0$ and 1.5 respectively. In the first two cases, the convergence seems to be working well: for $e = 0.5$, without correction terms the error is 0.17 taking the average over N from 2 to 20 and smooth, while the first-order correction term improves the accuracy to 0.0013, and the second-order term to roughly 1.3×10^{-5} . For $e = 1.0$, without correction terms the error is about 0.24. With the first-order correction the error reduces to 0.012, and with the second-order to 0.0027.

For $e = 1.5$, before comparing the order of magnitude of the different terms, it is useful to

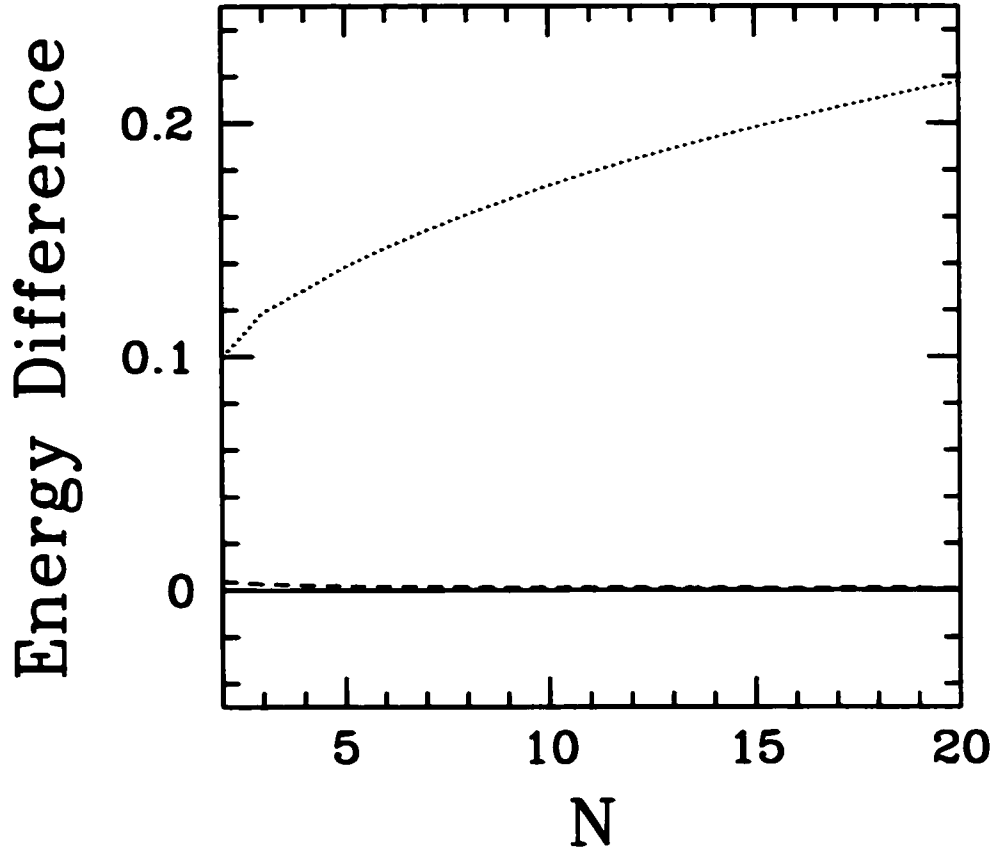


Figure 8.2: Convergence of approximations to the quantum ground state energy for electron charge $e = 0.5$. The curves are, from top to bottom, the error in the Strutinsky energy correction approach taken at zeroth, first, and second order: specifically $\Delta E \equiv E_{\text{DFT}} - E_{\text{GTF}}$ (dotted), $\Delta E - \Delta E^{(1)}$ (dashed), and $\Delta E - \Delta E^{(1)} - \Delta E^{(2)}$ (solid). The convergence in this case is excellent. The values of E_{GTF} are -6.835, -34.450, and -173.619 for $N = 5, 10$, and 20 respectively.

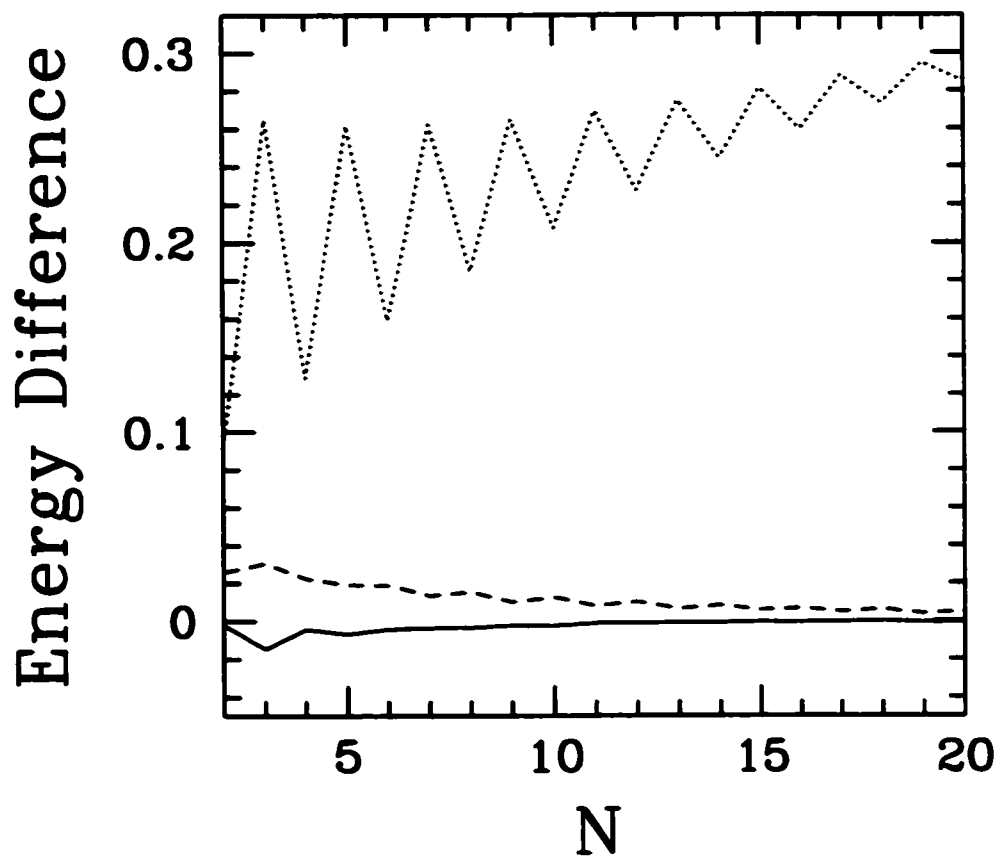


Figure 8.3: Convergence of approximations to the quantum ground state energy for electron charge $e = 1.0$. The curves are, from top to bottom, $\Delta E \equiv E_{\text{DFT}} - E_{\text{GTF}}$ (dotted), $\Delta E - \Delta E^{(1)}$ (dashed), and $\Delta E - \Delta E^{(1)} - \Delta E^{(2)}$ (solid). The values of E_{GTF} are -114.986, -579.496, and -2920.476 for $N = 5, 10$, and 20 respectively.

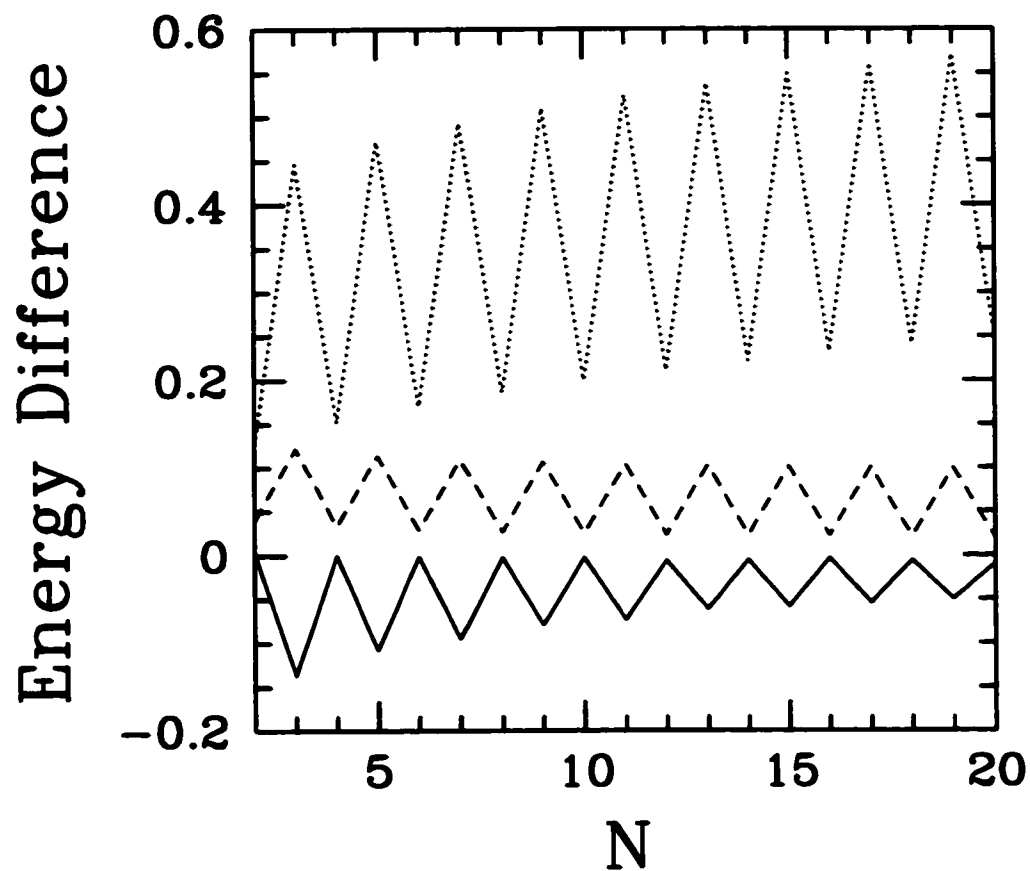


Figure 8.4: Convergence of approximations to the quantum ground state energy for electron charge $e = 1.5$. The curves are, from top to bottom, $\Delta E \equiv E_{\text{DFT}} - E_{\text{GTF}}$ (dotted), $\Delta E - \Delta E^{(1)}$ (dashed), and $\Delta E - \Delta E^{(1)} - \Delta E^{(2)}$ (solid). The values of E_{GTF} are -362.500, -1826.887, and -9206.935 for $N = 5, 10$, and 20 respectively.

say a few words about the odd-even structure clearly visible in Fig. 8.4, and actually already apparent for $e = 1.0$ at low N in Fig. 8.3. The origin of this behavior is not related to spin (which has not been included) but can be readily understood by looking at the lower panel of Fig. 8.5, which shows the effective Thomas-Fermi potential $V_{\text{eff}}[n_{\text{GTF}}]$ for $N = 20$, $e = 1.5$. Here, one sees that the latter has developed a barrier at the center of the well, the top of which lies very close to the chemical potential. For the quantum case, this means that the one particle levels below the Fermi energy are organized as quasi-doublets. This naturally leads to an odd-even effect since for N even (odd), the last occupied orbital has an energy consistently below (above) that suggested by the Weyl approximation.

Moreover, because the last occupied orbitals are close to the chemical potential and so near the top of the barrier, it is clear that semiclassical approximations will be “at risk” here. This is clearly seen for instance in Figs. 8.6 and 8.7, which, for coupling $e = 1.5$ and $N = 19$ and 20 particles, shows a comparison between the exact $\delta n(\mathbf{r}) \equiv n_{\text{DFT}}(\mathbf{r}) - n_{\text{GTF}}(\mathbf{r})$ and its approximation obtained using Eq. (6.26). The two curves are almost on top of each other everywhere, except in the middle of the well—that is, near the maxima of the barrier. In addition, one observes that in that place, the approximation is worse for an odd than for an even number of particles. This can be explained by the fact that in the former case the last occupied orbital is symmetric and thus has a probability maximum at the origin, while in the latter case the last occupied orbital is antisymmetric and so goes to zero. As a consequence the errors in the Strutinsky approximation scheme also display an odd-even structure clearly seen in Fig. 8.5. If, however, one concentrates on the even case, where the

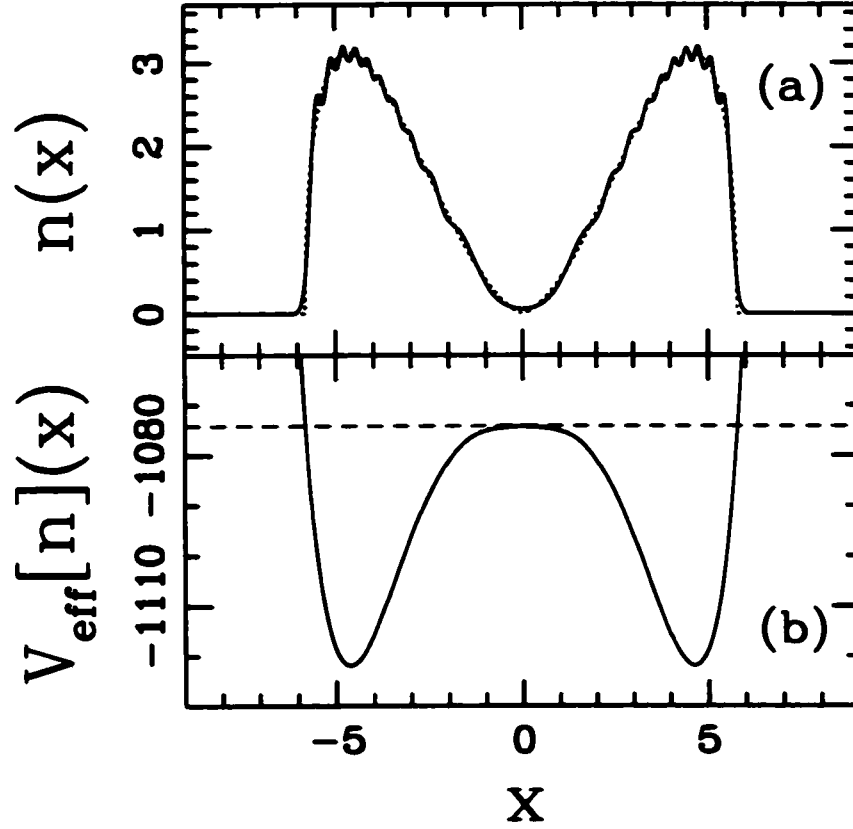


Figure 8.5: The electron density (upper panel) and effective potential (lower panel) for $N = 20$ particles and $e = 1.5$. In the upper panel, results for both the Thomas-Fermi (dashed) and quantum (solid) cases are given. In the lower panel, the dashed horizontal line is the position of the chemical potential μ_{TF} .

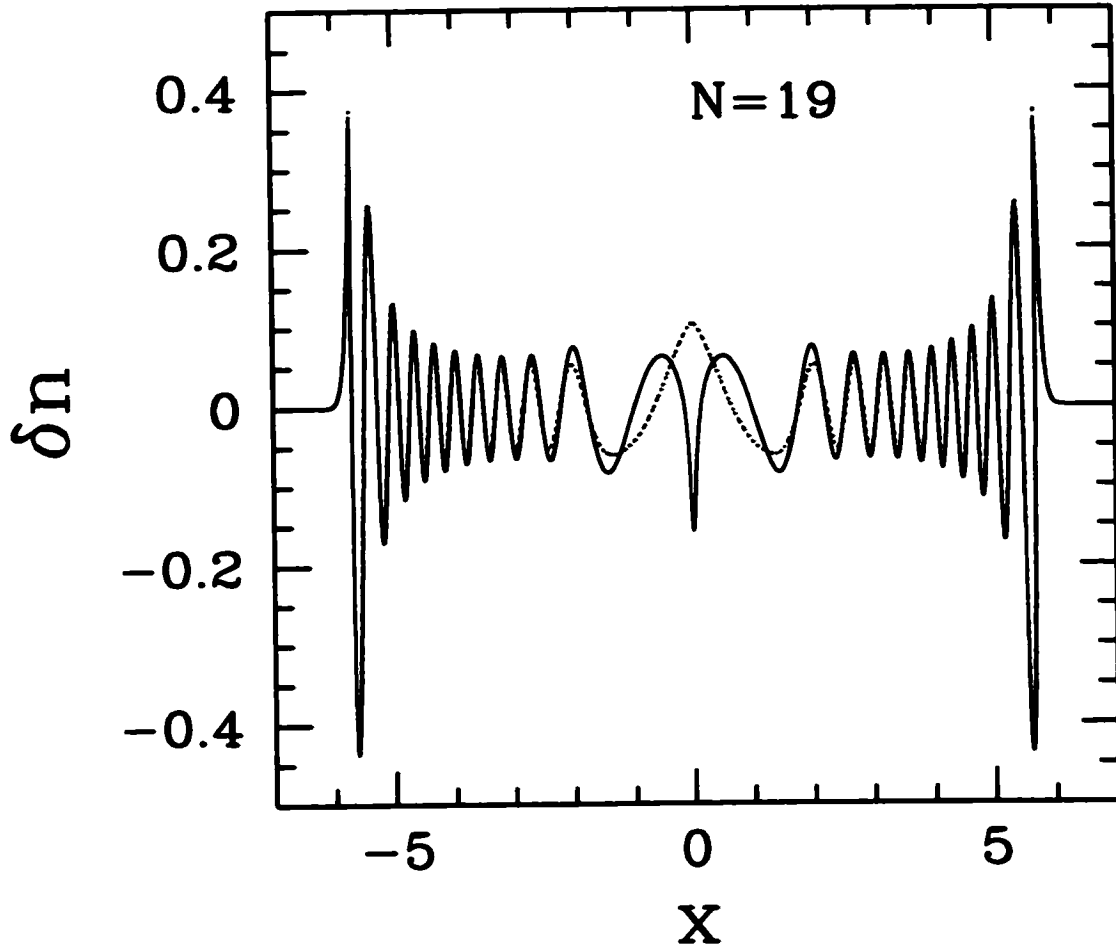


Figure 8.6: Comparison between the exact $\delta n \equiv n_{\text{DFT}} - n_{\text{GTF}}$ (dashed line) and its approximation derived from Eq. (6.26) (solid line) for $e = 1.5$ and $N = 19$.

effect of the central barrier is less important, without correction terms the error is about 0.35 taking the average over N from 2 to 20. With the first-order correction the error is reduced to 0.065, and further reduced to about 0.039 if one includes the second-order corrections.

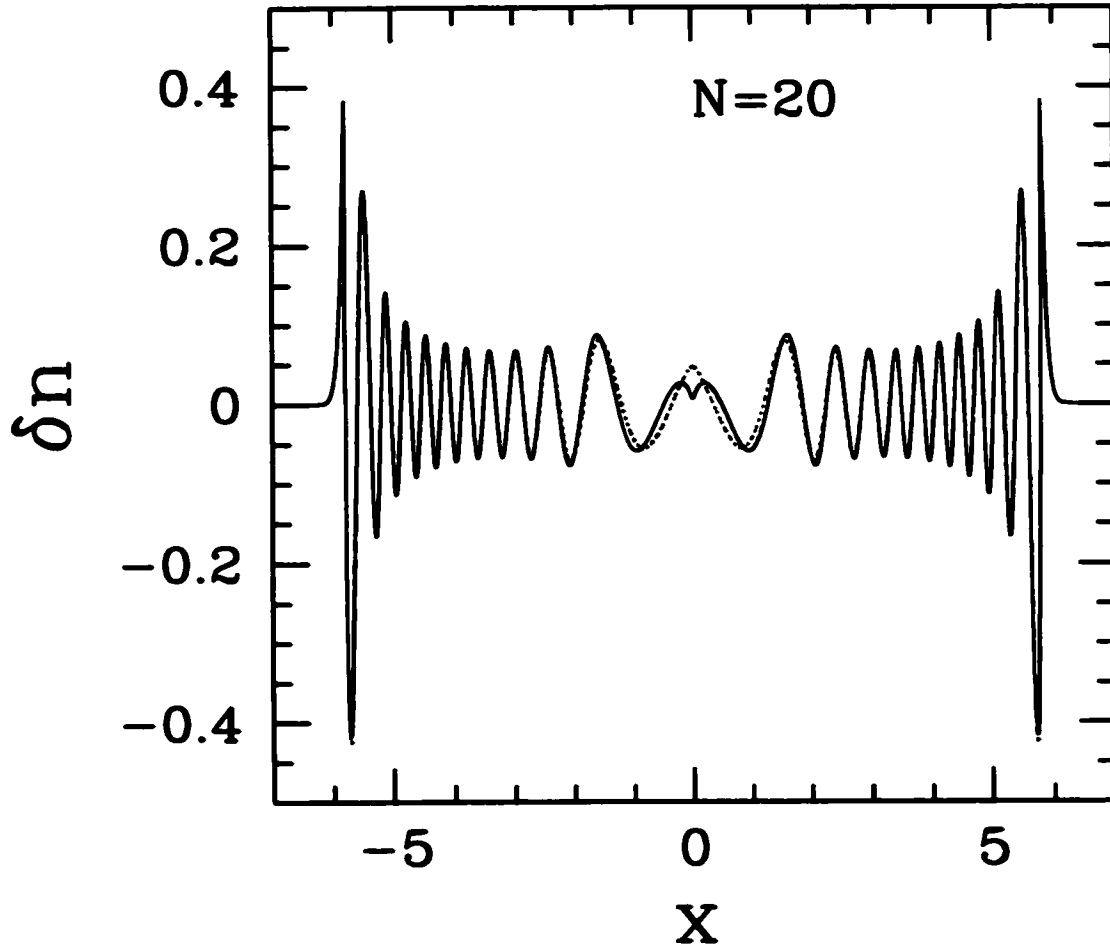


Figure 8.7: Comparison between the exact $\delta n \equiv n_{\text{DFT}} - n_{\text{GTF}}$ (dashed line) and its approximation derived from Eq. (6.26) (solid line) for $e = 1.5$ and $N = 20$.

8.4 Peak Spacings

Turning now to the inverse compressibility χ_N introduced in Sect. 7, we observe the same trend as for the ground-state energy. The approximation $\chi_N^{\text{STR}(0)}$, calculated strictly within the Thomas-Fermi approximation, already gives an excellent relative precision. Moreover, for $e = 0.5$ and $e = 1.0$, each term in the Strutinsky development significantly reduces the error. For these cases however the approximation is already much better than the mean spacing Δ if the first correction is included. We therefore show the data only for $e = 1.5$, for which the corrections are enhanced by the proximity of the chemical potential to the top of the inner barrier. In Fig. 8.8(a), the χ_N are shown. The discrete points represent the full quantum calculations and are taken as the reference points. It is seen that $\chi_N^{\text{STR}(0)}$ does not capture the odd-even double-well effect, but otherwise captures the essential peak spacing behavior. In Fig. 8.8(b), the relative errors are shown as a function of N . More specifically, the difference between the quantum χ_N and one, two, or three terms of the Strutinsky series— $\chi_N^{\text{STR}(0)}$, $\chi_N^{\text{STR}(1)}$ and $\chi_N^{\text{STR}(2)}$, respectively—is divided by Δ , the mean level separation. It is seen that the majority of the odd-even, double-well effect is captured by the first correction term. Reassuringly, even in this case for which the inner barrier degrades the quality of the semiclassical development, each inclusion of an extra term in the series reduces somewhat the relative errors of the Strutinsky method. Moreover the improvement due to the addition of the second order correction becomes more significant with increasing N . Thus we see that even in this more difficult case, the Strutinsky method gives an excellent scheme of approximation in the semiclassical limit.

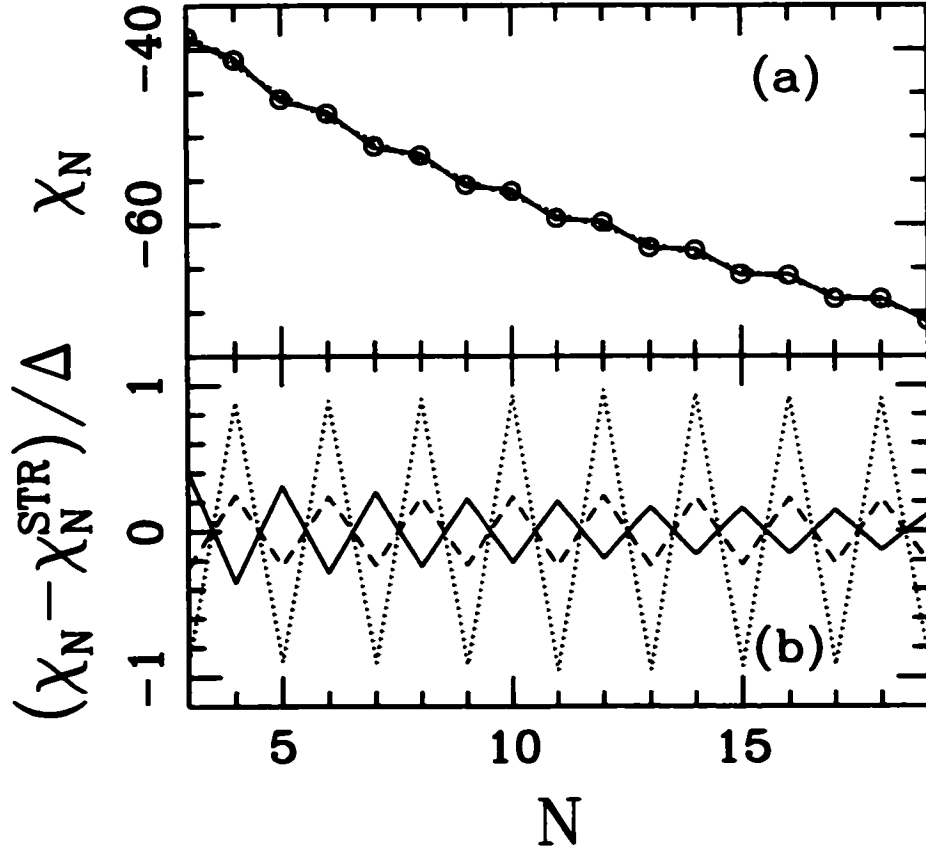


Figure 8.8: The discrete inverse compressibility as a function of electron number N . The open circles are χ_N using the quantum ground state energy (exact). Results using three approximate ground state energies are shown: (1) dotted: Thomas-Fermi, $\chi_N^{\text{STR}(0)}$ using E_{GTF} , (2) dashed: first-order Strutinsky, $\chi_N^{\text{STR}(1)}$ using $E_{\text{GTF}} + \Delta E^{(1)}$, and (3) solid: second-order Strutinsky, $\chi_N^{\text{STR}(2)}$ using $E_{\text{GTF}} + \Delta E^{(1)} + \Delta E^{(2)}$. The lower panel shows the relative errors, $(\chi_N - \chi_N^{\text{STR}})/\Delta$, of the same three approximations.

8.5 Deformation of the Effective Potential

Up to this point, we have been interested in the contributions of two quantum mechanical energy correction terms. As we have mentioned, the ground state energy in the generalized-Thomas-Fermi approximation, E_{GTF} , and the first-order correction constitute, in some sense, the same level of approximation as in the constant interaction model. By equating the expression for the ground state energy, one can derive the definition of capacitance C ,

$$E_{GTF} + \Delta E^{(1)} = -\frac{N^2 e^2}{2C} + \sum_{i=1}^N \epsilon_i \quad (8.20)$$

where the negative sign in the charging energy is due to the nature of our one-dimensional model system. The capacitance, as a function of particle number N , smoothly varies as $N^{-1/3}$ approximately, and it approaches zero with increasing N .

When one adds an extra particle to the system, it causes a deformation of the effective potential. In the constant interaction model, as often applied, this effect is ignored by assuming that locally the capacitance and single particle energies are independent of the particle number. On the other hand, since our energy correction approach calculates each system having different particle number independently, the “scrambling effect” on the ground state energy due to the changing effective potential is automatically included. To observe the significance of the scrambling for peak spacings, we have calculated the fluctuating part of the discrete inverse compressibility by both freezing the effective potential and allowing it to change self-consistently. We used only the GTF ground state energy and the first

order correction term turning off the residual interaction contribution. With scrambling, E_{GTF} basically contribute as the mean part of the discrete inverse compressibility and $\Delta E^{(1)}$ contribute as the fluctuating part. Without scrambling, the charging energy and the Weyl part of the single particle energy levels contribute as the mean part, and the remaining part in the single particle energy levels contribute as the fluctuating part. The results are depicted in Fig. 8.9. In our toy 1D model, the changes in χ_N^{fl} (fl for a fluctuating part) due to scrambling are seen to be getting smaller as N increases and less than the scale given by Δ_N . However, we caution against assuming that the scrambling of χ_N would occur on the same scale in more realistic multidimensional models with the Coulomb interaction. This question is under investigation and left for future work.

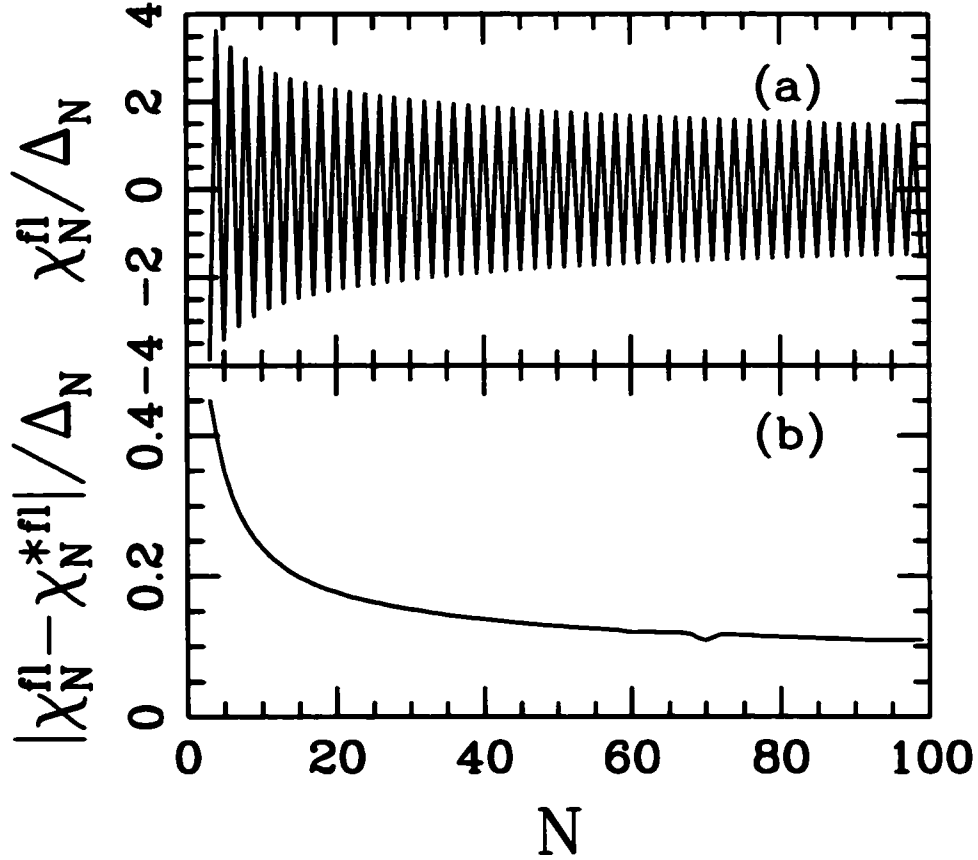


Figure 8.9: The fluctuating part of the discrete inverse compressibility scaled by the mean level spacing. The upper figure is the fluctuating part of χ_N with scrambling. The odd-even effects are due to the nature of the double well shaped effective potential. The lower figure is the difference in the fluctuating part with and without scrambling (* denotes the case for without scrambling). Both figures are generated with electron interaction strength $e = 1.5$.

Chapter 9

Role of Dynamics in Interacting Fermion Systems: Ground State Properties of Quantum Dots

9.1 Introduction

A quantum dot is a mesoscopic semiconductor electronic device containing one to few thousand electrons. Due to its small size, the allowed energies of electrons are quantized giving the discrete energy spectra with corresponding eigenstates. In electronic transport measurements, the conductance is suppressed due to the Coulomb repulsion among electrons. This is known as the Coulomb blockade (CB) and is a classical effect [91,92]. When the appropriate gate voltage is tuned such that the ground state energy of N electrons and that of $N+1$ become degenerate, a large conductance peak arises. By continuously changing the voltage, conductance peak oscillations are produced. These oscillations are periodic, and the spacing between peaks gives e^2/C which originates in the charging energy (C is the capacitance of the dot). At low temperature where $k_B T \ll \Delta$ (mean single-particle level spacing), quantum interference becomes significant. The conductance peaks grow and deviate due to the coupling between wave functions and leads attached to the dots, and the spacings fluctuate because of the quantum interference effects on the ground state energy.

The constant interaction (CI) model is the simplest approach to investigate Coulomb

blockaded quantum dots. The model approximates the ground state energy as

$$E_N = \frac{e^2 N^2}{2C} + \sum_{\text{occupied } i\sigma} \epsilon_{i\sigma} \quad (9.1)$$

where $\epsilon_{i\sigma}$ is the single-particle energy for orbital i and spin σ . Once the interaction among N particles are included as the classical charging energy, its quantum mechanical contribution comes from the total energy of non-interacting quasiparticles. It has been successful in explaining some of the experimentally observed statistical properties such as conductance peak height distributions and mean separation of the peaks. However, the experimental studies of the CB peak spacing fluctuations show significant disagreement with the CI model prediction. Since the peak spacing is proportional to the discrete inverse compressibility defined as the second difference of the ground state energy

$$\Delta^2 E_N \equiv E_{N+1} + E_{N-1} - 2E_N, \quad (9.2)$$

the CI model leads to the following expressions

$$\Delta^2 E_N = \frac{e^2}{C} + \epsilon_{N/2+1} - \epsilon_{N/2} \quad (N \text{ even}) \quad (9.3)$$

$$\Delta^2 E_N = \frac{e^2}{C} \quad (N \text{ odd}) \quad (9.4)$$

assuming mean field is unchanged by the number of electrons. Thus, the CI model predicts a strong odd-even effect due to the electron spin degeneracy. Assuming that the corresponding

classical dynamics is chaotic and the Bohigas-Giannoni-Schmit conjecture applies [64] (see later section), the single-particle energies behave statistically like the eigenvalues in RMT. Then, the above expressions lead to a bimodal structure for the peak spacing distribution: δ function and Wigner surmise. Yet, there is no such structure observed in measurements. Only a weak odd-even spin signature is captured [93]. In addition to the spacing distributions, spacing fluctuations are considerably larger (in experiments) than the theoretical description. These discrepancies between the CI model predictions and the experimental observations indicate that a more sophisticated treatment of the electron interaction is necessary for the study of CB peak spacing distributions.

For a finer approach to the electron-electron interaction, this is a perfect setting to apply the Strutinsky energy correction scheme discussed in the last chapter. The method gives the semiclassical expression for the ground state energy as

$$E_{\text{DFT}} \simeq E_{\text{GTF}} + \Delta E^{(1)} + \Delta E^{(2)} \quad (9.5)$$

where the correction terms are

$$\Delta E^{(1)} = \mathcal{E}_{\text{lp}}^{\text{osc}}[V_{\text{eff}}[n_{\text{GTF}}]] \quad (9.6)$$

$$\Delta E^{(2)} = \frac{1}{2} \int d\mathbf{r} d\mathbf{r}' \bar{n}^{\text{osc}}(\mathbf{r}) V_{\text{sc}}(\mathbf{r}, \mathbf{r}') \bar{n}^{\text{osc}}(\mathbf{r}'). \quad (9.7)$$

The physical interpretations (discussed in Chapter 6) of the above terms are given as follows: the first order correction is the fluctuation part of the single-particle energies computed in

the effective potential $V_{\text{eff}}[n_{\text{GTF}}]$. One can interpret this as the sum of the oscillating parts $\delta\epsilon_i$,

$$\mathcal{E}_{\text{lp}}^{\text{osc}}[V_{\text{eff}}[n_{\text{GTF}}]] \equiv \sum_{i=1}^N \delta\epsilon_i, \quad (9.8)$$

knowing that each energy ϵ_i has its smooth and fluctuating part as $\epsilon_i = \bar{\epsilon}_i + \delta\epsilon_i$. The second order correction is basically the energy due to the fluctuating part of the electron density interacting with itself through a screened potential, and it is interpreted as the residual interaction of the electron density. Let us consider the (discrete) inverse compressibility of the system for the purpose of illustrating the effect of the residual interaction term. As an example, if the standard up-down filling of the orbitals is assumed and also the mean field is unaffected by the electron number, the inverse compressibility becomes

$$\Delta^2 E_N = \Delta^2 E_{\text{GTF}} + \delta\epsilon_{n+1} - \delta\epsilon_n + 2 \sum_{i=1}^n (M_{n+1,i} - M_{n,i}) \quad (\text{N even}) \quad (9.9)$$

$$\Delta^2 E_{N+1} = \Delta^2 E_{\text{GTF}} + M_{n+1,n+1} \quad (\text{N odd}) \quad (9.10)$$

where we simplified the residual interaction term by defining matrix elements

$$M_{ij} \equiv \int d\mathbf{r} d\mathbf{r}' |\psi_i(\mathbf{r})|^2 V_{\text{sc}}(\mathbf{r}, \mathbf{r}') |\psi_j(\mathbf{r}')|^2. \quad (9.11)$$

Here, N represents the number of particles, and the subscript n is the orbital number. We note that \bar{n}^{osc} in the residual interaction term is replaced by $\bar{n} = \sum_i |\psi_i(\mathbf{r})|^2$. While this replacement shifts the smooth part of the inverse compressibility (one can always separate

any quantum mechanical quantity into an averaging smooth part and a fluctuating part), the fluctuating part remains unchanged. Since the Strutinsky scheme is based on the local density approximation, it only gives the “direct” interaction within the oscillatory part of density by M_{ij} , and misses the related “exchange” interaction term. Thus, the electron spin is not yet properly handled in the ground state energy representation. It is discussed in Ref. [94] that by physical considerations, the residual interaction must be modified with the exchange term as

$$E_N(\{n_{i\sigma}\}) = E_{\text{GTF}} + \sum_{i\sigma} n_{i\sigma} \delta\epsilon_i + \frac{1}{2} \sum_{i,j;\sigma,\sigma'} n_{i\sigma} M_{ij} n_{j\sigma'} - \frac{1}{2} \sum_{i,j;\sigma} n_{i\sigma} N_{ij} n_{j\sigma} \quad (9.12)$$

where

$$N_{ij} \equiv \int d\mathbf{r} d\mathbf{r}' \psi_i(\mathbf{r}) \psi_j^*(\mathbf{r}) V_{\text{sc}}(\mathbf{r}, \mathbf{r}') \psi_j(\mathbf{r}') \psi_i^*(\mathbf{r}) \quad (9.13)$$

represents the exchange interaction, $n_{i\sigma}$ is the occupation number which takes either the values 0 or 1, and $\sigma(= \pm 1)$ specifies the spin. A state for a N-particle system is thus characterized by the combination of the occupation numbers $(n_{1\sigma}, n_{2\sigma}, \dots)$, and the total number of particle is fixed with $N = \sum n_{i\sigma}$.

Suppose electrons fill the orbitals in the standard manner, i.e., simple up-down filling, the spin polarization of the ground state becomes either 0 or 1/2 depending on the number of electrons in the dot. This gives the equal probability distribution for both polarizations. However, it has been suggested that the standard orbital occupation is not always the preferable way for many-electron systems when particle interactions are taken into account.

Usaj *et al.* [95, 96] employ the universal Hamiltonian to show finite temperature effects on peak spacing distribution and spin of quantum dots. Brouwer *et al.* [97, 98] shows the non-standard orbital occupation studying RMT for the systems in both the presence and absence of time-reversal symmetry. Hirose *et al.* [99, 100] and Jiang *et al.* [101] independently study the ground state spin in terms of spin-density-functional theory. Although there are many other theoretical approaches [94, 102–105] indicating the importance of studying non-trivial electron orbital filling mechanism, explicit measurements have not been reported so far.

In this chapter, we apply the Strutinsky method to describe the system of two-degree-of-freedom quantum dots, and especially focus on the dynamical effects on the statistics of CB conductance peak spacings and the ground state spin polarizations. We introduce the two-dimensional coupled quartic oscillator potential as a sample realization of such systems.

The advantage of employing the coupled quartic oscillator is that one can continuously tune the degree of chaos from near-integrability to mostly-chaos by changing the value of mode coupling constant. The coupling constant can introduce disorder to systems. In addition, we include a time-reversal symmetry breaking term to reproduce experimentally accessible magnetic field effects. The time-reversal invariant quartic oscillator give us a means to study the dynamical effects on the connection between the residual interaction and wave functions. However, it fails to describe the ground state energy of quantum dots properly. The reason is that the higher order terms, which are ignored in the Strutinsky second order correction, significantly contribute to the interaction energy and reduce the total energy of the system. It was discussed in the context of diagrammatic perturbation

theory and semiclassical finite-temperature Green functions [106–108]. On the other hand, there are no such higher order interaction contributions for the time-reversal non-invariant systems, and the Strutinsky second order scheme successfully represents the ground state of quantum dots.

Chapter 10

Dynamical Systems - Coupled Quartic Oscillator

10.1 Semiclassical Effective Potential

There exist many types of quantum dots. One kind of quantum dots is fabricated in the interface of two metallic semiconductor layers (GaAs-AlGaAs for example) confining electrons vertically and forming the two-dimensional electron gas (2DEG). Negatively applied gate voltages create the potential barriers in the 2DEG, isolating the dot region from the electron reservoirs. To achieve an isolated quantum dot in the Coulomb blockade regime, coupling to the dot is very weak. The leads are called the quantum point contacts, and the electron transport is allowed only via tunneling. Combinations of the gate configurations and the applied voltages determine the shapes of the dots. In addition, there is a deformation of the potential (thus the dot shape) when extra electrons are added to the dot the so-called scrambling effect, which has to be taken into account.

In the Strutinsky method, three energy functionals contribute to determine the effective potential: external confinement, electron interaction, and the exchange-correlation effect. The scrambling effect is automatically included since systems with different electron numbers are treated independently in the scheme. Recognizing the gate confinement as the external potential (including the deformation due to the gate voltage adjustment), the Strutinsky method defines the model system for the quantum dot. Once the effective potential is

constructed, it becomes the only “confinement” for the system, and the electrons can be viewed as non-interacting quasiparticles. Whereas, in experiments, the dot shape results from the gate configurations; for theoretical studies, the effective potential can be modeled directly. This flexibility of choosing the effective potential is equivalent to the one of modifying the external gate configuration. For our purposes, choosing the two-dimensional coupled quartic oscillator potential as the Thomas-Fermi effective potential,

$$V_{\text{eff}}[n_{\text{GTF}}](\mathbf{r}) \equiv a(\lambda) \left[\frac{x^4}{b} + by^4 + 2\lambda x^2 y^2 \right], \quad (10.1)$$

has many advantages; see ahead. Furthermore, it is reasonably realistic since quantum dots can be built with the external gate configurations such that the resulting effective potential is similar to the quartic oscillator confinement. The quartic oscillator quantum dot’s statistical properties will thus be representative of the properties of true dots.

10.2 Two-Dimensional Coupled Quartic Oscillator

10.2.1 Classical Mechanical Level

Since the classical and quantum mechanical studies of the quartic oscillators have been previously investigated, we introduce some of the key ideas from the work of Bohigas, Tomsovic, and Ullmo [114]. The two-dimensional coupled quartic oscillator serves as a paradigm of simple non-integrable conservative systems. The two degrees of freedom are the fewest to exhibit a non-integrable dynamics in a conservative system. The classical Hamiltonian is

given as

$$H(\lambda, b) = \frac{p_1^2 + p_2^2}{2m} + a(\lambda)(q_1^4/b + bq_2^4 + 2\lambda q_1^2 q_2^2) \quad (10.2)$$

where the parameter λ denotes the strength of coupling of the two modes, and the constant b reduces the system's symmetry [114]. The system can be continuously tuned from integrability to (almost) complete chaos by changing the value of λ . Due to the homogeneity of the potential, only a single energy surface is needed to be investigated (classically). Since the potential satisfies

$$V(\alpha \mathbf{q}) = \alpha^4 V(\mathbf{q}), \quad (10.3)$$

the set of solutions $\mathbf{x}^0 = (\mathbf{p}^0(t), \mathbf{q}^0(t))$ which satisfy $H(\mathbf{x}^0) = E^0$ give the scaling properties

$$\mathbf{p}^E(t) = \sqrt{E/E^0} \mathbf{p}^0(\gamma t) \quad (10.4)$$

$$\mathbf{q}^E(t) = (E/E^0)^{1/4} \mathbf{q}^0(\gamma t) \quad (10.5)$$

where $\gamma = (E/E^0)^{1/4}$, providing the solutions $\mathbf{x}^E = (\mathbf{p}^E(t), \mathbf{q}^E(t))$ for the different energy $H(\mathbf{x}^E) = E$ without solving the latter system explicitly. In addition, the Hamiltonian is invariant under the following transformations, the reflection and time reversal operations:

$$P_i : \quad q_i \rightarrow -q_i, \quad p_i \rightarrow -p_i \quad (i = 1, 2) \quad (10.6)$$

$$T : \quad t \rightarrow -t \quad (\text{or } p_i \rightarrow -p_i \quad (i = 1, 2)). \quad (10.7)$$

Thus, for a given solution

$$\mathbf{x}(t) = (p_1(t), p_2(t), q_1(t), q_2(t)), \quad (10.8)$$

there exist three corresponding solutions due to the symmetry

$$(-p_1(t), p_2(t), -q_1(t), q_2(t)), \quad (10.9)$$

$$(p_1(t), -p_2(t), q_1(t), -q_2(t)), \quad (10.10)$$

$$(-p_1(-t), -p_2(-t), q_1(-t), q_2(-t)). \quad (10.11)$$

For the special case when $b = 1$, the system becomes further invariant under the combined operation $P_1 \cdot P_2$ (the symmetry under index exchange $1 \leftrightarrow 2$), but this case must be avoided for quantum mechanical considerations. Therefore, the choice for b is set $\pi/4$. The coupling of the two modes will be taken sufficiently strong to prevent the system from the possibility of effective one-dimensional decomposition.

The coupling constant λ represents the degree of chaoticity, and so determines the dynamical behavior of the system. For this reason, one of the proper approaches is to study the λ dependence of phase space structure using surfaces of section. The system has two degrees of freedom, and the corresponding phase space is a four-dimensional space spanned by the q_1, q_2, p_1 , and p_2 axes. Taking advantage of the reflection symmetries, two surfaces of sections are set at the $q_1 = 0$ and $q_2 = 0$ planes. Because each trajectory crosses at least one of the planes, no further surface is necessary. To construct the surfaces of section, consider

the $q_2 = 0$ plane, for example. Starting at one point (initial condition) in the phase space, let the system evolve in time. The point will follow a certain trajectory, and every time this trajectory crosses the $q_2 = 0$ plane with positive momentum p_2 , one records the coordinate (q_1, p_1) . For a given initial condition, there exist a Poincaré section of the trajectory. The section can appear as a finite number of points, a closed curve, or a two-dimensional region. Each corresponds to the initial condition, starting on a closed trajectory, an invariant torus, or a chaotic region respectively. Within the range of $-1 < \lambda \leq 0$, Ref. [114] shows the evolution of Poincaré sections as decreasing λ . For $\lambda = 0$, the motion is two uncoupled oscillators showing the invariant tori with concentric closed curves centered at the origin. When λ takes the value near -0.20 or less, all of the original irrational tori are destroyed. As λ decreases towards -1.0 , the chaotic region continuously grows, and at $\lambda = -0.60$ almost the entire surface is dominated by the chaotic region.

10.2.2 Quantum Mechanical Level

At the quantum mechanical level, systems are governed by the Hamiltonian

$$\hat{H} = \frac{\hat{\mathbf{p}}^2}{2m} + aV(\hat{\mathbf{q}}) \quad (10.12)$$

with the same homogeneity property for the potential $V(\alpha\hat{\mathbf{q}}) = \alpha^4 V(\hat{\mathbf{q}})$. Then the energy spectra and eigenstates have the following scaling properties

$$E_n^a = a^{1/3} E_n^0 \quad (10.13)$$

$$\Psi_n^a(\mathbf{q}) \propto \Psi_n^0(a^{1/6}\mathbf{q}) \quad (10.14)$$

where the superscript 0 represents the case with $a = 1$. Besides the scaling properties, there exist parity symmetries for the eigenstates. Due to the reflection symmetry under P_i operations (Eq. (10.6)), the eigenstates are classified into four parity sequences (ϵ_1, ϵ_2) where ϵ_i takes either +1 or -1 representing the parity for q_i . With the choice of $b = 1$ (see the b dependence of the potential, Eq. (10.2)), each state further possesses a symmetry under $P_1 \cdot P_2$, leading two-fold degeneracy, or one can consider it as the particle exchange symmetry. Since it will easily complicate the analysis, we avoid $b = 1$ to exclude this symmetry.

Quantum mechanical information of a system is often contained in fluctuations of physical quantities such as energy spectra. The study of the level density or counting function gives us insight into the fluctuation properties of energy spectra. For given discrete eigenspectra, the counting (or staircase) function is defined as

$$N(E) = \sum_{i=1}^{\infty} \Theta(E - E_i) = \sum_{E_i \leq E} 1 = \text{Tr}(\Theta(E - \hat{H})), \quad (10.15)$$

where Θ is the Heaviside step function, and the level density is obtained as its derivative

$$\rho(E) = \frac{dN(E)}{dE} = \sum_{i=1}^{\infty} \delta(E - E_i) = \text{Tr}(\delta(E - \hat{H})). \quad (10.16)$$

To extract the fluctuating part, one must decompose the quantity into its smooth (or average) and the fluctuating (or oscillating) parts. Based on the idea of the Wigner transform of a

quantum mechanical operator, the counting function for the quartic oscillator is separated as follows (see Ref. [114] for a detailed derivation)

$$N(E) = \bar{N}(E) + \delta N(E) \quad (10.17)$$

where the smooth part is calculated as

$$\bar{N}(E) = \frac{2K((1-\lambda)/2)}{3\pi} \frac{m}{\hbar^2 a(\lambda)^{1/2}} E^{3/2} - \frac{(b^{-1/2} + b^{1/2})(3+\lambda)}{24\sqrt{2(1+\lambda)}} + O(\hbar^2 E^{-3/2}), \quad (10.18)$$

and $K(z)$ is a complete elliptic integral of the first kind. Because of the four parity classes of the eigenspectra, $\bar{N}(E)$ can be modified for each parity sequences

$$\begin{aligned} \bar{N}_{\epsilon_1, \epsilon_2}(E) = & \frac{1}{4} \left[E^{3/2} + \frac{\Gamma(1/4)^2(\epsilon_1 b^{-1/4} + \epsilon_2 b^{1/4})}{2\sqrt{6}\pi K^{1/2}((1-\lambda)/2)} E^{3/4} \right. \\ & \left. - \frac{(b^{-1/2} + b^{1/2})(3+\lambda)}{24\sqrt{2(1+\lambda)}} + \frac{\epsilon_1 \epsilon_2}{4} \right] + O(E^{-3/4}) \end{aligned} \quad (10.19)$$

where the coefficient $a(\lambda)$ is set as

$$a(\lambda)^{1/2} = \frac{2K((1-\lambda)/2)}{3\pi} \frac{m}{\hbar^2}. \quad (10.20)$$

making the coefficient of the lowest order term unity, and this defines the scaling of the system.

10.3 Eigenstates of the System

10.3.1 Matrix Representation of Hamiltonian

Based on the idea developed in Ref [114], we use a matrix diagonalization approach to calculate the eigenstates of the system. First, the Hamiltonian \hat{H} must be expressed in matrix form, and the elements are numerically evaluated within some basis. A basis must be the set of (discrete) eigenfunctions of some other integrable Hamiltonian \hat{H}_0 (usually separable system). In most cases, the bases are an infinite set of eigenvectors which constitutes an orthonormal bases of a Hilbert space, and one must truncate the particular basis within some range of energy. With this truncated basis subset, the original Hamiltonian matrix is constructed in the subspace of the Hilbert space, and diagonalization proceeds on the finite matrix. To optimize the number of converged eigenstates, one must choose the best suited basis set for the Hamiltonian. In the semiclassical limit, the Wigner transformed quantity of an eigenstate is more or less localized on the energy surface in the analogous phase space. Then, the overlap between a basis state $|n\rangle$ (where $\hat{H}_0 |n\rangle = e_n |n\rangle$) and an eigenstate $|\Psi_i\rangle$ (where $\hat{H} |\Psi_i\rangle = E_n |\Psi_i\rangle$) gives a negligibly small number if the corresponding two energy surfaces do not cross. If the energy surfaces of the entire truncated basis set completely cover the energy surface of eigenstate, it will be well converged in the calculation.

To proceed with the matrix diagonalization of two-dimensional coupled quartic oscillators, it is suitable to choose the two-dimensional *uncoupled* quartic oscillator as the basis. Once the eigenstates are represented in terms of the truncated basis set, the uncoupled sys-

tem is just the direct product of two one-dimensional systems. To be more explicit, consider the two-dimensional quartic oscillator given in Eq. (10.1)

$$\hat{H} = \frac{\hat{p}^2}{2} + a(\lambda) \left[\frac{x^4}{b} + by^4 + 2\lambda x^2 y^2 \right], \quad (10.21)$$

and the Hamiltonian which gives the basis as

$$\hat{H}_0 = \frac{\hat{p}^2}{2} + a(\lambda) \left[\frac{x^4}{b} + by^4 \right]. \quad (10.22)$$

This is easily separated into two Hamiltonians

$$\hat{H}_0 = \hat{H}_x + \hat{H}_y \quad (10.23)$$

where

$$\hat{H}_x = \frac{\hat{p}_x^2}{2} + \frac{a}{b} x^4 \quad (10.24)$$

$$\hat{H}_y = \frac{\hat{p}_y^2}{2} + aby^4. \quad (10.25)$$

The last step is to compute the one-dimensional quartic oscillator eigenstates in terms of harmonic oscillator basis. Let us consider the following one-dimensional Hamiltonians

$$\hat{H}_{\text{Q.O.}} = \frac{\hat{p}^2}{2} + cq^4 \quad (10.26)$$

$$\hat{H}_{\text{H.O.}} = \frac{\hat{p}^2}{2} + \frac{\omega^2 q^2}{2}. \quad (10.27)$$

The advantage of employing the harmonic oscillator is that all of the necessary information and analytical expressions are known. Using the properties of the ladder operator \hat{a} and \hat{a}^\dagger , the matrix elements of $\hat{H}_{\text{Q.O.}}$ are given as

$$\begin{aligned} \langle m | \hat{H}_{\text{Q.O.}} | n \rangle = & \frac{c}{4\omega^2} \left(\sqrt{n(n-1)(n-2)(n-3)} \delta_{m,n-4} \right. \\ & + \left[2(2n-1) - \frac{\omega^3}{c} \right] \sqrt{n(n-1)} \delta_{m,n-2} \\ & + \left[6n^2 + \left(3 + \frac{\omega^3}{c} \right) (2n+1) \right] \delta_{m,n} \\ & + \left[2(2n+3) - \frac{\omega^3}{c} \right] \sqrt{(n+1)(n+2)} \delta_{m,n+2} \\ & \left. + \sqrt{(n+1)(n+2)(n+3)(n+4)} \delta_{m,n+4} \right). \end{aligned} \quad (10.28)$$

The bases are optimized with the appropriate angular frequency ω ; see Appendix C for details.

For the two-dimensional quartic oscillator system, one decomposes the original $N \times N$ matrix into four submatrices with the reduced dimension of $N/4$ since the wave functions are classified into four parity sequences. The resulting eigenstates are constructed in terms of the basis having the same parity sequence.

10.3.2 Spectra

To study the dynamical properties of the quantum mechanical quartic oscillator, we investigate systems in three different regimes classified with the mode coupling constant λ . Although the chaotic nature of a quantum system is difficult to define, the system's classical counterpart can characterize the degree of chaos (or regularity of the system). Thus, based on the behavior of the surfaces of section (see Ref. [114]), we choose $\lambda = -0.05, -0.35$, and -0.55 for near integrability, mixed, and chaotic systems respectively.

For some time, random matrix theory (RMT) has been applied to the study of compound nuclear models, and it has successfully described the excited states of such many-body strongly interacting systems. Approximately twenty years ago, this was generalized according to the Bohigas-Giannoni-Schmit conjecture [64]. It asserts that the energy level fluctuations of a single-particle quantum system whose classical analogue shows chaotic behavior can also be interpreted within the context of RMT [109]. It predicts statistics for generic chaotic systems depending only on the symmetry of the system [31–34, 112]. To illustrate “degree of chaos” in quantum systems, we show the number variance statistics of the energy spectra (see Appendix D) and compare with the Poisson and Gaussian orthogonal ensemble (GOE) statistics. When the system is in the chaotic regime, the corresponding RMT statistics are represented by the GOE since the systems preserve time reversal symmetry. On the other hand, the Poisson statistics [110] gives a reference for integrability.

To compare the fluctuations of two spectra from different systems, one must first remove the effects of the global, smooth behavior of the level density; i.e. the energy spectra must

be unfolded [111]. Unfolding proceeds by mapping the original spectra $\{E_i\}$ onto $\{E'_i\}$ by $E'_i = \bar{N}(E_i)$; see Eq. (10.15) to (10.19). As a result of this mapping, unfolded spectra $\{E'_i\}$ have the same average part $\bar{N}(E'_i) = E'_i$, and the mean level spacing becomes unity. This process is necessary especially when one considers the statistics of ensemble or spectral averages. For the quantum quartic oscillator system, we use analytical results Eq. (10.19) to unfold the energy spectra in each parity sequence.

Figure (10.1) shows the number variance statistics $\Sigma^2(r)$ of the spectra for the three dynamical systems; see Appendix D for $\Sigma^2(r)$. Dropping off the first 200 spectra, the statistics are computed using the data from $i = 201$ to 600 (500 for $\lambda = -0.05$). With the reference lines of Poisson and GOE statistics, one can observe that for the near integrable case ($\lambda = -0.05$), the curve due to the spectral fluctuation is located close to the Poisson; for the chaotic case ($\lambda = -0.55$), the curve is on the GOE reference line (except for some known dynamical effects for $r > 1$); and for the mixed case ($\lambda = -0.35$), the data is in between the two reference curves. These behaviors coincide with the classical study of the surfaces of section as expected; see figures in Ref. [114].

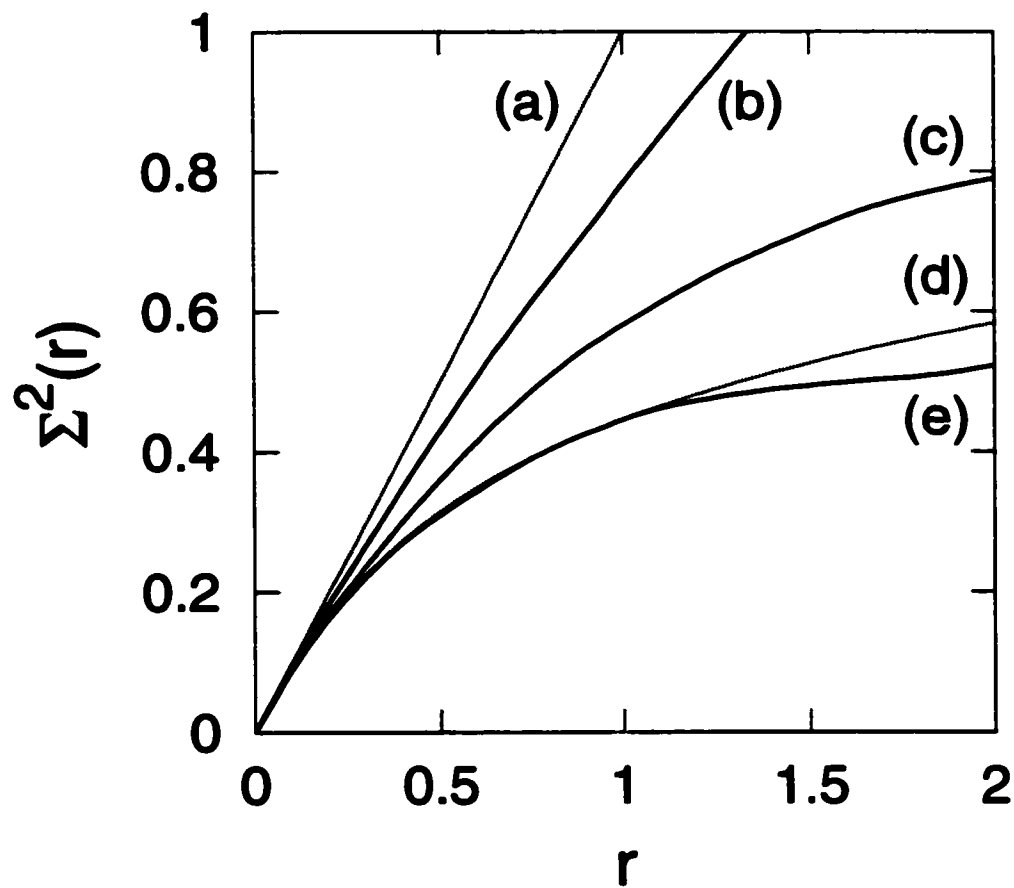


Figure 10.1: Number Variance $\Sigma^2(r)$ versus r . (a) Poisson, (b) $\lambda = -0.05$, (c) $\lambda = -0.35$, (d) GOE, and (e) $\lambda = -0.55$. Poisson and GOE results are displayed for the sake of comparison.

10.4 Residual Interaction: Study of M_{ij}

10.4.1 Local Approximation to the Screened Potential

Before we start investigating the behavior of the residual interaction, let us consider the property of the screened potential. According to the Strutinsky method, the relation

$$\int d\mathbf{r}' \frac{\delta V_{\text{eff}}}{\delta n}(\mathbf{r}, \mathbf{r}') \delta n(\mathbf{r}') = \int d\mathbf{r}' V_{\text{sc}}(\mathbf{r}, \mathbf{r}') \tilde{n}^{\text{osc}}(\mathbf{r}') \quad (10.29)$$

serves as the definition of the screened potential, and we recall the closure equation for δn

$$\int d\mathbf{r}' \frac{\delta V_{\text{eff}}}{\delta n}(\mathbf{r}, \mathbf{r}') \delta n(\mathbf{r}') + \int d\mathbf{r}' \frac{\delta^2 \mathcal{T}_{\text{TF}}}{\delta n^2}(\mathbf{r}, \mathbf{r}') [\delta n(\mathbf{r}') - \tilde{n}^{\text{osc}}(\mathbf{r}')] = \Delta\mu \quad (10.30)$$

where $\delta n = n_{\text{DFT}} - n_{\text{GTF}}$ and $\Delta\mu = \mu_{\text{DFT}}^W - \mu_{\text{GTF}}$. It should be noted that the second order functional derivatives are given as follows,

$$\frac{\delta^2 \mathcal{T}_{\text{TF}}}{\delta n^2}(\mathbf{r}, \mathbf{r}') = \frac{\delta(\mathbf{r} - \mathbf{r}')}{\rho^W(\mathbf{r})}, \quad (10.31)$$

and the potential contribution,

$$\frac{\delta V_{\text{eff}}}{\delta n}(\mathbf{r}, \mathbf{r}') = \frac{\delta^2 E_{\text{tot}}}{\delta n^2}(\mathbf{r}, \mathbf{r}') = \frac{e^2}{|\mathbf{r} - \mathbf{r}'|} \equiv V_{\text{coul}}(\mathbf{r} - \mathbf{r}'). \quad (10.32)$$

Recalling the definition $E_{\text{tot}}[n] = E_{\text{ext}}[n] + E_{\text{coul}}[n] + E_{\text{xc}}[n]$, the second equality in Eq. (10.32) holds for the following reasons. The confinement energy is independent of the electron

density, and energy due to the exchange-correlation is approximated by taking the exact results for the uniform electron gas (local density approximation). Thus, both contributions vanish when the second derivatives are taken, and what is left is the Coulomb interaction energy functional. Introducing the following Fourier transforms

$$\hat{V}_{\text{coul}}(\mathbf{k}) = \int d\mathbf{r} e^{-i\mathbf{k}\cdot\mathbf{r}} V_{\text{coul}}(\mathbf{r}) \quad (10.33)$$

$$\delta\hat{n}(\mathbf{k}) = \int d\mathbf{r} e^{-i\mathbf{k}\cdot\mathbf{r}} \delta n(\mathbf{r}) \quad (10.34)$$

$$\hat{n}^{\text{osc}}(\mathbf{k}) = \int d\mathbf{r} e^{-i\mathbf{k}\cdot\mathbf{r}} \tilde{n}^{\text{osc}}(\mathbf{r}) \quad (10.35)$$

$$\hat{V}_{\text{sc}}(\mathbf{k}) = \int d\mathbf{r} e^{-i\mathbf{k}\cdot\mathbf{r}} V_{\text{sc}}(\mathbf{r}), \quad (10.36)$$

convolutions of Eqs. (10.29) and (10.30) become

$$\frac{1}{(2\pi)^d} \int d\mathbf{k} e^{i\mathbf{k}\cdot\mathbf{r}} \hat{V}_{\text{coul}}(\mathbf{k}) \delta\hat{n}(\mathbf{k}) = \frac{1}{(2\pi)^d} \int d\mathbf{k} e^{i\mathbf{k}\cdot\mathbf{r}} \hat{V}_{\text{sc}}(\mathbf{k}) \hat{n}^{\text{osc}}(\mathbf{k}) \quad (10.37)$$

$$\frac{1}{(2\pi)^d} \int d\mathbf{k} e^{i\mathbf{k}\cdot\mathbf{r}} \hat{V}_{\text{coul}}(\mathbf{k}) \delta\hat{n}(\mathbf{k}) + \frac{1}{(2\pi)^d} \int d\mathbf{k} e^{i\mathbf{k}\cdot\mathbf{r}} \frac{\delta\hat{n}(\mathbf{k}) - \hat{n}^{\text{osc}}(\mathbf{k})}{\rho^W(\mathbf{r})} = \Delta\mu \int d\mathbf{k} e^{i\mathbf{k}\cdot\mathbf{r}} \delta(\mathbf{k}). \quad (10.38)$$

where d is dimensionality of system, and $V_{\text{sc}}(\mathbf{r} - \mathbf{r}')$ is assumed. Then, the Fourier transform of the screened potential is obtained as

$$\hat{V}_{\text{sc}}(\mathbf{k}) = \frac{\hat{V}_{\text{coul}}(\mathbf{k})}{1 + \rho^W(\mathbf{r}) \hat{V}_{\text{coul}}(\mathbf{k})}. \quad (10.39)$$

For the two-dimensional system, one has

$$\hat{V}_{\text{coul}}(\mathbf{k}) = \frac{2\pi e^2}{|\mathbf{k}|} \quad (10.40)$$

$$\rho^W = \frac{g_s m}{2\pi \hbar^2}, \quad (10.41)$$

where g_s is the electron spin degree of freedom, and the screened potential is written as

$$\hat{V}_{\text{sc}}(\mathbf{k}) = \frac{a_0}{a_0 + k^{-1}} \hat{V}_{\text{coul}}(\mathbf{k}) = \frac{2\pi e^2}{|\mathbf{k}| + a_0^{-1}}. \quad (10.42)$$

where $a_0 = \hbar^2/me^2$ is Bohr radius. The rightmost quantity recovers the Thomas-Fermi approximation to the screened potential in two-dimension. There are two limiting cases for the potential,

$$\hat{V}_{\text{sc}}(\mathbf{k}) \simeq \hat{V}_{\text{coul}}(\mathbf{k}) \quad (\text{for } |\mathbf{k}|^{-1} \ll a_0) \quad (10.43)$$

$$\hat{V}_{\text{sc}}(\mathbf{k}) \simeq \frac{1}{\rho^W} \quad (\text{for } |\mathbf{k}|^{-1} \gg a_0). \quad (10.44)$$

For the case of the length scale $|\mathbf{k}|^{-1} \gg a_0$, inverse Fourier transform gives

$$V_{\text{sc}}(\mathbf{r}, \mathbf{r}') = \frac{\delta(\mathbf{r} - \mathbf{r}')}{\rho^W}, \quad (10.45)$$

and we call this regime as the local approximation to the screened interaction. For the experimentally relevant electronic densities, the screened interaction must be treated as a

short range potential, and in this report, we study the behavior of M_{ij} focusing on this limit by

$$V_{sc}(\mathbf{r}, \mathbf{r}') = \frac{\zeta}{\rho W} \delta(\mathbf{r} - \mathbf{r}') \quad (10.46)$$

where $0 \leq \zeta \leq 1$. Since δ -function makes the interaction local, the direct and exchange energies are combined, and the modified residual interaction is given as

$$\begin{aligned} \frac{1}{2} \sum_{i,j;\sigma,\sigma'} n_{i\sigma} M_{ij} n_{j\sigma'} - \frac{1}{2} \sum_{i,j;\sigma} n_{i\sigma} N_{ij} n_{j\sigma} &= \frac{1}{2} \sum_{i,j;\sigma,\sigma'} \int d\mathbf{r} d\mathbf{r}' |\phi_i(\mathbf{r})|^2 V_{sc}(\mathbf{r} - \mathbf{r}') |\phi_j(\mathbf{r}')|^2 \\ &- \frac{1}{2} \sum_{i,j;\sigma=\sigma'} \int d\mathbf{r} d\mathbf{r}' \phi_i(\mathbf{r}) \phi_j^*(\mathbf{r}) V_{sc}(\mathbf{r} - \mathbf{r}') \phi_j(\mathbf{r}') \phi_i^*(\mathbf{r}') \\ &= \frac{1}{2} \sum_{i,j;\sigma \neq \sigma'} M_{ij} \end{aligned} \quad (10.47)$$

where in the last equality we used

$$M_{ij} = \frac{1}{\rho W} \int d\mathbf{r} |\phi_i(\mathbf{r})|^2 |\phi_j(\mathbf{r}')|^2. \quad (10.48)$$

10.4.2 Numerical Approach to M_{ij}

The constant interaction model, or equivalently Strutinsky scheme with up to the first order correction, deals with the model system of quantum dots based on non-interacting quasi-particle description treating the electron interaction as the classical charging energy. At this level of approximation, electrons occupy orbitals in the standard up/down fillings taken into account the spin degree of freedom. For an N -electron system, the lowest $N/2$ (for N even, and $(N+1)/2$ for odd case) orbitals are occupied. On the other hand, with the inclusion

of the residual interaction, it is expected that the situation is no longer the same, and the system seeks the orbital configuration which gives the lowest possible energy by exciting some of the electrons to higher states. For this to happen, the size of the residual interaction must be large enough so that it is comparable to the single-particle mean level spacing of the system. If the effects of the residual interaction are small, a transition from the CI model predictions will not occur. Therefore, it is important to carefully study the matrix elements M_{ij} .

Given the eigenstates of the coupled quartic oscillator confined system, one constructs the matrix elements M_{ij} based on Eq. (10.48), and the systems in three coupling regimes are considered: $\lambda = -0.05$ (near integrable), -0.35 (mixed), and -0.55 (chaotic). In Fig. (10.2), (10.3), and (10.4), the M_{ij} matrix elements from $i, j = 401$ to 500 are plotted for $\lambda = -0.05, -0.35, -0.55$ respectively. The overlap of wavefunctions is enhanced when nodes of two wavefunctions coincide with each other, and so the diagonal elements give larger peaks than the off-diagonals. In Fig. (10.5), the diagonal elements are plotted as a function of orbital number i . The data are scaled by the single-particle mean level spacing Δ_i , and demonstrate that the size is comparable to the level spacing; see Table (10.1). There lies the cause of the CI model failure. For all three cases, the scaled M_{ii} rapidly increase as i changes from 1 to 200, then becomes stable for $i > 200$. There exists a lower bound for all cases near $M_{ii} \simeq 1.5$. The peaks are more pronounced as the coupling is decreased (as the system becomes less chaotic). The distribution of the scaled M_{ii} elements are shown in Fig. (10.6). The peaks in M_{ii} make the fluctuations larger, and lead to larger widths for the distribution.

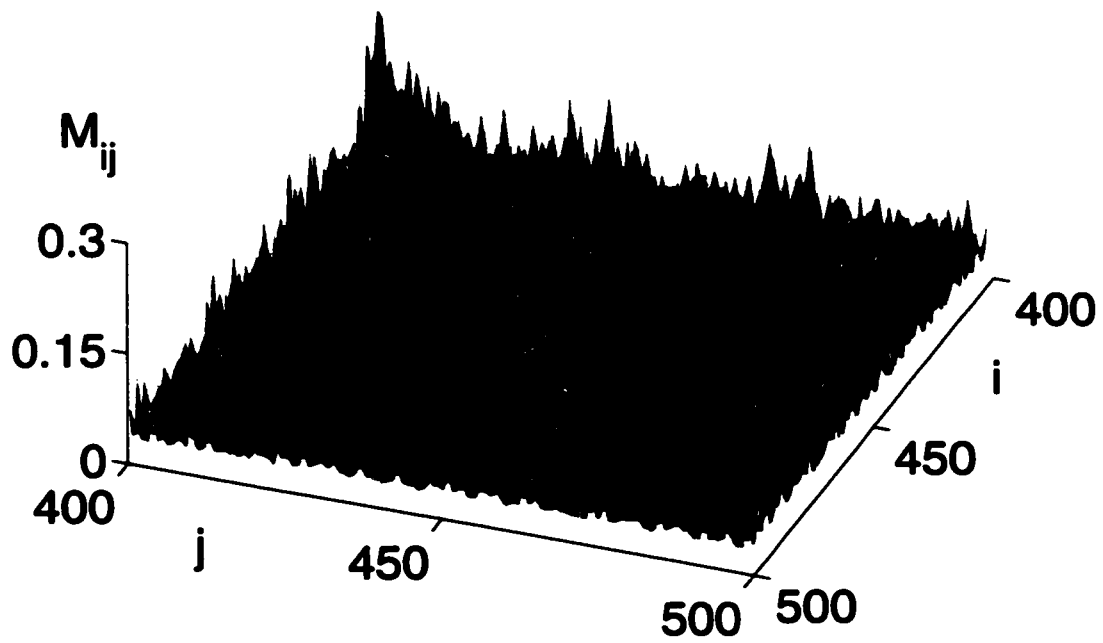


Figure 10.2: The matrix elements M_{ij} are plotted for the TRI system with the coupling constant $\lambda = -0.05$. M_{ij} is not scaled by mean level spacing in this figure. The ranges of index are $i, j = 401$ to 500 .

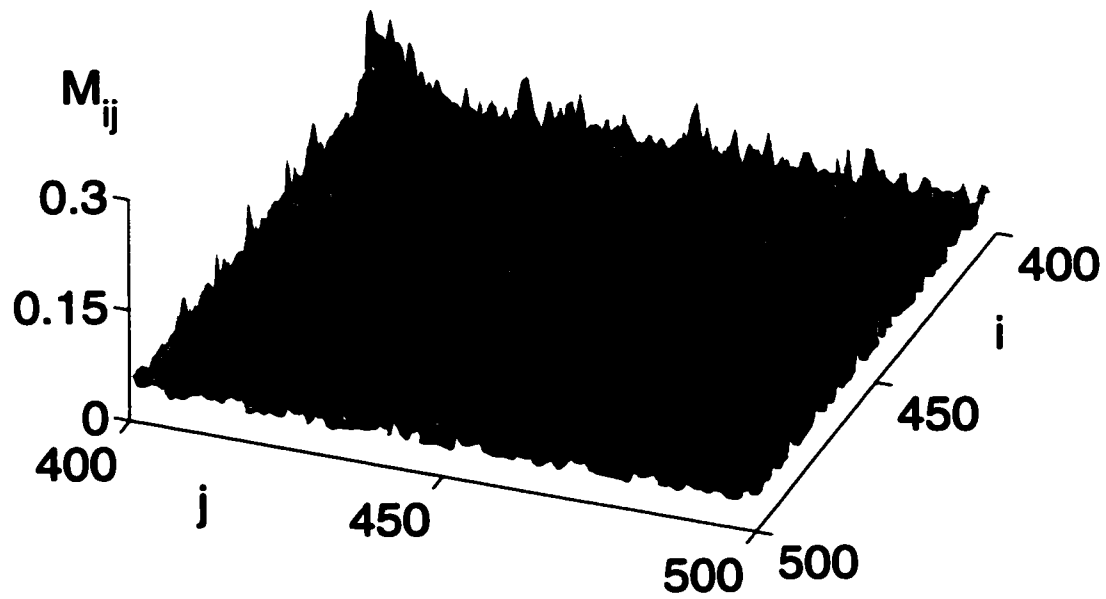


Figure 10.3: The matrix elements M_{ij} are plotted for the TRI system with the coupling constant $\lambda = -0.35$. M_{ij} is not scaled by mean level spacing in this figure. The ranges of index are $i, j = 401$ to 500 .

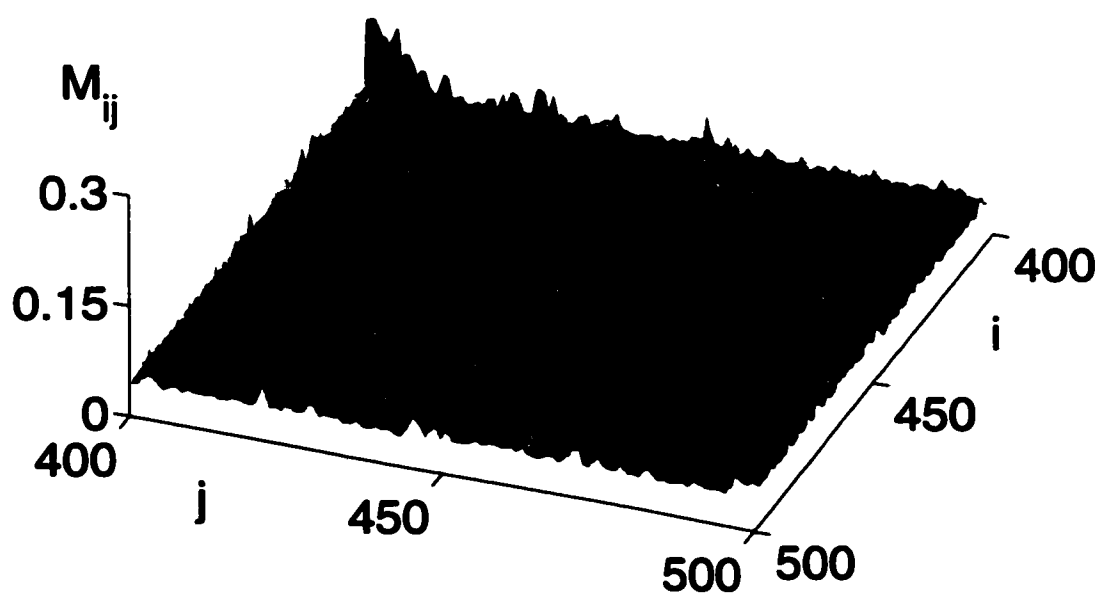


Figure 10.4: The matrix elements M_{ij} are plotted for the TRI system with the coupling constant $\lambda = -0.55$. M_{ij} is not scaled by mean level spacing in this figure. The ranges of index are $i, j = 401$ to 500 .

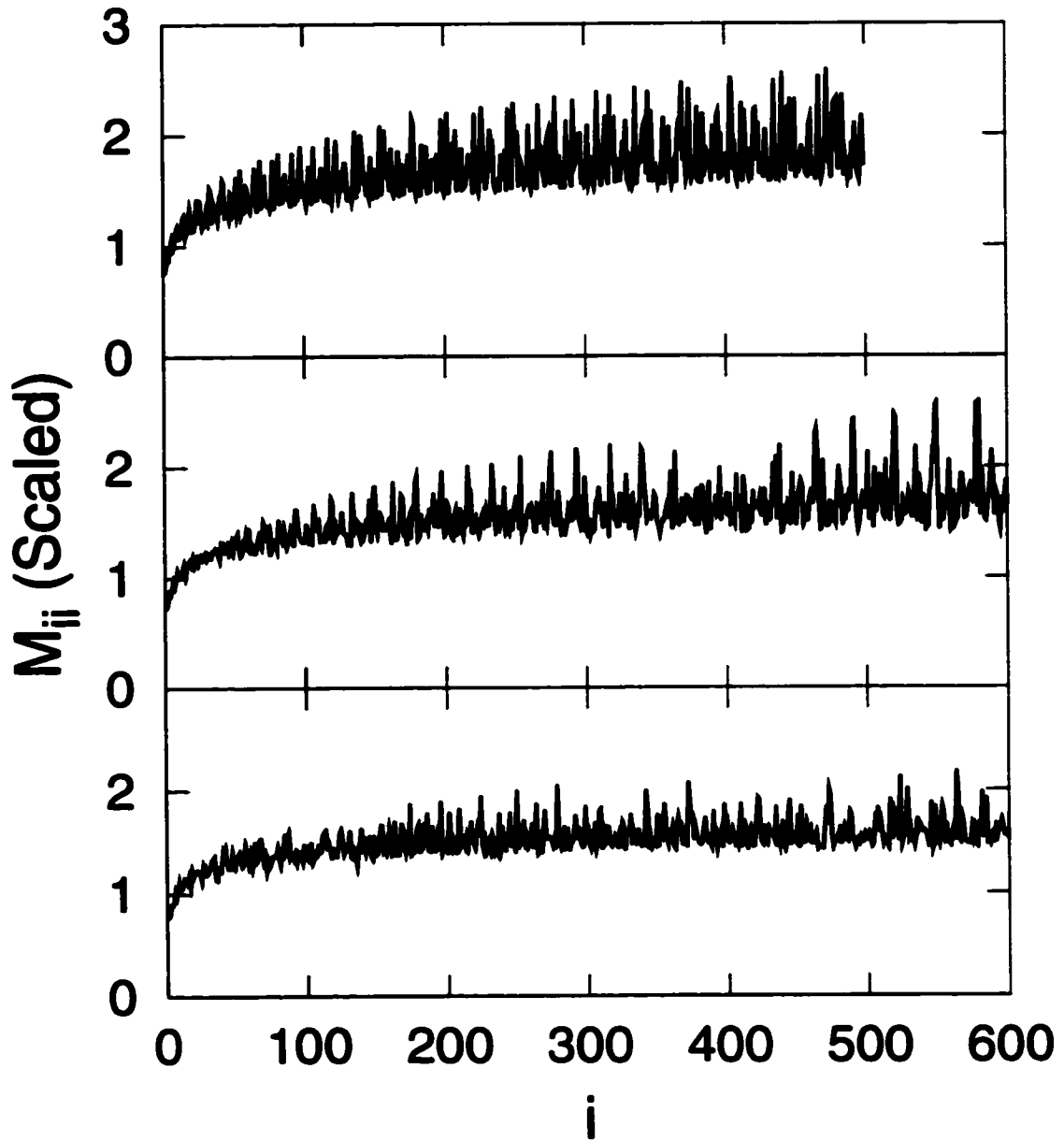


Figure 10.5: Diagonal elements of M_{ij} ($i = j$) versus orbital number i . M_{ii} are scaled by the single-particle mean level spacing of orbitals. Top figure: coupling constant $\lambda = -0.05$, middle: $\lambda = -0.35$, and bottom: $\lambda = -0.55$. Data are available for the lowest 600 (500 for $\lambda = -0.05$) orbitals.

Moments	Integrable	Mixed	Chaotic
1	1.800051	1.654756	1.575006 [1.5]
2	6.718166×10^{-2} ($\sigma = 0.2591942$)	5.127600×10^{-2} ($\sigma = 0.2264420$)	2.002593×10^{-2} [3.896926×10^{-2}] ($\sigma = 0.1415130$)
3	1.851345×10^{-2} ($\gamma_1 = 1.063191$)	1.850391×10^{-2} ($\gamma_1 = 1.593647$)	4.177686×10^{-3} ($\gamma_1 = 1.474167$)
4	1.456817×10^{-2} ($\gamma_2 = 0.2277764$)	1.595251×10^{-2} ($\gamma_2 = 3.067373$)	2.098844×10^{-3} ($\gamma_2 = 2.233531$)

Table 10.1: Moments of scaled M_{ii} distribution for quartic oscillator system (TRI). First four moments are calculated for the near-integrable, mixed, and chaotic regimes. Standard deviation σ , skewness γ_1 , and kurtosis γ_2 are also computed for each related moment. The values in the square brackets are obtained by the analytical expressions with $N = 500$ given in Appendix F. All the higher moments (≥ 3) vanish in the large N limit according to Ullmo and Baranger [94].

In addition, it gives the long right tail especially for the near integrable case $\lambda = -0.05$. As the chaoticity is increased, the peak values are decreased and the distribution width and tails becomes smaller. On the other hand, the off-diagonal elements M_{ij} with $0 < |i - j| < 5$ (near diagonal) show smaller means and deviations. The means are roughly 3 times smaller than the diagonal; see Fig. (10.7) for the distributions. Now, to understand some of the behavior of diagonal elements, let us look at the eigenstates shown in Fig. (10.8). There are six wavefunctions plotted, and all of them belong to about the same energy range giving the eigenenergy $\epsilon_i \sim 52.0$. While the three states in the right column ($\lambda = -0.05, -0.35, -0.55$ from top to bottom) have node spreading roughly over classically allowed regions, the other three states in the left column are spatially localized having many fewer nodes in y -direction (vertical direction in figure). Since the diagonal elements are calculated with the fourth

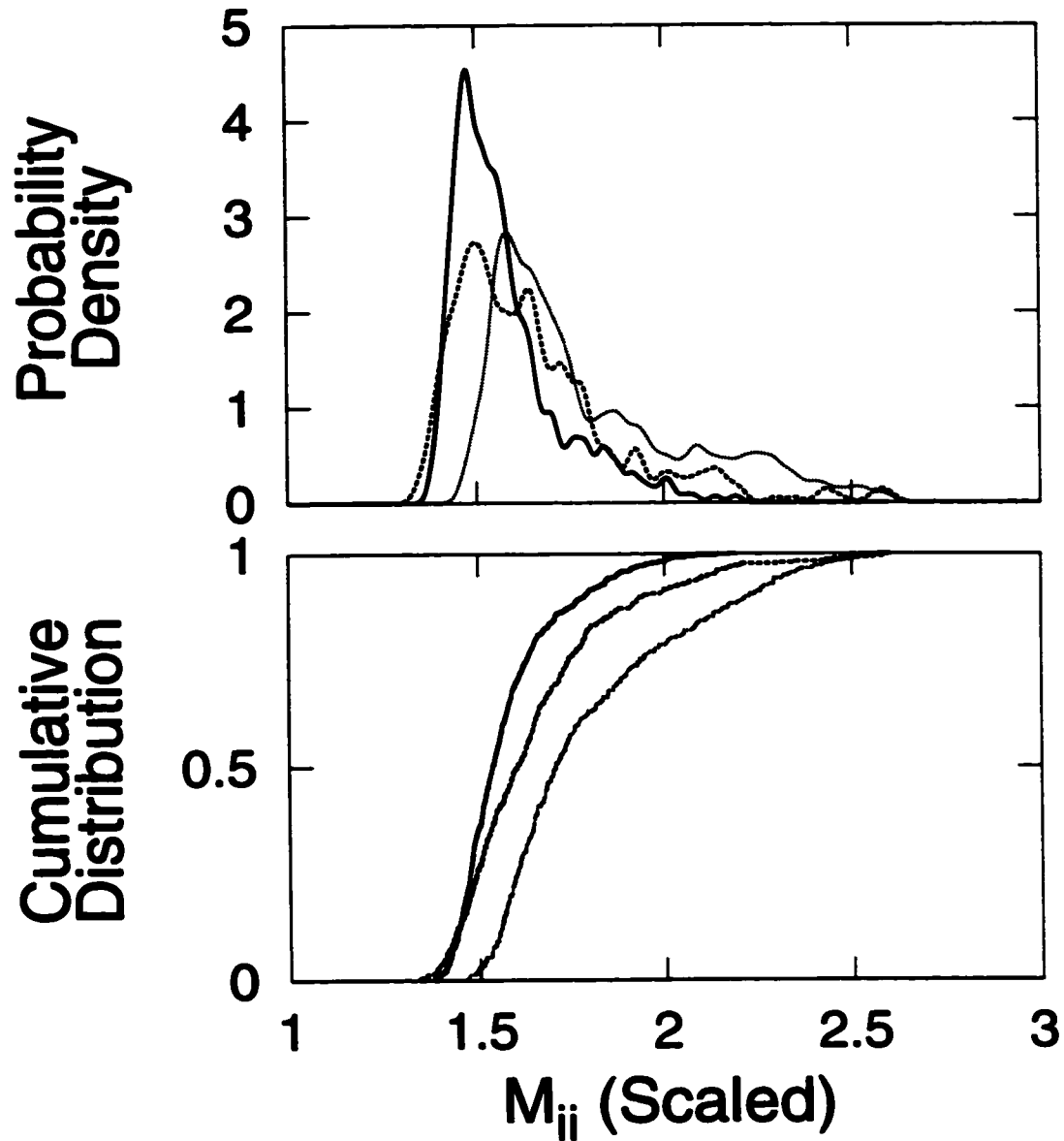


Figure 10.6: Distribution of diagonal elements M_{ii} . M_{ii} are scaled by the single-particle mean level spacing of orbitals. Top figure: probability density, bottom: cumulative distribution. For both figures, $\lambda = -0.05, -0.35$, and -0.55 are represented by dotted, dashed, and solid lines respectively.

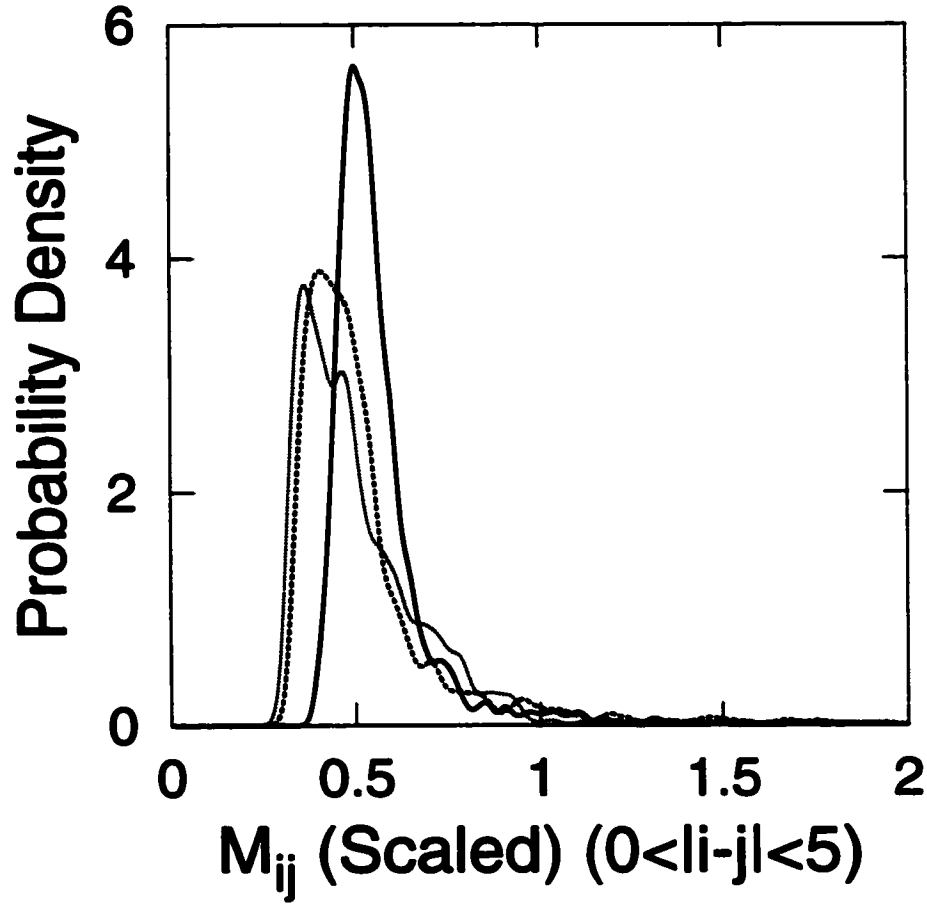


Figure 10.7: Distribution (probability density) of off-diagonal elements M_{ij} . M_{ij} are scaled by the single-particle mean level spacing of orbitals Δ_i . Only the near diagonal elements ($0 < |i - j| < 5$) are used. $\lambda = -0.05, -0.35$, and -0.55 are represented by dotted, dashed, and solid lines respectively.

power of the wavefunctions, the localized states give large values once they are integrated. The lower bound seen in Fig. (10.5) are given by the states similar to the eigenstates in the right column. In the chaotic regime, the eigenstates are more likely to be smeared out over the coordinate space, and the localization becomes weaker than it would be for more regularized systems. As a result, less pronounced peaks are observed.

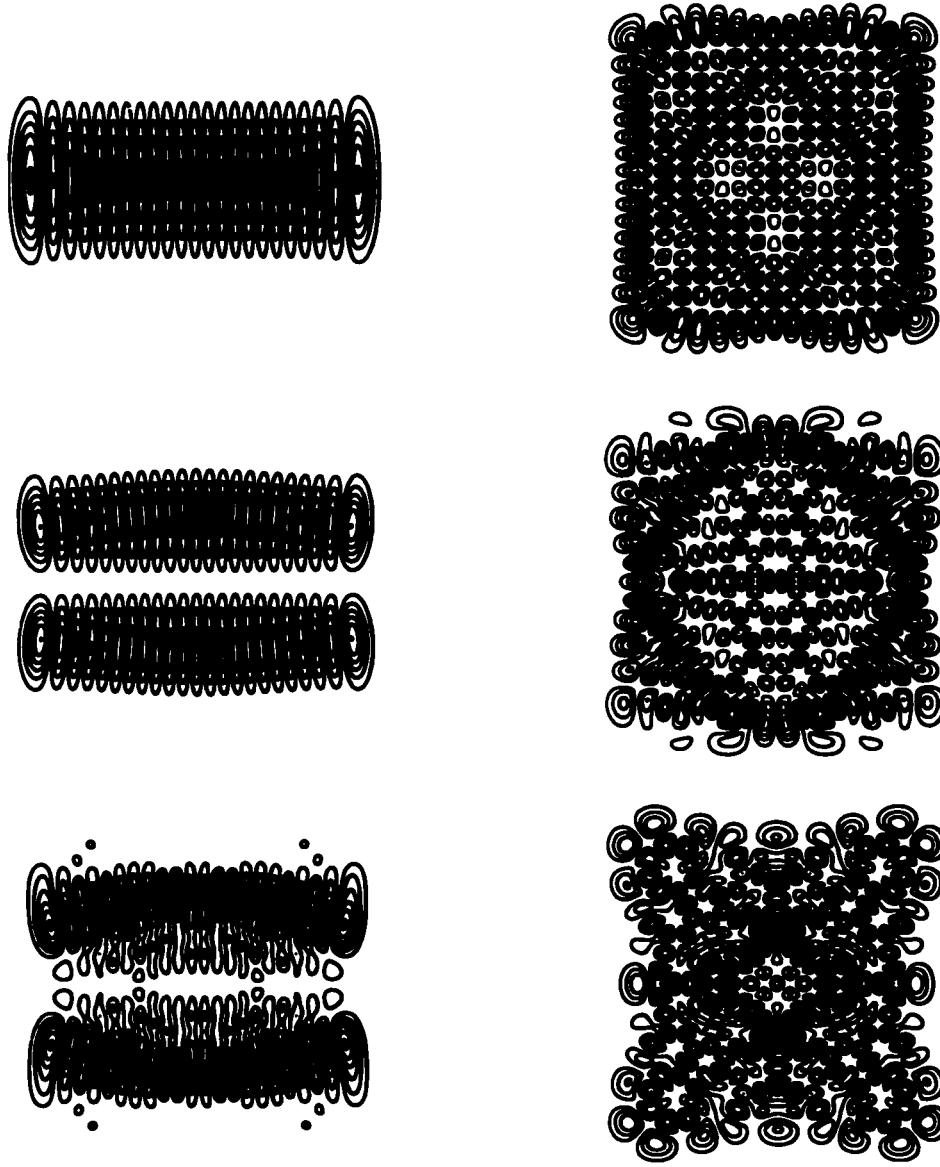


Figure 10.8: Coupled quartic oscillator eigenstates (contour levels are equidistant). While the states in the left column lead to high peaks in M_{ii} , the ones in right column give the lower bound values. Top row ($\lambda = -0.05$): the 99th eigenstate in $(+,+)$ sequence giving $M_{ii}/\Delta_i = 2.4746$ (left), the 101th state in $(+,-)$ sequence giving $M_{ii}/\Delta_i = 1.5584$ (right). Middle row ($\lambda = -0.35$): the 99th state in $(+,-)$ sequence giving $M_{ii}/\Delta_i = 1.9974$ (left), the 95th state in $(-,+)$ sequence giving $M_{ii}/\Delta_i = 1.5446$ (right). Bottom row ($\lambda = -0.55$): the 88th eigenstate in $(-,-)$ sequence giving $M_{ii}/\Delta_i = 2.0813$ (left), the 99th state in $(+,+)$ sequence giving $M_{ii}/\Delta_i = 1.4403$ (right).

Chapter 11

Breaking anti-unitary symmetry

11.1 Anti-Unitary Symmetries

Although the transition from GOE to GUE (Gaussian unitary ensemble) is well known in the context of RMT [113], our interest here is to understand statistical behavior of explicitly defined dynamical systems whose energy level fluctuations correspond to the GUE. Applying magnetic fields to classically chaotic systems makes the system time-reversal non-invariant. However, this is not enough to ensure GUE statistics [115]. Let us consider the two-dimensional system confined in the xy -plane, having a magnetic field applied in the perpendicular z -direction. The Hamiltonian includes a term like $B(y p_x - x p_y)$ where B represents the magnetic field. It breaks the time-reversal symmetry. However, the combined operations of time-reversal and spatial reflection leave the system invariant. These actions can be viewed as reversing the direction of magnetic field and turn the system upside down. It recovers exactly the same previous situation. Therefore one cannot expect the energy spectra of this system to lead to GUE statistics. To achieve this, one needs to break all anti-unitary symmetries. Any combinations of spatial reflection (unitary) with time-reversal (anti-unitary) constitutes an anti-unitary operation. For example, in a Cartesian coordinate

system, the spatial reflections are

$$P_x : x \rightarrow -x, p_x \rightarrow -p_x \quad (11.1)$$

$$P_y : y \rightarrow -y, p_y \rightarrow -p_y \quad (11.2)$$

and the time-reversal operation is

$$T : p_x \rightarrow -p_x, p_y \rightarrow -p_y . \quad (11.3)$$

Excluding difficult to discover dynamical symmetries, the possible anti-unitary operations are T , TP_x , TP_y , and TP_xP_y since each operation commutes, and contributions only come from an odd number of operations. xp_x and yp_y are the simplest terms to break the anti-unitary symmetries. These terms multiplied by functions of the following quantities, p_x^{2a} , p_y^{2b} , x^{2c} , and y^{2d} where a, b, c, d are integers, break symmetries as well.

11.2 Hamiltonian of System

Based on the previous two-dimensional coupled quartic oscillator Eq. (10.21), we add a new term and modify the confining potential to break all anti-unitary symmetries within the system. There are some constraints needed to be satisfied besides breaking the symmetries: preservation of all reflection symmetries, homogeneity, Hermiticity, level density, and energy scaling properties should remain unchanged. Having reflection symmetries allow us to clas-

sify the resulting quantum states into four parity groups. This is not only for computational convenience, but also for statistical considerations. We will treat four parity classes as completely independent systems, which will be discussed later in more detail. Other constraints are necessary to utilize the results of the quartic oscillator study [114].

We find that the following modified Hamiltonian meets all the requirements,

$$\hat{H} = \frac{\hat{p}^2}{2} + a(\lambda) \left[\left(\frac{1}{b} + \frac{\epsilon^2}{2} \right) x^4 + by^4 + 2\lambda x^2 y^2 \right] + \frac{\epsilon}{2} \sqrt{a(\lambda)} (r\hat{p}_r r + \hat{p}_r r^2) \cos^2 \theta \quad (11.4)$$

where $\hbar = m = 1$, and $\hat{p}_r = \hat{p}_x \cos \theta + \hat{p}_y \sin \theta$. ϵ represents the strength of anti-unitary symmetry breaking (third term), and when $\epsilon \rightarrow 0$, the previous Hamiltonian (GOE) is recovered. In the classical limit of this operator, the modified coefficient $\epsilon^2/2$ on x^4 guarantees that the semiclassical level density expression is kept unchanged. The third term can be included in $p_r^2 + \epsilon^2 a x^4$ when completing the square. Thus, the classical Hamiltonian is given as

$$H = \frac{1}{2} \left(\mathbf{p} + \epsilon \sqrt{a} x^2 \frac{\mathbf{r}}{r} \right)^2 + a \left[x^4/b + by^4 + 2\lambda x^2 y^2 \right]. \quad (11.5)$$

The only change is a shift in radial direction of momentum, and this does not alter the behavior of the level density when integrating over all space. $(r\hat{p}_r r + \hat{p}_r r^2)/2$ simply makes the system Hermitian. In the classical limit, the equations of motion cancel the effect of the symmetry breaking without $\cos^2 \theta$, and they become invariant under some anti-unitary operation. Inclusion of $\cos^2 \theta$ avoids this cancellation and keeps the system non-invariant

under any operation. The equations of motions are

$$\ddot{x} = -4a \left(\frac{x^3}{b} + \lambda xy^2 \right) - \frac{2\epsilon\sqrt{a} xy\dot{y}}{\sqrt{x^2 + y^2}} \quad (11.6)$$

$$\ddot{y} = -4a (by^3 + \lambda x^2y) + \frac{2\epsilon\sqrt{a} x\dot{x}y}{\sqrt{x^2 + y^2}} \quad (11.7)$$

where $xy\dot{y}$ and $x\dot{x}y$ make the system anti-unitary non-invariant. We have two dynamical systems having different symmetry properties. One is the coupled quartic oscillator system studied in the last chapter without an anti-unitary symmetry breaking term. We denote this as the TRI (time reversal invariant) system. The other is the quartic oscillator system with the symmetry breaking term. We denote this as the TRNI (time reversal non-invariant) system. However, it has to be mentioned that the time reversal symmetry is just one of the anti-unitary symmetry classes, and we use this short hand notation mainly for convenience.

11.3 Numerical Calculations: Energy Spectra

To solve the time-independent Schrödinger equation for the system, we construct a numerical Hamiltonian matrix using the harmonic oscillator basis, and then diagonalize it to obtain the energy spectra and wave functions. It is suitable to work in the polar coordinate system because of the form of the symmetry breaking term, especially for the radial direction of momentum operator \hat{p}_r . While many introductory quantum mechanics books deal with harmonic oscillator in Cartesian coordinate, its radial basis studies are rare. Instead, they can be found in the nuclear physics literature dealing with isotropic potentials [116–120].

11.3.1 Radial harmonic oscillator basis

Adapting the study of Bera *et al.* [116] in the N -dimensional harmonic oscillator, we set $N = 2$ and modify their results to fit our system. Starting with the time-independent Schrödinger equation for the two-dimensional isotropic harmonic potential, one obtains differential equations for the radial and angular coordinates,

$$\left[-\frac{1}{2}\nabla^2 + V(\mathbf{r}) \right] \phi = E\phi \implies \quad (11.8)$$

$$\left[\frac{d^2}{dr^2} + \frac{1}{r} \frac{d}{dr} + 2E_{n,\alpha} - 2V(r) - \frac{\alpha^2}{r^2} \right] R_{n,\alpha}(r) = 0 \quad (11.9)$$

$$\frac{d^2\Theta_\alpha}{d\theta^2} + \alpha^2\Theta_\alpha = 0 \quad (11.10)$$

where $\phi_{n,\alpha}(\mathbf{r}) = R_{n,\alpha}(r) \cdot \Theta_\alpha(\theta)$ and $V(\mathbf{r}) = \omega^2 r^2/2$. The normalized solutions are,

$$R_{n,\alpha} = \sqrt{\frac{2n!}{(n+\alpha)!}} \omega^{(\alpha+1)/2} r^\alpha e^{-\omega r^2/2} L_n^\alpha(\omega r^2) \quad (11.11)$$

$$\Theta_\alpha = \frac{e^{i\alpha\theta}}{\sqrt{2\pi}} \quad (11.12)$$

where $E_{n,\alpha} = (2n + \alpha + 1)\omega$, $n \geq 0, \alpha \geq -n$, and L_n^α is a Laguerre polynomial. For $\alpha < 0$, Laguerre polynomials satisfy [122],

$$L_n^\alpha(x) = \frac{(n+\alpha)!}{n!} (-x)^\alpha L_{n+\alpha}^{-\alpha}(x) \quad (11.13)$$

or in more convenient form

$$R_{n,\alpha}(r) = (-1)^\alpha R_{n+\alpha,-\alpha}(r) . \quad (11.14)$$

This relation has the advantage of reducing the order of large n polynomials to $n+\alpha$ ($\alpha < 0$), and decreases the risk of divergence in numerical calculations.

11.3.2 Basis rotation and parity

Since the system retains the reflection symmetries about x and y axis, the eigenstates can be grouped into four parity classes: even-even $(+,+)$, even-odd $(+,-)$, odd-even $(-,+)$, and odd-odd $(-,-)$. It is reasonable to group the basis set into the same parity classes. Let us rotate the basis functions in Hilbert space and define new basis as follows:

$$\phi_{n,\alpha}^\pm \equiv \frac{1}{\sqrt{2}} (\phi_{n-\alpha,\alpha} \pm \phi_{n,-\alpha}) \quad (11.15)$$

$$= \frac{1}{\sqrt{2}} R_{n-\alpha,\alpha} [\Theta_\alpha \pm (-1)^\alpha \Theta_{-\alpha}] \quad (11.16)$$

using Eq. (11.14), or for each parity

$$\text{Even-Even: } \phi_{n,\alpha}^+ = R_{n-\alpha,\alpha} \frac{\cos \alpha \theta}{\sqrt{\pi}} \quad (\alpha \text{ even}) \quad (11.17)$$

$$\text{Even-Odd: } \phi_{n,\alpha}^+ = R_{n-\alpha,\alpha} \frac{\sin \alpha \theta}{\sqrt{\pi}} \quad (\alpha \text{ odd}) \quad (11.18)$$

$$\text{Odd-Even: } \phi_{n,\alpha}^- = R_{n-\alpha,\alpha} \frac{\cos \alpha \theta}{\sqrt{\pi}} \quad (\alpha \text{ odd}) \quad (11.19)$$

$$\text{Odd-Odd: } \phi_{n,\alpha}^- = R_{n-\alpha,\alpha} \frac{\sin \alpha \theta}{\sqrt{\pi}} \quad (\alpha \text{ even}) \quad (11.20)$$

where $n \geq 0$ and $\alpha > 0$, and $\phi_{n,0}^+ = \phi_{n,0}$ for $\alpha = 0$.

11.3.3 Operator recurrence formulas

The ladder operators for the harmonic oscillator have an important role in constructing the numerical Hamiltonian matrix in Cartesian coordinates. They allow us to calculate matrix elements from direct spatial integration to simple manipulation of quantum numbers. For systems in polar coordinate, Swainson and Drake [121] have derived a Laplace-transform method to study the hydrogen atom in three dimensions. Bera *et al.* [116] further developed this method to investigate the N -degree-of-freedom Schrödinger equation and derived the recurrence formulas for the general radial wave functions of the harmonic oscillator and Coulomb problems. Since their theory is valid for systems with $N \geq 3$, we made some modifications to fit systems in two dimensions ($N=2$). Followings are the operator recurrence formulas used in constructing our Hamiltonian system,

$$\left[-\frac{d}{dr} - \frac{\alpha}{r} + \omega r \right] R_{n,\alpha} = -2\sqrt{(n+1)\omega} R_{n+1,\alpha-1} \quad (11.21)$$

$$\left[-\frac{d}{dr} - \frac{\alpha}{r} - \omega r \right] R_{n,\alpha} = -2\sqrt{(n+\alpha)\omega} R_{n,\alpha-1} \quad (11.22)$$

$$\left[\frac{d}{dr} - \frac{\alpha}{r} + \omega r \right] R_{n,\alpha} = -2\sqrt{n\omega} R_{n-1,\alpha+1} \quad (11.23)$$

$$\left[\frac{d}{dr} - \frac{\alpha}{r} - \omega r \right] R_{n,\alpha} = -2\sqrt{(n+\alpha+1)\omega} R_{n,\alpha+1} . \quad (11.24)$$

Position and momentum operators can be expressed as,

$$r = \frac{\hat{a} - \hat{b}}{2\omega} = \frac{\hat{c} - \hat{d}}{2\omega} \quad (11.25)$$

$$\hat{p}_r = -i \frac{d}{dr} = \frac{i(\hat{a} - \hat{c})}{2} = \frac{i(\hat{b} - \hat{d})}{2} \quad (11.26)$$

where

$$\hat{a} = -\frac{d}{dr} - \frac{\alpha}{r} + \omega r \quad (11.27)$$

$$\hat{b} = -\frac{d}{dr} - \frac{\alpha}{r} - \omega r \quad (11.28)$$

$$\hat{c} = \frac{d}{dr} - \frac{\alpha}{r} + \omega r \quad (11.29)$$

$$\hat{d} = \frac{d}{dr} - \frac{\alpha}{r} - \omega r. \quad (11.30)$$

All operators commute except two cases, $[\hat{a}, \hat{c}] = -[\hat{b}, \hat{d}] = -4\omega$. One can easily see that the commutator of position and momentum operators satisfies $[r, \hat{p}_r] = i$.

11.3.4 Matrix representation of Hamiltonian

Let us now solve the time-independent Schrödinger equation. Physical constants \hbar and m are set to unity, and the system is characterized by λ which determines degree of chaoticity and ϵ the strength of symmetry breaking (both negative). While increasing $|\lambda|$ corresponds to increasing the extent of chaos, increasing $|\epsilon|$ regularizes the system. Three dynamical regimes are of interest, near integrable, mixed, and chaotic. Hence, we choose three sets

of values for λ and ϵ , based on the behavior of Poincaré surfaces of section. Our choices are confirmed by a study of the number variance statistics $\Sigma^2(r)$, which will be discussed in section 11.3.5.

The matrix elements are evaluated in terms of the radial harmonic oscillator basis, and bases are optimized choosing an appropriate value for the angular frequency ω (see Appendix C). The construction of the matrix requires the following decomposition. Instead of directly evaluating the kinetic energy operator, we add the isotropic harmonic potential. This is because the eigenvalues are already given, and it is much easier to evaluate the harmonic potential than to calculate the kinetic energy. This artificial addition is adjusted by subtracting off the same harmonic potential. Thus we write,

$$\hat{H} = \hat{H}_0 + \hat{H}_1 \quad (11.31)$$

where

$$\hat{H}_0 = \hat{H}_{H.O} - \frac{\omega^2 r^2}{2} + \hat{V}_{Q.O.} \quad (11.32)$$

$$\hat{H}_1 = \frac{\epsilon}{2} \sqrt{a(\lambda)} (r \hat{p}_r r + \hat{p}_r r^2) \cos^2 \theta. \quad (11.33)$$

The symmetry breaking term is purely imaginary, while the other terms are all real, and

$$\hat{H}_{H.O} = \frac{\hat{p}^2}{2} + \frac{\omega^2 r^2}{2} \quad (11.34)$$

$$\hat{V}_{Q.O.} = a(\lambda) \left[\left(\frac{1}{b} + \frac{\epsilon^2}{2} \right) x^4 + b y^4 + 2\lambda x^2 y^2 \right]. \quad (11.35)$$

Using the orthonormality of the basis, The first term in Eq. (11.32) simply gives eigenvalues of the radial harmonic oscillator,

$$\langle m, \beta | \hat{H}_{H.O} | n, \alpha \rangle = (2n + \alpha + 1) \omega \delta_{n,m} \delta_{\alpha,\beta}. \quad (11.36)$$

The second term in Eq. (11.32) is,

$$\begin{aligned} \left\langle m, \beta \left| \left(-\frac{\omega^2 r^2}{2} \right) \right| n, \alpha \right\rangle &= -\frac{\omega^2}{2} \cdot \frac{1}{2\pi} \int_0^{2\pi} d\theta e^{i(\alpha-\beta)\theta} \cdot \int_0^\infty dr r R_{m,\beta} r^2 R_{n,\alpha} \\ &= -\frac{\omega}{2} \delta_{\alpha,\beta} \left[(2n + \alpha + 1) \delta_{n,m} - \sqrt{(n+1)(n+\alpha+1)} \delta_{n+1,m} - \sqrt{n(n+\alpha)} \delta_{n-1,m} \right], \end{aligned} \quad (11.37)$$

where the operator r^2 acts on $R_{n,\alpha}$ as

$$\begin{aligned} r^2 R_{n,\alpha} &= \frac{1}{4\omega^2} (\hat{a} - \hat{b}) (\hat{c} - \hat{d}) R_{n,\alpha} \\ &= \frac{1}{\omega} \left[(2n + \alpha + 1) R_{n,\alpha} - \sqrt{(n+1)(n+\alpha+1)} R_{n+1,\alpha} - \sqrt{n(n+\alpha)} R_{n-1,\alpha} \right] \end{aligned} \quad (11.38)$$

and the orthonormality of the radial function is expressed as

$$\int_0^\infty dr r R_{m,\alpha} R_{n,\alpha} = \delta_{m,n}. \quad (11.39)$$

The third term, the quartic oscillator, is

$$\begin{aligned}
& \langle m, \beta | \hat{V}_{\text{Q.O.}} | n, \alpha \rangle = \frac{a(\lambda)}{16\omega^2} \\
& \cdot \left(\left(\frac{1}{b} + \frac{\epsilon^2}{2} + b - 2\lambda \right) \delta_{\alpha-4, \beta} \left[\sqrt{(n+1)(n+2)(n+3)(n+4)} \delta_{n+4, m} \right. \right. \\
& \quad - 4\sqrt{(n+1)(n+2)(n+3)(n+\alpha)} \delta_{n+3, m} \\
& \quad + 6\sqrt{(n+1)(n+2)(n+\alpha)(n+\alpha-1)} \delta_{n+2, m} \\
& \quad - 4\sqrt{(n+1)(n+\alpha)(n+\alpha-1)(n+\alpha-2)} \delta_{n+1, m} \\
& \quad \left. + \sqrt{(n+\alpha)(n+\alpha-1)(n+\alpha-2)(n+\alpha-3)} \delta_{n, m} \right] \\
& + 4 \left(\frac{1}{b} + \frac{\epsilon^2}{2} - b \right) \delta_{\alpha-2, \beta} \left[-\sqrt{n(n+\alpha)(n+\alpha-1)(n+\alpha-2)} \delta_{n-1, m} \right. \\
& \quad + (4n+\alpha+1)\sqrt{(n+\alpha)(n+\alpha-1)} \delta_{n, m} \\
& \quad - 3(2n+\alpha+1)\sqrt{(n+1)(n+\alpha)} \delta_{n+1, m} \\
& \quad + (4n+3\alpha+3)\sqrt{(n+1)(n+2)} \delta_{n+2, m} \\
& \quad \left. - \sqrt{(n+1)(n+2)(n+3)(n+\alpha+1)} \delta_{n+3, m} \right] \\
& + 6 \left(\frac{1}{b} + \frac{\epsilon^2}{2} + b + \frac{2}{3}\lambda \right) \delta_{\alpha, \beta} \left[\sqrt{n(n-1)(n+\alpha)(n+\alpha-1)} \delta_{n-2, m} \right. \\
& \quad - 2(2n+\alpha)\sqrt{n(n+\alpha)} \delta_{n-1, m} \\
& \quad + [n(n-1) + (n+\alpha+1)(5n+\alpha+2)] \delta_{n, m} \\
& \quad - 2(2n+\alpha+2)\sqrt{(n+1)(n+\alpha+1)} \delta_{n+1, m} \\
& \quad \left. + \sqrt{(n+1)(n+2)(n+\alpha+1)(n+\alpha+2)} \delta_{n+2, m} \right] \\
& + 4 \left(\frac{1}{b} + \frac{\epsilon^2}{2} - b \right) \delta_{\alpha+2, \beta} \left[-\sqrt{n(n-1)(n-2)(n+\alpha)} \delta_{n-3, m} \right. \\
& \quad \left. + (4n+3\alpha+1)\sqrt{n(n-1)} \delta_{n-2, m} \right]
\end{aligned}$$

$$\begin{aligned}
& -3(2n + \alpha + 1)\sqrt{n(n + \alpha + 1)} \delta_{n-1,m} \\
& + (4n + \alpha + 3)\sqrt{(n + \alpha + 1)(n + \alpha + 2)} \delta_{n,m} \\
& - \sqrt{(n + 1)(n + \alpha + 1)(n + \alpha + 2)(n + \alpha + 3)} \delta_{n+1,m} \Big] \\
& + \left(\frac{1}{b} + \frac{\epsilon^2}{2} + b - 2\lambda \right) \delta_{\alpha+4,\beta} \Big[\sqrt{n(n-1)(n-2)(n-3)} \delta_{n-4,m} \\
& - 4\sqrt{n(n-1)(n-2)(n+\alpha+1)} \delta_{n-3,m} \\
& + 6\sqrt{n(n-1)(n+\alpha+1)(n+\alpha+2)} \delta_{n-2,m} \\
& - 4\sqrt{n(n+\alpha+1)(n+\alpha+2)(n+\alpha+3)} \delta_{n-1,m} \\
& + \sqrt{(n+\alpha+1)(n+\alpha+2)(n+\alpha+3)(n+\alpha+4)} \delta_{n,m} \Big] \Big) .
\end{aligned} \tag{11.40}$$

All three terms in Eq. (11.32) are given in terms of the original radial basis (no rotation), and the ranges of indices are $n \geq 0$ and $\alpha \geq -n$. Since the Hamiltonian is invariant under spatial reflection symmetries, its eigenstates are grouped into four parity classes. Then, it is convenient to use the basis having the same parities. The new basis can be obtained by rotating the original radial basis in the Hilbert space, and we call this new basis as the “rotated” basis. As a consequence, the Hamiltonian matrix becomes blocked diagonalized, and each sub-matrix corresponds to one of the four parity classes. Then, the matrix diagonalization is proceeded on each sub-matrix independently.

$$\begin{aligned}
\langle \phi_{n,\alpha}^\pm | \hat{H}_0 | \phi_{m,\beta}^\pm \rangle &= \frac{1}{2} \left[\langle n, -\alpha | \hat{H}_0 | m, -\beta \rangle + \langle n - \alpha, \alpha | \hat{H}_0 | m - \beta, \beta \rangle \right. \\
&\quad \left. \pm \langle n, -\alpha | \hat{H}_0 | m - \beta, \beta \rangle \pm \langle n - \alpha, \alpha | \hat{H}_0 | m, -\beta \rangle \right] \tag{11.41}
\end{aligned}$$

where all the indices now refer to the rotated basis, $n, m \geq 0$ and $\alpha, \beta > 0$. When α and/or β equal zero, one finds

$$\langle \phi_{n,0}^+ | \hat{H}_0 | \phi_{m,\beta \neq 0}^+ \rangle = \frac{1}{\sqrt{2}} [\langle n, 0 | \hat{H}_0 | m, -\beta \rangle + \langle n, 0 | \hat{H}_0 | m - \beta, \beta \rangle] \quad (11.42)$$

$$\langle \phi_{n,\alpha \neq 0}^+ | \hat{H}_0 | \phi_{m,0}^+ \rangle = \frac{1}{\sqrt{2}} [\langle n, -\alpha | \hat{H}_0 | m, 0 \rangle + \langle n - \alpha, \alpha | \hat{H}_0 | m, 0 \rangle] \quad (11.43)$$

$$\langle \phi_{n,0}^+ | \hat{H}_0 | \phi_{m,0}^+ \rangle = \langle n, 0 | \hat{H}_0 | m, 0 \rangle. \quad (11.44)$$

We describe the last symmetry breaking term for each parity separately using the rotated basis,

$$\langle \phi_{m,\beta}^\pm | \hat{H}_1 | \phi_{n,\alpha}^\pm \rangle = I \cdot J_k \quad (11.45)$$

where

$$I = \int_0^\infty dr \, r R_{m-\beta,\beta} \left[\frac{\epsilon}{2} \sqrt{a} (r \hat{p}_r r + \hat{p}_r r^2) \right] R_{n-\alpha,\alpha} \quad (11.46)$$

$$J_1 = \frac{1}{\pi} \int_0^{2\pi} d\theta \cos \beta \theta \cos^2 \theta \cos \alpha \theta \quad (11.47)$$

$$J_2 = \frac{1}{\pi} \int_0^{2\pi} d\theta \sin \beta \theta \cos^2 \theta \sin \alpha \theta \quad (11.48)$$

or

$$\begin{aligned} I = & -i \frac{\epsilon}{2} \sqrt{\frac{a(\lambda)}{\omega}} \left[2 \sqrt{(n+1)(n+2)(n-\alpha+1)} \int_0^\infty dr \, r R_{m-\beta,\beta} R_{n-\alpha+1,\alpha+1} \right. \\ & - 2(2n-\alpha+1) \sqrt{n+1} \int_0^\infty dr \, r R_{m-\beta,\beta} R_{n-\alpha,\alpha+1} \\ & \left. + 2n \sqrt{n-\alpha} \int_0^\infty dr \, r R_{m-\beta,\beta} R_{n-\alpha-1,\alpha+1} \right] \end{aligned}$$

$$\begin{aligned}
& -(2n+1)\sqrt{n-\alpha+1} \int_0^\infty dr \, r R_{m-\beta,\beta} R_{n-\alpha+1,\alpha-1} \\
& + (4n-2\alpha+1)\sqrt{n} \int_0^\infty dr \, r R_{m-\beta,\beta} R_{n-\alpha,\alpha-1} \\
& - 2\sqrt{n(n-1)(n-\alpha)} \int_0^\infty dr \, r R_{m-\beta,\beta} R_{n-\alpha-1,\alpha-1} \Big] \tag{11.49}
\end{aligned}$$

$$J_k = \frac{1}{2} (\delta_{\alpha,\beta} \pm \delta_{\alpha,-\beta}) + \frac{1}{4} (\delta_{\alpha,\beta+2} + \delta_{\alpha,\beta-2} \pm \delta_{\alpha,-\beta+2}) \quad (+/- \text{ for } k = 1 \text{ or } 2). \tag{11.50}$$

In Eq. (11.49), the radial integrations need to be evaluated numerically. For even-even parity, we use the ϕ^+ basis with even α, β and $J_k = J_1$; for even-odd parity, we use the ϕ^+ basis with odd α, β and $J_k = J_2$; for odd-even parity, we use the ϕ^- basis with odd α, β and $J_k = J_1$; and for odd-odd parity, we use the ϕ^- basis with even α, β and $J_k = J_2$. Finally, one adds Eqs. (11.41) and (11.45) to construct the numerical Hamiltonian matrix. Hermiticity of this complex Hamiltonian is obtained with the following conditions: for the real part, we require $(H_0)_{i,j} = (H_0)_{j,i}$ and for the imaginary part, we require $(H_1)_{i,j} = -(H_1)_{j,i}$.

11.3.5 Spectra

To observe the dynamical effects on the resulting statistical properties, we investigate the Hamiltonian system in three different dynamical regimes, near integrable, mixed, and chaotic. The degree of chaoticity can be controlled by tuning the coupling constant of the quartic oscillator λ . In each regime, three cases with slightly different λ values are arranged to constitute a statistical ensemble. The reflection symmetries in every system allow one to classify the eigenstates into four parity sequences. Instead of taking this parity decomposition

just as the property of eigenstates or computational convenience, we treat them as completely independent physical systems. In doing so, four sub-systems are derived as follows ('sub' is because four systems stem from the original one). Sub-systems are governed by the same Hamiltonian discussed in previous section, but with additional boundary conditions applied. For even-even parity sequence, spatial derivative of wave functions must vanish, $\partial_x \psi = 0$ and $\partial_y \psi = 0$, at $x = 0$ and $y = 0$ respectively. For even-odd, $\partial_x \psi = 0$ at $x = 0$ and $\psi = 0$ at $y = 0$. For odd-even, $\psi = 0$ at $x = 0$ and $\partial_y \psi = 0$ at $y = 0$. For odd-odd, $\psi = 0$ both at $x = 0$ and $y = 0$. One can consider these as the systems confined by the quartic oscillator and hard walls at $x = y = 0$, and so 1/4 of coordinate space, say $x \geq 0$ and $y \geq 0$, as allowed region of motion. (Strictly speaking, this hard wall picture is only valid for the odd-odd case. To obtain $\psi' = 0$, one must have different type of wall.)

Since we are interested in the systems leading to GUE statistics, the cases treated here are those with broken anti-unitary symmetries, and so ϵ must be chosen to be non-zero. With the studies of Poincaré surfaces of section (see Figs. (11.1), (11.2), (11.3)), we find that the following coupling constants lead to the three dynamical regimes of interest: $\lambda = 0.20$ (near integrable), -0.20 (mixed), and -0.80 (chaotic).

Eigenvalues and eigenvectors are generated by the matrix diagonalization of the numerically evaluated Hamiltonian in all three regimes. Once the energy eigenvalues are calculated, spectral unfolding is performed. Since the Hamiltonian was designed to preserve the scaling properties of the system, the same expression for the counting function of the quartic oscillator discussed in chapter 10 can be applied. As given in Eq. (10.19), the counting function

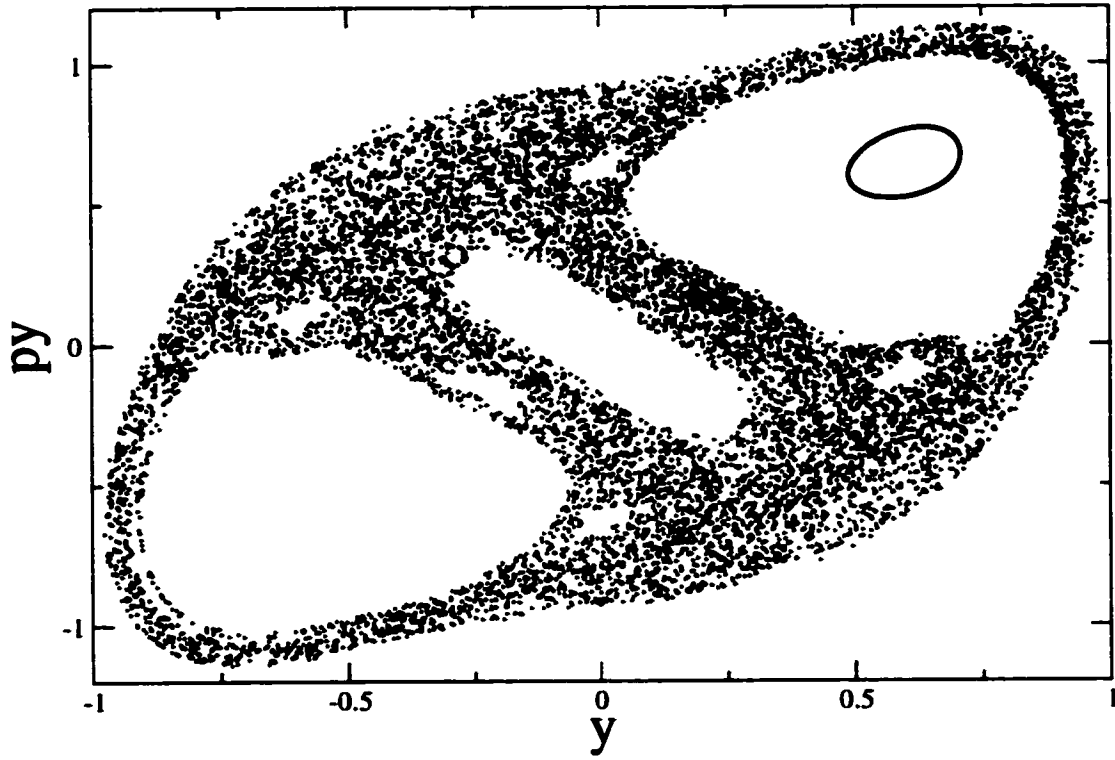


Figure 11.1: Poincaré surface of section for the coupled quartic oscillator system (TRNI) with $\lambda = 0.20$ and $\epsilon = -1.0$. Figure shows $x = 0$ surface, and the data points are recorded when a momentum is positive $p_x > 0$. The solid curve around $(y, p_y) = (0.6, 0.6)$ represents the stable motion. (Figure courtesy of D.Ullmo).

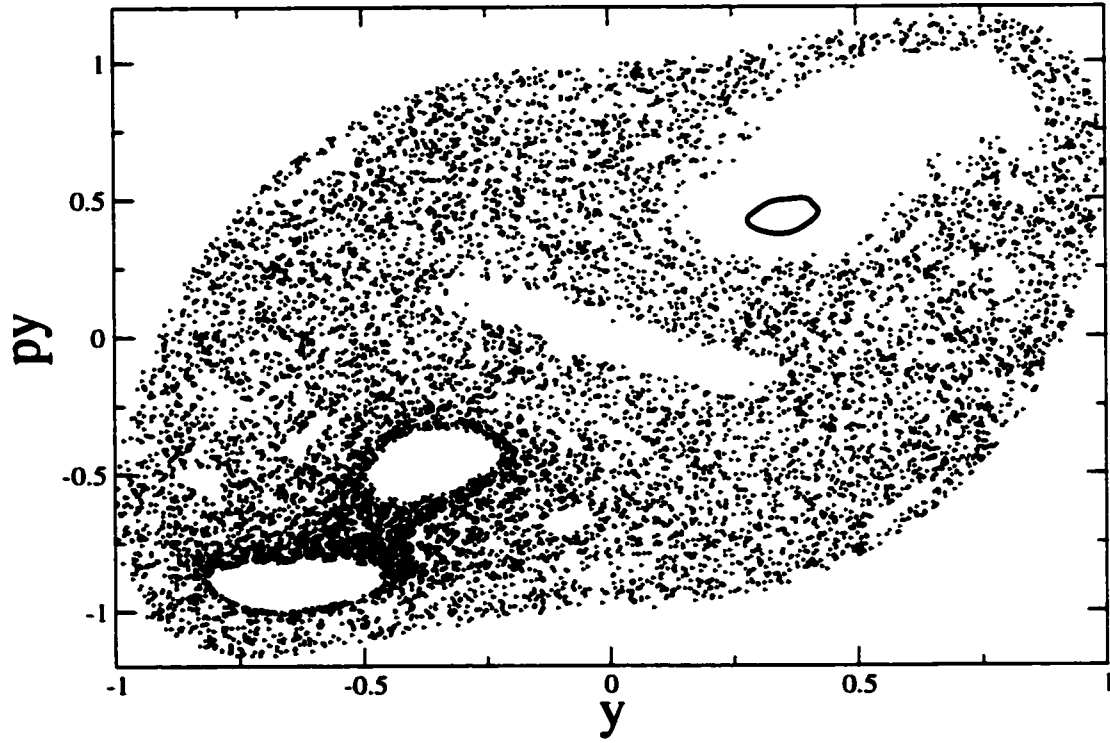


Figure 11.2: Poincaré surface of section for the coupled quartic oscillator system (TRNI) with $\lambda = -0.20$ and $\epsilon = -1.0$. Data represent $x = 0$ surface with positive momentum $p_x > 0$. The solid curve around $(y, p_y) = (0.4, 0.5)$ represents the stable motion. (Figure courtesy of D.Ullmo).

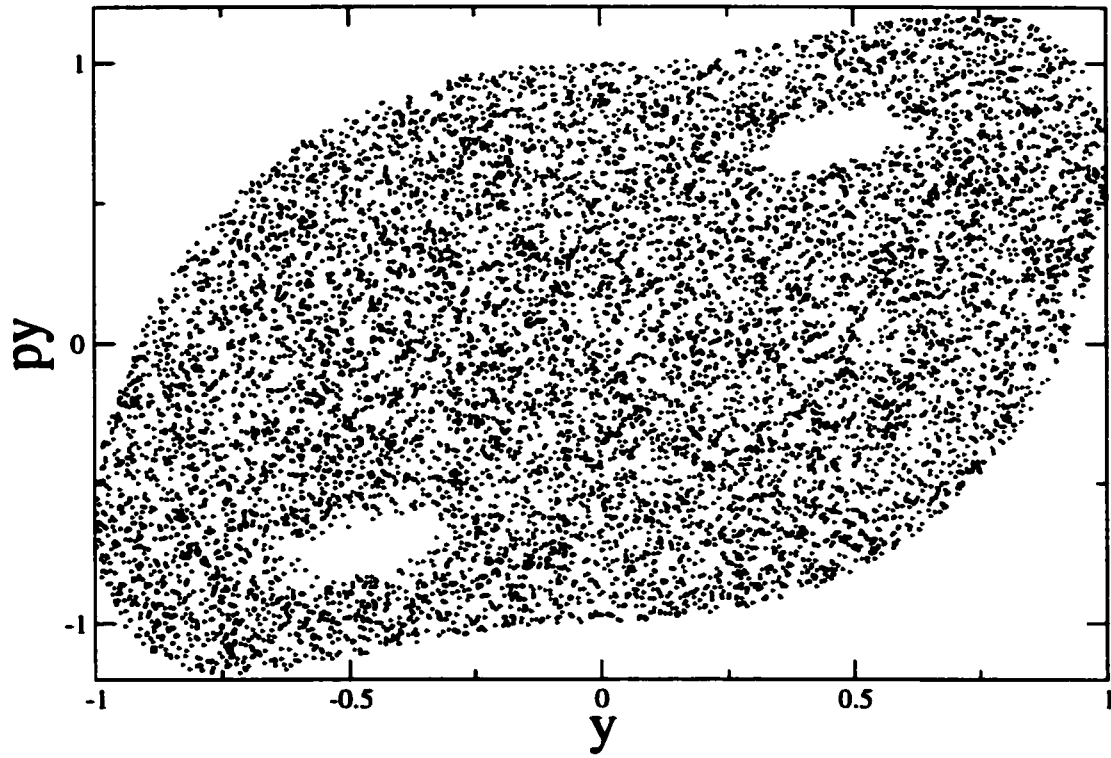


Figure 11.3: Poincaré surface of section for the coupled quartic oscillator system (TRNI) with $\lambda = -0.80$ and $\epsilon = -1.0$. Data represent $x = 0$ surface with positive momentum $p_x > 0$. (Figure courtesy of D.Ullmo).

is

$$\bar{N}_{\epsilon_1, \epsilon_2}(E) = \frac{1}{4} (a_0 E^{3/2} + a_1 E^{3/4} + a_2) + O(E^{-3/4}), \quad (11.51)$$

where

$$a_0 = \frac{2K((1-\lambda)/2)}{3\pi} \frac{1}{a(\lambda)^{1/2}} = 1 \quad (11.52)$$

$$a_1 = \frac{\Gamma(1/4)^2(\epsilon_1 b^{-1/4} + \epsilon_2 b^{1/4})}{2\sqrt{6}\pi K^{1/2}((1-\lambda)/2)}. \quad (11.53)$$

As expected, it is found that the coefficients are exactly the same as the previous case except for a_2 . However, a_2 does not contribute to some derived relations such as level density.

Once the spectra are unfolded, one can test the convergence of eigenvalues for each sequence by examining the oscillatory part of the counting function δN . Since the deviation of the energy levels from the Weyl counting function is mapped onto fluctuations from a uniform spacing of unfolded spectra, one can subtract the average part and extract the fluctuation. With all the spectra considered, we use following ranges as the converged spectra: for $\lambda = 0.20$, $i = 0$ to 199; for $\lambda = -0.20$, $i = 0$ to 149; and for $\lambda = -0.80$, $i = 0$ to 124.

Using the converged unfolded spectra, one can obtain the number variance statistics and observe the dynamical regime of the three systems; see Fig. (11.5). For the case with coupling strength $\lambda = 0.20$, the number variance curve (b) is close to the Poisson result (a) indicating the system is in the near-integrable regime. For $\lambda = -0.20$, the curve (c) is located in between the Poisson and GOE (d) representing the mixed regime. For $\lambda = -0.80$,

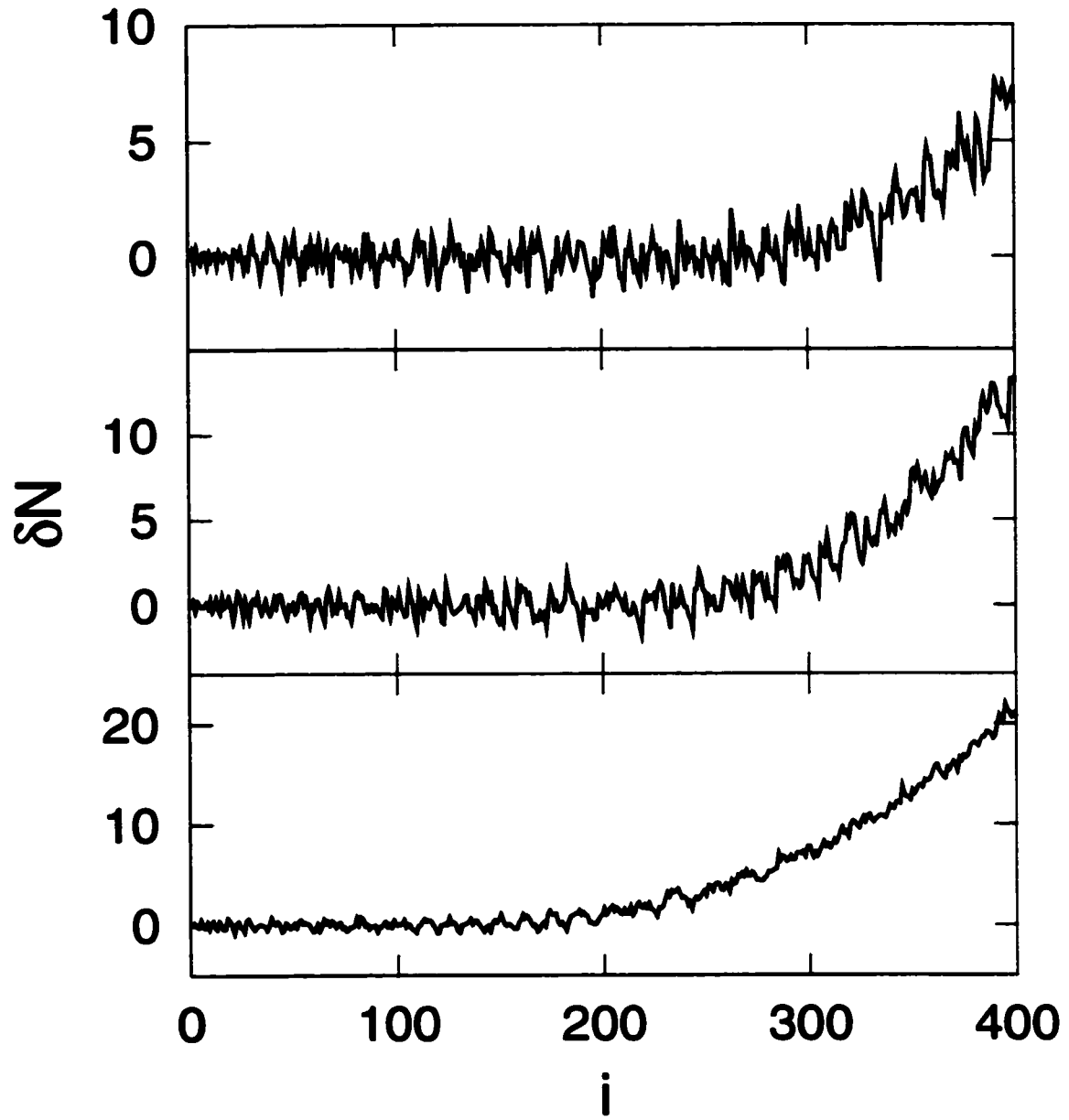


Figure 11.4: Oscillatory part of the counting function $\delta N = N(E) - \bar{N}(E)$ for energy levels $i = 0 - 400$. Top figure: $\lambda = 0.20$, middle: $\lambda = -0.20$, and bottom: $\lambda = -0.80$. For all cases, the reflection symmetry $(+,+)$. The other symmetry cases behave similarly. Figures show full range of spectra data (including non-converged data, for example $i > 200$ in the near-integrable case) for the sake of convergence study.

the curve (F) follows the GUE curve (e) and starts separating with small oscillations at $r = 1$. The statistics are generated with the spectral ensembles: for near integrability, data for $\lambda = 0.18, 0.20, 0.22$ are used, each giving four parity sequences; for mixed case, $\lambda = -0.18, -0.20, -0.22$ are used; and for chaotic case, $\lambda = -0.78, -0.80, -0.82$ are used. For each spectral set, the first 50 states are dropped. We set the symmetry breaking strength to $\epsilon = -1.0$, and find that it is strong enough to shift the systems into the dynamical regime of fully broken anti-unitary symmetry. It is confirmed by the behavior of the chaotic case $\lambda = -0.80$.

With the parity decomposition, the single-particle mean level spacings are derived from the counting function

$$\Delta_N = \left(\frac{dN}{dE} \right)^{-1} = \frac{16}{3\sqrt{a_1^2 - 4a_0(a_2 - 4N)}} \left[\frac{-a_1 + \sqrt{a_1^2 - 4a_0(a_2 - 4N)}}{2a_0} \right]^{1/3}. \quad (11.54)$$

While a_0 and a_1 are given by the analytical expressions, a_2 must be determined by numerical non-linear fitting of the energy spectra.

11.4 Residual Interaction and M_{ij}

In the previous study of the quartic oscillator (TRI) system, the numerical computation involved the matrix diagonalization of the truncated Hamiltonian, and it proceeded using the following steps: two-dimensional coupled quartic oscillator \rightarrow two-dimensional uncoupled quartic oscillator \rightarrow one-dimensional quartic oscillator \rightarrow one-dimensional harmonic

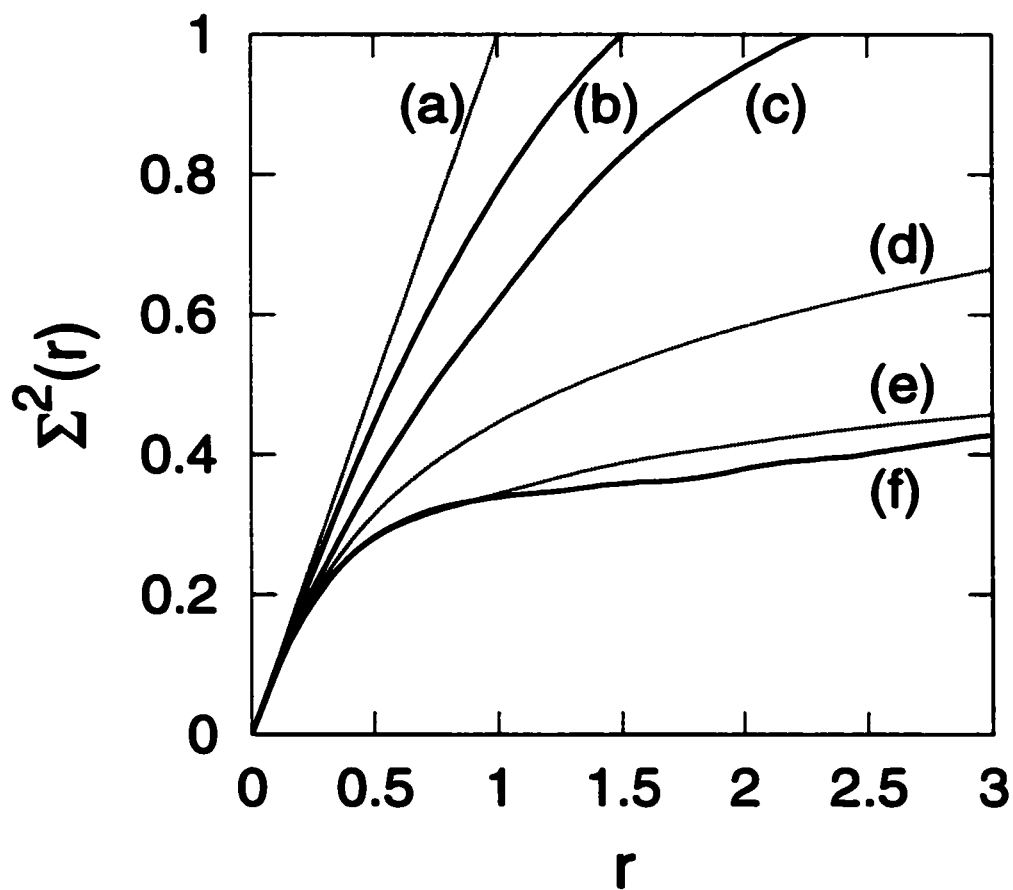


Figure 11.5: Number Variance $\Sigma^2(r)$ versus r . (a) Poisson, (b) $\lambda = 0.20$, (c) $\lambda = -0.20$, (d) GOE, (e) GUE, and (f) $\lambda = -0.80$. Poisson, GOE, and GUE results are displayed for the sake of comparison.

oscillator, where the arrow indicates matrix diagonalization with the choice of basis given on the right side of each arrow. For TRNI case, due to the radial dependence of the symmetry breaking term, the system must be computed in a one-step matrix diagonalization with the radial harmonic oscillator basis. Therefore, one cannot avoid dealing with large numerical Hamiltonian matrices and calculation time issues. Otherwise, one must be satisfied with a reduced number of converged states. One way to construct wavefunctions is to use eigenvectors (as expansion coefficients) and basis functions. Then, the matrix elements M_{ij} can be calculated using the wavefunctions. This approach is simple, but it is not always the best choice. The reason is that, in general, the convergence of eigenvectors are not as good as that of eigenvalues. For the purpose of constructing the matrix elements M_{ij} , one should avoid such an approach, to the extent possible, which requires grid point evaluations such as finite difference methods or functional evaluations, for example. The allowed range of numerical error is always determined by the size of the single-particle mean level spacing, in other words, the numerical error can be acceptable if it is negligible compared to the mean level spacing. For these reasons, we compute M_{ij} with the following approach.

First of all, we note the condition for the eigenstate normalization. For many circumstances, it is convenient to deal with the full coordinate space rather than restricting oneself to the $x > 0, y > 0$ space. However, since the parity decomposed systems are defined in the quarter space, one has to have a means to transform back to the quarter space. In the

quarter space, the wavefunction is normalized such that

$$\int_0^\infty dx \int_0^\infty dy |\phi(x, y)|^2 = 1, \quad (11.55)$$

and the matrix elements M_{ij} become

$$M_{ij} = \frac{1}{\rho w} \int_0^\infty dx \int_0^\infty dy |\phi_i(x, y)|^2 |\phi_j(x, y)|^2. \quad (11.56)$$

On the other hand, if one uses the entire coordinate space, the normalization and M_{ij} becomes

$$\int_{-\infty}^\infty dx \int_{-\infty}^\infty dy |\phi'(x, y)|^2 = 1 \quad (11.57)$$

$$M'_{ij} = \frac{1}{\rho w} \int_{-\infty}^\infty dx \int_{-\infty}^\infty dy |\phi'_i(x, y)|^2 |\phi'_j(x, y)|^2, \quad (11.58)$$

where the prime sign is used to indicate a different normalization rule. The following relations are derived,

$$|\phi|^2 = 4|\phi'|^2 \quad (11.59)$$

$$M_{ij} = 4M'_{ij}. \quad (11.60)$$

Similarly for the mean level spacings, we obtain

$$\Delta_i = 4\Delta'_i, \quad (11.61)$$

so that the scaled matrix elements are unchanged

$$\frac{M_{ij}}{\Delta_i} = \frac{M'_{ij}}{\Delta'_i}. \quad (11.62)$$

Now let us consider the construction of M_{ij} using the rotated basis with the local approximation to the screened interaction.

$$M_{ij} = \frac{4}{\rho^W} \int_0^\infty r dr \int_0^{2\pi} d\theta |\phi_i(\mathbf{r})|^2 |\phi_j(\mathbf{r})|^2 \quad (11.63)$$

$$= \frac{4}{\rho^W} \sum_{n_1, \alpha_1, n_2, \alpha_2, n_3, \alpha_3, n_4, \alpha_4} c_{n_1, \alpha_1}^i c_{n_2, \alpha_2}^{i*} c_{n_3, \alpha_3}^j c_{n_4, \alpha_4}^{j*} \times I_\theta \cdot \int_0^\infty r dr R_{n_1 - \alpha_1, \alpha_1} R_{n_2 - \alpha_2, \alpha_2} R_{n_3 - \alpha_3, \alpha_3} R_{n_4 - \alpha_4, \alpha_4}, \quad (11.64)$$

where the factor of 4 comes from the normalization of the angular functions integrating over 0 to 2π for all space. The angular integration is given by,

$$I_\theta = \begin{cases} (1/\pi^2) \int_0^{2\pi} d\theta \cos \alpha_1 \theta \cos \alpha_2 \theta \cos \alpha_3 \theta \cos \alpha_4 \theta & \text{for } (+, +), (-, +) \\ (1/\pi^2) \int_0^{2\pi} d\theta \sin \alpha_1 \theta \sin \alpha_2 \theta \sin \alpha_3 \theta \sin \alpha_4 \theta & \text{for } (+, -), (-, -). \end{cases}$$

Introducing $\gamma = \alpha_1 - \alpha_2$ and $\sigma = \alpha_1 + \alpha_2$, the above expressions reduce to

$$I_\theta = \frac{1}{4\pi} [\delta_{\alpha_2, -\alpha_1 + \sigma} (\delta_{\alpha_4, -\alpha_3 - \sigma} \pm \delta_{\alpha_4, \alpha_3 + \sigma} \pm \delta_{\alpha_4, \alpha_3 - \sigma} + \delta_{\alpha_4, -\alpha_3 + \sigma}) + \delta_{\alpha_2, \alpha_1 - \gamma} (\delta_{\alpha_4, \alpha_3 + \gamma} \pm \delta_{\alpha_4, -\alpha_3 - \gamma} \pm \delta_{\alpha_4, -\alpha_3 + \gamma} + \delta_{\alpha_4, \alpha_3 - \gamma})]. \quad (11.65)$$

Then, M_{ij} becomes

$$\begin{aligned}
M_{ij} = & \frac{1}{\pi \rho^W} \sum_{\sigma} \sum_{n_1, \alpha_1, n_2, n_3, \alpha_3, n_4} \left[c_{n_1, \alpha_1}^i c_{n_2, -\alpha_1 + \sigma}^{i*} \int_0^\infty r dr R_{n_1 - \alpha_1, \alpha_1} R_{n_2 - (-\alpha_1 + \sigma), (-\alpha_1 + \sigma)} \right. \\
& \times \left(c_{n_3, \alpha_3}^j c_{n_4, -\alpha_3 - \sigma}^{j*} \int_0^\infty r dr R_{n_3 - \alpha_3, \alpha_3} R_{n_4 - (-\alpha_3 - \sigma), (-\alpha_3 - \sigma)} \right. \\
& \pm c_{n_3, \alpha_3}^j c_{n_4, \alpha_3 + \sigma}^{j*} \int_0^\infty r dr R_{n_3 - \alpha_3, \alpha_3} R_{n_4 - (\alpha_3 + \sigma), (\alpha_3 + \sigma)} \\
& \pm c_{n_3, \alpha_3}^j c_{n_4, \alpha_3 - \sigma}^{j*} \int_0^\infty r dr R_{n_3 - \alpha_3, \alpha_3} R_{n_4 - (\alpha_3 - \sigma), (\alpha_3 - \sigma)} \\
& \left. \left. + c_{n_3, \alpha_3}^j c_{n_4, -\alpha_3 + \sigma}^{j*} \int_0^\infty r dr R_{n_3 - \alpha_3, \alpha_3} R_{n_4 - (-\alpha_3 + \sigma), (-\alpha_3 + \sigma)} \right) \right] \\
& + \frac{1}{\pi \rho^W} \sum_{\gamma} \sum_{n_1, \alpha_1, n_2, n_3, \alpha_3, n_4} \left[c_{n_1, \alpha_1}^i c_{n_2, \alpha_1 - \gamma}^{i*} \int_0^\infty r dr R_{n_1 - \alpha_1, \alpha_1} R_{n_2 - (\alpha_1 - \gamma), (\alpha_1 - \gamma)} \right. \\
& \times \left(c_{n_3, \alpha_3}^j c_{n_4, \alpha_3 + \gamma}^{j*} \int_0^\infty r dr R_{n_3 - \alpha_3, \alpha_3} R_{n_4 - (\alpha_3 + \gamma), (\alpha_3 + \gamma)} \right. \\
& \pm c_{n_3, \alpha_3}^j c_{n_4, -\alpha_3 - \gamma}^{j*} \int_0^\infty r dr R_{n_3 - \alpha_3, \alpha_3} R_{n_4 - (-\alpha_3 - \gamma), (-\alpha_3 - \gamma)} \\
& \pm c_{n_3, \alpha_3}^j c_{n_4, -\alpha_3 + \gamma}^{j*} \int_0^\infty r dr R_{n_3 - \alpha_3, \alpha_3} R_{n_4 - (-\alpha_3 + \gamma), (-\alpha_3 + \gamma)} \\
& \left. \left. + c_{n_3, \alpha_3}^j c_{n_4, \alpha_3 - \gamma}^{j*} \int_0^\infty r dr R_{n_3 - \alpha_3, \alpha_3} R_{n_4 - (\alpha_3 - \gamma), (\alpha_3 - \gamma)} \right) \right]. \tag{11.66}
\end{aligned}$$

Note that the summation indices α_2 and α_4 are replaced by σ and γ . Furthermore, we introduce the following definitions

$$W_{i, \xi}(r) \equiv \sum_{n, m, \alpha} c_{n, \alpha}^i c_{m, \alpha - \xi}^{i*} R_{n - \alpha, \alpha} R_{m - (\alpha - \xi), (\alpha - \xi)} \tag{11.67}$$

$$Y_{i, \xi}(r) \equiv \sum_{n, m, \alpha} c_{n, \alpha}^i c_{m, -\alpha - \xi}^{i*} R_{n - \alpha, \alpha} R_{m - (-\alpha - \xi), (-\alpha - \xi)}. \tag{11.68}$$

One must multiply each expansion coefficient $c_{n, \alpha}^i$ by $1/\sqrt{2}$ whenever α encounters zero,

based on the fact $\phi_{n,0}^+ = \phi_{n,0}$. Eq. (11.66) is written as

$$M_{ij} = \frac{1}{\pi \rho^W} \sum_{\sigma} \int_0^{\infty} r dr Y_{i,-\sigma} (Y_{j,\sigma} \pm W_{j,\sigma} \pm W_{j,-\sigma} + Y_{j,-\sigma}) \\ + \frac{1}{\pi \rho^W} \sum_{\gamma} \int_0^{\infty} r dr W_{i,\gamma} (W_{j,\gamma} \pm Y_{j,\gamma} \pm Y_{j,-\gamma} + W_{j,-\gamma}), \quad (11.69)$$

where for all cases, the upper sign represents parity sequences $(+, +)$ and $(-, +)$ and the lower sign the sequences $(+, -)$ and $(-, -)$. Now the main task is to compute $W_{i,\pm\gamma}$, $W_{i,\pm\sigma}$, $Y_{i,\pm\gamma}$, and $Y_{i,\pm\sigma}$. Once the Hamiltonian matrix diagonalization is done, there is a finite number of converged eigenstates. They give the range of indices for the rotated basis: $0 \leq n \leq n_{max}$, $\alpha_{min} \leq \alpha \leq \alpha_{max} = n_{max}$. α_{min} is 0 for $(+, +)$, 1 for $(+, -)$ or $(-, +)$, and 2 for $(-, -)$. Since $\gamma = \alpha_1 - \alpha_2$ and $\sigma = \alpha_1 + \alpha_2$, their limits are

$$|\gamma| \leq \alpha_{max} - \alpha_{min} \\ 2\alpha_{min} \leq \sigma \leq 2\alpha_{max}. \quad (11.70)$$

If one writes $W_{i,\xi}$ and $Y_{i,\xi}$, the range of ξ is $|\xi| \leq 2\alpha_{max}$. However, the expansion coefficients (eigenvectors of the Hamiltonian matrix) $c_{n,\alpha}^i$ are available only for $\alpha \geq \alpha_{min}$, the factor $c_{m,\pm\alpha-\xi}^{i*}$ limits the range of ξ in W and Y ('+' for W and '-' for Y). To be more explicit, the following index ranges give non-zero $W_{i,\xi}$ and $Y_{i,\xi}$.

$$|\xi| \leq \alpha_{max} - \alpha_{min} \quad (\text{for } W_{i,\xi} \neq 0) \\ -2\alpha_{max} \leq \xi \leq -2\alpha_{min} \quad (\text{for } Y_{i,\xi} \neq 0). \quad (11.71)$$

In this representation, the normalization of the wavefunctions ϕ_i for all space can be obtained as follows

$$\int d\mathbf{r} |\phi_i|^2 = \sum_{n,\alpha} \sum_{m,\beta} c_{n,\alpha}^i c_{m,\beta}^{i*} \int_0^\infty r dr R_{n-\alpha,\alpha} R_{m-\beta,\beta} \cdot I_\theta. \quad (11.72)$$

Using

$$I_\theta = \delta_{\alpha-\beta,0} \pm \delta_{\alpha+\beta,0}, \quad (11.73)$$

the expression in Eq. (11.72) can be rewritten as

$$\int d\mathbf{r} |\phi_i|^2 = \int_0^\infty r dr (W_{i,0} \pm Y_{i,0}), \quad (11.74)$$

where the upper sign represents parity sequences $(+, +)$ and $(-, +)$ and the lower sign the sequences $(+, -)$ and $(-, -)$ as before.

To construct M_{ij} from the eigenvectors of the Hamiltonian matrix, there are mainly three approaches. The first approach is to directly construct wavefunctions and integrate them. This is the simplest way to calculate M_{ij} and it is easy to understand the procedure. Because it involves evaluation of wavefunctions on some mesh (grid points), the accuracy is the worst. The second approach is to proceed with the manipulation of the expansion coefficients and use the orthonormality of the basis. Since the evaluation of functions is avoided with the basis orthonormality, this is the most preferable approach if one's goal is to achieve high accuracy. However, since M_{ij} involves the fourth power of wavefunctions and each four summations independently run from zero to few hundred, the products of expansion coefficients require a huge storage space, which makes this approach practically impossible to use. The last

approach combines the two approaches we just described. The idea is to take advantage of both approaches. The direct evaluation of wavefunctions is avoided by the manipulation of the expansion coefficients through $W_{i,\xi}$ and $Y_{i,\xi}$ (radial functions still need to be evaluated). Then, one carries out summations over two indices σ and γ once the integrations are done. This combined approach preserves a reasonable level of accuracy, and solves the problem of data storage space.

The M_{ij} are calculated for three coupling regimes $\lambda = 0.20, -0.20$, and -0.80 (symmetry breaking strength $\epsilon = -1.0$). Figures (11.6), (11.7), and (11.8) show M_{ij} for $\lambda = 0.20, -0.20$, and -0.80 respectively. Data are plotted for the lowest 200, 150, and 125 states for $\lambda = 0.20, -0.20$, and -0.80 respectively. As seen in the TRI system, the diagonal elements are larger than the off-diagonal elements. The diagonal elements are shown in Fig. (11.9). The data is scaled by the single-particle mean level spacing of the energy levels. The localization of the wavefunction produces large spikes, and the magnitudes of the peaks increase as the system gains regularity. The lower bound of M_{ii} is about 1.0, the size is comparable to Δ_i ; this is consistent for all three regimes. The distribution of the diagonal elements are plotted in Fig. (11.10), and the moments are computed in Table (11.1). Statistics are obtained treating systems with slightly shifted coupling constants: for near integrable, $\lambda = 0.18, 0.20$, and 0.22 ; for mixed, $\lambda = -0.18, -0.20$, and -0.22 ; for chaotic, $\lambda = -0.78, -0.80$, and -0.82 . All four parity sequence data are included in each ensemble. Since the first 50 states in each sequence are not stable, we threw them out by hand. Because of the stronger localization of the wavefunction in the near-integrable regime, large peaks in M_{ii} are responsible for

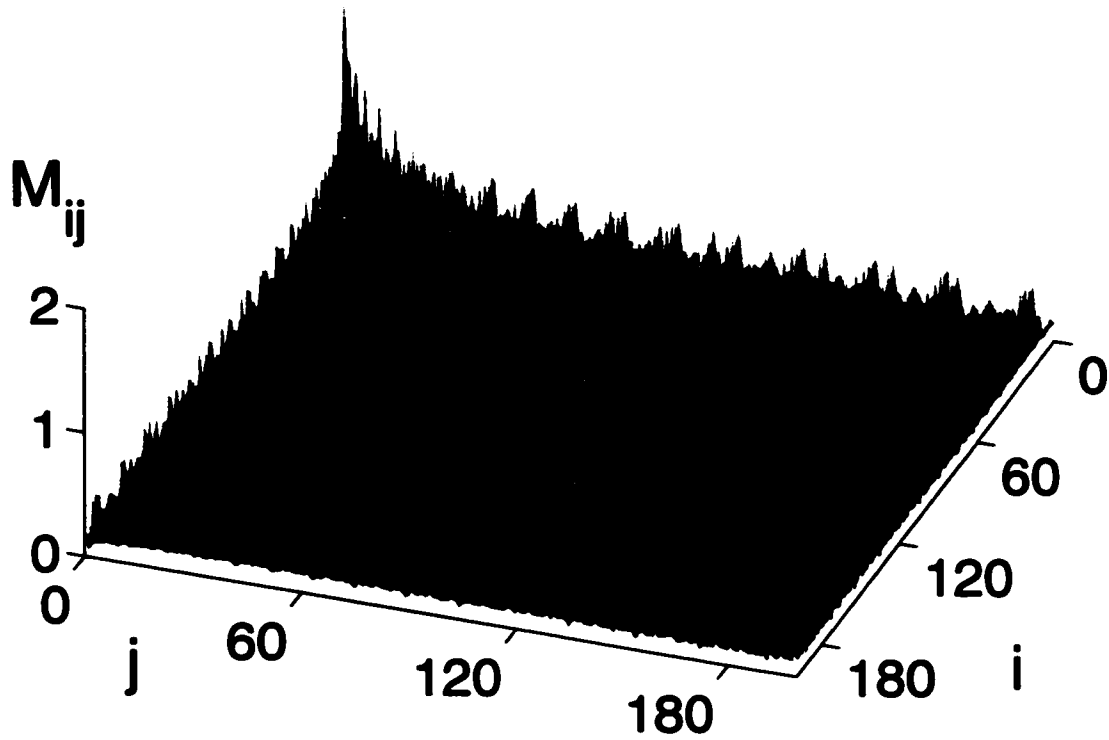


Figure 11.6: The matrix elements M_{ij} are plotted for the TRNI system with the coupling constant $\lambda = 0.20$. M_{ij} is not scaled by the mean level spacing in this figure. The ranges of the indices are $i, j = 0$ to 199. The parity sequence is set to $(+, +)$.

the long right tail in the distribution. To show these long tails, the figure inset shows the same data in a logarithmic scale. The chaotic regime exhibits much shorter tails than the near-integrable case. Localization of wavefunctions is unlikely to occur in the chaotic case. Figure (11.11) shows the probability density of the scaled off-diagonal M_{ij} elements (near diagonal). Generally, the overlap between two states is likely to destruct pattern of the wavefunction unless both of the states are localized.

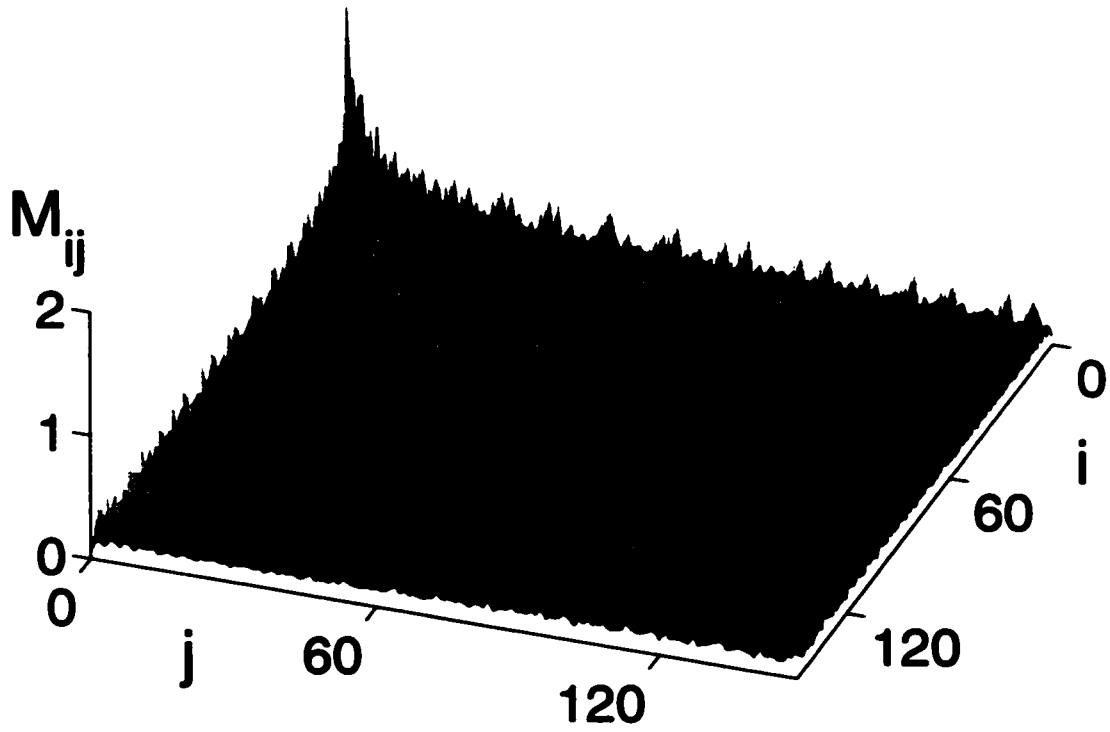


Figure 11.7: The matrix elements M_{ij} are plotted for the TRNI system with the coupling constant $\lambda = -0.20$. M_{ij} is not scaled by the mean level spacing in this figure. The ranges of the indices are $i, j = 0$ to 149. The parity sequence is set to $(+,+)$.

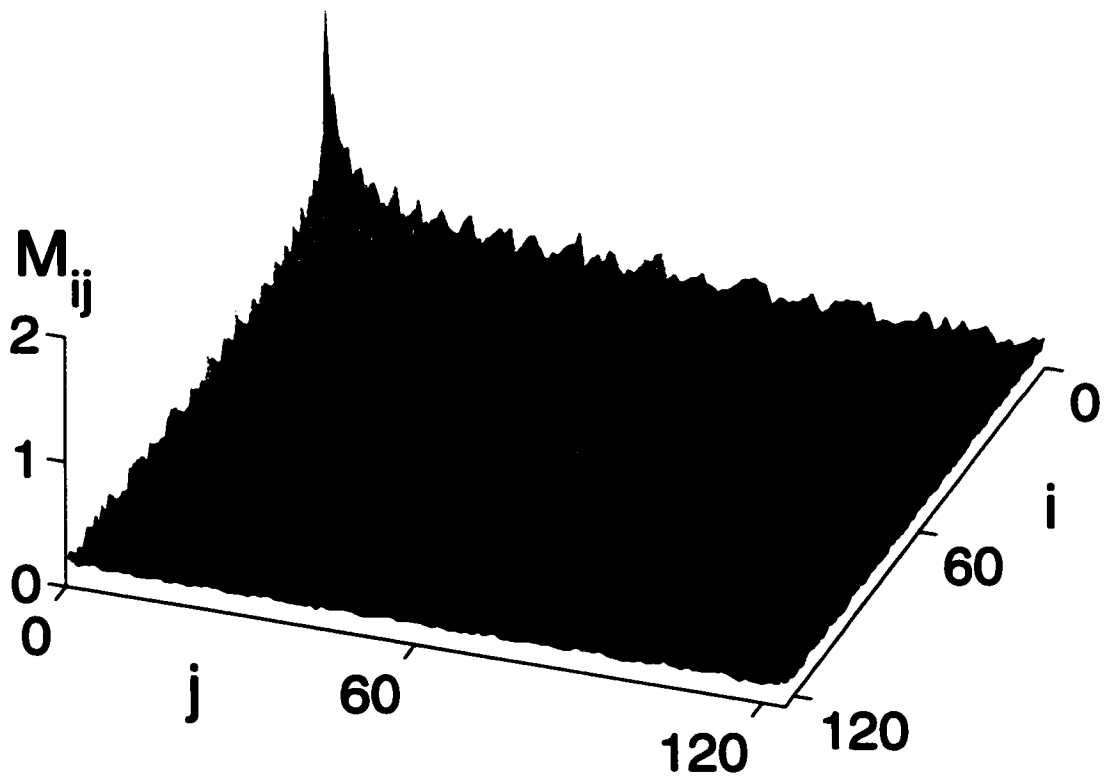


Figure 11.8: The matrix elements M_{ij} are plotted for the TRNI system with the coupling constant $\lambda = -0.80$. M_{ij} is not scaled by the mean level spacing in this figure. The ranges of indices are $i, j = 0$ to 124. The parity sequence is set to $(+, +)$.

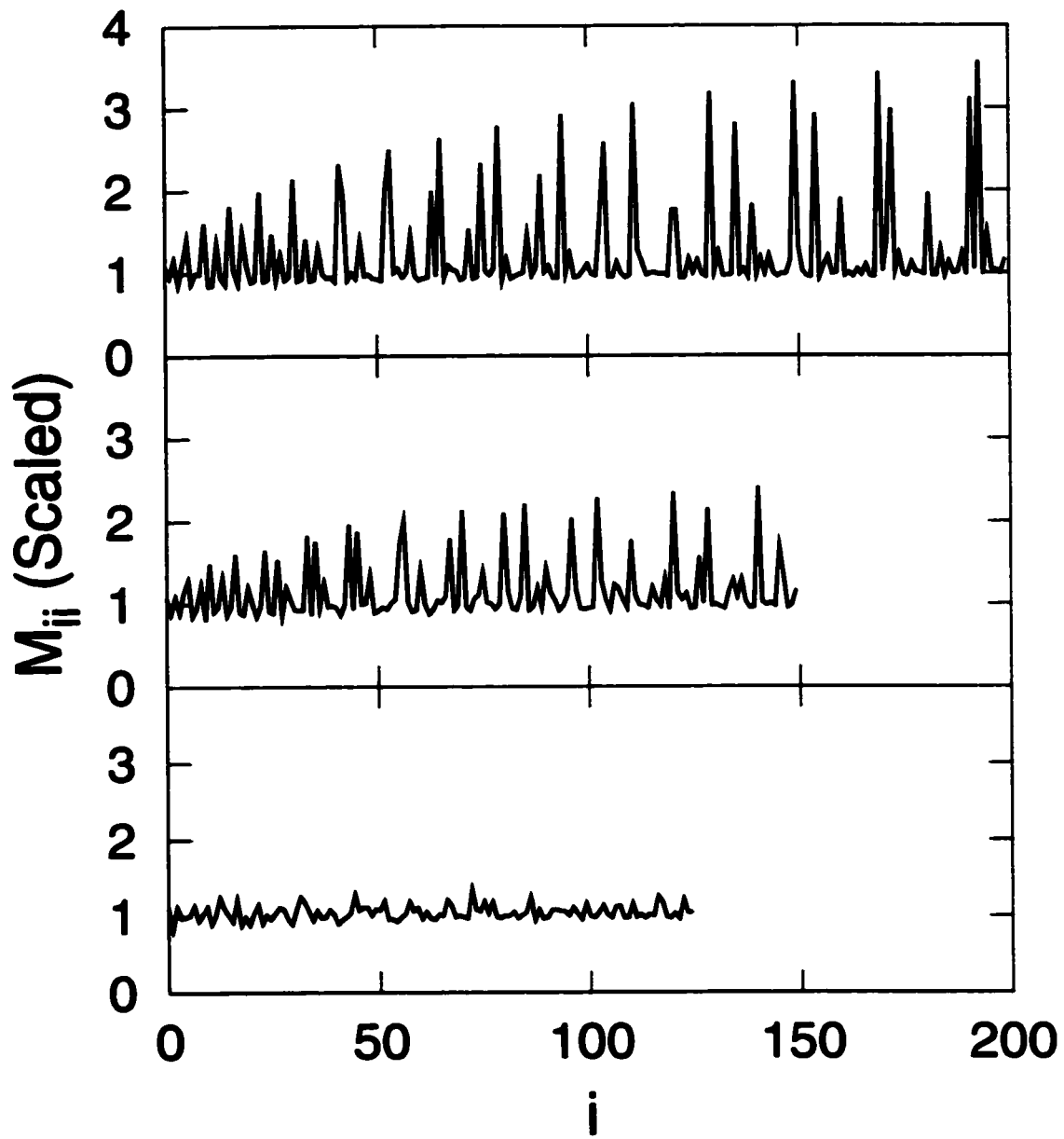


Figure 11.9: Diagonal elements of M_{ij} ($i = j$) versus orbital number i for the system of all anti-unitary symmetry broken. M_{ii} are scaled by the single-particle mean level spacing of the energy levels. Top figure: coupling constant $\lambda = 0.20$, middle: $\lambda = -0.20$, and bottom: $\lambda = -0.80$. Data have been calculated for the lowest 200, 150, and 125 orbitals for $\lambda = 0.20, -0.20$, and -0.80 respectively.

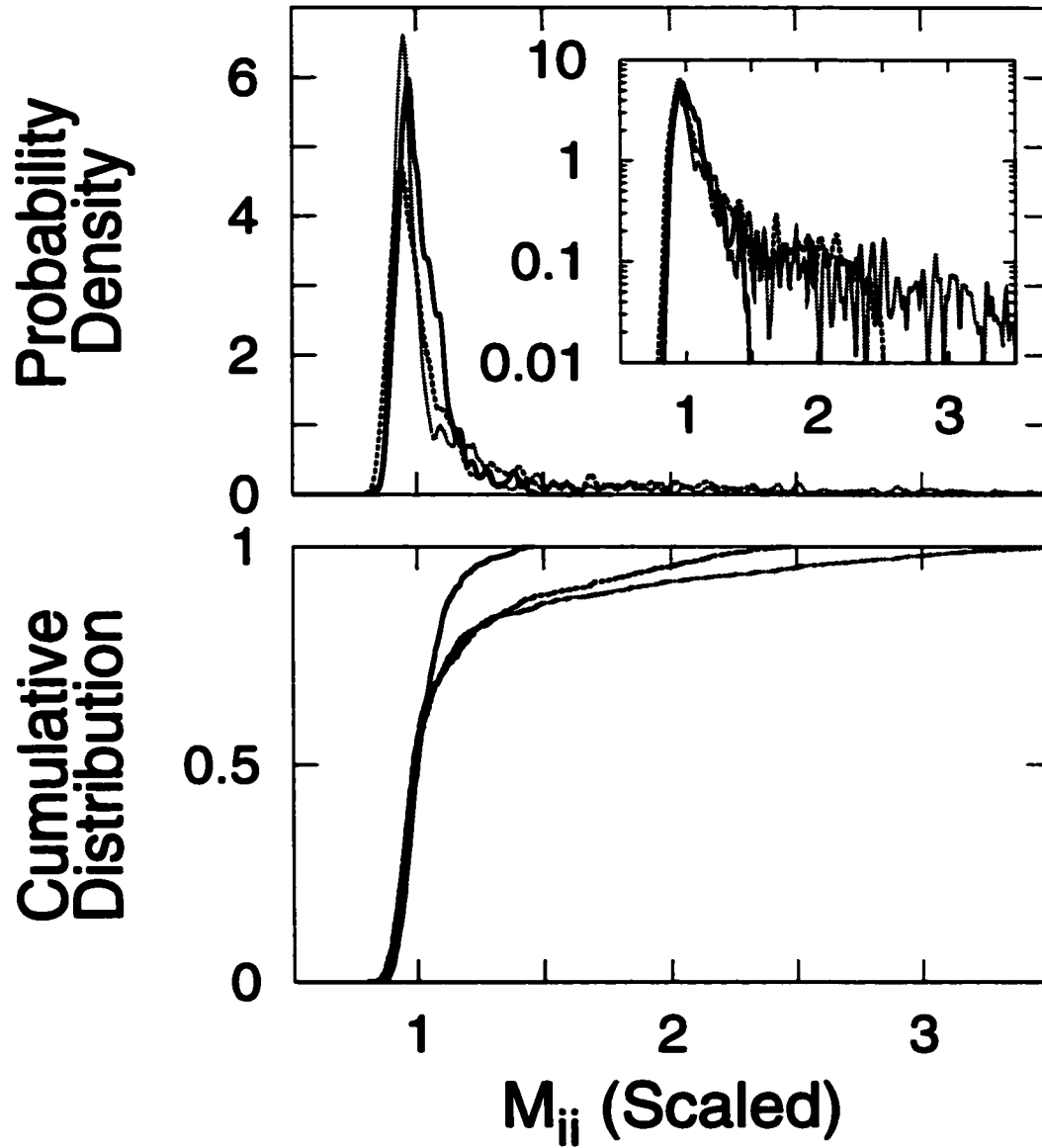


Figure 11.10: Distribution of diagonal elements M_{ii} for the system of all anti-unitary symmetry broken. M_{ii} are scaled by the single-particle mean level spacing of orbitals. Top figure: probability density, bottom: cumulative distribution. Inset: the same probability density but on a logarithmic scale to show long tail on the right side. For all figures, $\lambda = 0.20, -0.20$, and -0.80 are represented by dotted, dashed, and solid lines, respectively.

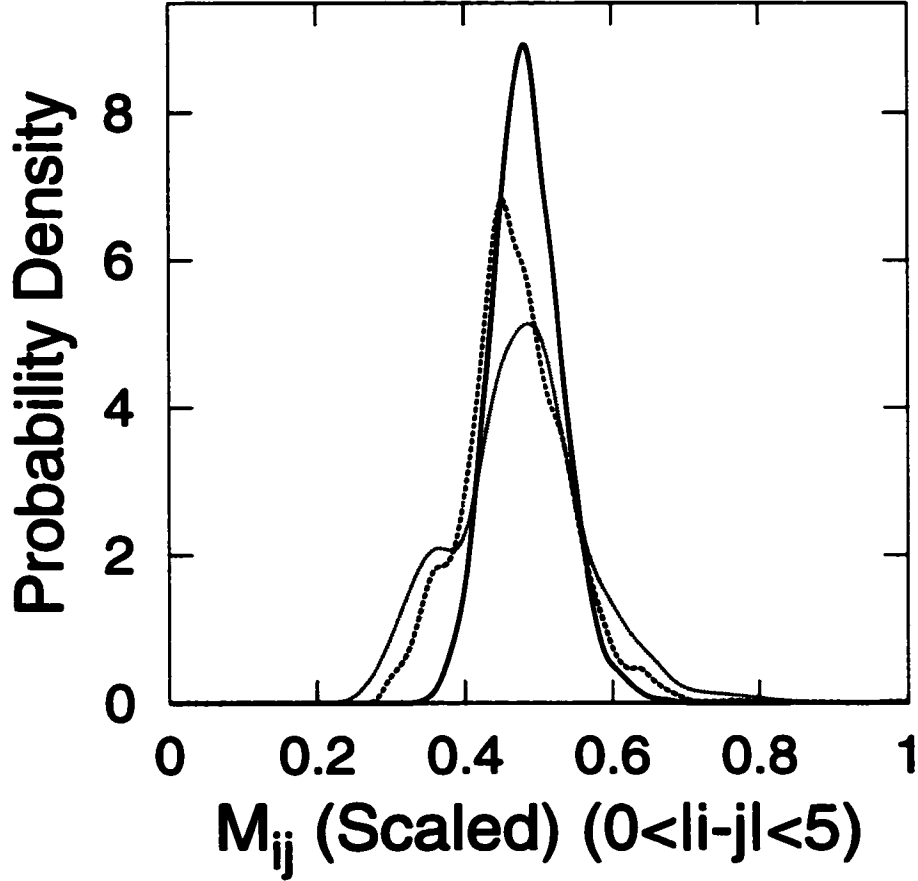


Figure 11.11: Distribution (probability density) of off-diagonal elements M_{ij} for the system of all anti-unitary symmetry broken. M_{ij} are scaled by the single-particle mean level spacing of the energy levels Δ_i . Only the near diagonal elements ($0 < |i - j| < 5$) are used. $\lambda = 0.20, -0.20$, and -0.80 are represented by dotted, dashed, and solid lines respectively.

Moments	Integrable	Mixed	Chaotic
1	1.181882	1.118237	1.023174 [1.0]
2	0.2481074 ($\sigma = 0.4981038$)	0.1048870 ($\sigma = 0.3238626$)	1.012331×10^{-2} [0.6494882×10^{-2}] ($\sigma = 0.1006146$)
3	3.352951×10^{-1} ($\gamma_1 = 2.713111$)	7.461422×10^{-2} ($\gamma_1 = 2.196540$)	1.506123×10^{-3} ($\gamma_1 = 1.478689$)
4	6.152538×10^{-1} ($\gamma_2 = 6.994819$)	7.987730×10^{-2} ($\gamma_2 = 4.260726$)	5.921898×10^{-4} ($\gamma_2 = 2.778512$)

Table 11.1: Moments of scaled M_{ii} distribution for quartic oscillator system in TRNI case. The first four moments are calculated for the near-integrable, mixed, and chaotic regimes. Standard deviation σ , skewness γ_1 , and kurtosis γ_2 are also computed for each related moment. The values in the square brackets are obtained by the analytical expressions with $N = 500$ given in Appendix F. All the higher moments (≥ 3) vanish in the large N limit according to Ullmo and Baranger [94].

Chapter 12

Random Superposition of Plane Waves

In the study of quantum systems whose classical counterparts exhibit chaotic behavior, Berry [124,125] made the conjecture that the spatially irregular wave functions, not too close to the boundaries, were well approximated by a random superposition of plane waves. Let us abbreviate it as PWSA - plane wave superposition approximation. The construction of wave functions is given as

$$\phi(\mathbf{r}) = \sum_n a_n \exp(i\mathbf{k}_n \cdot \mathbf{r}) \quad (12.1)$$

where each plane wave has a random amplitude and random phase shift, and also a random orientation of the wave vector with constant modulus. Unlike an eigenstate of a bound system, the random plane wave completely ignores the boundary conditions. However, the approximation is good as long as the wavelength is small compared to the system scale. As a consequence of the approximation, the spatial correlations of an irregular eigenfunction is given in terms of a zeroth-order Bessel function of the first kind whose argument depends only on the energy and the distance, $\langle \phi_\epsilon(\mathbf{r}_1) \phi_\epsilon(\mathbf{r}_2) \rangle = \text{const} \times J_0(k|\mathbf{r}_1 - \mathbf{r}_2|)$ where $\epsilon = (\hbar k)^2/2m$. This was verified by McDonald and Kaufman [126,127] in their numerical study of the stadium billiard system.

In contrast to the familiar speckle pattern of random waves, O'Connor *et al.* [128] found that the waves always show a network of ridge structure and mentioned the possible connection to the periodic orbit localization of wave functions called scarring [129,130]. For

the spatial correlation function, Prigodin *et al.* [131] investigated chaotic systems with time-reversal symmetry and explained the experimental wave functions in microwave cavities. Prigodin [132] also studied the case of broken time-reversal symmetry and derived a joint probability for the given electron density at two different space points within the same eigenstate. Srednicki [133] obtained the same result of the spatial correlations in wave functions of quantum dots using Berry's conjecture to simplify the approach. Since there exists a large number of studies employing the random wave idea, we only introduce a few; others can be found elsewhere [134].

12.1 Construction of Wave Functions

To construct wave functions for the time-reversal invariant system, only the real part of plane waves must be taken, while for the broken time-reversal system, each plane wave must be complex. Since there is no spatial reflection symmetry in PWSA, the presence or absence of time-reversal symmetry characterizes the system's statistical behavior, GOE or GUE respectively. As stated in the introduction, a two-dimensional wave function is built by

$$\phi(x, y) = \sum_n a_n \exp[i(k_x^n x + k_y^n y + 2\pi\delta_n)]. \quad (12.2)$$

We use Gaussian distributed random numbers [135] for the amplitudes a_n , and uniformly distributed random numbers for the phases δ_n ($0 \leq \delta_n \leq 1$) and the direction of the wave vectors \mathbf{k}^n . More precisely, given uniformly distributed random numbers κ_n between 0 to 1,

the two components of the wave vector are given by

$$k_x^n = k^n \cos(2\pi\kappa_n) \quad (12.3)$$

$$k_y^n = k^n \sin(2\pi\kappa_n), \quad (12.4)$$

where the magnitude of the wave vector, $(k^n)^2 = (k_x^n)^2 + (k_y^n)^2$, is fixed to be constant.

To mimic the eigenstates of the coupled quartic oscillators (in the chaotic regime), let us first consider the following. Combining all four parity sequences of eigenstates of the quartic oscillator, the smooth part of the counting function is given by Eq. (10.18)

$$\bar{N}_{\text{Q.O.}}(E_{\text{Q.O.}}) \simeq E_{\text{Q.O.}}^{3/2} + O(1) \quad (12.5)$$

using only the lowest order term. For a given energy and a mode coupling constant λ not too close to -1 , the area of the classically allowed region can be approximated by a rectangle. The area of the rectangle can be defined by the turning points, $|x| \leq x_{\text{turn}}$ and $|y| \leq y_{\text{turn}}$, as follows

$$A_{\text{Q.O.}} \simeq 2x_{\text{turn}} \cdot 2y_{\text{turn}} = 4a(\lambda)^{-1/2} N_{\text{Q.O.}}^{1/3}, \quad (12.6)$$

where the classical turning points along the x and y axes are given as

$$x_{\text{turn}}(N_{\text{Q.O.}}) = (b/a)^{1/4} N_{\text{Q.O.}}^{1/6} \quad (12.7)$$

$$y_{\text{turn}}(N_{\text{Q.O.}}) = (ab)^{-1/4} N_{\text{Q.O.}}^{1/6} \quad (12.8)$$

with $E_{\text{Q.O.}} = N_{\text{Q.O.}}^{2/3} = a(x^4/b + by^4 + 2\lambda x^2y^2)$.

In contrast, for the system of PWSA, we assume the two-dimensional infinite potential well to confine the system. The smooth part of the counting function is

$$\bar{N}(E) = \int \frac{d\mathbf{q}d\mathbf{p}}{h^d} \Theta(E - H(\mathbf{q}, \mathbf{p})) = \frac{mA}{2\pi\hbar^2} E, \quad (12.9)$$

where A represents the area of the bounded region, $d = 2$ is the degree of freedom, and the spin degeneracy is not considered. It should be mentioned that the system does not require the wavefunctions to vanish at the boundary. Using Eq. (12.9), the wave number is given by

$$k = \frac{\sqrt{2mE}}{\hbar} = \sqrt{\frac{4\pi N}{A}}, \quad (12.10)$$

where \bar{N} is shortened by N . In addition, the mean level spacing is expressed as

$$\Delta_N = \frac{1}{dN/dE} = \frac{2\pi\hbar^2}{mA}. \quad (12.11)$$

Now, to make connection between the PWSA system and the quartic oscillator system, we set the counting functions and the area of the classical bounded region as follows

$$\bar{N}(E) \equiv \bar{N}_{\text{Q.O.}}(E_{\text{Q.O.}}) \quad (12.12)$$

$$A(N) \equiv A_{\text{Q.O.}}(N_{\text{Q.O.}}). \quad (12.13)$$

Then, the wave number and the mean level spacing are written as

$$k(N_{\text{Q.O.}}) = \sqrt{\pi} a(\lambda)^{1/4} N_{\text{Q.O.}}^{1/3}. \quad (12.14)$$

$$\Delta(N_{\text{Q.O.}}) = \frac{\pi \hbar^2}{2m} \sqrt{a(\lambda)} N_{\text{Q.O.}}^{-1/3}, \quad (12.15)$$

and the i th quartic oscillator eigenstate is approximated by the PWSA wavefunction of wave number $k(i)$ and boundary given by $|x| \leq x_{\text{turn}}(i)$ and $|y| \leq y_{\text{turn}}(i)$. We note that the equivalence in Eq. (12.12) does not necessary mean the equality between E and $E_{\text{Q.O.}}$. Since Eq. (12.5) does not carry quantum mechanical fluctuation information, one must employ RMT to study energy spectra of PWSA if needed.

12.2 Validity of the Plane Wave Superposition Approximations

To verify the validity of our approach, we compare the level of complexity of the quartic oscillator and a PWSA system. As the measure of complexity, we count the number of nodes in the wave functions along x and y axes. Nodes are counted simply by recording the number of points where the second derivative of the wave function along each axes changes sign. We use the eigenstates of the TRI (time-reversal invariant) case as a reference since there are 600 eigenstates available in the chaotic regime ($\lambda = -0.55$). Due to the reflection symmetries of the quartic oscillator, odd parity gives node count zero. Figure (12.1) shows the node

count comparison of the quartic oscillator eigenstates and the PWSA wave functions. As a result, PWSA reconstructs the eigenstates reasonably well. Especially the overall trends of how node numbers increases shows close similarities to the curve based on the full quantum calculations.

12.3 Distribution of Diagonal Elements M_{ii}

In the last two sections, we studied dynamical systems, using the coupled quartic oscillator as an examples and characterized the statistical behavior of the residual interaction by analyzing the matrix elements M_{ij} . It was found that the magnitude of the matrix elements, especially the diagonal elements, were pronounced and comparable to the mean level spacings. To investigate the role of the diagonal elements from a different perspective, we now consider a non-dynamical system represented by PWSA. Compared to explicitly defined dynamical systems (such as the quartic oscillator systems), PWSA (non-dynamical) systems allow us to calculate eigenstates in a high energy domain easily. Therefore, it gives us a means to observe asymptotic behavior of the matrix elements M_{ii} .

We consider three energy domains represented by the orbital number i , $1 \leq i \leq 600$, $2000 \leq i \leq 2500$, and $5000 \leq i \leq 5500$, and denote them as low, middle, and high energy domains, respectively. The low energy domain is designed to simulate the same range as existing exact quantum mechanical eigenstate data of the quartic oscillator. For PWSA wavefunctions, 100 plane waves are superposed, and each wavefunction is normalized over the bounded region of area A . There are roughly 15, 25, and 40 wavelength on the shorter

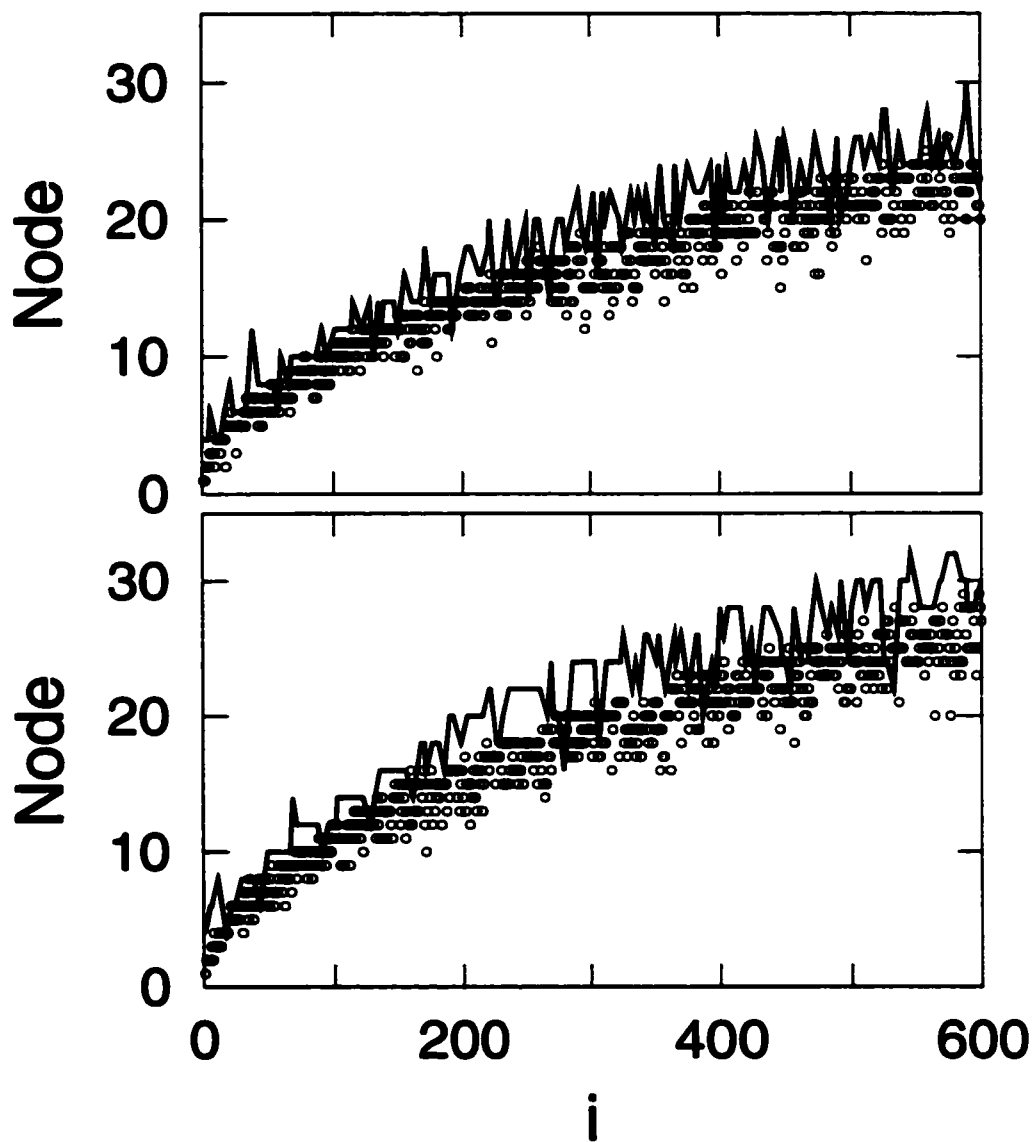


Figure 12.1: Node counts of wave functions vs. orbital number. For both, the coupled quartic oscillator eigenstates and the PWSA wave functions, the number of nodes are counted along the x axis (top) and the y axis (bottom). A solid line represents the number of nodes for the quartic oscillator eigenstates ((+, +) reflection symmetry only) and circles that for the PWSA wave functions.

side of the rectangular boundary for the low, middle, and high energy domains, respectively. These estimations are given by

$$\frac{2x_{\text{turn}}}{\lambda} = \pi^{-1/2} b^{1/4} N^{1/2}, \quad (12.16)$$

where λ donates the wavelength of the plane waves. Figure (12.2) shows the real part of the complex wavefunction for the three different energy domains.

The M_{ii} diagonal elements M_{ii} are computed by directly proceeding the integration of wavefunction over the boundary of the area A ($M_{ii} = \int_A d\mathbf{r} |\phi_i|^4$), and then we scale M_{ii} by the mean level spacing given by Eq. (12.15). To reduce the size of the statistical error bar, 20 (30 for the low energy domain) sets of data ensemble are calculated for each energy domain. For TRI case, wavefunctions are real and constructed only by cosine waves. In Fig. (12.3), the scaled M_{ii} are shown as a function of the orbital number i . In contrast to the previous dynamical case, there are no pronounced peaks observed since the spatial localization of wavefunctions cannot occur in the PWSA systems. However, in the low energy domain, PWSA captures well the lower bound of fluctuations around $M_{ii}/\Delta_i \sim 1.4$ and it is slowly increasing. In the middle and high energy domain, the fluctuations become smaller and remain closer to their mean. The statistical distributions of the matrix elements are shown in Fig. (12.4). In the low energy domain, the first 200 wavefunctions are dropped and the following 400 stable states are used for the statistics. Due to the absence of localized states, the width of the distribution is narrow compared to the distributions obtained within the quartic oscillator systems. The mean value is slowly increasing, and the width becomes even

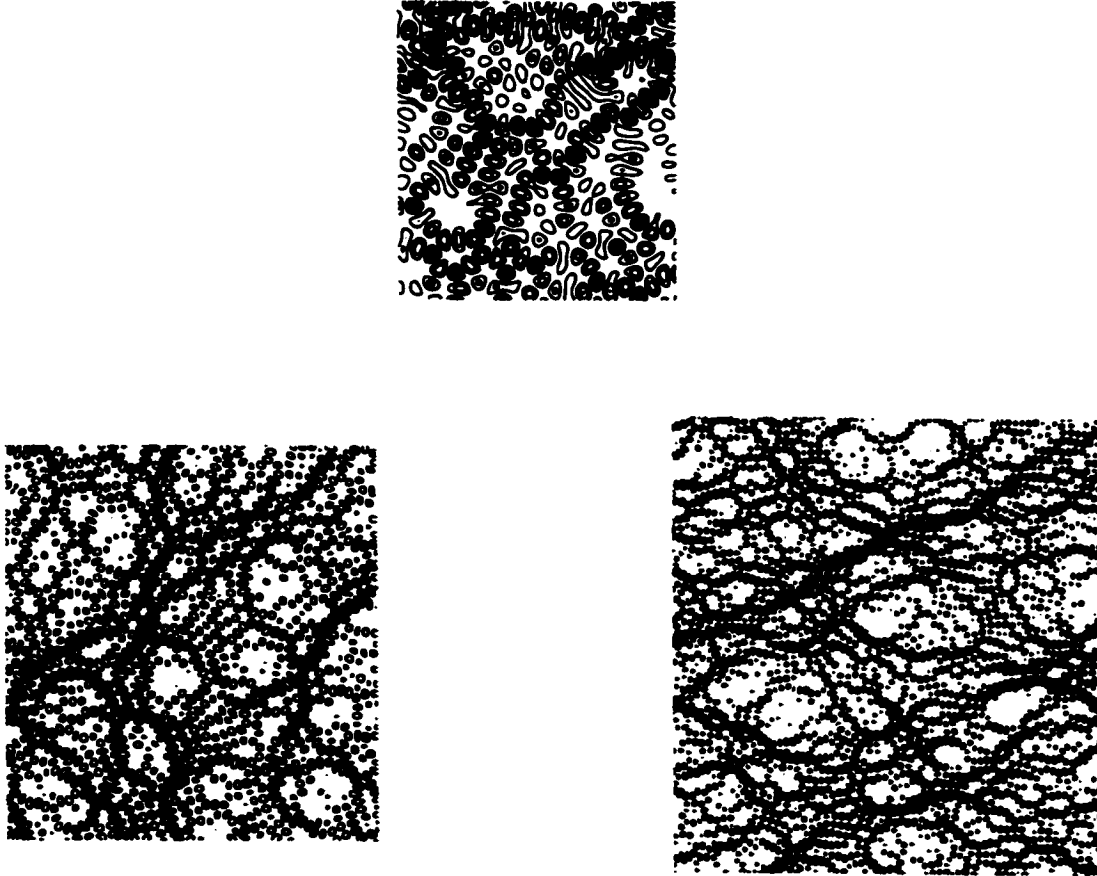


Figure 12.2: Contour map of random superpositions of plane waves for three energy domains. Based on the energy scale of quartic oscillator system, corresponding effective orbital numbers are 400 (top), 2200 (bottom left), and 5200 (bottom right) for the low, middle, and high energy domains respectively (see text for detail). Contours are set to constant, and all figures are shown at the same magnification. Only the real part of the complex waves is shown, and the imaginary part is similar. The wave functions are constructed with 100 cosine (sine for imaginary part) waves. Each wave has a Gaussian random amplitude, a random orientation of wave vector, and a random phase shift.

Moments	Low Energy	Middle Energy	High Energy
1	1.383437 [1.5]	1.443644 [1.5]	1.448141 [1.5]
2	2.417734×10^{-3} [3.582661×10^{-3}] ($\sigma = 4.917045 \times 10^{-2}$)	6.314935×10^{-4} [8.465977×10^{-4}] ($\sigma = 2.512953 \times 10^{-2}$)	3.298077×10^{-4} [4.137801×10^{-4}] ($\sigma = 1.816061 \times 10^{-2}$)
3	8.216135×10^{-5} ($\gamma_1 = 6.911223 \times 10^{-1}$)	9.614301×10^{-6} ($\gamma_1 = 6.058490 \times 10^{-1}$)	2.100260×10^{-6} ($\gamma_1 = 3.506566 \times 10^{-1}$)
4	3.259792×10^{-5} ($\gamma_2 = 2.576644$)	2.091303×10^{-6} ($\gamma_2 = 2.244198$)	4.520104×10^{-7} ($\gamma_2 = 1.155534$)

Table 12.1: Moments of scaled M_{ii} distribution for PWSA system in TRI case. First four moments are calculated for the low, middle, and high energy domain. Standard deviation σ , skewness γ_1 , and kurtosis γ_2 are also computed for each related moment. The values in the square brackets are obtained by the analytical expressions with $N = 500, 2500, 5500$ for each energy domain; see Appendix F. All the higher moments (≥ 3) vanish in the large N limit according to Ullmo and Baranger [94].

narrower as energy increases. Table (12.1) shows moments of the distributions. The third and fourth moments decrease as energy increases indicating the distribution is slowly shifting towards the Gaussian.

For TRNI case, wave functions are constructed with complex plane waves including both sine and cosine parts. To study the behavior of M_{ii} , we compare two scaled M_{ii} data sets, one for the dynamical system in chaotic regime by the quartic oscillator (Fig. (11.9)) and the other for the non-dynamical case in low energy domain by PWSA (Fig. (12.5)). It should be noted that for the dynamical system, the orbital number must be multiplied by the factor of four to compare with one of PWSA due to the parity sequence decomposition. Following properties are observed in the PWSA system, but they are basically the same as in the case of TRI: there is no large pronounced peak, the fluctuations are smaller than the dynamical

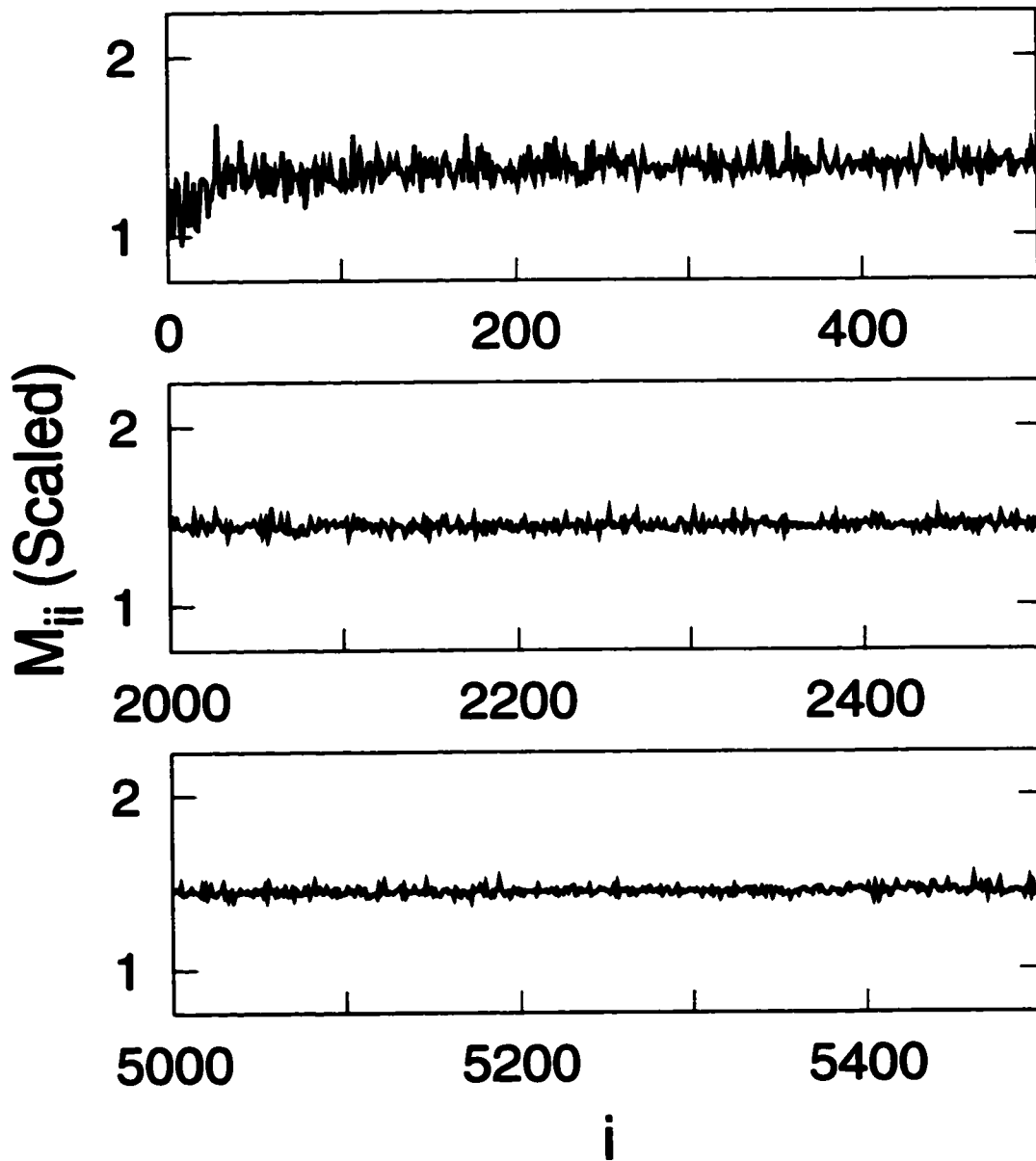


Figure 12.3: Diagonal elements of M_{ij} ($i = j$) versus orbital number i for the system of the real random superposition of plane waves. M_{ii} are scaled by the single-particle mean level spacing. Top figure: the lowest energy domain $i = 0$ to 500, middle: the middle energy domain $i = 2000$ to 2500, and bottom: the highest energy domain $i = 5000$ to 5500.

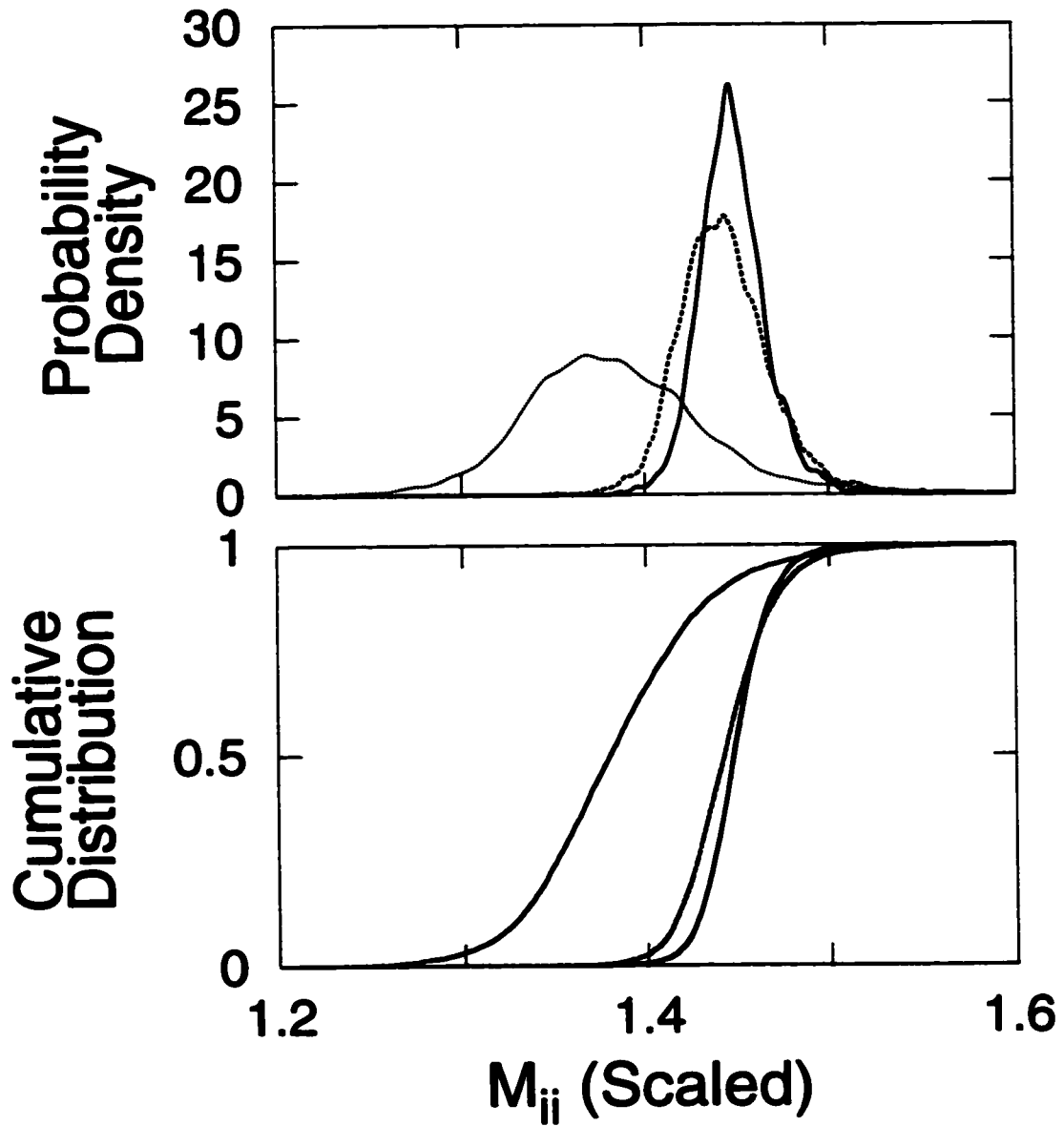


Figure 12.4: Distribution of diagonal elements M_{ii} for the system of the real random superposition of plane waves. M_{ii} are scaled by the single-particle mean level spacing. Top figure: probability density, bottom: cumulative distribution. For both figures, the lowest, middle and the highest energy domains are represented by dotted, dashed, and solid lines respectively.

Moments	Low Energy	Middle Energy	High Energy
1	0.9248654 [1.0]	0.9674039 [1.0]	0.9688490 [1.0]
2	1.824599×10^{-3} [0.5971102×10^{-3}] ($\sigma = 4.271532 \times 10^{-2}$)	1.357828×10^{-4} [1.411000×10^{-4}] ($\sigma = 1.165259 \times 10^{-2}$)	6.968438×10^{-5} [6.896335×10^{-5}] ($\sigma = 8.347717 \times 10^{-3}$)
3	-2.460342×10^{-5} ($\gamma_1 = -0.3156781$)	5.196338×10^{-7} ($\gamma_1 = 0.3284205$)	1.016164×10^{-7} ($\gamma_1 = 0.1746870$)
4	4.549127×10^{-5} ($\gamma_2 = 10.66449$)	7.732884×10^{-8} ($\gamma_2 = 1.194227$)	1.871578×10^{-8} ($\gamma_2 = 0.8542240$)

Table 12.2: Moments of scaled M_{ii} distribution for PWSA system in TRNI case. First four moments are calculated for the low, middle, and high energy domain. Standard deviation σ , skewness γ_1 , and kurtosis γ_2 are also computed for each related moment. The values in the square brackets are obtained by the analytical expressions with $N = 500, 2500, 5500$ for each energy domain; see Appendix F. All the higher moments (≥ 3) vanish in the large N limit according to Ullmo and Baranger [94].

system and they are around the mean value of ~ 1.0 , the PWSA regenerate the lower bound of oscillation, and the fluctuation reduces as one increases the energy. The distribution of M_{ii} is shown in Fig. (12.6). The long tail observed in the dynamical system is completely washed out, and the distribution is symmetric about the mean value. We note how small the third moment is, as opposed to the dynamical case; see Table (12.2). As the energy increases, the higher moments (≥ 3) are being diminished, and so the distributions are changing into one of Gaussian.

Overall, the tendency of the M_{ii} distributions are gradually shifting into Gaussian distribution for both TRI and TRNI systems. In the energy domain of typical quantum dots, which corresponds to the low energy domain of the PWSA systems, there is no such indication detected. The PWSA requires system to have large boundary compare to the wavelength of

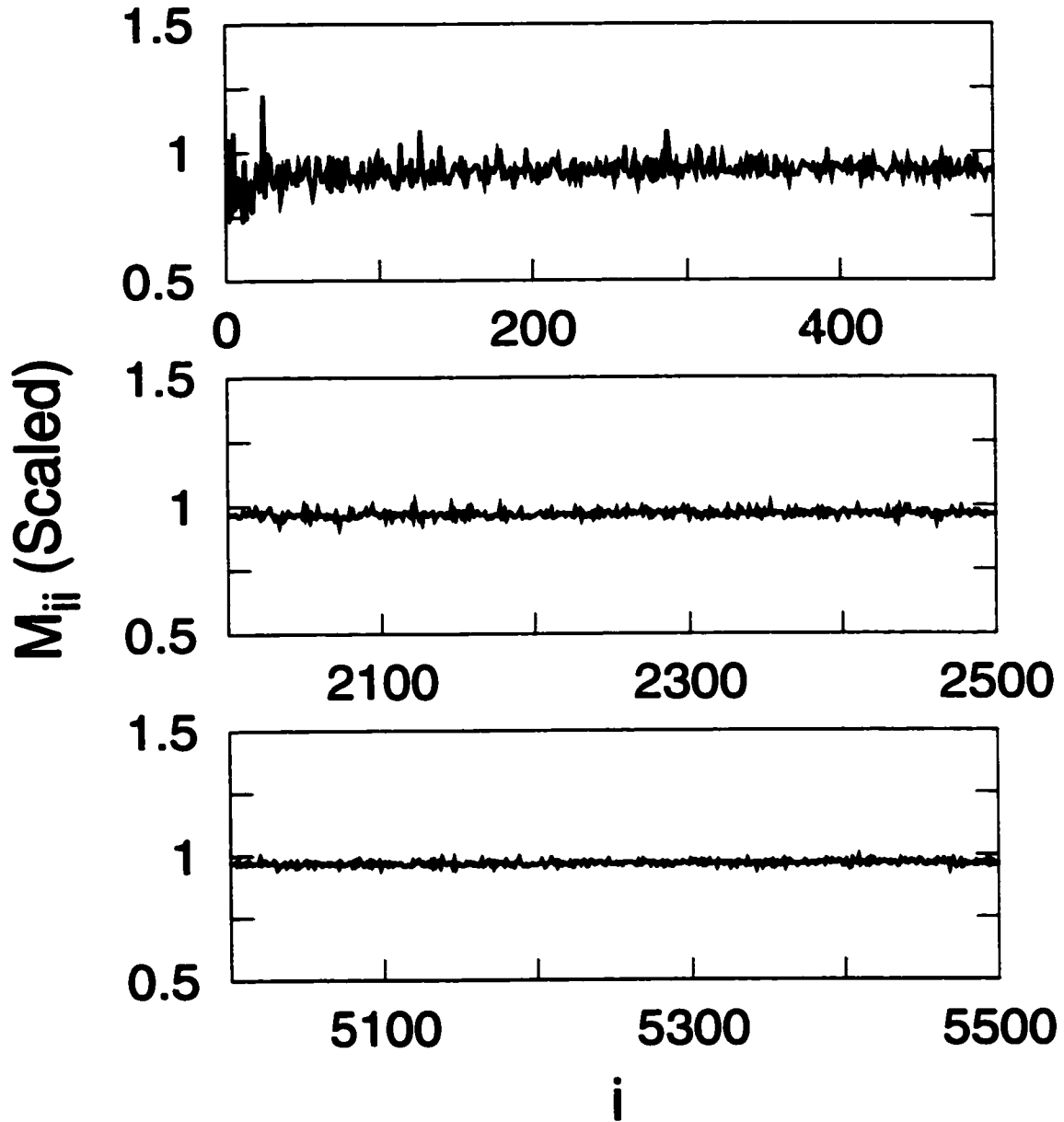


Figure 12.5: Diagonal elements of M_{ij} ($i = j$) versus orbital number i for the system of the complex random superposition of plane waves. M_{ii} are scaled by the single-particle mean level spacing. Top figure: the lowest energy domain $i = 0$ to 500, middle: the middle energy domain $i = 2000$ to 2500, and bottom: the highest energy domain $i = 5000$ to 5500.

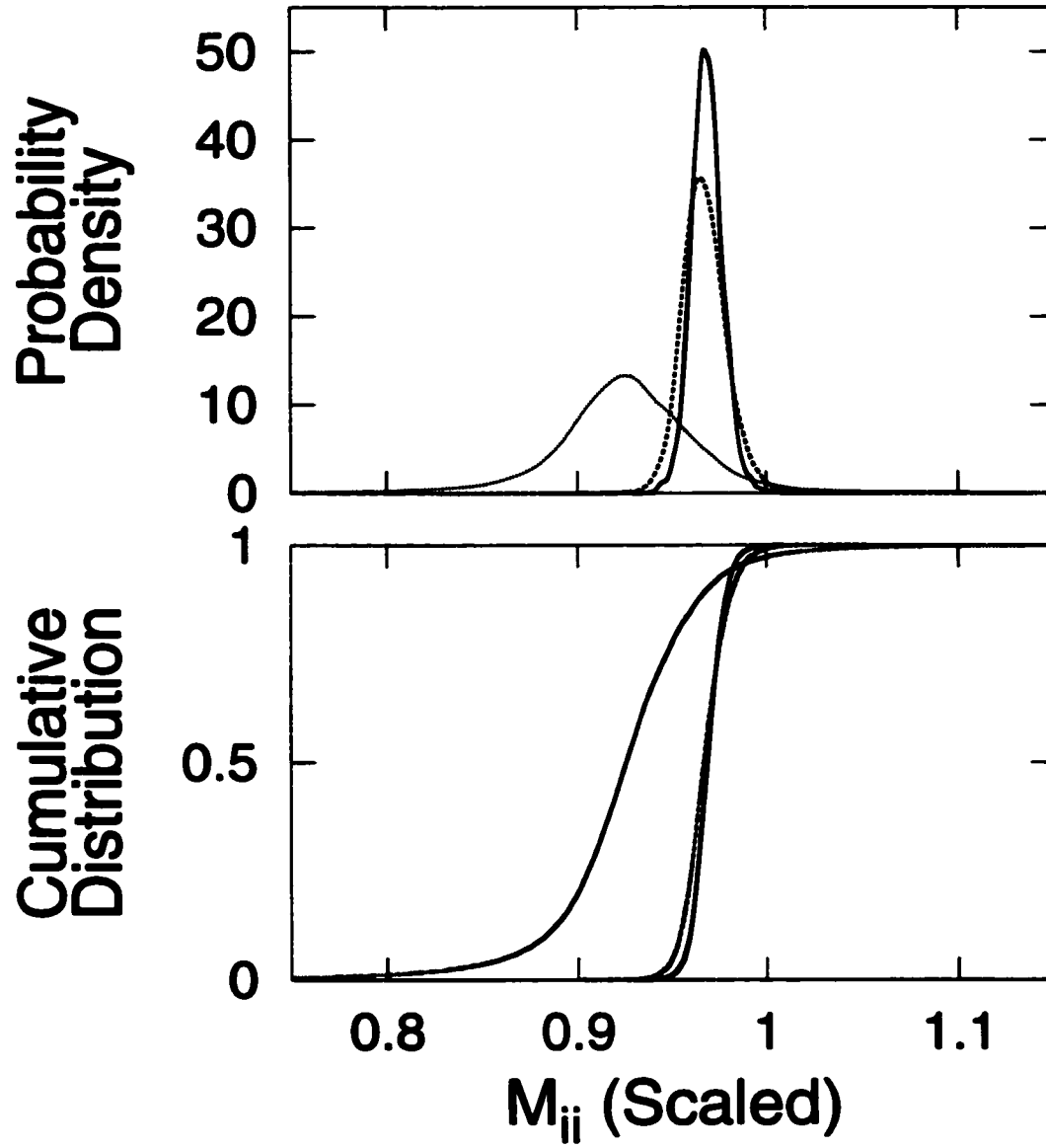


Figure 12.6: Distribution of diagonal elements M_{ii} for the system of the complex random superposition of plane waves. M_{ii} are scaled by the single-particle mean level spacing. Top figure: probability density, bottom: cumulative distribution. For both figures, the lowest, middle and the highest energy domains are represented by dotted, dashed, and solid lines respectively.

plane waves for validity. In the low energy domain, there are only 15 wavelengths along one side of the boundary. However, this is compensated by having an ensemble of 30 data sets to ensure the randomness of the statistically independent data. As discussed in Ref. [128], a network of ridge structure can be found in the PWSA wavefunctions especially in the wavefunctions of the high energy domain although it seems there is no significant role in the distribution of M_{ii} .

12.4 Fluctuations of M_{ii}

For the TRI system, the size of the diagonal elements M_{ii} are roughly 1.5Δ ($M_{ii} \sim \Delta$ for the TRNI system), almost independent of orbital numbers or at least slowly converging to the values. However, the variance of the M_{ii} distribution decreases as the energy increases. To learn more about the behavior of the two moments, we employ analytical formulae derived by Ullmo and Baranger [94]. Based on Berry's conjecture, they obtained the following expressions using the spatial correlation function $A \langle \phi(\mathbf{r}_1) \phi^*(\mathbf{r}_2) \rangle = J_0(k_F |\mathbf{r}_1 - \mathbf{r}_2|)$, where A is the area of confined region and k_F is Fermi wave vector. With the local approximation to the screened interaction, mean and variance are given as

$$\langle M_{ij} \rangle = (1 + \delta_{ij}) \frac{\Delta}{2} \quad (12.17)$$

$$\text{var}(M_{ij}) = \frac{3\Delta^2 \ln(k_F L)}{4\pi (k_F L)^2} (1 + 3\delta_{ij}) \quad (12.18)$$

where L is size of the confined region, and their system belongs to TRNI case. For TRI case, the means and variances of the diagonal elements are related as $\langle M_{ii}^{\text{TRI}} \rangle = 1.5 \langle M_{ii}^{\text{TRNI}} \rangle$ and $\text{Var}(M_{ii}^{\text{TRI}}) = 6.0 \text{Var}(M_{ii}^{\text{TRNI}})$; see Appendix F. While their expression uses $k_F L$ as a parameter, our variance depends on the orbital numbers, so one needs to know the connection between $k_F L$ them. In our expression, the wave vector and system size were

$$\begin{aligned}
 k &= \sqrt{\pi} a^{1/4} N^{1/3} \\
 L &= 2y_{\text{turn}} = 2(ab)^{-1/4} N^{1/6} \\
 \Rightarrow \quad kL &= \sqrt{2^3 \pi^{1/2} N}
 \end{aligned} \tag{12.19}$$

where N represents the orbital number. Their estimate gives $kL = \sqrt{4\pi N}$ (where N is converted from their particle number to the orbital number), and two estimates roughly agrees. The numerical data and the analytical results are compared in Table (12.1) and (12.1) for the TRI and TRNI cases respectively. For both cases, the means and variances show reasonable agreements. The numerical data seem to converge slowly into the analytical predictions as the energy increases.

Chapter 13

Peak Spacing distribution and Ground State Spin Polarization

The study of the behavior of the residual interaction mainly focused on the matrix elements M_{ij} . In this section, the ground state and CB conductance peak spacings are constructed using the result of the M_{ij} calculations. In addition, the statistical properties of the spacing distribution and the spin polarization of the ground states are considered for the TRNI coupled quartic oscillator system.

13.1 Ground State Energy

Let us first start with calculating the ground state energy of an N-electron system. As expressed in Eq. (9.12), the total energy is given as

$$E_N(\{n_{i\sigma}\}) = E_{\text{GTF}} + \sum_{i\sigma} n_{i\sigma} \delta\epsilon_i + \frac{\zeta}{2} \sum_{i,j;\sigma \neq \sigma'} n_{i\sigma} M_{ij} n_{j\sigma'}$$

using the local approximation to the screened potential. The ground state is obtained by finding the combination of occupation numbers $\{n_{i\sigma}\}$ which minimizes $E_N(\{n_{i\sigma}\})$ under the constraint $N = \sum n_{i\sigma}$. It is obvious that the orbital occupation becomes the standard up/down filling if the residual interaction is turned off, taken into account the electron spin degree of freedom. By the standard up/down filling, we mean the following. Consider the

system which contains N electrons. When N is even, the lowest $N/2$ orbitals are doubly occupied, and when N is odd, the lowest $(N - 1)/2$ orbitals are double occupied and the last $(N + 1)/2$ orbital is singly occupied. Once the residual interaction is turned on, the above picture does not always give a valid description. Since it costs energy when two electrons have opposite spins (this is the special case when the screened potential is local), sometimes the system promotes one electron to the next higher orbital to lower the total energy. This situation is likely to happen when the size of a particular M_{ij} is comparable to the mean level spacing.

To illustrate this effect, we consider the following example. The total energy of the N -electron system can be rewritten as

$$E_N = E_c + \sum_{i\sigma} n_{i\sigma} \epsilon_i + \frac{\zeta}{2} \sum_{i,j;\sigma \neq \sigma'} n_{i\sigma} M_{ij} n_{j\sigma'}. \quad (13.1)$$

where we note that the first two terms are replaced by the CI model expression. This is safely done since the levels of approximation for the CI model and the first order Strutinsky method are proven to be equivalent. Now, we describe the total energy in two cases: the standard filling

$$E_N^{(s)} = E_c + 2 \sum_{i=1}^n \epsilon_i + \zeta \sum_{i,j=1}^n M_{ij}, \quad (13.2)$$

and the case of promoting one electron at the last orbital to the next energy level while at

the same time changing its spin orientation,

$$\begin{aligned}
E_N^{(p)} &= E_c + 2 \sum_{i=1}^n \epsilon_i - \epsilon_n + \epsilon_{n+1} + \zeta \left(\sum_{i,j=1}^n M_{ij} - \sum_{j=1}^n M_{n,j} + \sum_{j=1}^{n-1} M_{n+1,j} \right) \\
&= E_N^{(s)} + \epsilon_{n+1} - \epsilon_n + \zeta \left[\sum_{j=1}^{n-1} (M_{n+1,j} - M_{n,j}) - M_{nn} \right].
\end{aligned} \tag{13.3}$$

The superscript 's' and 'p' represent the case of standard filling and promotion of one electron, respectively, the orbital number n is $N/2$ (even N is considered for simplicity), and the factor of 2 on each summation is due to the spin degeneracy. Neglecting the off-diagonal M_{ij} contribution, the following relation is derived,

$$\zeta M_{nn} > \epsilon_{n+1} - \epsilon_n \sim \Delta_n \implies E_N^{(p)} < E_N^{(s)}. \tag{13.4}$$

It means that when the diagonal elements M_{nn} are large enough to be comparable to the mean level spacing Δ_n , the residual interaction between two electrons at the last n th level becomes costly, so the system promotes one of them to the next orbital. In general, both diagonal and off-diagonal elements are expected to come into play, and so the standard up/down filling does not always give the lowest energy. Therefore, the residual interaction can lead to unusual orbital occupations that define the ground state of the system.

13.2 Conductance Peak Spacings

The interplay of the matrix elements M_{ij} and the single-particle energy plays a significant role in determining the ground state orbital occupation, and it is expected that the conductance peak spacings show the influence of the unusual electron fillings as well. As we mentioned earlier, current through a quantum dot is suppressed except when the gate voltage is adjusted such that N th and $(N + 1)$ th energies of the dot are degenerate. The conductance peak positions are, thus, proportional to the differences between two energies, and the spacings between adjacent two peaks are obtained by the second differences of the energies,

$$\begin{aligned}\Delta^2 E(N) &= [E(N + 1) - E(N)] - [E(N) - E(N - 1)] \\ &= E(N + 1) + E(N - 1) - 2E(N)\end{aligned}$$

where $E(N)$ is the ground state energy of the dot containing N electrons (Eq. (9.12)). Since our interest here is to study the quantum mechanical information contained in the peak spacing fluctuations, the ground state energy needs to be decomposed into a “(semi)classical” averaging part and a “quantum mechanical” oscillating part. Let us recall the ingredients of the ground state energy as obtained by the Strutinsky method. It consists of four contributions: the generalized Thomas-Fermi energy, the oscillatory part of the single-particle energy, the direct and exchange interaction energies. The generalized Thomas-Fermi energy is basically a classical contribution and it varies smoothly as a function of particle number. The oscillatory part of the single-particle energy is purely quantum mechanical and the av-

eraging part is already removed. Since we modified the direct interaction by replacing \bar{n}^{osc} with \bar{n} in the Strutinsky second order correction term, it includes a smooth part due to $\bar{n}^W (= \bar{n} - \bar{n}^{\text{osc}})$. For the same reason, the exchange energy involves both smooth and oscillating parts. However, the majority of the averaging part can be separated out by excluding E_{GTF} from the ground state energy.

We first compute the ground state energy by $E(N) - E_{\text{GTF}}$ using the previously calculated single-particle energies $\{\epsilon_i\}$ and the matrix elements $\{M_{ij}\}$ for three dynamical regimes, the near-integrable, the mixed, and the chaotic, with the coupling constant $\lambda = 0.20, -0.20$ and -0.80 respectively. Then, the second difference is computed as $\Delta^2 E(N) - \Delta^2 E_{\text{GTF}}$, which it gives peak spacing fluctuations with some constant shift. Once the second difference is obtained as a function of the electron number, the oscillation curves are fitted by linear regression to extract the fluctuation part. Figure (13.1) shows the fluctuation part of the second difference. The linear fit to the averaging part gives a slope of $\sim 1.0 \times 10^{-3}$ and the constant shift ~ 0.7 . The spacing fluctuations are measured in the unit of the mean level spacing, $[\Delta^2 E(N) - \langle \Delta^2 E(N) \rangle] / \Delta_n$, where Δ_n with $n = N/2$ ($(N+1)/2$) for even (odd) N . We note that the mean level spacing is a slowly varying quantity except for small N . The oscillation amplitude is largest in the near integrable case and decreases as the system becomes more chaotic. Note that sometimes the fluctuations are as large as 4Δ in the near integrable regime, but are always less than 2Δ in the chaotic regime.

The distribution of peak spacings is plotted in Fig. (13.2). There are long tails on both sides and they are enhanced as the system acquires regularity. One can observe the same

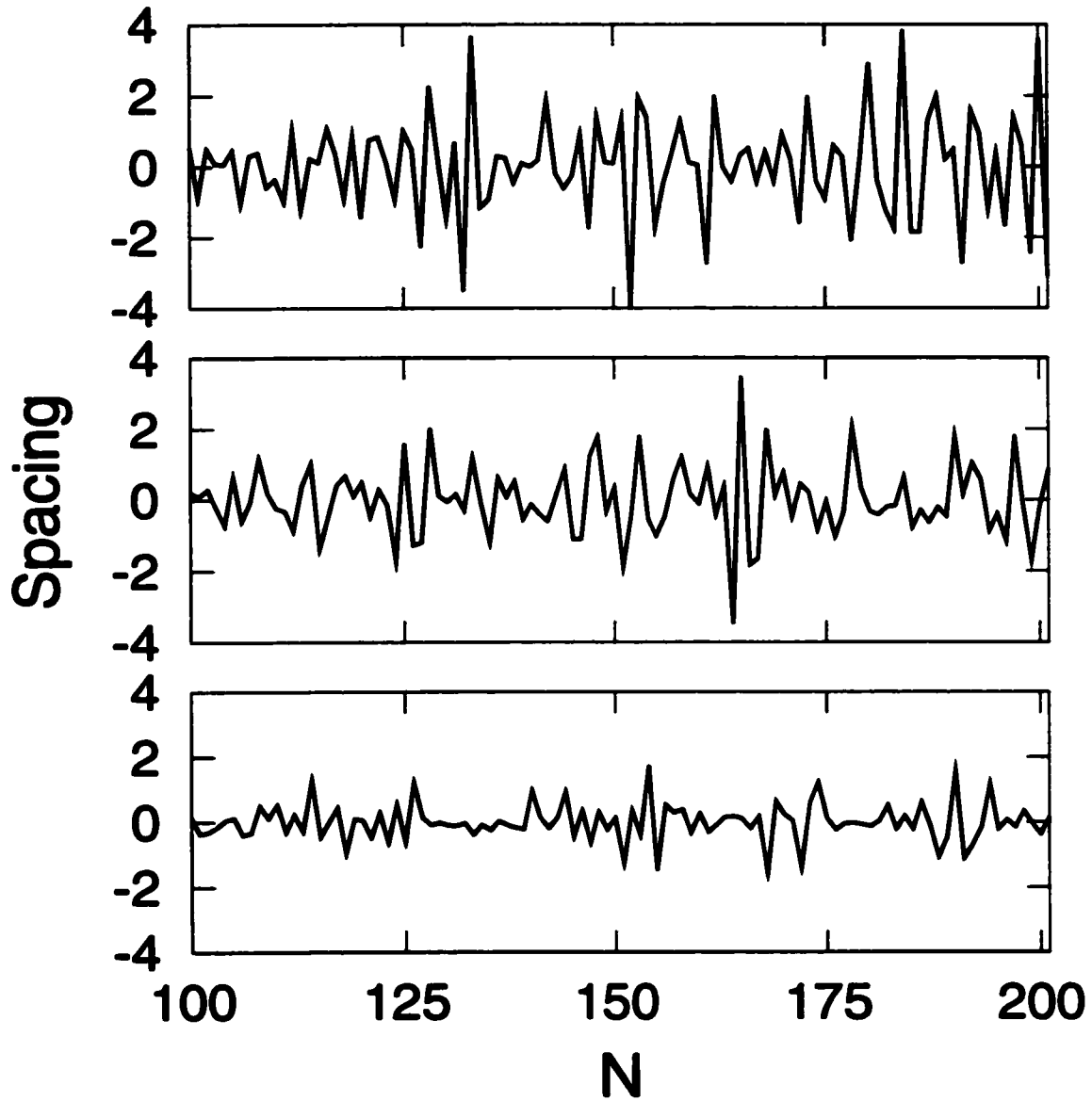


Figure 13.1: Fluctuating part of peak spacing is plotted from 100th to 201st spacings, and they are scaled by the mean level spacing. The average part is subtracted off by linear fit since it is almost a flat straight line for all cases. The spacings are computed for the TRNI quartic oscillator system in three dynamical regimes: near integrable $\lambda = 0.20$ (top), mixed $\lambda = -0.20$ (middle), and chaotic $\lambda = -0.80$ (bottom). For all three cases, the parity sequence (+,+) is shown.

trends in the increasing variance of the distribution; see Table (13.1). For the near integrable case, the variance is twice (6 times) as large as the value for the mixed (chaotic) regime. Since the averaging part is subtracted off, the mean value is close to zero for all three cases. Compared to the CI model prediction of a δ -function plus Wigner surmise for chaotic systems (δ -function plus Poissonian for integrable systems), the probability density is drastically altered by the interaction, the δ -function is completely washed out, the distribution is almost symmetric about their mean as represented in the third moment, and there is no strong bimodal structure observed. In Fig. (13.3), we plot the distributions for even and odd spacings separately. We denote the distributions, obtained with spacings when adding even (odd) numbered electron to the system, as even (odd) distribution. There still remains some odd-even effect and possibly bimodal structure, but it is significantly reduced due to the residual interaction; see Table (13.2). While the CI model gives the widths of the even spacing distributions $\sigma_{\text{even}} = 0.87$ and 0.58 in the near-integrable and chaotic regimes, our dynamical system gives $\sigma_{\text{even}} = 1.32, 0.92$, and 0.57 for near integrable, mixed, and chaotic regimes, respectively (measured in Δ). For the odd spacing distributions, the CI model shows zero width due to the δ -function, and the dynamical system gives $\sigma_{\text{odd}} = 1.17, 0.80$, and 0.43 for near integrable, mixed, and chaotic regimes. The even/odd combined statistics gives the widths for the dynamical systems, $\sigma = 1.25, 0.87$, and 0.52 for near integrable, mixed, and chaotic regimes, and the CI model gives $\sigma = 0.87$ and 0.58 for the near-integrable and chaotic cases. The spacing distributions are also calculated with the RMT (non-dynamical) approach [94] giving the width of $\sigma = 0.24$. The third moments are significantly smaller

than the CI model predictions, and they exhibit rather symmetric distributions.

The root of the long-tail distribution originates in the localization of wavefunctions. The localized states give large matrix elements M_{ij} especially on its diagonal, and in many cases, they are larger than the mean level spacing. Since the matrix elements make the residual interaction expensive, the system rearranges the orbital occupation and it produces significant fluctuations in the ground state energies. As a consequence, the peak position deviates from the location predicted by the system in the absence of the residual interaction, and the spacing is also affected. Thus, if the localization is strong, the spacing fluctuations are enhanced and contribute to the tails of the distribution. Since the wavefunctions in the near integrable regime are likely to be more localized than in the chaotic regime, the spacing fluctuations are larger, and the distribution tails are broadened. We remark that while the diagonal elements M_{ii} often give values 2 to 3 times larger than Δ for the near integrable system, they are reduced to 1.5 to 2 in the mixed case, and further suppressed to 1.2 in the chaotic regime; see Fig. (11.9).

In order to decrease the statistical error bars, we generate an ensemble of data sets. In each dynamical regime, we calculated three sets of data with slightly different coupling constants: $\lambda = 0.18, 0.20, 0.22$ for the near integrable, $\lambda = -0.22, -0.20, -0.18$ for the mixed, and $\lambda = -0.82, -0.80, -0.78$ for the chaotic regime (for all cases, the symmetry breaking strength ϵ is set to -1.0). In addition, since there exist four parity sequences due to the reflection symmetry in the confining potential, a total of 12 data sets constitute the ensemble for each dynamical regime. Peak spacings are constructed from $N = 100$ to 201, resulting

Moments	Integrable	Mixed	Chaotic
1	-4.338480×10^{-8}	2.067565×10^{-8}	2.807189×10^{-9}
2	1.573654 ($\sigma = 1.254454$)	0.7512421 ($\sigma = 0.8667422$)	0.2675636 ($\sigma = 0.5172655$)
3	3.921296×10^{-2} ($\gamma_1 = 1.986395 \times 10^{-2}$)	0.1278263 ($\gamma_1 = 0.1963135$)	1.050898×10^{-2} ($\gamma_1 = 7.593115 \times 10^{-2}$)
4	10.36801 ($\gamma_2 = 1.186747$)	2.671355 ($\gamma_2 = 1.733383$)	0.4292751 ($\gamma_2 = 2.996274$)

Table 13.1: Moments are shown for the distributions of the peak spacing fluctuations (scaled). First four moments are calculated for the near integrable, mixed, and chaotic regimes for the TRNI coupled quartic oscillator system. Standard deviation σ , skewness γ_1 , and kurtosis γ_2 are also computed for each related moment.

in a total of 102 spacings in each data set.

13.3 Ground State Spin Polarization

The non-standard orbital occupations not only influence the peak spacings, but also affect the spin polarization of the ground states. If the standard occupation is employed, the ground state spin is either zero (even N) or $1/2$ (odd N), giving equal probability of 50%. Here, we made the assumption that electrons always occupy the orbital with spin up whenever there is a freedom of choosing their orientation without costing extra energy. If, on the other hand, spin down is assumed, the ground state spin simply changes its sign and takes either 0 or $-1/2$ with the same probability. Thus, we use the “spin-up” assumption throughout this section. Figure (13.4) shows the distribution of the ground state spins in three dynamical regimes. Remarkably, there exist significant portions of higher spin states especially in both, the near integrable and the mixed cases, due to the non-standard orbital occupations. It is reasonable

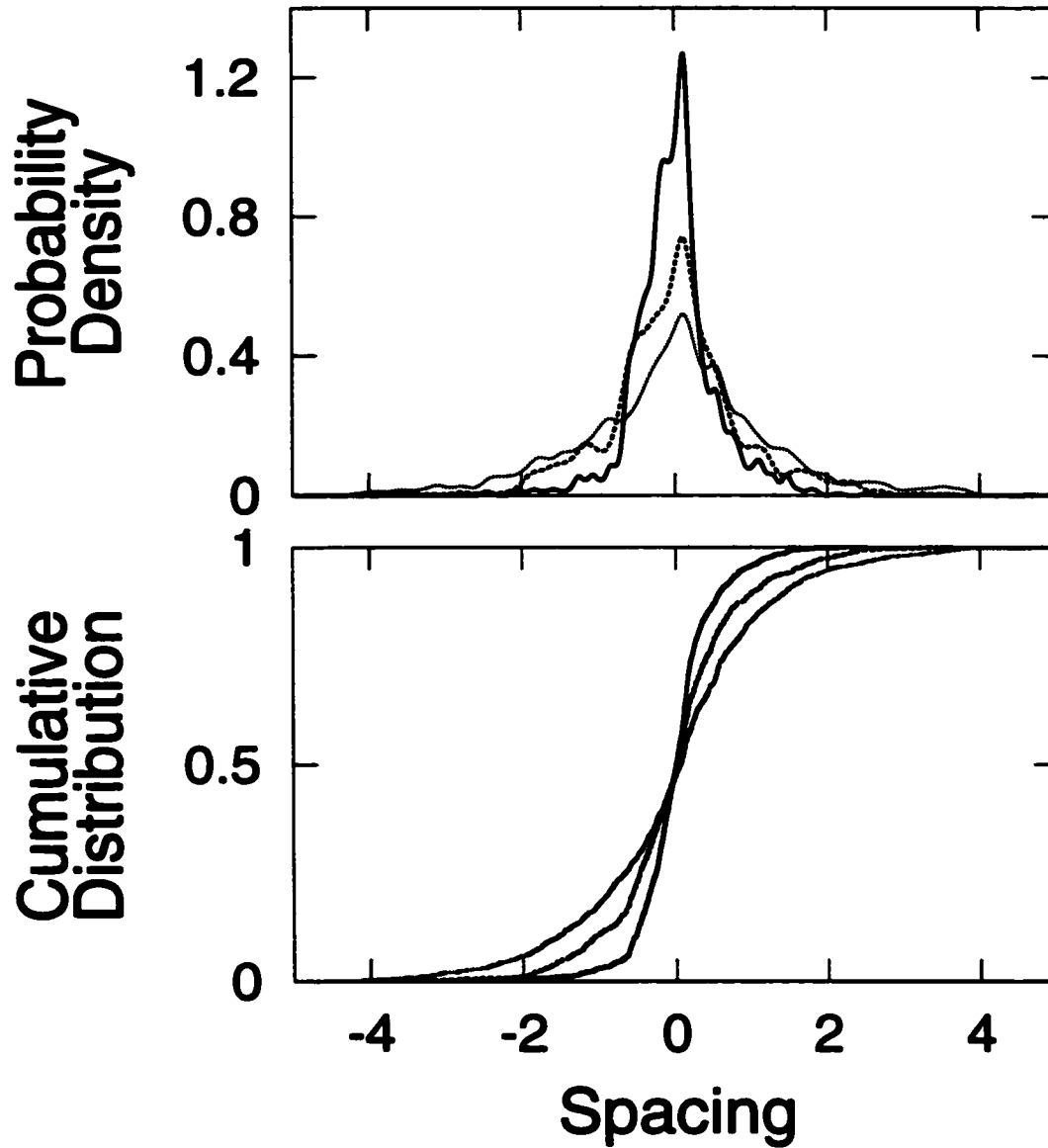


Figure 13.2: Probability density (top) and cumulative distribution (bottom) of the fluctuating part of the peak spacings (scaled by mean level spacing). Distributions are obtained using both even and odd spacings combined. The dynamical regimes are set to near integrable (dotted line), mixed (dashed), and chaotic (solid) for the TRNI quartic oscillator system.

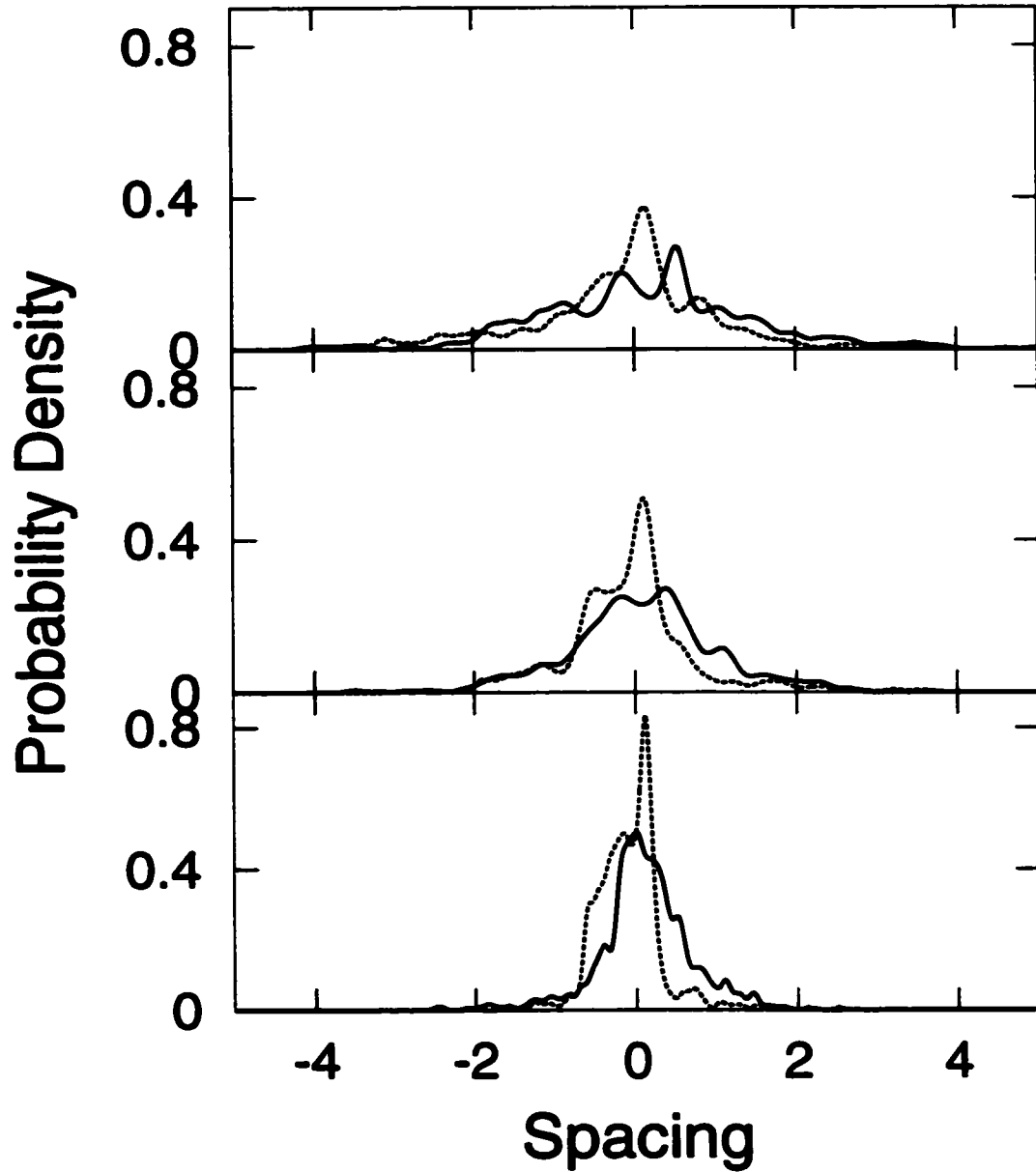


Figure 13.3: Probability density of peak spacings distributions for even/odd spacings. The distributions are obtained using the fluctuating part of the peak spacing scaled by the orbital mean level spacing. The dynamical regimes are near integrable (top), mixed (middle), and chaotic (bottom) for the TRNI quartic oscillator system. For each case, two distributions are computed to observe the behaviors of even spacing (when adding an even numbered electron to the system) and odd spacing (when adding an odd numbered electron to the system). The solid line represents the even spacing distribution and the dashed line the odd spacing distribution.

	Integrable		Mixed		Chaotic	
	even	odd	even	odd	even	odd
σ	1.3171 (0.86603)	1.1763 (0.0)	0.92389	0.79822	0.57458 (0.58228)	0.43315 (0.0)
μ_3	0.025161 (1.7500)	-0.073031 (0.0)	-0.13197	0.33785	-0.092811 (0.15183)	0.073985 (0.0)

Table 13.2: Widths (standard deviations) and third moments of the peak spacing distributions are shown separately for the even/odd spacings in units of Δ . The moments in the near integrable, mixed, and chaotic regimes for the TRNI coupled quartic oscillator system are compared to the CI model predictions (δ -function and Wigner surmise for the chaotic case, and δ -function and Poisson statistics for the integrable case). The numbers in parenthesis represent the CI model predictions.

to expect that the fraction of higher spins in the mixed regime is less pronounced than the near integrable case in accordance with the fluctuation size of M_{ij} . However, the fraction of higher spins for the mixed case is almost the same as the one for the near-integrable case.

To see more explicitly how spins are distributed, we consider the distribution of ground states based on the orbital occupations. Including the standard up/down filling, the most favorable nine orbital occupation patterns are considered (in the sense that the system seeks the least expensive energy states realizing the interplay of single-particle energy and the residual interaction). The orbital occupation patterns are labeled by the code numbers from 0 to 8 for even and odd cases separately. Starting with the standard occupation, the patterns are determined by promoting electrons to higher energy states and/or changing its spin orientation. This is actually how one finds the ground states. The orbital occupation codes and associated distributions are plotted in Figs. (13.5, 13.6) for even and odd N ground states, respectively. For even N , the first thing to notice is that the standard occupation

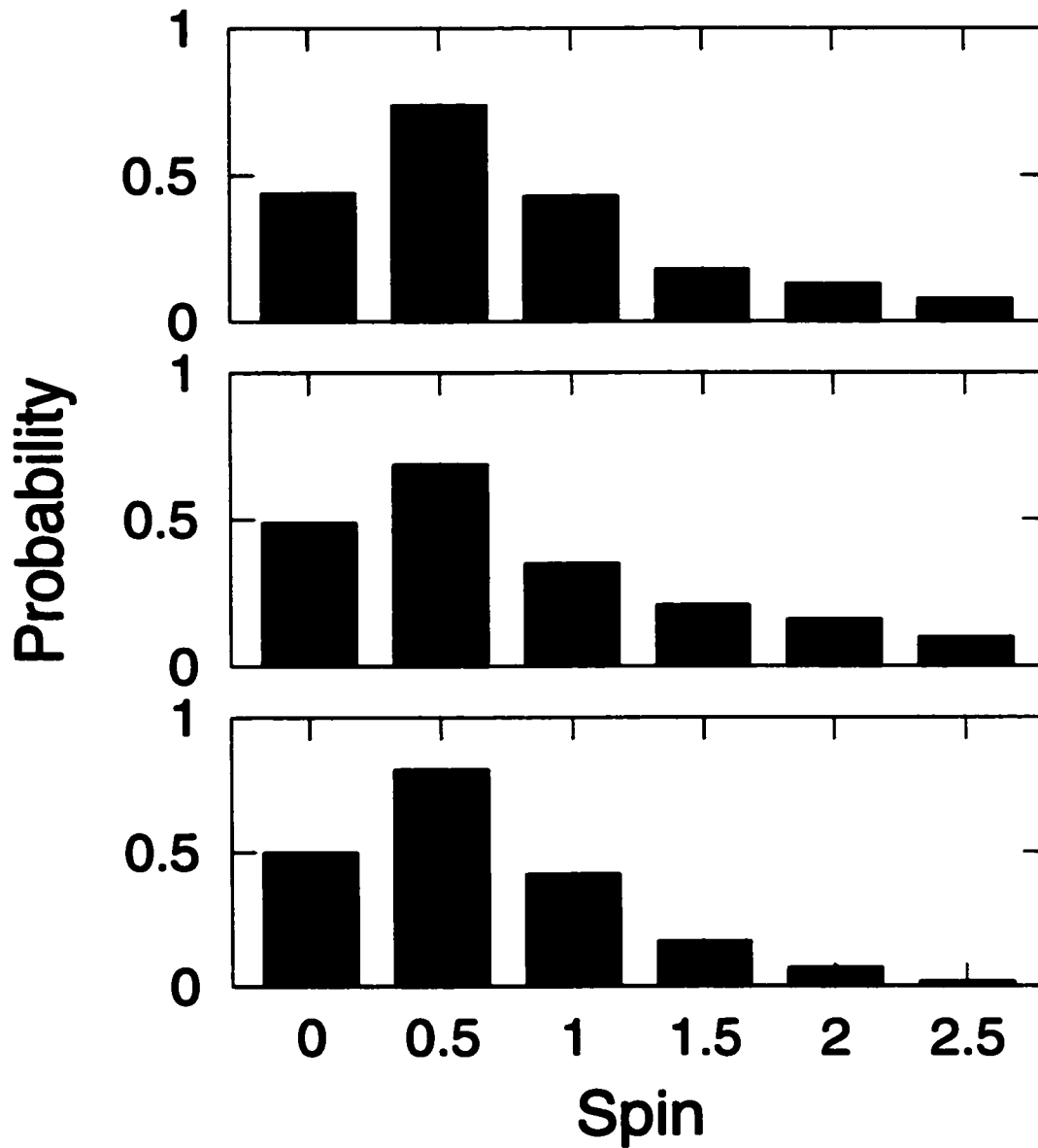


Figure 13.4: Distribution of ground state spin polarization for the system of TRNI quartic oscillator. The dynamical regimes are near integrable (top), mixed (middle), and chaotic (bottom). Black bars represent the distribution of spin polarization when the ground state consists of an even number of electrons, and gray bars represent that when the ground state consists of odd electrons.

gives the largest probability, and the spin 0 states consist of two different configurations (code 0 and 3). In the near integrable and the mixed case, the probability of ground states in code 3 is enhanced from the chaotic case. There are four codes to give spin 1: code 1, 2, 4, and 6. Starting with the standard occupation, the code 1 is simply to promote one electron to the next level flipping its spin orientation. The other codes 2, 4, and 6 are obtained by further promoting a few more electrons without changing the spins. For the chaotic system, code 1 dominates out of 4, indicating the occurrence of reconfiguration of occupation due to the expensive residual interactions at the last $n(= N/2)$ th orbital. On the other hand, for the integrable and mixed systems, the probability is not the largest at the code 1, but it is spread out to the rest representing more involved orbital occupation processes. Interestingly, the codes 2 and 4 have more than 10% in these regimes. This is a sign of significant residual interaction energies near the n th level, suggesting the importance of an off-diagonal matrix element study. For odd N , the standard occupation is the largest only for the chaotic case. The codes 0, 1, 2, 3, and 5 give the ground state spin $1/2$, and the probabilities are roughly distributed over the five configurations ($\sim 15\%$) for the near integrable case, and the code 0, 1, and 2 are dominant for the mixed case. Contributions of the rest of the higher spin configurations are small except for the code 4 with spin $3/2$. The code 4 is simply to promote an electron at $(N - 1)/2$ th level to $(N + 3)/2$ th level to change the orientation of spin from down to up and reduce the residual interaction.

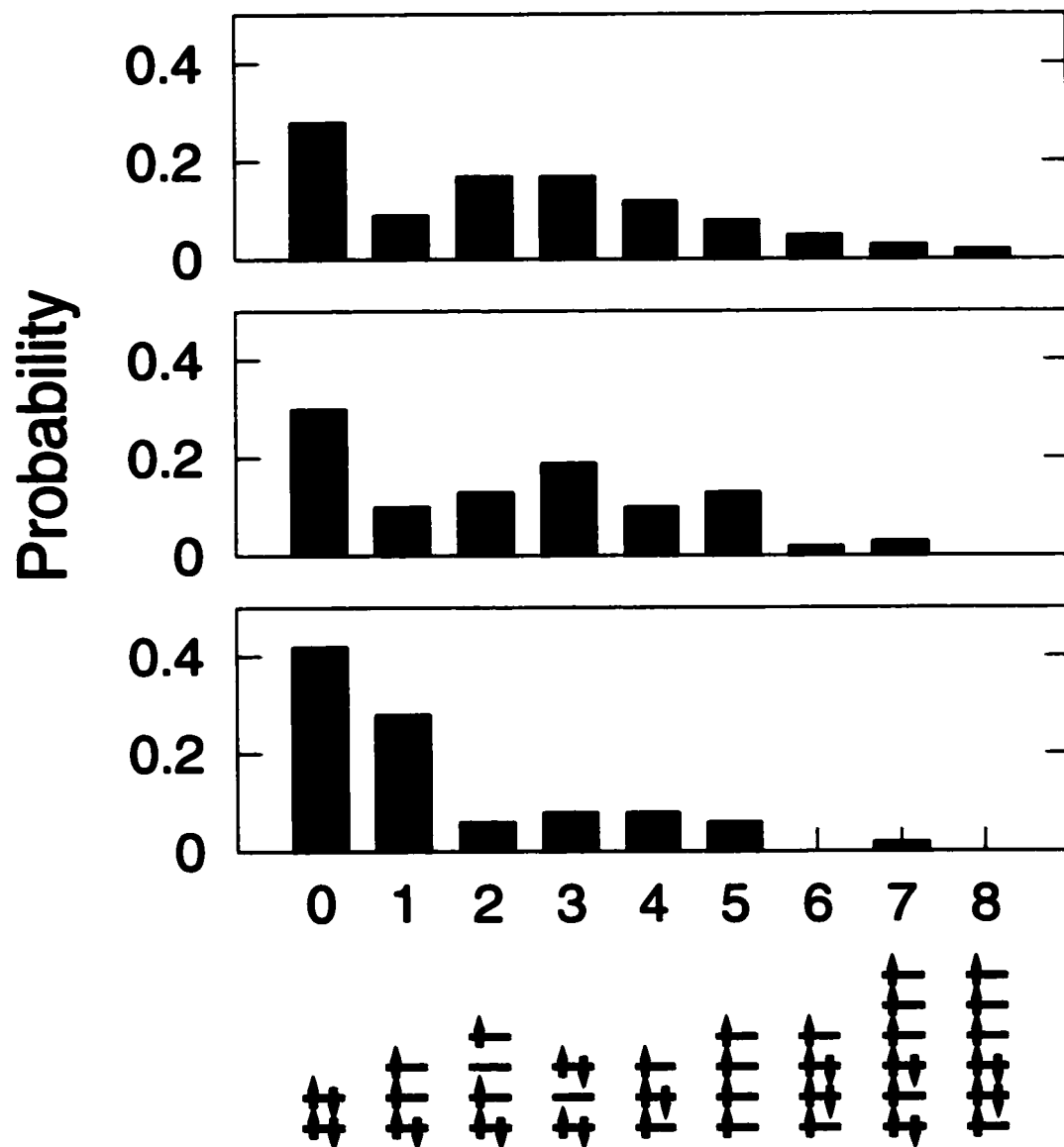


Figure 13.5: Distribution of ground state orbital occupation for the TRNI quartic oscillator system having even number of electrons. The nine configurations of orbital occupancy are shown on the horizontal axis with code numbers, and the arrow represents electron spin; see text. Three dynamical regimes are considered: near integrable (top), mixed (middle), and chaotic (bottom).

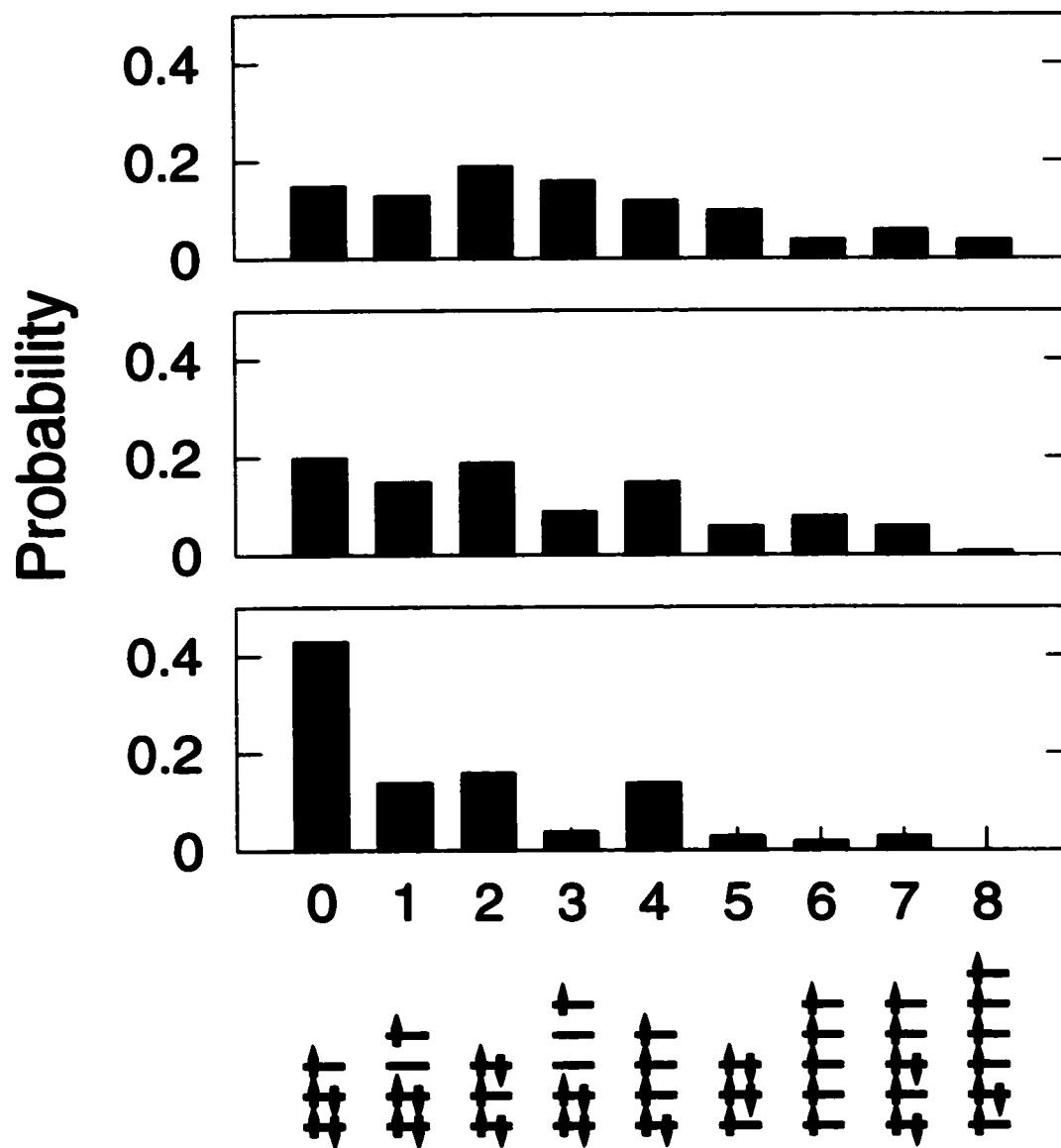


Figure 13.6: Distribution of ground state orbital occupation for the TRNI quartic oscillator system having odd number of electrons. The nine configurations of orbital occupancy are shown on the horizontal axis with code numbers, and the arrow represents electron spin; see text. Three dynamical regimes are considered: near integrable (top), mixed (middle), and chaotic (bottom).

13.3.1 Orbital Occupation Scenario

It has been observed that the ground state orbital occupation was greatly affected by the size of matrix elements M_{ij} . By looking at the process of how electrons fill orbitals, we further investigate the mechanism of ground state configurations and the role of the matrix elements. In Figs. (13.7, 13.8), successive orbital fillings of the electrons are demonstrated for near integrable and mixed systems. These two dynamical regimes, especially for the near integrable case, are chosen since dramatic non-standard fillings are likely to occur due to the considerable size of matrix elements. Let us first study the case of the near integrable system. The electrons are added one by one from $N=124$ to 135. When $N=124$, the standard occupation gives the ground state, and from $N=125$ to 128, the system tries to avoid occupying the 64th orbital and fills neighboring the 63rd and the 65th orbitals. When adding the 129th electron, the system has two choices, either to locate at the 64th or the 66th orbital. If the electron fills the 66th level, it costs the system an extra single-particle energy of $\epsilon_{66} - \epsilon_{64}$ (note this is larger than $\epsilon_{65} - \epsilon_{64}$ or $\epsilon_{64} - \epsilon_{63}$), while if the 64th orbital is filled, the system pays more energy for the residual interaction. In the current case, the electron occupies the 64th level. From $N=130$ to 133, the system again stays away from filling the 64th orbital. If two electrons occupy the same orbital, their spin orientations must be opposite to each other. This invokes the diagonal elements M_{ii} , and it gives a large contribution to the residual interaction energy. Since $M_{64,64}$ is pronounced, the system refuses to place two electrons at the 64th orbital for a while. When the 134th electron is added paying the expensive diagonal contribution to the residual interaction, it increases the

ground state energy $E(134)$. As a result, a large spacing fluctuation is produced at $N=133$ (since $\Delta^2 E(133) = E(134) + E(132) - 2E(133)$). For $N=135$ or above, electrons are expected to avoid filling the 66th level because of the substantial size of $M_{66,66}$, and it should follow a similar orbital occupation process as that of the 64th orbital. The situation of avoiding a particular orbit leads to the following observation: the off-diagonal elements M_{ij} associated with the large diagonal element M_{ii} must have large values especially near the diagonal $i \sim j$. This will be investigated more in the context of the conditional probability; see later in this section.

Now, let us consider the orbital occupations for the mixed system. Knowing that $M_{68,68}$ is large, the system fills the 67th and 69th orbitals avoiding the 68th level for $N=132, 133$, and 134. Interestingly, the 135th electron fills the 68th orbital first instead of the 67th, but as soon as the next electron is added, it escapes to the neighboring orbital. Except for the $N=135$ case, the orbital occupation follows similar behavior as seen in the near integrable case. For the chaotic system, the localization of wavefunctions is not as strong as the near integrable or the mixed systems. Thus, the orbital occupation scenario does not differ significantly from the standard up/down filling. At most, weak orbital avoidance can occur.

Overall, the localized states cause the orbital avoidance in the electron filling process. Given the i th orbital which is associated with large M_{ii} , it has a tendency to refuse having even one electron occupied. Once filled, the orbital still remains singly occupied for a long time, and the system prefers to polarize the newly added electrons in the neighboring orbitals.

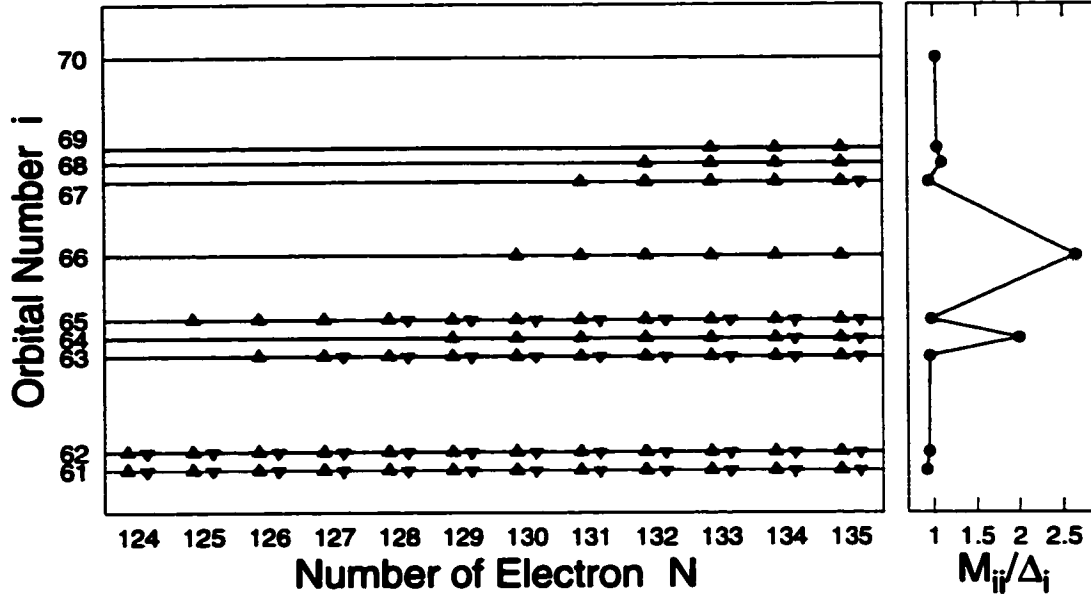


Figure 13.7: Electron orbital occupation scenario for the TRNI quartic oscillator system in the near integrable regime ($\lambda = 0.20$, reflection symmetry $(+, +)$, and $\zeta = 0.8$). The main (left) figure shows orbital occupations of the ground states for the N electron systems with N from 124 to 135. The horizontal line represents energy levels, and the vertical axis is adjusted such that the location of each line corresponds to its energy value. Each triangular point represents an electron, while the head of the triangle indicates the spin orientation, up or down. The right figure shows scaled M_{ii} diagonal elements. The scaled magnitude of M_{ii} is given by the horizontal axis, and the orbital number i is adjusted to match the vertical axis of the left figure. (The figure is modified from the original generated by D. Ullmo with permission.)

It should be mentioned that this situation is special when the screened potential is local. The local approximation makes the direct and exchange interaction equivalent, and the residual interaction becomes effective only when two electrons have opposite spins. At some point, the i th orbital becomes doubly occupied paying all the interaction energy saved, and the peak spacing shows a large fluctuation as a consequence.

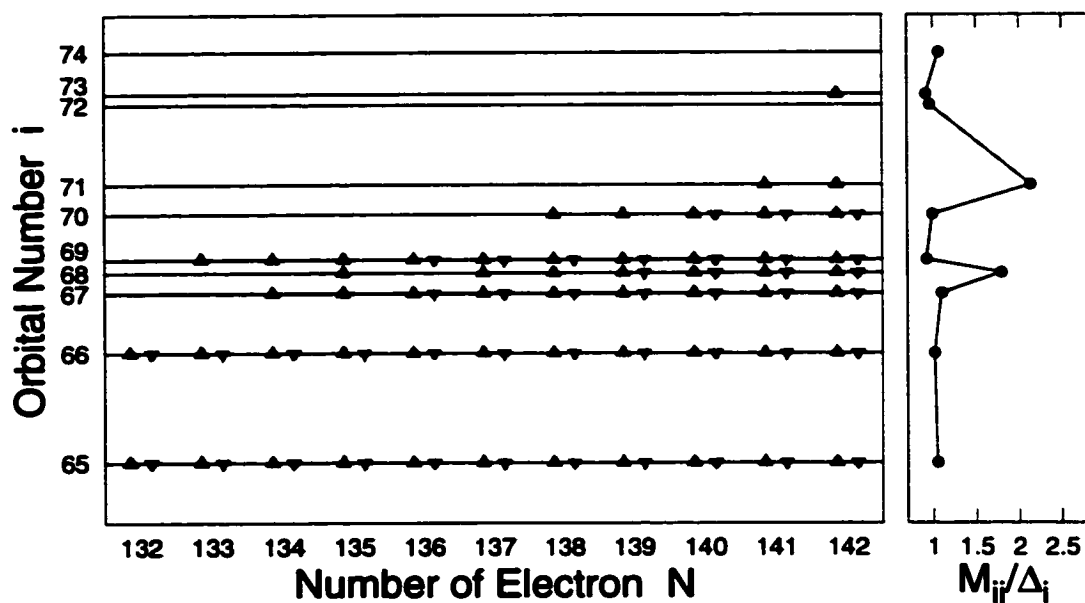


Figure 13.8: Electron orbital occupation scenario for the TRNI quartic oscillator system in the mixed regime ($\lambda = -0.20$, reflection symmetry $(+, +)$, and $\zeta = 0.8$). The main (left) figure shows orbital occupations of the ground states for the N electron systems with N from 132 to 142. The horizontal line represents energy levels, and the vertical axis is adjusted such that the location of each line corresponds to its energy value. Each triangular point represents an electron, while the head of the triangle indicates the spin orientation, up or down. The right figure shows scaled M_{ii} diagonal elements. The scaled magnitude of M_{ii} is given by the horizontal axis, and the orbital number i is adjusted to match the vertical axis of the left figure.

13.3.2 Conditional Probability

Since the study of orbital occupations indicates the importance of the off-diagonal matrix elements, we look closely at the particular off-diagonal elements by considering the conditional probability of the matrix elements. As shown in Fig. (13.9), the large off-diagonal elements M_{ij} in the i th row are associated with the large diagonal element M_{ii} giving several peaks on both sides of the diagonal. The size of the off-diagonal peaks reduces far from the diagonal. On the other hand, the off-diagonal elements associated with the small diagonal element M_{ii} show no such pronounced peaks. The conditional probability is obtained as follows. Given a dynamical regime, large diagonal elements are selected by scanning through all M_{ii} except for the first 50 orbitals. For each selected row number i , one collects off-diagonal elements M_{ij} over the j th column restricted to near diagonal by $0 < |i - j| < d$ with $d = 10$. One repeats this process on each of the 12 data sets to construct the ensemble. We also collect small data sets related to small M_{ii} to see the difference in two statistics, “large” and “small” distributions. Figure (13.10) shows the distributions in the three dynamical regimes. The “large” off-diagonal distribution has a long tail on the right side representing the manifestation of localized states, while the “small” distribution does not have such a tail and it is basically the same behavior as observed in Fig. (11.11), the distribution of the off-diagonal elements near the diagonal. The variances of the “large” (“small”) distribution are, 0.024 (0.0061), 0.027 (0.0057), and 0.017 (0.0022) for the near integrable, mixed, and chaotic cases respectively. The differences in “large” and “small” distributions are enhanced as the system gains regularity because it is more likely to form localized wavefunctions in the

integrable case than the chaotic case. In addition, the peaks of two distributions come close as the chaoticity is increased. The mean values are 0.43 (0.49), 0.45 (0.49), and 0.48 (0.50) for the “large” (“small”) distribution in the near integrable, mixed, and chaotic regimes. We note that the case of the near diagonal width condition, $d = 30$, showed essentially the same distribution curves.

Let us summarize the connection between the orbital avoidance and large matrix elements. Suppose the i th orbital corresponds to the large diagonal element M_{ii} . There are two cases of the orbital avoidance: first, when no electron occupies the orbital, and second, when one electron is already present. In the first case, the system tries to locate newly added electrons at the neighboring j th levels ($j \sim i$ but $j \neq i$). This is because some of the M_{ij} are large, and placing an electron in the orbital requires paying an expensive energy cost due to the interaction with the neighboring electrons having opposite spin. The existence of large off-diagonal M_{ij} was confirmed in the right tail of the “large” distribution of the conditional probability. In the second case, the system again refuses to locate an electron in the i th level. If an electron needs to occupy the orbital, it is necessary to pay not only the interaction energy with neighboring electrons, but also the most expensive diagonal contribution. If only the diagonal elements are the large quantities and the off-diagonals are not, the first case of orbital avoidance would not happen, and the second case of singly occupied orbitals should be resolved without paying the extra energy cost for the neighboring interactions.

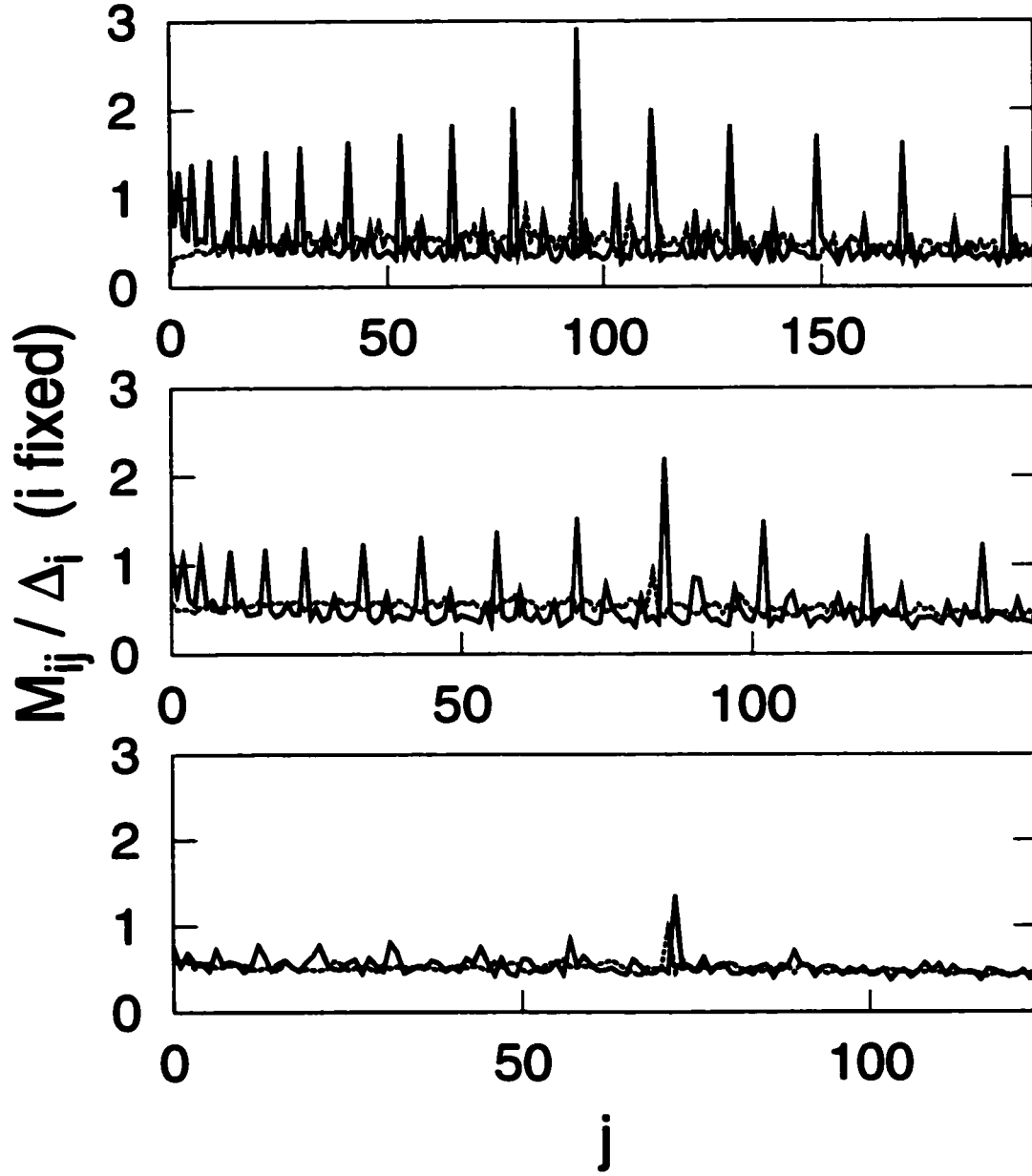


Figure 13.9: Slice of M (scaled) matrix at i th row. i is determined such that corresponding M_{ii} gives either a large or a small value compared to other M_{ii} . M_{ij} are calculated for the TRNI quartic oscillator system in three dynamical regimes. Top figure is for $\lambda = 0.20$, $i=93$ (dashed) and 94 (solid), middle figure is for $\lambda = -0.20$, $i=83$ (dashed) and 85 (solid), and bottom figure is for $\lambda = -0.80$, $i=71$ (dashed) and 72 (solid). For all three cases, the solid line corresponds to large M_{ii} and the dashed line corresponds to small M_{ii} . The system's reflection symmetry is $(+, +)$ for each case.

Probability Density

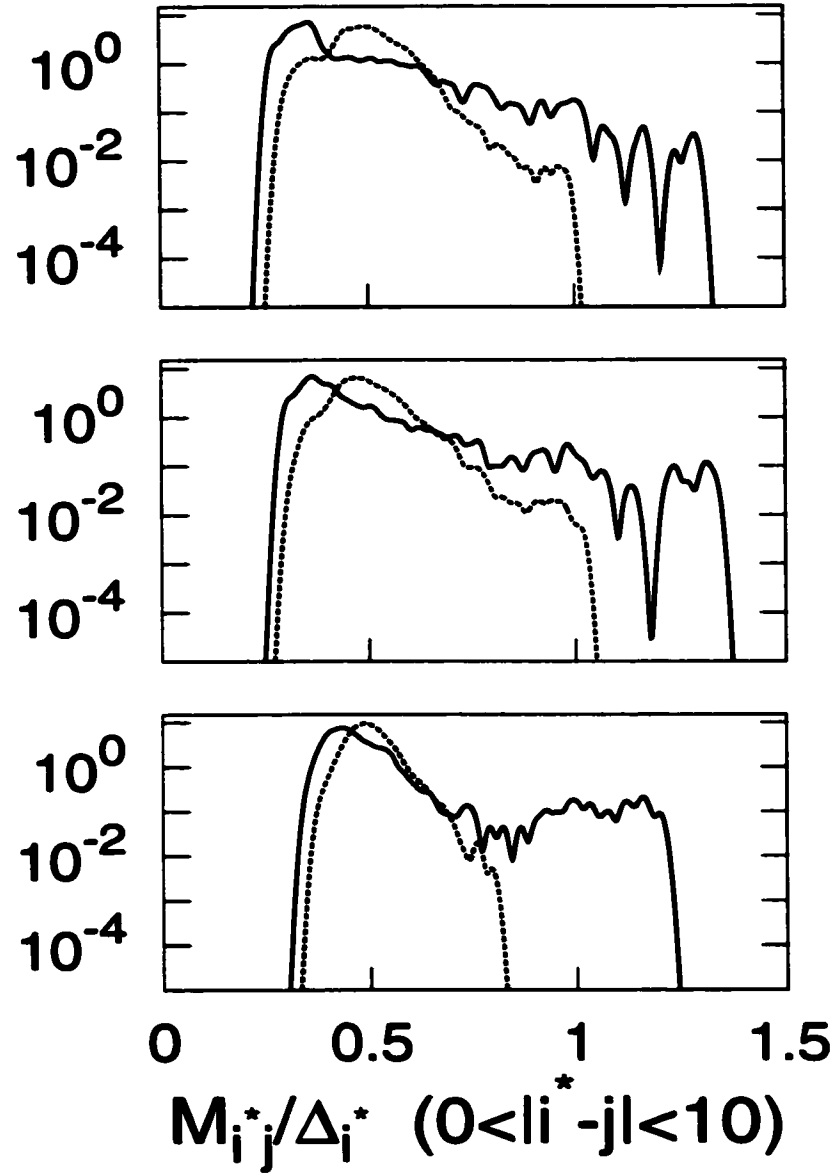


Figure 13.10: Conditional probability of off-diagonal elements M_{ij} (scaled) with $|i - j| < 10$ (plotted on log scale to show tails). Calculations are done in three dynamical regimes, near integrable (top), mixed (middle), and chaotic (bottom). Two kinds of M_{ij} are collected by looking at the index i : i which gives either large or small M_{ii} , and i^* is used to indicate this restriction. Probability density is plotted for large M_{ii} (solid) and for small M_{ii} (dashed) in each figure. The criterion of “large” (“small”) is given for each dynamical regime by $M_{ii} \geq 2.0(\leq 1.2)$, $M_{ii} \geq 1.8(\leq 1.2)$, and $M_{ii} \geq 1.2(\leq 1.0)$ for the near integrable, mixed, chaotic regimes.

Chapter 14

Conclusion

Motivated by the discrepancy of the constant interaction model in predicting the statistical behavior of the CB conductance peak spacing, we pursued a many-body theory which explicitly includes the electron-electron interaction in the framework of the density functional theory. Our primary interest was to probe the missing physical factors and to investigate further the statistical behaviors of quantum dots. The study has proceeded in two stages.

In the first part of this report, we have developed an approximate series expansion for studying the ground state of interacting systems using the idea of the Strutinsky shell correction method. We tested the validity of the Strutinsky scheme by numerical calculations of interacting electron systems in a one-dimensional, externally applied quartic potential. By varying the electron charge strength, we were able to confirm the stability of the method. It approximated extremely well the quantum mechanical DFT quantities using [semi]classical Thomas-Fermi data for three different charge strengths. One exceptional circumstance giving less reliable results was noted with respect to a barrier in V_{eff} approaching the chemical potential. The calculations show a tendency for the series to converge as the electron number increases. This is consistent with expectations for systems with large numbers of particles because of the increasing reliability of the Thomas-Fermi calculations as the system goes deeper into the semiclassical regime.

The method discussed could serve two purposes. On the one hand, it gave us an efficient

way to proceed with numerical calculations, and it is conceivable that this approach could be of some help for larger scale, realistic DFT calculations [74–77, 80]. On the other hand, it also provides some physical insight by decomposing the total DFT energy into various contributions, each of them receiving an intuitive interpretation.

In the context of quantum dots, for instance, one of its simple but presumably useful applications could be to justify, and make more precise, the constant interaction model. Indeed, this is usually presented as an ad-hoc model motivated essentially by its simplicity. Here, up to some reinterpretation of what is the capacitance of the dot, we see that the constant interaction model can be understood as the first-order approximation in a Strutinsky development of a DFT calculation. One obtains, in addition, that the various parameters of the model (classical energy and potential governing the motion of the independent particles) are specified, and, in principle, can be computed explicitly. This makes it possible, for instance, to study the sensitivity of the dot's energy to the variation of an external parameter [89].

In the same way, the second-order correction term gives insight into the “residual” interactions between electrons. In the context of DFT it gives some basis to the fact that electrons in quantum dots behave as Landau quasi-particles interacting weakly through a screened Coulomb interaction. It moreover explicitly specifies how the screening process is affected by the confinement of the electrons, which might be relevant in the limit where the screening length is not much smaller than the size of the dots.

In the second part of the report, we have applied the Strutinsky method to study quan-

tum dots and understand the statistical properties of the system focusing on the behavior of the residual interactions. Knowing that the irregularly shaped dot region is defined by the negatively applied gates, the confinement produces the steep but still smooth potential for the electrons. For the theoretical description, we have employed the two-dimensional coupled quartic oscillators as the effective potential within a non-interacting quasiparticle picture, realizing the smooth and steep wall confinement. Among the standard theoretical approaches, RMT has been recognized as one of the most powerful tools to investigate the statistical aspects of quantum dots based on the assumption that the irregularity of the dot shape introduces chaos in the system. However, many of the dots fabricated for the measurements are weak disordered systems, and they retain some regularity in the corresponding classical dynamics. For this reason, the choice of the quartic oscillator has the advantage that the degree of chaos can be tuned continuously from near integrability, mixed to complete chaos. In addition, it gave us a means to investigate the role of dynamics in the statistical behaviors of the system, and it turned out to be the most important effect in our present study.

In experiments, each dot comes in various shapes, and they give different patterns for the conductance peak oscillations. Measurements are performed on several dots, and data are collected to construct the statistical ensembles. While there is no significance in emphasizing the specific geometry of each dot, their symmetry greatly affects the statistical behaviors. According to RMT, when the system's classical dynamics are chaotic, the resulting statistics are represented by GOE (GUE) in the absence (presence) of a magnetic field

preserving (breaking) time reversal symmetry. In the theoretical illustration, we studied two systems which lead to GOE and GUE statistics, depending on the symmetry response under anti-unitary operations. The reflection symmetry of the confining potential demanded one to consider not only the time reversal symmetry, but also all anti-unitary symmetries to distinguish two statistical classes.

The expression of the ground state energy has been modified from the Strutinsky description by adding the exchange interaction term to handle properly the electron spin degree of freedom. Using the local approximation to the screened interaction, the residual interaction only counts the interaction energy among electrons having opposite spin orientations. By defining the matrix M_{ij} , the study of the residual interaction was mapped onto the analysis of the single-particle wavefunctions.

For the TRI quartic oscillator system, we have computed the matrix elements M_{ij} for three dynamical regimes, near integrable, mixed, and chaotic. The first thing we noticed was the considerable size of the diagonal elements and their fluctuations. The magnitude of the elements were of the order the orbital mean level spacing. Since the conductance peak spacings are significantly affected by the energy of this order, it indicates the reason for the failure of the CI model missing the residual interaction energy contribution. By plotting M_{ii} as a function of the orbital number, we observed the repetition of the pronounced peaks and their response to the changing degree of chaos. As the system becomes more regular, the M_{ii} spikes are amplified and the peak oscillation pattern becomes simple. The lower bound of the oscillation grows rapidly at the low energy domain, but soon it saturates and stays

almost constant. The same trends were observed in all dynamical regimes. In the chaotic regime, the peak values are roughly 1.8 measured in the unit of the mean level spacings while in the mixed regime, the sizes are as large as 2.2, and 2.5 for the near integrable case. The lower bound gives a value close to 1.5 for all three cases. The fluctuations of the diagonal elements are related to the spatial distribution of probability amplitude of wavefunctions. For the large M_{ii} peaks, the corresponding wavefunction is localized in configuration space having few nodes in one direction, while for the small M_{ii} , the probability amplitude of wavefunctions are evenly spread out over the classically bounded regions with many node in every direction. For the distribution of the diagonal elements, the large M_{ii} lead the long tail on the right side, and its length grows as the degree of chaos reduces. This is because localization is more likely to occur in regularized systems than chaotic systems. On the other hand, most of the off-diagonal matrix elements do not show a strong sign of the wavefunction localization (there are some exceptions; see later).

Although the TRI quartic oscillator system brought us a means to understand the connection between the diagonal elements M_{ii} and the eigenstates, the second order Strutinsky energy correction method missed the higher order contribution which happens to reduce the residual interaction energy and thus failed to correctly describe the ground state energy of quantum dots in this particular symmetry class. Therefore, we had to switch into the system which the higher order terms can be safely neglected. This was done by introducing a new term to the Hamiltonian which breaks all anti-unitary symmetries, and we denoted this as the TRNI quartic oscillator system. Interestingly, we found that even if the Hamiltonian

breaks all anti-unitary symmetries, there existed the case leading to GOE statistics. To achieve the GUE statistics, one must break all the symmetries not only in the Hamiltonian, but also in the equations of motion. Although it is not our main interest of the current research, the study of this “hidden” symmetry would give us an insight into the fundamental properties of dynamical systems. The TRNI system is characterized by two parameters, the coupling constant λ which determines the degree of chaos, and the symmetry breaking strength ϵ . While increasing the coupling constant enhances the degree of chaos, boosting the breaking strength regularizes the dynamics. With the analysis of Poincaré surfaces of sections, we found three dynamical regimes which represent near integrability, mixed, and chaos. In the study of the matrix elements M_{ij} , the same trends were observed as seen in the TRI case except for the enhanced tail in the diagonal elements distributions especially in the near integrable regime. While the peak patterns and size showed similarity, the lower values of M_{ii} were reduced from 1.5 to 1.0 making the fraction of the tail portion larger in the distributions.

Based on Berry’s conjecture, we constructed wavefunctions using the random superposition of plane waves to simulate the eigenstates of chaotic systems. The aim of this study was to observe the asymptotic behavior of the diagonal elements M_{ii} in the high energy domain and to extract dynamical information through the comparison between the quartic oscillator systems (dynamical) and the PWSA systems (non-dynamical). As opposed to the quartic oscillator system or any dynamical system, the PWSA approach allows one to calculate easily the wavefunctions in a high energy domain, and, in principle, the approximation gains

reliability as energy is raised due to the increasing randomness of wavefunctions, which is related to the ratio of wavelength to the system size. The diagonal elements M_{ii} were generated for three different energy domains, low ($i = 1$ to 600), middle ($i = 2000$ to 2500), and high ($i = 5000$ to 5500), where the low energy range matched the dynamical quartic oscillator systems. Since there is no spatial reflection symmetry in the PWSA system, the statistical property of the wavefunctions are characterized by the response under the time reversal operation. When wavefunctions consist of real (complex) plane waves, the corresponding dynamical system is the TRI (TRNI) quartic oscillator, leading to GOE (GUE) statistics. For the system with real random waves, M_{ii} did not show any pronounced peak oscillations in all ranges. The fluctuations were much suppressed in amplitudes, and the mean was evolving very slowly from 1.4 in the low energy domain to 1.5 in the high domain. The distributions had no long tails, and the shapes were symmetric about the mean. As the energy increased, the distribution width became narrower. The higher moments were gradually decreasing, and the distributions were seeming to converge into the Gaussian shape centered at the mean 1.5 in the high energy limit. In the case of complex random waves, M_{ii} showed similar behavior except for the following. The mean values were approaching 1.0 instead of 1.5 , and the variance sizes were smaller in all energy scales. For both cases, the comparison of the means and variances to the analytical expressions [94], which derived from the correlation function of random waves, showed reasonable agreement, and the accuracy increased as energy increased. Two important facts can be learned from the PWSA study: one is that the distribution of M_{ii} changes, at best, slowly into a Gaussian density in the

high energy limit, and the other is that the pronounced peaks in M_{ii} are unique to dynamical systems.

Having the eigenenergy and the matrix elements M_{ij} of the TRNI quartic oscillator system calculated, the ground state energy of the quantum dot was obtained by finding the orbital occupation which minimizes the total energy. The peak spacings were computed by taking the second difference of the ground state energies, and the averaging part was subtracted off to study the fluctuation behavior. Since most of the smooth varying (semi)classical contribution was removed by excluding the generalized Thomas-Fermi energy from the ground state energy, the remainders were the quantum mechanical oscillation part and the constant shift due to the Weyl part of the wavefunctions. By using the linear regression, the shift in the second difference was found to be 0.7Δ (Δ is the orbital mean level spacing) and almost independent of electron number giving the slope of 1.0×10^{-3} . The fluctuations of the second difference were obtained for three dynamical regimes, and in each regime, 12 data sets constituted the statistical ensembles. One can consider this as taking the data from independent 12 quantum dots. The data showed different patterns of oscillations, but there was a tendency that the fluctuation size reduced as the degree of chaos was increased. The distributions of the peak spacings were symmetric about the means and have widely spread long tails on both sides. The mean values were zero, and the widths of the distributions were enhanced as the system gained regularity. As opposed to the prediction of the constant interaction model, there was no strong bimodal structure observed. The δ -function peak is completely washed out, and only weak even/odd differences were detected.

The wide width and the long tails in the spacing distributions are a manifestation of localized wavefunctions. This can be understood by considering the electron orbital occupation behavior. We looked at a dot to study how electrons filled orbitals when the eigenstates showed localization. Suppose the i th eigenstate is localized and M_{ii} is large, one can observe the orbital avoidance in two stages. First, the system refuses to fill even one electron to the i th orbital. Then, once an electron filled, it remains singly occupied for a wide range of electron number N , and the system polarizes newly added electrons by promoting them to the higher energy levels. At some point where the system is no longer able to save energy by polarizing the electrons, the system locates an electron at the i th orbital paying all the interaction energy stored up to this point. This process produces the deviation in the ground state energy, and as a result, induces the peak spacing fluctuations. Interestingly, the system even refused to fill one electron to an orbital when the corresponding M_{ii} is large, suggesting the importance of the off-diagonal elements. In fact, wavefunction localization not only enhances the diagonal elements, but also affects the size of the associated off-diagonal elements. This is confirmed by investigating the conditional probability of the off-diagonal elements near the diagonal. We plotted the slices of M_{ij} in two different rows: one at M_{ii} large, and the other at M_{ii} small. While the off-diagonal elements associated with large M_{ii} have several pronounced peaks on both sides of the diagonal, the other off-diagonal elements do not have such peaks. The off-diagonal peaks are reduced as the system loses regularity. The distribution of the off-diagonal elements associated with the large M_{ii} clearly showed a tail on the right side representing the pronounced peaks, while for the off-diagonal elements

associated with small M_{ii} , the distributions were narrowly peaked at their respective means.

As a result of the non-standard orbital occupations, the occurrence of the ground state spin is no longer 50% spin 0 and 50% spin 1/2. Due to the orbital avoidance, the system promotes electrons to the higher orbitals and causes the polarizations. The distribution of the ground state spin polarization, together with the orbital occupation probabilities, showed a considerable portion of higher spin state occurrences. As the system gains regularity, there is more chance of having the non-standard occupation for the ground states.

In the end, we emphasize the following observations. In the dynamical system, the localized states greatly affect the electron orbital occupation behavior of determining the ground state. Thus, the standard up/down orbital occupation does not always represent the lowest energy of the system. With the non-standard orbital occupation, the ground state spin polarization showed significant fractions of occurrence of the higher spin configurations. Due to the large diagonal and the associated off-diagonal elements, the system avoided filling particular orbits and polarized newly added electrons. As a consequence, the ground state energy deviated and the second difference often showed large fluctuations. The peak spacing distributions are symmetric about the mean with extended tails on both sides, and little bimodal structure was found. This result agrees with the experimentally observed distributions. Since the eigenstate localizations are more likely to occur in regularized systems, the near integrable and mixed systems showed more influence of this dynamical effects on the statistical properties such as the occurrence of the non-standard orbital occupations and the enhancement of the peak spacing fluctuations, compared to the chaotic system.

There are still possibilities of modifying the system to make the model even more realistic. Although we employed the two-dimensional coupled quartic oscillator as the effective potential in the Strutinsky method, one can add the scrambling effect, the deformation of the potential due to the electron addition, to the system perturbatively. However, this contribution is expected to be small for the systems containing a large number of electrons [94]. The other modification could be to introduce temperature effects to the system. In Appendix G, we tested the accuracy of the matrix elements by looking at the response under finite temperature. Although it is not extended to the study of the finite temperature effect on the ground state or the peak spacing distributions, it would be an interesting problem to investigate. Finally, since we have used the local approximation to the screened interaction, one removes this assumption and proceeds to Fourier transformation explicitly to obtain the exact form of the screened potential. The local approximation was the special case making the direct and exchange interaction combine. With the explicit form of the screened potential, the role of the localized eigenstates might act differently on the orbital occupations and the peak spacing distributions.

Appendix A

Functional Differentiation

Given the functional $F[n]$ with $n = n(\mathbf{r})$, its derivative is defined as

$$\frac{\delta F}{\delta n}[n](\mathbf{r}) \equiv \lim_{\epsilon \rightarrow 0} \frac{F[n(\mathbf{r}') + \epsilon \delta(\mathbf{r} - \mathbf{r}')] - F[n(\mathbf{r}')] }{\epsilon}. \quad (\text{A.1})$$

As a simple example, consider a functional

$$F[n] = \int d\mathbf{r} \, n(\mathbf{r})^2. \quad (\text{A.2})$$

the derivative is give by

$$\frac{\delta F}{\delta n}[n](\mathbf{r}) = \lim_{\epsilon \rightarrow 0} \frac{\int d\mathbf{r}' [n(\mathbf{r}') + \epsilon \delta(\mathbf{r} - \mathbf{r}')]^2 - \int d\mathbf{r}' n(\mathbf{r}')^2}{\epsilon} = 2n(\mathbf{r}). \quad (\text{A.3})$$

It should be mentioned that while a functional itself is a scalar value given a function n , the derivative is both a functional of n and a function of \mathbf{r} .

We also note the functional Taylor expansion. Given a functional $F[n]$, the Taylor series expanded about n_0 where $n = n_0 + \Delta n$ is

$$\begin{aligned} F[n] &= F[n_0] + \int d\mathbf{r} \, \frac{\delta F}{\delta n}[n_0](\mathbf{r}) \Delta n(\mathbf{r}) \\ &+ \frac{1}{2!} \int \int d\mathbf{r} d\mathbf{r}' \, \frac{\delta^2 F}{\delta n^2}[n_0](\mathbf{r}, \mathbf{r}') \Delta n(\mathbf{r}) \Delta n(\mathbf{r}') + \dots \end{aligned} \quad (\text{A.4})$$

Appendix B

Perturbation on the Single-Particle Energy

Consider a Hamiltonian $H = \mathbf{p}^2/2m + V(\mathbf{r})$ and its perturbed Hamiltonian $H' = H + \delta V(\mathbf{r})$. We denote the eigenvalues and eigenvectors as ϵ_i and $\phi_i(\mathbf{r})$ [ϵ'_i and $\phi'_i(\mathbf{r})$] for H (H').

To second order in δV , the perturbed eigenvalues are

$$\epsilon'_i = \epsilon_i + \epsilon_i^{(1)} + \epsilon_i^{(2)} \quad (\text{B.1})$$

where

$$\begin{aligned} \epsilon_i^{(1)} &= \langle \phi_i | \delta V | \phi_i \rangle \\ \epsilon_i^{(2)} &= \sum_{j \neq i} \frac{|\langle \phi_i | \delta V | \phi_j \rangle|^2}{\epsilon_i - \epsilon_j}, \end{aligned} \quad (\text{B.2})$$

assuming non-degenerate eigenstates.

Similarly, taking H' as the original Hamiltonian and $H = H' - \delta V$ as the perturbed Hamiltonian, one can write

$$\epsilon_i = \epsilon'_i + \epsilon_i'^{(1)} + \epsilon_i'^{(2)} \quad (\text{B.3})$$

where

$$\epsilon_i'^{(1)} = -\langle \phi'_i | \delta V | \phi'_i \rangle$$

$$\epsilon_i'^{(2)} = \epsilon_i^{(2)} + o(\delta V^3) . \quad (\text{B.4})$$

Subtracting Eq.(B.3) from Eq.(B.1), one obtains to second order in δV

$$\begin{aligned} \epsilon_i' - \epsilon_i &= \frac{1}{2} (\epsilon_i^{(1)} - \epsilon_i'^{(1)}) \\ &= \frac{1}{2} (\langle \phi_i | \delta V | \phi_i \rangle + \langle \phi_i' | \delta V | \phi_i' \rangle) . \end{aligned} \quad (\text{B.5})$$

Summing over i , one obtains

$$\begin{aligned} \mathcal{E}_{1p}[V + \delta V] - \mathcal{E}_{1p}[V] &= \frac{1}{2} \sum_{i=1}^N (\langle \phi_i | \delta V | \phi_i \rangle + \langle \phi_i' | \delta V | \phi_i' \rangle) \\ &= \frac{1}{2} \int \delta V(\mathbf{r}) (n(\mathbf{r}) + n'(\mathbf{r})) d\mathbf{r} . \end{aligned} \quad (\text{B.6})$$

Appendix C

Optimization of Radial Basis: Choice of Angular Frequency

In the semiclassical limit, an eigenstate of some N -dimensional quantum system has a corresponding $2N$ -dimensional energy surface in phase space, i.e. the Wigner transformation of an eigenstate is localized on the classical energy surface [123]. In the case of the two-dimensional quartic oscillator, a unique four-dimensional closed energy surface corresponds to each state. Consider the construction of coupled quartic oscillator eigenstates in terms of a harmonic oscillator basis. Since we employ a matrix diagonalization technique, choosing the best suited basis is critical. Suppose we are interested in describing one particular eigenstate. Having the corresponding energy surface specified semiclassically, one needs to find minima and maxima of basis energies whose surfaces entirely enclose the given shell as lower and upper bounds. Then the eigenstate will be reasonably well represented if all the basis states whose energies are within the bound contribute to the expansion series of eigenstate. In other words, the eigenstate is built in the subspace spanned by the subset of basis vectors which are defined by the energy bound, and this subspace is truncated from the space constituted by the complete set of harmonic oscillator basis vectors. When one considers this in terms of overlap between basis vectors and the eigenstate, the contributing basis vector subset gives non-zero overlap and the rest are negligible (see section 3.3 in [114]). For computational convenience, it would be desirable that the number of contributing basis

states is as small as possible without sacrificing the accuracy of resulting wave function. Therefore, one should choose the angular frequency of the harmonic oscillator to minimize the number of contributing basis states.

First, let us consider the case of quartic oscillator without anti-unitary symmetry breaking term, and later expand this argument to include the breaking term. Define the Hamiltonian for the quartic oscillator and the harmonic oscillator basis as,

$$H_{Q.O.} = \frac{p^2}{2m_0} + a \left(\frac{x^4}{b} + by^4 + 2\lambda x^2 y^2 \right) \quad (C.1)$$

$$H_{H.O.} = \frac{p^2}{2m} + \frac{m\omega^2}{2}(x^2 + y^2) . \quad (C.2)$$

Suppose eigenstates from the lowest to some energy level $E_{Q.O.}$ are required, one only needs to find the upper bound of the basis. The energy surface of the upper bound completely encloses the surfaces of all the eigenstates, and circumscribes the outer-most surface of eigenstates. These two surfaces contact only by points and they should never cross each other. Using a Lagrange multiplier method, one finds these phase space points which maximize $H_{H.O.}$ under the constraint that the energy is fixed as $E_{Q.O.} = H_{Q.O.}$. Set a Lagrange multiplier ξ as,

$$\nabla H_{Q.O.} = \xi \nabla H_{H.O.} \quad (C.3)$$

or

$$\frac{p_x}{m_0} = \xi \frac{p_x}{m} \quad (C.4)$$

$$\frac{p_y}{m_0} = \xi \frac{p_y}{m} \quad (\text{C.5})$$

$$4a \left(\frac{x^3}{b} + \lambda xy^2 \right) = \xi m \omega^2 x \quad (\text{C.6})$$

$$4a (by^3 + \lambda x^2 y) = \xi m \omega^2 y . \quad (\text{C.7})$$

We have 5 equations (including $E_{\text{Q.O.}} = H_{\text{Q.O.}}$) and 5 unknowns, x, y, p_x, p_y , and ξ . There are 8 solutions for the extrema of $H_{\text{H.O.}}$,

$$E_{\text{H.O.}}^{(1)} = \frac{m_0}{m} E_{\text{Q.O.}} \quad (\text{C.8})$$

$$E_{\text{H.O.}}^{(2)} = \frac{m_0}{m} E_{\text{Q.O.}} + \frac{m^3 \omega^4}{16am_0} \frac{1}{b} \quad (\text{C.9})$$

$$E_{\text{H.O.}}^{(3)} = \frac{m_0}{m} E_{\text{Q.O.}} + \frac{m^3 \omega^4}{16am_0} b \quad (\text{C.10})$$

$$E_{\text{H.O.}}^{(4)} = \frac{m_0}{m} E_{\text{Q.O.}} + \frac{m^3 \omega^4}{16am_0} \frac{b + \frac{1}{b} - 2\lambda}{1 - \lambda^2} \quad (\text{C.11})$$

$$E_{\text{H.O.}}^{(5)} = 0 \quad (\text{C.12})$$

$$E_{\text{H.O.}}^{(6)} = \frac{m\omega^2}{2} \sqrt{\frac{E_{\text{Q.O.}}}{a} \frac{1}{b}} \quad (\text{C.13})$$

$$E_{\text{H.O.}}^{(7)} = \frac{m\omega^2}{2} \sqrt{\frac{E_{\text{Q.O.}}}{a} b} \quad (\text{C.14})$$

$$E_{\text{H.O.}}^{(8)} = \frac{m\omega^2}{2} \sqrt{\frac{E_{\text{Q.O.}}}{a} \frac{b + \frac{1}{b} - 2\lambda}{1 - \lambda^2}} . \quad (\text{C.15})$$

With the conditions $0 < b < 1$ and $-1 < \lambda < 0$, the global maximum of $E_{\text{H.O.}}$ is

$$E_{\text{H.O.}} = \frac{m_0}{m} E_{\text{Q.O.}} + \frac{m^3 \omega^4}{16am_0} \frac{b + \frac{1}{b} - 2\lambda}{1 - \lambda^2} . \quad (\text{C.16})$$

Now that the outer energy shell is found, the angular frequency ω which minimizes the

number of contributing basis functions is given as follows: the frequency, $\Omega \equiv m\omega$ which minimize $E_{\text{H.O.}}/\omega$ is

$$\Omega = \left[\frac{16}{3} a m_0^2 \frac{1 - \lambda^2}{b + \frac{1}{b} - 2\lambda} E_{\text{Q.O.}} \right]^{\frac{1}{4}} \quad (\text{C.17})$$

and setting $m = m_0 = 1$ gives,

$$\omega = \left[\frac{16}{3} a \frac{1 - \lambda^2}{b + \frac{1}{b} - 2\lambda} E_{\text{Q.O.}} \right]^{\frac{1}{4}} . \quad (\text{C.18})$$

With this choice of angular frequency, two energy values are related as,

$$E_{\text{H.O.}} = \frac{4}{3} \frac{m_0}{m} E_{\text{Q.O.}} . \quad (\text{C.19})$$

Having Weyl part of counting functions for both quartic and harmonic oscillators, $\bar{N}_{\text{Q.O.}} = \bar{E}_{\text{Q.O.}}^{3/2}$ and $\bar{N}_{\text{H.O.}} = \bar{E}_{\text{H.O.}}^2 / 2\omega^2$ respectively, one can estimate the number of participating basis to construct $\bar{N}_{\text{Q.O.}}$ of quartic oscillator eigenstates by the following formula,

$$\bar{N}_{\text{H.O.}} = \frac{2}{9} \sqrt{\frac{3}{a} \frac{b + \frac{1}{b} - 2\lambda}{1 - \lambda^2}} \bar{N}_{\text{Q.O.}} . \quad (\text{C.20})$$

Now let us consider the system with the symmetry breaking term. Expressing the Hamiltonian in terms of polar coordinate,

$$H_{\text{Q.O.}} = \frac{p_r^2}{2m_0} + \frac{p_\theta^2}{2m_0 r^2} + f(\theta) r^4 + \epsilon \sqrt{a} r^2 p_r \cos^2 \theta \quad (\text{C.21})$$

$$H_{\text{H.O.}} = \frac{p_r^2}{2m} + \frac{p_\theta^2}{2m r^2} + \frac{m\omega^2}{2} r^2 \quad (\text{C.22})$$

where

$$f(\theta) = a \left[\left(\frac{1}{b} + \frac{\epsilon^2}{2} \right) \cos^4 \theta + b \sin^4 \theta + 2\lambda \sin^2 \theta \cos^2 \theta \right] . \quad (\text{C.23})$$

Using the Lagrange multiplier method, one obtains 5 equations (including $E_{\text{Q.O.}} = H_{\text{Q.O.}}$)

and 5 unknowns, p_r, p_θ, r, θ and ξ ,

$$\frac{p_r}{m_0} + \epsilon \sqrt{a} r^2 \cos^2 \theta = \xi \frac{p_r}{m} \quad (\text{C.24})$$

$$\frac{p_\theta}{m_0 r^2} = \xi \frac{p_\theta}{m r^2} \quad (\text{C.25})$$

$$4f(\theta)r^3 + 2\epsilon\sqrt{a}rp_r \cos^2 \theta = \xi m \omega r \quad (\text{C.26})$$

$$2\sqrt{a}r^2 \left((b - \lambda) \sin^2 \theta - \left[\left(\frac{1}{b} + \frac{\epsilon^2}{2} \right) - \lambda \right] \cos^2 \theta \right) = \epsilon p_r . \quad (\text{C.27})$$

Assuming $r \neq 0$ and $\epsilon \neq 0$, the first two equations gives,

$$p_\theta = 0 \quad (\text{C.28})$$

$$\xi = \frac{m}{m_0} + \epsilon \sqrt{a} m \frac{r^2 \cos^2 \theta}{p_r} \quad (\text{C.29})$$

and so, the third equation becomes,

$$\left(4f(\theta) - \epsilon \sqrt{a} m^2 \omega^2 \frac{\cos^2 \theta}{p_r} \right) r^2 = \frac{m^2 \omega^2}{m_0} - 2\epsilon \sqrt{a} p_r \cos^2 \theta . \quad (\text{C.30})$$

Solving above equations is rather involved, so let us consider perturbatively in ϵ . Set the

variables as,

$$r = r^{(0)} + \epsilon r^{(1)} + \epsilon^2 r^{(2)} + \dots \quad (\text{C.31})$$

$$\theta = \theta^{(0)} + \epsilon \theta^{(1)} + \epsilon^2 \theta^{(2)} + \dots \quad (\text{C.32})$$

$$p_r = p_r^{(0)} + \epsilon p_r^{(1)} + \epsilon^2 p_r^{(2)} + \dots \quad (\text{C.33})$$

and they give

$$r^2 = r^{(0)2} + 2\epsilon r^{(0)} r^{(1)} + \dots \quad (\text{C.34})$$

$$r^4 = r^{(0)4} + 4\epsilon r^{(0)3} r^{(1)} + \dots \quad (\text{C.35})$$

$$\sin^2 \theta = \sin^2 \theta^{(0)} + 2\epsilon \theta^{(1)} \sin \theta^{(0)} \cos \theta^{(0)} + \dots \quad (\text{C.36})$$

$$\cos^2 \theta = \cos^2 \theta^{(0)} - 2\epsilon \theta^{(1)} \sin \theta^{(0)} \cos \theta^{(0)} + \dots \quad (\text{C.37})$$

$$\sin^4 \theta = \sin^4 \theta^{(0)} + 4\epsilon \theta^{(1)} \sin^3 \theta^{(0)} \cos \theta^{(0)} + \dots \quad (\text{C.38})$$

$$\cos^4 \theta = \cos^4 \theta^{(0)} - 4\epsilon \theta^{(1)} \sin \theta^{(0)} \cos^3 \theta^{(0)} + \dots \quad (\text{C.39})$$

and

$$f(\theta) = f^{(0)}(\theta) + \epsilon f^{(1)}(\theta) + \dots \quad (\text{C.40})$$

where

$$f^{(0)} = a \left(\frac{1}{b} \cos^4 \theta^{(0)} + b \sin^4 \theta^{(0)} + 2\lambda \sin^2 \theta^{(0)} \cos^2 \theta^{(0)} \right) \quad (\text{C.41})$$

$$f^{(1)} = 4\theta^{(1)} \sin \theta^{(0)} \cos \theta^{(0)} \left[(b - \lambda) \sin^2 \theta^{(0)} - \left(\frac{1}{b} - \lambda \right) \cos^2 \theta^{(0)} \right] \quad (\text{C.42})$$

Equation (C.27) can be decomposed by the order in ϵ . For the lowest two orders,

$$2\sqrt{a}r^{(0)2} \left[(b - \lambda) \sin^2 \theta^{(0)} - \left(\frac{1}{b} - \lambda \right) \cos^2 \theta^{(0)} \right] = 0 \quad (\text{C.43})$$

$$4\sqrt{a}r^{(0)}r^{(1)} \left[(b - \lambda) \sin^2 \theta^{(0)} - \left(\frac{1}{b} - \lambda \right) \cos^2 \theta^{(0)} \right] + 4\sqrt{a}r^{(0)2}\theta^{(1)} \sin \theta^{(0)} \cos \theta^{(0)} \left(b - \frac{1}{b} \right) = p_r^{(0)} \quad (\text{C.44})$$

and they give

$$\sin^2 \theta^{(0)} = \frac{\frac{1}{b} - \lambda}{b + \frac{1}{b} - 2\lambda} \quad (\text{C.45})$$

$$\cos^2 \theta^{(0)} = \frac{b - \lambda}{b + \frac{1}{b} - 2\lambda} \quad (\text{C.46})$$

$$\theta^{(1)} = \frac{1}{4\sqrt{a} \left(b - \frac{1}{b} \right)} \frac{p_r^{(0)}}{r^{(0)2} \sin \theta^{(0)} \cos \theta^{(0)}}. \quad (\text{C.47})$$

Similarly, Eq. (C.30) is expressed as

$$4f^{(0)}r^{(0)2} = \frac{m^2\omega^2}{m_0} \quad (\text{C.48})$$

$$8f^{(0)}r^{(0)}r^{(1)} + 4f^{(1)}r^{(0)2} - \sqrt{a}m^2\omega^2 \frac{r^{(0)2} \cos^2 \theta^{(0)}}{p_r^{(0)}} = -2\sqrt{a}p_r^{(0)} \cos^2 \theta^{(0)} \quad (\text{C.49})$$

and

$$r^{(0)} = \sqrt{\frac{m^2\omega^2}{4m_0f^{(0)}}} \quad (\text{C.50})$$

$$r^{(1)} = \frac{1}{8f^{(0)}r^{(0)}} \left(-4f^{(1)}r^{(0)2} + \sqrt{a}m^2\omega^2 \frac{r^{(0)2} \cos^2 \theta^{(0)}}{p_r^{(0)}} - 2\sqrt{a}p_r^{(0)} \cos^2 \theta^{(0)} \right) \quad (\text{C.51})$$

Since we are given $E_{\text{Q.O.}}$,

$$E_{\text{Q.O.}}^{(0)} = \frac{p_r^{(0)2}}{2m_0} + f^{(0)}r^{(0)4} \quad (\text{C.52})$$

$$\Rightarrow p_r^{(0)} = \sqrt{2m_0 \left(E_{\text{Q.O.}}^{(0)} - \frac{m^4 \omega^4}{16m_0^2 f^{(0)}} \right)}. \quad (\text{C.53})$$

Having the expressions for $r^{(0)}$, $r^{(1)}$, $\theta^{(0)}$, $\theta^{(1)}$, $p_r^{(0)}$ and p_θ , now look at the variation of harmonic oscillator energy with up to first order,

$$E_{\text{H.O.}} = \frac{p_r^2}{2m} + \frac{m\omega^2}{2}r^2 \quad (\text{C.54})$$

$$= \frac{m_0}{m} E_{\text{Q.O.}}^{(0)} + \frac{m\omega^2}{2}r^2 - \frac{m_0}{m} f^{(0)}r^4 \quad (\text{C.55})$$

$$= E_{\text{H.O.}}^{(0)} + \epsilon E_{\text{H.O.}}^{(1)} + \dots \quad (\text{C.56})$$

where

$$E_{\text{H.O.}}^{(0)} = \frac{m_0}{m} E_{\text{Q.O.}}^{(0)} + \frac{m\omega^2}{2}r^{(0)2} - \frac{m_0}{m} f^{(0)}r^{(0)4} \quad (\text{C.57})$$

$$E_{\text{H.O.}}^{(1)} = r^{(0)}r^{(1)} \left(m\omega^2 - \frac{4m_0 f^{(0)}}{m} r^{(0)2} \right) = 0. \quad (\text{C.58})$$

Since the first order term vanishes, there is no variation of harmonic oscillator energy, and so as angular frequency ω . Therefore, one can use the same angular frequency for both cases with or without the symmetry breaking term at this level of approximation.

Appendix D

Number Variance Statistics

In characterizing the statistical properties of a system, one of the most important processes is to measure spectral fluctuations. There exist various kinds of fluctuation (or correlation) measures [112,136], and each approach has different advantages depending on which statistical aspect one is interested in.

Suppose one has a spectrum, E_1, \dots, E_N for a given system. Since every system has different spectral behavior, one must unfold them to be able to compare fluctuations among different systems. Let us denote the unfolded spectra as x_1, \dots, x_N , and express the probability of finding each spectrum x_i in the interval $[x_i, x_i + dx_i]$ as

$$P_N(x_1, \dots, x_N) dx_1 \dots dx_N. \quad (D.1)$$

Then, one way to measure the statistical property of the spectra is to use the n -level correlation function defined by

$$R_n(x_1, \dots, x_n) = \frac{N!}{(N-n)!} \int P_N(x_1, \dots, x_N) dx_{n+1} \dots dx_N \quad (D.2)$$

which gives the probability density of finding the n levels x_1, \dots, x_n regardless of the location of all other levels. In terms of the correlation functions, the pure n -point functions are given

by

$$\hat{R}_n(r) = \int_0^r \dots \int_0^r R_n(x_1, \dots, x_n) dx_1 \dots dx_n. \quad (\text{D.3})$$

Using this function, $\hat{R}_n(r)/n!$ gives the probability that n levels are contained in the interval of distance r (for small r).

It is often convenient to introduce the n -level cluster function Y_n which is the n th order cumulant derived from the correlation functions. For our purpose of studying energy spectra, the case with $n = 2$ suffice,

$$Y_2(x_1, x_2) = -R_2(x_1, x_2) + R_1(x_1)R_1(x_2). \quad (\text{D.4})$$

The cluster function Y_2 vanishes when the separation $|x_1 - x_2|$ becomes large, giving the means to exclude the lower order correlations. When the spectral fluctuations are independent of the location of the spectrum, the cluster function only depends on the separation $|x| = |x_1 - x_2|$.

Expressing the density distribution of spacings between two levels x_{i+k+1} and x_i as $p(k; s)$ where $s = x_{i+k+1} - x_i$ and $(k = 0, 1, \dots)$, the previous functions can be rewritten as

$$R_2(x) = 1 - Y_2(x) = \sum_{k=0}^{\infty} p(k; |x|). \quad (\text{D.5})$$

In the case of $k = 0$, $p(0; s)$ represents the nearest neighbor spacing distribution and is written as $p(s)$.

The number variance $\Sigma^2(r)$ is constructed as the variance of $n(r)$, the number of levels

contained in the interval of distance r .

$$\Sigma^2(r) \equiv \langle n^2(r) \rangle - \langle n(r) \rangle^2. \quad (\text{D.6})$$

The number variance is connected to the cluster function by

$$\Sigma^2(r) = r - 2 \int_0^r (r-s) Y_2(s) ds \quad (\text{D.7})$$

$$\frac{d^2}{dr^2} \Sigma^2(r) = -2Y_2(r). \quad (\text{D.8})$$

It is also related to \hat{R}_2 by

$$\hat{R}_2(r) = \Sigma^2(r) + r(r-1). \quad (\text{D.9})$$

The number variance can be considered as the fluctuation of the counting function by interpreting $n(r)$ as the counting function and r as the energy measured in the unit of mean level spacing.

For the purpose of comparison, one can construct an uncorrelated spectrum by

$$x_{i+1} = x_i + s_i, \quad x_1 = 0, \quad (i = 1, 2, \dots) \quad (\text{D.10})$$

where s_i are random numbers whose probability density gives e^{-s} . This is called a Poisson

spectrum, and the correlation functions are given as

$$R_n(x_1, \dots, x_n) = 1 \quad (\text{D.11})$$

$$Y_2(x_1, x_2) = 0, \quad (\text{D.12})$$

and the spacing distributions are

$$p(s) = e^{-s} \quad (\text{D.13})$$

$$\hat{R}_n(r) = r^n \quad (\text{D.14})$$

$$\Sigma^2(r) = r. \quad (\text{D.15})$$

As the reference curves, we show the expressions obtained for the Gaussian ensembles from RMT. The conventional notations: $\beta = 1$ represents Gaussian orthogonal ensemble (GOE), and $\beta = 2$ is for Gaussian unitary ensemble (GUE), (symplectic case is omitted here).

The nearest neighbor spacing distributions:

$$P(s) = \frac{\pi}{2} s e^{-(\pi/4)s^2} \quad (\text{GOE}) \quad (\text{D.16})$$

$$P(s) = \frac{32}{\pi^2} s^2 e^{-(4/\pi)s^2} \quad (\text{GUE}). \quad (\text{D.17})$$

The two-level cluster function:

$$Y_2(x) = \left(\frac{\sin \pi x}{\pi x} \right)^2 - \left[\text{Si}(\pi x) - \frac{1}{2} \pi \text{sgn}(x) \right] \left[\frac{\cos \pi x}{\pi x} - \frac{\sin \pi x}{(\pi x)^2} \right] \quad (\text{GOE}) \quad (\text{D.18})$$

$$Y_2(x) = \left(\frac{\sin \pi x}{\pi x} \right)^2 \quad (\text{GUE}) \quad (\text{D.19})$$

where $\text{Si}(x) = \int_0^x dt \sin t/t$. For $x \ll 1$, the functions are approximated as

$$Y_2(x) = 1 - \frac{\pi^2}{6} x + \frac{\pi^4}{60} x^3 - \frac{\pi^4}{135} x^4 + \dots \quad (\text{GOE}) \quad (\text{D.20})$$

and for $x \gg 1$,

$$Y_2(x) = \frac{1}{(\pi x)^2} - \frac{1 + \cos^2 \pi x}{(\pi x)^4} + \dots \quad (\text{GOE}) \quad (\text{D.21})$$

$\hat{R}_2(r)$ with $r \ll 1$:

$$\hat{R}_2(r) = \frac{\pi^2}{18} r^3 + \dots \quad (\text{GOE}) \quad (\text{D.22})$$

$$\hat{R}_2(r) = \frac{\pi^2}{18} r^4 + \dots \quad (\text{GUE}). \quad (\text{D.23})$$

Number variance $\Sigma_\beta^2(r)$:

$$\Sigma_{\beta=1}^2(r) = 2\Sigma_{\beta=2}^2(r) + \left[\frac{\text{Si}(\pi r)}{\pi} \right]^2 - \frac{\text{Si}(\pi r)}{\pi} \quad (\text{GOE}) \quad (\text{D.24})$$

$$\begin{aligned} \Sigma_{\beta=2}^2(r) &= \frac{1}{\pi^2} [\ln(2\pi r) + \gamma + 1 - \cos(2\pi r) - \text{Ci}(2\pi r)] \\ &+ r \left[1 - \frac{2}{\pi} \text{Si}(2\pi r) \right] \quad (\text{GUE}). \end{aligned} \quad (\text{D.25})$$

where $\text{Ci}(x) = \gamma + \ln x + \int_0^x dt(\cos t - 1)/t$ and γ is Euler's constant, $\gamma \simeq 0.5772$. For $r \gg 1$, they behave as

$$\Sigma_{\beta=1}^2(r) = \frac{2}{\pi^2} \left[\ln(2\pi r) + \gamma + 1 - \frac{\pi^2}{8} \right] + O(r^{-1}) \quad (\text{D.26})$$

$$\Sigma_{\beta=2}^2(r) = \frac{1}{\pi^2} [\ln(2\pi r) + \gamma + 1] + O(r^{-1}). \quad (\text{D.27})$$

The logarithmic dependence is an expression of the celebrated spectral rigidity of random matrix ensembles.

Appendix E

Moments of a Distribution

The moments are the quantities which characterize a set of numbers. These are especially useful when the set of numbers show a tendency to cluster around some values.

For a given set of numbers x_1, \dots, x_N , the mean is given by

$$\mu = \bar{x} = \frac{1}{N} \sum_{i=1}^N x_i. \quad (\text{E.1})$$

This is also known as the first moment of the distribution.

The variance which characterizes the “width” of the set around the mean is

$$\mu_2 = \frac{1}{N} \sum_{i=1}^N (x_i - \bar{x})^2. \quad (\text{E.2})$$

This is the second (central) moment. It is “central” because the mean value is subtracted from each data. The standard deviation is given by $\sigma = \sqrt{\mu_2}$.

The third (central) moment measures the degree of asymmetry of the distribution around the mean,

$$\mu_3 = \frac{1}{N} \sum_{i=1}^N (x_i - \bar{x})^3, \quad (\text{E.3})$$

and the skewness is $\gamma_1 = \mu_3/\sigma^3$. For a distribution that has an asymmetric tail on the right (left) side, the skewness gives positive (negative) value. While the mean and the standard

deviation have the same dimensionality as the original data, the skewness is defined as non-dimensional quantity.

The fourth (central) moment characterizes the degree of peakedness relative to a normal distribution. It is defined as

$$\mu_4 = \frac{1}{N} \sum_{i=1}^N (x_i - \bar{x})^4, \quad (\text{E.4})$$

and the kurtosis is given by $\gamma_2 = \mu_4/\sigma^4 - 3$ where the subtraction of 3 makes the kurtosis of a normal distribution zero. The positive kurtosis represents that the distribution is more peaked around the mean value compared to a normal distribution, and the negative value means more flattened distribution. The kurtosis is also a non-dimensional quantity.

Appendix F

Fluctuations of M_{ij}

Based on Berry's conjecture, Srednicki [133] derived the spatial correlation functions in quantum dots. If the wavefunctions can be treated as the Gaussian distributed quantities, the following two point correlation function holds for $|\mathbf{r} - \mathbf{r}'| \ll L$,

$$A \langle \phi_i(\mathbf{r}) \phi_j^*(\mathbf{r}') \rangle = \delta_{ij} J_0(k_F |\mathbf{r} - \mathbf{r}'|), \quad (\text{F.1})$$

where A is the two-dimensional dot area, L is the system size ($A \sim L^2$), and k_F is the Fermi wave number. The expressions derived were, in the case of time-reversal invariance (TRI),

$$A^{n+m} \langle |\phi(\mathbf{r})|^{2n} |\phi(\mathbf{r}')|^{2m} \rangle = \sum_{q=0}^{\min(n,m)} \frac{(2n)!(2m)!}{2^{n+m-2q}(n-q)!(m-q)!(2q)!} J_0^{2q}(k_F |\mathbf{r} - \mathbf{r}'|), \quad (\text{F.2})$$

and in the case of broken time-reversal invariance (TRNI),

$$A^{n+m} \langle |\phi(\mathbf{r})|^{2n} |\phi(\mathbf{r}')|^{2m} \rangle = \sum_{q=0}^{\min(n,m)} \frac{(n!)^2(m!)^2}{(n-q)!(m-q)!(q!)^2} J_0^{2q}(k_F |\mathbf{r} - \mathbf{r}'|). \quad (\text{F.3})$$

Applying the spatial correlation functions, Ullmo and Baranger [94] computed the means and variances of the matrix elements M_{ij} . Here, we introduce the brief derivation of mean and variance of the diagonal elements M_{ii} . Setting $n = m = 1$ in Eq. (F.2) and (F.3), the

spatial correlation functions give

$$A^2 \langle |\phi(\mathbf{r})|^2 |\phi(\mathbf{r}')|^2 \rangle = 1 + 2J_0^2(k_F |\mathbf{r} - \mathbf{r}'|) \quad \text{for TRI} \quad (\text{F.4})$$

$$= 1 + J_0^2(k_F |\mathbf{r} - \mathbf{r}'|) \quad \text{for TRNI}, \quad (\text{F.5})$$

and lead the local correlations at $\mathbf{r} = \mathbf{r}'$ as,

$$A^2 \langle |\phi(\mathbf{r})|^4 \rangle = 3 \quad \text{for TRI} \quad (\text{F.6})$$

$$= 2 \quad \text{for TRNI}. \quad (\text{F.7})$$

The means of the diagonal elements M_{ii} are obtained,

$$\langle M_{ii} \rangle = \frac{1}{N(0)} \int d\mathbf{r} \langle |\phi(\mathbf{r})|^4 \rangle = \frac{3}{AN(0)} = \frac{3\Delta}{2} \quad \text{for TRI} \quad (\text{F.8})$$

$$= \frac{2}{AN(0)} = \Delta \quad \text{for TRNI} \quad (\text{F.9})$$

$$\Rightarrow \langle M_{ii}^{\text{TRI}} \rangle = \frac{3}{2} \langle M_{ii}^{\text{TRNI}} \rangle \quad (\text{F.10})$$

where the orbital mean level spacing is $\Delta = 2/AN(0)$ taken into account the electron spin degree of freedom in $N(0)$, the local approximation to the screened potential is assumed, and $N(0) \equiv \rho^W$.

For the variance of M_{ii} , one needs to compute $\langle M_{ii}^2 \rangle$. The spatial correlation functions

for $n = m = 2$ give

$$A^4 \langle |\phi(\mathbf{r})|^4 |\phi(\mathbf{r}')|^4 \rangle = 24J_0^4 + 72J_0^2 + 9 \quad \text{for TRI} \quad (\text{F.11})$$

$$= 4J_0^4 + 16J_0^2 + 4 \quad \text{for TRNI}, \quad (\text{F.12})$$

and

$$\langle M_{ii}^2 \rangle = \frac{1}{A^4 N(0)^2} \int d\mathbf{r} d\mathbf{r}' (24J_0^4 + 72J_0^2 + 9) \quad \text{for TRI} \quad (\text{F.13})$$

$$= \frac{1}{A^4 N(0)^2} \int d\mathbf{r} d\mathbf{r}' (4J_0^4 + 16J_0^2 + 4) \quad \text{for TRNI}, \quad (\text{F.14})$$

where the argument of the Bessel function is $k_F |\mathbf{r} - \mathbf{r}'|$. The contributions of the constant terms are canceled when $\langle M_{ii} \rangle^2$ is subtracted off, and the terms with the second power of the Bessel functions are discarded because of the normalization conditions for both TRI and TRNI cases. Then, the variances are given by

$$\begin{aligned} \text{Var}(M_{ii}) &= \langle M_{ii}^2 \rangle - \langle M_{ii} \rangle^2 \\ &= \frac{24}{A^4 N(0)^2} \int d\mathbf{s}' \int d\mathbf{s} J_0^4(k_F s) \quad \text{for TRI} \end{aligned} \quad (\text{F.15})$$

$$= \frac{4}{A^4 N(0)^2} \int d\mathbf{s}' \int d\mathbf{s} J_0^4(k_F s) \quad \text{for TRNI}, \quad (\text{F.16})$$

where $\mathbf{s} = \mathbf{r} - \mathbf{r}'$ and $\mathbf{s}' = \mathbf{r} + \mathbf{r}'$. Since the Bessel function can be approximated as

$$J_0(x) \simeq \begin{cases} 1 & x \ll 1 \\ 0 & x \gg 1 \\ \frac{\sin(x-\pi/4)}{\sqrt{\pi x/2}} & \text{otherwise} \end{cases} \quad (\text{F.17})$$

we perform the integration as follows,

$$\int d\mathbf{s} J_0^4(k_F s) = 2\pi \left(\int_0^{1/k_F} + \int_{1/k_F}^L + \int_L^\infty \right) J_0^4(k_F s) s ds \quad (\text{F.18})$$

$$\sim 2\pi \int_{1/k_F}^L ds s \langle J_0^4(k_F s) \rangle = \frac{3}{\pi k_F^2} \ln(k_F L) \quad (\text{F.19})$$

where the first integration vanishes because $1/k_F^2 = (\lambda/2\pi)^2 \ll 1$ and the second integration is calculated taking advantage of its oscillating behavior

$$\langle J_0^4(x) \rangle \simeq \left\langle \frac{4 \sin^4(x - \pi/4)}{(\pi x)^2} \right\rangle = \frac{3}{2(\pi x)^2}. \quad (\text{F.20})$$

Thus, the variances are given as

$$\text{Var}(M_{ii}) = 24 \cdot \frac{3\Delta^2 \ln(k_F L)}{4\pi (k_F L)^2} \quad \text{for TRI} \quad (\text{F.21})$$

$$= 4 \cdot \frac{3\Delta^2 \ln(k_F L)}{4\pi (k_F L)^2} \quad \text{for TRI} \quad (\text{F.22})$$

$$\Rightarrow \text{Var}(M_{ii}^{\text{TRI}}) = 6 \cdot \text{Var}(M_{ii}^{\text{TRNI}}) \quad (\text{F.23})$$

where $\int d\mathbf{s}' = A = L^2$. In Ref. [94], the expressions of mean and variance of the matrix

elements including off-diagonals are given as

$$\langle M_{ij} \rangle = (1 + \delta_{ij})\Delta/2 \quad (\text{F.24})$$

$$\text{Var}(M_{ij}) = \frac{3\Delta^2 \ln(k_F L)}{4\pi (k_F L)^2} (1 + 3\delta_{ij}), \quad (\text{F.25})$$

where we note that they are computed exclusively for the time reversal non-invariant systems in the chaotic regime. In addition, there is no dynamical confining potential or boundary conditions (or one can think of this as the infinite well confinement with vanishing wave-functions at the boundary).

While the analytical expressions are directly applicable to the system of plane wave superposition approximation, they are not suitable for the coupled quartic oscillator systems. Since the formulae are derived for the steep wall potential, one needs to adjust them for the smooth potential. Let us consider the following integral,

$$I \equiv \frac{1}{(k_F L)^2} \sim \frac{1}{A^2} \int_{E-V>0} \frac{d\mathbf{r}}{k_F^2} = \frac{1}{A^2} \frac{\hbar^2}{2m} \int_{E-V>0} \frac{d\mathbf{r}}{E - V(\mathbf{r})} \quad (\text{F.26})$$

where the Fermi wave number is given by

$$k_F = \frac{p}{\hbar} = \frac{\sqrt{2m(E - V(\mathbf{r}))}}{\hbar}. \quad (\text{F.27})$$

To use the scaling property of the quartic oscillator, we set $\mathbf{r} = E^{1/4} \mathbf{r}_0$,

$$V(\mathbf{r}) = EV(\mathbf{r}_0) \quad (\text{F.28})$$

$$A = \int_{E-V>0} d\mathbf{r} = E^{1/2} \int_{E-V>0} d\mathbf{r}_0 = E^{1/2} A_0, \quad (\text{F.29})$$

and then

$$I = \frac{\hbar^2}{2m} \frac{1}{A_0^2 E^{3/2}} \int_{1-V(\mathbf{r}_0)>0} \frac{d\mathbf{r}_0}{1-V(\mathbf{r}_0)}. \quad (\text{F.30})$$

For the case that the coupling constant is not too far from $\lambda = 1.0$, the potential can be taken as $V = ar^4$, and it gives $E = ar_{\max}^4$ at the boundary. The area of classically allowed region are then

$$A = \pi r_{\max}^2 = \pi \sqrt{E/a} \quad (\text{F.31})$$

$$A_0 = \pi / \sqrt{a}. \quad (\text{F.32})$$

These give the integral

$$I = \frac{\hbar^2}{2m} \frac{a}{\pi^2 E^{3/2}} \int_{1-V(\mathbf{r}_0)>0} \frac{d\mathbf{r}_0}{1-V(\mathbf{r}_0)} \quad (\text{F.33})$$

$$\sim \frac{\hbar^2}{2m} \frac{a}{\pi^2 E^{3/2}} \cdot \frac{\pi}{a^{1/2}} \ln(k_F L) \quad (\text{F.34})$$

$$\sim \frac{\hbar^2}{2m} \frac{a^{1/2}}{\pi E^{3/2}} \ln(k_F L). \quad (\text{F.35})$$

Using the counting functions of the quartic oscillator $\tilde{N}(E) \simeq E^{3/2}$, the integral is written

as

$$I \sim \frac{\ln(k_F L)}{6\pi \bar{N}(E)} \quad (\text{F.36})$$

where

$$a^{1/2} = \frac{2K((1-\lambda)/2)}{3\pi} \frac{m}{\hbar^2} = \frac{m}{3\hbar^2}. \quad (\text{F.37})$$

Even though the quartic oscillator potential has smooth wall, the wall is steep enough to approximate the followings,

$$k_F \sim \frac{\sqrt{2mE}}{\hbar} \quad (\text{F.38})$$

$$L \sim r_{\max} = (E/a)^{1/4} \quad (\text{F.39})$$

$$\Rightarrow (k_F L)^2 \sim \frac{2mE^{3/2}}{\hbar^2 a^{1/2}} = 6\bar{N}(E). \quad (\text{F.40})$$

Therefore, we obtain the expression of the variance for the (TRNI) two-dimensional quartic oscillator system as

$$\text{Var}(M_{ij}) \sim \frac{3\Delta^2}{4\pi} \ln(k_F L) \cdot I \cdot (1 + 3\delta_{ij}) \quad (\text{F.41})$$

$$\sim \frac{3\Delta^2}{4\pi^2} \frac{[\ln(6\bar{N})]^2}{6\bar{N}} (1 + 3\delta_{ij}). \quad (\text{F.42})$$

For the TRI quartic oscillator system, the variance of the diagonal elements is given by

$$\text{Var}(M_{ii}^{\text{TRI}}) = 6\text{Var}(M_{ii}^{\text{TRNI}}).$$

Appendix G

Finite Temperature Effects on M_{ij}

For a system with N Fermion, the lowest N energy levels are occupied in the limit of temperature $T \rightarrow 0$ ignoring spin degeneracy for simplicity. The electron density is expressed as

$$n(\mathbf{r}) = \sum_{i=1}^N |\phi_i(\mathbf{r})|^2 \quad (\text{G.1})$$

where ϕ_i are eigenfunctions of the system. Using the Fermi occupation factor $f(\epsilon - \mu) = [e^{(\epsilon - \mu)/k_B T} + 1]^{-1}$, the electron density at finite temperature $T > 0$ becomes

$$n(\mathbf{r}) = \sum_{i=1}^{\infty} |\phi_i(\mathbf{r})|^2 f(\epsilon_i - \mu) \quad (\text{G.2})$$

where the Fermi energy μ must be determined by the normalization conditions of the electron density $N = \int n(\mathbf{r}) d\mathbf{r}$. In the low T domain however, one can still approximate $\mu \simeq \mu_N = \epsilon_N$. On the other hand, as T increases, the quantum mechanical fluctuation part of the electron density $n^{\text{osc}}(\mathbf{r})$ becomes smaller, and so its Weyl part $n^{\text{W}}(\mathbf{r})$ becomes good approximation to $n(\mathbf{r})$. Thus, one obtains

$$n^{\text{W}}(\mathbf{r}) \simeq \sum_{i=1}^N |\phi_i(\mathbf{r})|^2 f(\epsilon_i - \mu_N) . \quad (\text{G.3})$$

With this relation, temperature effects on M_{ij} is given by

$$\frac{1}{N(0)} \int d\mathbf{r} [n^W(\mathbf{r})]^2 \simeq \sum_{i,j=1}^N M_{ij} f(\epsilon_i - \mu_N) f(\epsilon_j - \mu_N) \quad (\text{G.4})$$

where integration on the left hand side takes over classically allowed region $\mu_N - V > 0$, and the local approximation is applied to M_{ij} . The Weyl part of the electron density is defined as

$$n^W(\mathbf{r}) = \frac{1}{h^d} \int d\mathbf{p} \Theta(\mu_N - H) \quad (\text{G.5})$$

where $H = \mathbf{p}^2/2m + V$ and d is degrees of freedom. If the potential is assumed to be independent of momentum, one obtains for $d = 2$

$$n^W(\mathbf{r}) = \frac{m}{2\pi\hbar^2} [\mu_N - V(\mathbf{r})] \quad (\text{G.6})$$

$$N(0) = \rho^W = \frac{dn^W}{d\mu_N} = \frac{m}{2\pi\hbar^2} . \quad (\text{G.7})$$

Then Eq. (G.4) can be approximated as

$$\frac{m}{2\pi\hbar^2} \int d\mathbf{r} [\mu_N - V(\mathbf{r})]^2 \simeq \sum_{i,j=1}^N M_{ij} f(\epsilon_i - \mu_N) f(\epsilon_j - \mu_N) \quad (\text{G.8})$$

where integration takes over the region with $\mu_N - V(\mathbf{r}) > 0$.

To proceed numerical calculation, one must evaluate thermal energy $k_B T$. First, we consider two kinds of dots both attached to two leads respectively. If the dot is in diffusive regime, that is to contain significant amount of impurities, an electron entered from one lead

scatters elastically from the impurities, and so the mean free path of the electron becomes $l \ll L$ where L is the dot size. In this case, the system is characterized by the time scale τ_D , which is the time for the electron to diffuse across the system, and the associated energy scale $E_c = \hbar/\tau_D$ is known as the Thouless energy. Similarly, for the dot in ballistic regime, once an electron enters the dot, it travels through inside being scattered several times from boundaries before exiting the dot. Assuming the boundaries are irregular shape, the electron's classical dynamics represents chaos. The characteristic time scale of this dot is roughly determined by the time of flight across the dot t_F , and the associated energy scaled is the ballistic Thouless energy $E_{TH} = \hbar/t_F$. The connection between conductance fluctuations of disordered systems and RMT are reported in Ref. [137–139]. The statistical fluctuations of energy eigenvalues and eigenvectors of chaotic systems can be described by RMT and show universality if system's energy scale is below E_{TH} . Thus, the Thouless energy serves as an additional energy scale which is critical for RMT study.

Since we are interested in dots in the ballistic regime, we need to compute the time of flight across the system. With the two-dimensional coupled quartic oscillator confinement, $V = a(x^4/b + by^4 + 2\lambda x^2 y^2)$, the shortest periodic orbit is on the x-axis (for $0 < b < 1$), and the classical period for this orbit is given by

$$T = 4 \int_0^{x_t} \frac{dx}{\sqrt{2(E - \frac{a}{b}x^4)}} = 2\sqrt{2\pi} \frac{\Gamma(5/3)}{\Gamma(3/4)} \left(\frac{b}{aE}\right)^{1/4} \quad (\text{G.9})$$

where x_t is the classical turning point in $x > 0$ region. One obtains the Thouless energy by

setting $t_F = T/2$,

$$E_{\text{TH}} = \frac{\hbar}{\sqrt{2\pi}} \frac{\Gamma(3/4)}{\Gamma(5/3)} \left(\frac{aE}{b} \right)^{1/4}. \quad (\text{G.10})$$

We note that for the systems having boundary at $x, y = 0$ and restricted within the region $x, y \geq 0$, the shortest periodic orbit is reduced by factor of two, so the Thouless energy becomes twice as large as the above quantity. To use Eq. (G.8), one sets the temperature near the Thouless energy $k_B T \geq E_{\text{TH}}$.

The relationship of Eq. (G.4) can be used to determine the accuracy of M_{ij} data sets under the temperature broadening by studying the difference between both sides. Taking the particle number as an independent variable, we compute the differences as a function of N . For the system confined by the two-dimensional coupled quartic oscillator and without anti-unitary symmetry breaking term, potential is independent of momentum, and so Eq. (G.8) becomes a suitable approximation. Figure (G.1) shows the absolute difference divided by value of the right hand side. Since the accuracy of semiclassical approximation decreases as the system gets into the low energy domain in general, the data in small N show larger error. The error reduces quickly as N increases and becomes stable for large N . The same is true for a system with a symmetry breaking term; see Fig. (G.1). In the latter system, we separated each parity class and considered them as independent systems. Thus the energy domain belongs to the same ranges as in the former system, although the particle numbers are reduced.

Our major concern here is how reliable M_{ij} data are especially compared to the mean level spacing of energy spectra. The curves show reasonable behavior within the idea of

semiclassical theory, and it becomes stable in large N domain. Most importantly, no divergence occurs. The source of amplified error for the system with symmetry breaking term is originated in the crude approximation of the potential: the breaking term introduces momentum dependence to the effective potential. Rigorously speaking, one has to use Eq. (G.4) and proceed with momentum space integration properly using Eq. (G.5). One last thing we mention is the oscillation of curves. While the localization of wave function causes the pronounced spikes in M_{ii} , there are no such peaks observed in the current data. This is because the summation of M_{ij} averages the large value of diagonal elements, and as a result, only the quantum fluctuation remains.

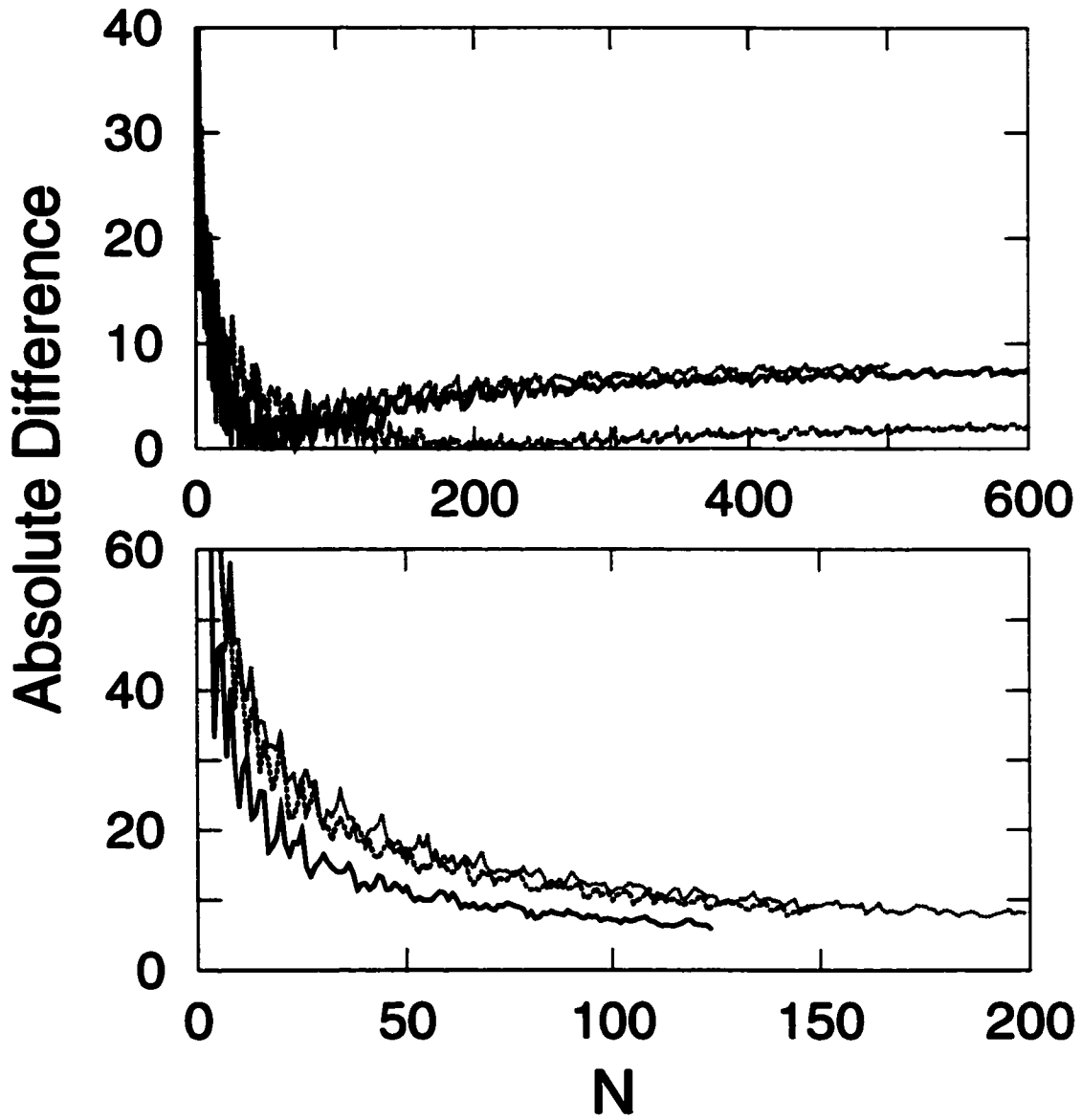


Figure G.1: Absolute differences between both sides of Eq. (G.8) as a function of the particle number N . The upper figure: confining potential is two-dimensional coupled quartic oscillator. The solid line is for $\lambda = -0.55$, dashed line is for $\lambda = -0.35$, and dotted line is for $\lambda = -0.05$. The lower figure: confining potential is two-dimensional coupled quartic oscillator with anti-unitary symmetry breaking term. The solid line is for $\lambda = -0.80$, dashed line is for $\lambda = -0.20$, and dotted line is for $\lambda = 0.20$. The strength of symmetry breaking term ϵ is -1.0 , and parity sequence $(+, +)$ is used for all three cases. For both figures, the data are divided by the value of right hand side and measured in percentage.

References

- [1] N. G. van Kampen, *Stochastic Processes in Physics and Chemistry* (North-Holland, Amsterdam, 1981).
- [2] H. U. Baranger and P. A. Mello, Phys. Rev. Lett. **73**, 142 (1994).
- [3] C. W. J. Beenakker, Phys. Rev. B **47**, 15763 (1993).
- [4] B. L. Altshuler, D. Khmel'nitzkii, A. I. Larkin, and P. A. Lee, Phys. Rev. B **22**, 5142 (1980).
- [5] N. Argaman, Phys. Rev. B **53**, 7035 (1996).
- [6] E. Doron, U. Smilansky, and A. Frenkel, Physica D **50**, 367 (1991).
- [7] R. A. Jalabert, H. U. Baranger, and A. D. Stone, Phys. Rev. Lett. **65**, 2442 (1990).
- [8] I. H. Chan, R. M. Clarke, C. M. Marcus, K. Campman, and A. C. Gossard, Phys. Rev. Lett. **74**, 3876 (1995).
- [9] C. M. Marcus, A. J. Rimberg, R. M. Westervelt, P. F. Hopkins, and A. C. Gossard, Phys. Rev. Lett. **69**, 506 (1992).

- [10] R. A. Jalabert, J. -L. Pichard, C. W. J. Beenakker, *Europhys. Lett.* **27**, 255 (1994).
- [11] M. A. Kastner, *Physics Today*, 24 (January 1993).
- [12] K. -F. Berggren, T. J. Thornton, D. J. Newson, and M. Pepper, *Phys. Rev. Lett.* **57**, 1769 (1986).
- [13] B. J. van Wees, H. van Houten, C. W. J. Beenakker, J. G. Williamson, L. P. Kouwenhoven, D. van der Marel, and C. T. Foxon, *Phys. Rev. Lett.* **60**, 848 (1988).
- [14] J. A. Nixon, J. H. Davies, and H. U. Baranger, *Phys. Rev. B* **43**, 12638 (1991).
- [15] M. J. Laughton, J. R. Barker, J. A. Nixon, J. H. Davies, *Phys. Rev. B* **44**, 1150 (1991).
- [16] H. van Houten, C. W. J. Beenakker, *Physics Today*, 22 (July 1996).
- [17] Y. Meir, N. S. Wingreen, and P. A. Lee, *Phys. Rev. Lett.* **66**, 3048 (1991).
- [18] D. R. Stewart, Ph.D. thesis, Stanford University (1999).
- [19] S. M. Cronenwett, Ph.D. thesis, Stanford University (2001).
- [20] M. Switkes, Ph.D. thesis, Stanford University (1999).
- [21] C. W. J. Beenakker, H. van Houten, Quantum Transport in Semiconductor Nanostructures, in *Solid State Physics vol. 44*, H. Ehrenreich, D. Turnbull, Eds. (Academic Press. New York, 1991).
- [22] J. A. Nixon and J. H. Davies, *Phys. Rev. B* **41**, 7929 (1990).

- [23] D. A. Wharam, T. J. Thornton, R. Newbury, M. Pepper, H. Ahmed, J. E. F. Frost, D. G. Hasko, D. C. Peacock, D. A. Ritchie, and G. A. C. Jones, *J. Phys. C* **21**, L209 (1988).
- [24] L. P. Kouwenhoven, Quantum adiabatic electron transport in ballistic conductors, in *Physics of low-dimensional semiconductor structures*, P. Butcher, H. H. March, M. P. Tosi, Eds. (Plenum Press, New York, 1993).
- [25] L. I. Glazman, G. B. Lesovik, D. E. Khmel'nitskii, and R. I. Shekhter, *JETP lett.* **48**, 238 (1988).
- [26] G. D. Mahan and K. R. Subbaswamy, *Local Density Theory of Polarizability* (Plenum Publishing, New York, 1990).
- [27] R. Berkovits, *Phys. Rev. Lett* **81**, 2128 (1998).
- [28] M. Stopa, *Phys. Rev. B* **54**, 13767 (1996).
- [29] H. Jiang, H. U. Baranger, and W. Yang, preprint arXiv:cond-mat/0208146.
- [30] Y. Alhassid, *Rev. Mod. Phys.* **72**, 895 (2000).
- [31] E. P. Wigner, *Ann. Math.* **53**, 36 (1951).
- [32] E. P. Wigner, *Ann. Math.* **62**, 548 (1955).
- [33] E. P. Wigner, *Ann. Math.* **65**, 203 (1957).
- [34] E. P. Wigner, *Ann. Math.* **67**, 325 (1958).

- [35] C. E. Poter and N. Rosenzweig, Phys. Rev. **120**, 1698 (1960).
- [36] M. L. Mehta and M. Gaudin, Nucl. Phys. **18**, 420 (1960).
- [37] M. L. Mehta and M. Gaudin, Nucl. Phys. **25**, 447 (1961).
- [38] F. J. Dyson, J. Math. Phys. **3**, 140,157,166,1191,1199 (1962).
- [39] K. B. Efetov, Adv. Phys. **32**, 53 (1983).
- [40] L. D. Landau and E. M. Lifshitz, *Quantum Mechanis* (Pergamon Press, New York, 1977) pp. 259-263, 275.
- [41] N. H. March, *Self-Consistent Field in Atoms: Hartree and Thomas-Fermi Atoms* (Pergamon Press, New York, 1975).
- [42] B.-G. Englert and J. Schwinger, Phys. Rev. A **32**, 26 (1985).
- [43] M. G. Mayer, Phys. Rev. **60**, 184 (1941).
- [44] R. Latter, Phys. Rev. **99**, 510 (1955).
- [45] O. Bohigas, X. Campi, H. Krivine, and J. Treiner, Phys. Lett. **64**, 381 (1976).
- [46] V. M. Strutinsky, Nucl. Phys. **A122**, 1 (1968).
- [47] M. Brack, J. Damgaard, A. S. Jensen, H. C. Pauli, V. M. Strutinsky, and C. Y. Wong, Rev. Mod. Phys. **44**, 320 (1972).
- [48] C. Yannouleas and U. Landman, Phys. Rev. B **48**, 8376 (1993)

- [49] For a recent review see M. Brack and R. K. Bhaduri, *Semiclassical Physics* (Addison-Wesley, Reading MA, 1997).
- [50] For recent reviews see L. L. Sohn, L. P. Kouwenhoven, and G. Schön, editors, *Mesoscopic Electron Transport* (Kluwer Academic, Boston, 1997) and G. Timp, editor, *Nanotechnology* (Springer-Verlag, New York, 1999).
- [51] C. J. Gorter, *Physica* **17**, 777 (1951).
- [52] C. W. J. Beenakker, *Phys. Rev. B* **44**, 1646 (1991).
- [53] H. van Houten, C. W. J. Beenakker, and A. A. M. Staring in *Single Charge Tunneling Coulomb Blockade Phenomena in Nanostructures*, edited by H. Grabert and M. H. Devoret (Plenum Press, New York, 1992) pp. 167-216.
- [54] A. M. Chang, H. U. Baranger, L. N. Pfeiffer, K. W. West, and T. Y. Chang, *Phys. Rev. Lett.* **76**, 1695 (1996).
- [55] J. A. Folk, S. R. Patel, S. F. Godijn, A. G. Huibers, S. M. Cronenwett, and C. M. Marcus, *Phys. Rev. Lett.* **76**, 1699 (1996).
- [56] S. R. Patel, D. R. Stewart, C. M. Marcus, M. Gokcedag, Y. Alhassid, A. D. Stone, C. I. Duruos, and J. S. Harris, Jr., *Phys. Rev. Lett.* **81** 5900 (1998).
- [57] U. Sivan, R. Berkovits, Y. Aloni, O. Prus, A. Auerbach, and G. Ben-Yoseph, *Phys. Rev. Lett.* **77**, 1123 (1996).

- [58] S. R. Patel, D. R. Stewart, A. G. Huibers, C. M. Marcus, C. I. Duruos, J. S. Harris, Jr., K. Campman, and A. C. Gossard, *Phys. Rev. Lett.* **80** 4522 (1998).
- [59] F. Simmel, T. Heinzel, and D. A. Wharam, *Europhys. Lett.* **38**, 123 (1997)
- [60] F. Simmel, D. Abusch-Magder, D. A. Wharam, M. A. Kastner, and J. P. Kotthaus, *Phys. Rev. B* **59**, R10441 (1999)
- [61] S. Lüscher, T. Heinzel, K. Ensslin, W. Wegscheider, and M. Bichler, preprint arXiv:cond-mat/0002226.
- [62] For a review of random matrix theory in the context of quantum transport see C. W. J. Beenakker, *Rev. Mod. Phys.* **69**, 731 (1997).
- [63] R. A. Jalabert, A. D. Stone, and Y. Alhassid, *Phys. Rev. Lett.* **68**, 3468 (1992).
- [64] O. Bohigas, M.-J. Giannoni, and C. Schmit, *Phys. Rev. Lett.* **52**, 1 (1984); *J. Physique Lett.* **45**, L-1015 (1984).
- [65] T. A. Brody, J. Flores, J. B. French, P. A. Mello, A. Pandey, and S. S. M. Wong, *Rev. Mod. Phys.* **53**, 385 (1981).
- [66] Y. Alhassid, M. Gökcedag, and A. D. Stone, *Phys. Rev. B* **58**, 7524 (1998).
- [67] E. E. Narimanov, N. R. Cerruti, H. U. Baranger, and S. Tomsovic, *Phys. Rev. Lett.* **83**, 2640 (1999); E. E. Narimanov, H. U. Baranger, N. R. Cerruti, and S. Tomsovic, submitted to *Phys. Rev. B*.

- [68] Y. M. Blanter, A. D. Mirlin, and B. A. Muzykantskii, Phys. Rev. Lett. **78**, 2449 (1997).
- [69] R. O. Vallejos, C. H. Lewenkopf, and E. R. Mucciolo, Phys. Rev. Lett. **81**, 677 (1998);
Phys. Rev. B **60**, 13682 (1999).
- [70] D. R. Stewart, D. Sprinzak, C. M. Marcus, C. I. Duruoz, and J. S. Harris Jr., Science **278**, 1784 (1997).
- [71] P. N. Walker, G. Montambaux, Y. Gefen, Phys. Rev. Lett. **82**, 5329 (1999); Phys. Rev. **B 60**, 2541 (1999).
- [72] A. Cohen, K. Richter, and R. Berkovits, Phys. Rev. **B 60**, 2536 (1999).
- [73] K.-H. Ahn, K. Richter, and I.-H. Lee, Phys. Rev. Lett. **83**, 4144 (1999).
- [74] M. Stopa, Physica B **251**, 228 (1998).
- [75] M. Koskinen, M. Manninen, S. M. Reimann, Phys. Rev. Lett. **79**, 1389 (1997).
- [76] In-Ho Lee, Vivek Rao, Richard M. Martin, Jean-Pierre Leburton, Phys. Rev. B **57**, 9035 (1998).
- [77] K. Hirose, N. S. Wingreen, Phys. Rev. B **59**, 4604 (1999).
- [78] P. Hohenberg and W. Kohn, Phys. Rev. **136**, B 864 (1964).
- [79] W. Kohn and L. J. Sham, Phys. Rev. **140**, A 1133 (1965).
- [80] P. Fulde, *Electron Correlations in Molecules and Solids* (Springer, New York, 1995)
Chapter 3.

- [81] R. G. Parr and W. Yang, *Density-Functional Theory of Atoms and Molecules* (Oxford University Press, New York, 1989) pp. 51-60, 142-152.
- [82] R. M. Dreizler and E. K. Gross, *Density Functional Theory* (Springer-Verlag, New York, 1990) pp. 4-15, 44-52, and Chapter 7.
- [83] J. Ziman, *Principles of the Theory of Solids* (Cambridge University Press, Cambridge, 1972) pp. 157-160.
- [84] M. C. Gutzwiller, *Chaos in Classical and Quantum Mechanics* (Springer-Verlag, New York, 1990) pp. 254-275.
- [85] Note that even though Eq. (6.10) holds, $\mathcal{F}_{\text{DFT}}[n]$ is generally not equal to $F_{\text{H}}[n] \equiv \mathcal{E}_{\text{ip}}[V_{\text{eff}}[n]] - \int d\mathbf{r} V_{\text{eff}}[n]n(\mathbf{r}) + \mathcal{E}_{\text{tot}}[n]$ for an arbitrary density $n(\mathbf{r})$. Because of the fact that $\delta\mathcal{E}_{\text{ip}}/\delta V = n(r)$ [cf. Eq. (6.11)], it can nevertheless be shown that $(\delta F_{\text{H}}/\delta n)[n_{\text{DFT}}] = 0$. F_{H} is known as the Harris functional; see J. Harris, Phys. Rev. B **31**, 1770 (1985).
- [86] D. Ullmo, unpublished.
- [87] P. W. Brouwer, Y. Oreg, and B. I. Halperin, Phys. Rev. B **60**, R13977 (1999).
- [88] H. U. Baranger, D. Ullmo, and L. I. Glazman, Phys. Rev. B **61**, R2425 (2000).
- [89] D. Ullmo and H. U. Baranger, in preparation.
- [90] F. Herman and S. Skillman, *Atomic Structure Calculations*, (Prentice Hall, 1963).
- [91] R. I. Shekhter, Zh. Eksp. Teor. Fiz. **63**, 1410 (1972) [Sov. Phys. - JETP **36**, 747 (1973)].

- [92] I. O. Kulik and R. I. Shekhter, Zh. Eksp. Teor. Fiz. **68**, 623 (1975) [Sov. Phys. - JETP **41**, 308 (1975)].
- [93] S. Lüscher, T. Heinzl, K. Ensslin, W. Wegscheider, and M. Bichler, Rhys. Rev. Lett. **86**, 2118 (2001)
- [94] D. Ullmo and H. U. Baranger, Phys. Rev. B **64**, 245324 (2001).
- [95] G. Usaj and H. U. Baranger, Phys. Rev. B **64**, R201319 (2001).
- [96] G. Usaj and H. U. Baranger, arXiv:cond-mat/0203074 (2002).
- [97] P. W. Brouwer, Y. Oreg, and B. I. Halperin, Phys. Rev. B **60**, R13977 (1999).
- [98] Y. Oreg, P. W. Brouwer, X. Waintal, and B. I. Halperin, arXiv:cond-mat/0109541 (2001).
- [99] K. Hirose, F. Zhou, and N. S. Wingreen, Phys. Rev. B **63**, 075301 (2001).
- [100] K. Hirose and N. S. Wingreen, Phys. Rev. B **65**, 193305 (2002).
- [101] H. Jiang, H. U. Baranger, and W. Yang, arXiv:cond-mat/0208146 (2002).
- [102] P. Jacquod and A. D. Stone, Phys. Rev. B **64**, 214416 (2001).
- [103] H. U. Baranger, D. Ullmo, and L. I. Glazman, Phys. Rev. B **61**, R2425 (2000).
- [104] I. L. Kurland, I. L. Aleiner, and B. L. Altshuler, Phys. Rev. B **62**, 14886 (2000).
- [105] E. Eisenberg and R. Berkovits, Phys. Rev. B **60**, 15261 (1999).

- [106] D. Ullmo, H. U. Baranger, K. Richter, F. von Oppen, and R. A. Jalabert, Phys. Rev. Lett. **80**, 895 (1998).
- [107] H. U. Baranger, D. Ullmo, and L. I. Glazman, Phys. Rev. B **61**, R2425 (2000).
- [108] F. von Oppen, D. Ullmo, and H. U. Baranger, Phys. Rev. B **62**, 1935 (2000).
- [109] M. L. Mehta, *Random Matrices*, 2nd ed., (Academic Press, Boston, 1991).
- [110] M. V. Berry and M. Tabor, Proc. Roy. Soc. A **356**, 357 (1977).
- [111] O. Bohigas and M. -J. Giannoni, in: Mathematical and Computational Methods in Nuclear Physics, eds., J. S. Dehesa, J. M. G. Gomez and A. Polls, Proceedings of the 6th Granada Workshop, Spain, 1983, Lecture Notes in Physics 209 (1984) 1 (Springer Verlag).
- [112] O. Bohigas, in *Les Houches LII, Chaos and Quantum Physics*, edited by M.-J. Giannoni, A. Voros, and J. Zinn-Justin (North-Holland, Amsterdam 1991).
- [113] O. Bohigas, M.-J. Giannoni, A. M. Ozorio de Almeida, and C. Schmit, Nonlinearity **8**, 203 (1995).
- [114] O. Bohigas, S. Tomsovic, and D. Ullmo, Phys. Rep. **223**, 43 (1993).
- [115] M. Robnik and M. V. Berry, J. Phys. A: Math. Gen. **19**, 669 (1986).
- [116] P. K. Bera, S. Bhattacharyya, U. Das, and B. Talukdar, Phys. Rev. A **48**, 4764 (1993).
- [117] R. D. Lawson, M. Goeppert-Mayer, Phys. Rev. **117**, 174 (1960).

- [118] J. M. Richard, Phys. Rep. **212**, 1 (1992).
- [119] S. M. Blinder, J. Math. Phys. **25**, 905 (1984).
- [120] J. Besprosvany and M. Moshinsky, Phys. Rev. A **57**, 4401 (1998).
- [121] R. A. Swainson and G. W. F. Drake, J. Phys. A **24**, 79 (1991).
- [122] A. F. Nikiforov and V. B. Uvarov, *Special Functions of Mathematical Physics* (Birkhäuser, Basel, Boston, 1988).
- [123] M. V. Berry, Philos. Trans. R. Soc. Lond. A **287**, 237 (1977).
- [124] M. V. Berry, J. Phys. A: Math. Gen. **10**, 2083 (1977).
- [125] M. V. Berry, Proc. R. Soc. Lond. A **413**, 183 (1987).
- [126] S. W. McDonald and A. N. Kaufman, Phys. Rev. Lett. **42**, 1189 (1979).
- [127] S. W. McDonald and A. N. Kaufman, Phys. Rev. A **37**, 3067 (1988).
- [128] P. O'Connor, J. Gehlen, and E. J. Heller, Phys. Rev. Lett. **58**, 1296 (1987).
- [129] E. J. Heller, Phys. Rev. Lett. **53**, 1515 (1984).
- [130] E. J. Heller, in *Les Houches LII, Chaos and Quantum Physics*, edited by M.-J. Gannoni, A. Voros, and J. Zinn-Justin (North-Holland, Amsterdam 1991).
- [131] V. N. Prigodin, N. Taniguchi, A. Kudrolli, V. Kidambi, and S. Sridhar, Phys. Rev. Lett. **75**, 2392 (1995).

- [132] V. N. Prigodin, *Phys. Rev. Lett.* **74**, 1566 (1995).
- [133] M. Srednicki, *Phys. Rev. E* **54**, 954 (1996).
- [134] M. Barth and H.-J. Stöckmann, *Phys. Rev. E* **65**, 66208 (2002); M. Barth, U. Kuhl, and H.-J. Stöckmann, *Phys. Rev. Lett.* **82**, 2026 (1999); P. A. Chinnery and V. F. Humphrey, *Phys. Rev. E* **53**, 272 (1996); B. L. Lan and D. M. Wardlaw, *Phys. Rev. E* **47**, 2176 (1993); B. L. Lan, A. Shushin, and D. M. Wardlaw, *Phys. Rev. A* **46**, 1775 (1992).
- [135] W. H. Press *et. al.*, *Numerical recipes in C : the art of scientific computing, 2nd ed.*, (Cambridge University Press, New York, 1992).
- [136] Y. Alhassid, *Rev. Mod. Phys.* **72**, 895 (2000).
- [137] J. T. Edwards and D. J. Thouless, *J. Phys. C* **5**, 807 (1972).
- [138] D. J. Thouless, *Phys. Rep.* **13**, 93 (1974).
- [139] D. J. Thouless, *Phys. Rev. Lett.* **39**, 1167 (1977).